MODELING AND SIMULATION OF RESPIRATORY SYSTEM

Ph. D. THESIS

by

KM. JYOTI

DEPARTMENT OF MATHEMATICS
INDIAN INSTITUTE OF TECHNOLOGY ROORKEE
ROORKEE – 247 667 (INDIA)
MAY, 2019

MODELING AND SIMULATION OF RESPIRATORY SYSTEM

A THESIS

Submitted in partial fulfilment of the requirements for the award of the degree

of

DOCTOR OF PHILOSOPHY

in

MATHEMATICS

by

KM. JYOTI

DEPARTMENT OF MATHEMATICS
INDIAN INSTITUTE OF TECHNOLOGY ROORKEE
ROORKEE - 247 667 (INDIA)
MAY, 2019

INDIAN INSTITUTE OF TECHNOLOGY ROORKEE ROORKEE

CANDIDATE'S DECLARATION

I hereby certify that the work which is being presented in the thesis entitled **"MODELING AND SIMULATION OF RESPIRATORY SYSTEM"** in partial fulfilment of the requirements for the award of the Degree of Doctor of Philosophy and submitted in the Department of Mathematics of the Indian Institute of Technology Roorkee, Roorkee is an authentic record of my own work carried out during a period from July, 2013 to May, 2019 under the supervision of Dr. Pratibha, Associate Professor, Department of Mathematics, Indian Institute of Technology Roorkee, Roorkee.

The matter presented in this thesis has not been submitted by me for the award of any other degree of this or any other Institution.

(KM. JYOTI)

This is to certify that the above statement made by the candidate is correct to the best of my knowledge.

(Pratibha)
Supervisor

Date: 17/05/2019

The Ph.D Viva-Voce Examination of **Km. Jyoti**, Research Scholar, has been held on **06/09/2019**.

Chairperson, SRC **Signature of External Examiner**

This is to certify that the student has made all the corrections in the thesis.

Signature of Supervisor **Head of the Department**

Abstract

Respiration is the act of breathing, which is not possible without respiratory system. The respiratory system combines nose, throat, and lung. Lung [1] is the main organ, which performs the process of respiration. Airways inside lung bifurcate from the trachea to terminal airways (known as alveoli) in 23 generations and are collectively termed as *tracheobronchial tree*. Generations 0 to 15 take part to conduct air in other airways and generations 16 to 23 perform the process of gas exchange. When we inhale, gases such as nitrogen (78 %), oxygen (21 %), argon (0.965 %), carbon dioxide (0.04 %), helium other gases, and water droplets present in the air enter our lungs. The hemoglobin in red blood cells contains iron due to which oxygen is immediately absorbed whereas other gases remain inert with respect to the blood's constituents, and are sent out during exhalation. Not only gases and water droplets but also other environmental particles with different shapes and sizes are inhaled with air and flow with air stream in different generations of the lung. Deposition of these particles causes various lung diseases such as asthma, chronic obstructive pulmonary disease, emphysema, fibrosis, stenosis, atherosclerosis, cancer, apnea, etc. Because of the structural change during respiration engineers, physicists, and mathematicians viewed lung as a mechanical system and performed theoretical, experimental and mathematical studies [39, 179, 204, 225] by applying sophisticated mathematical and computational methods over the past few decades.

In respect of particle deposition inside lung generations, many studies [27, 79, 141, 224] have focused on various sizes and shapes particles. In most of the studies, microparticles have been considered, while some studies focused on nanoparticles (average size of particles are below 100 nm). But in real situations, many particles generated industrially are not necessarily spherical in shape. Many particles found in industries (cosmetic, textile, timber, material, grinding and polishing, etc), harvesting, coal mines, cigarette smoke, cooking smoke, incomplete combustion, organic fragments, fine hairs from plants and animals, and atmospheric dust differ in their flow characteristics and can

---

[1] Combines left and right lungs

be categorized as nonspherical nanoparticles. Due to the irregular shape and different flow characteristic of nanoparticles such as stretched spheroid, elongated or oblate, pollen, it is not yet possible to provide a single constitutive equation describing the properties of all shape nonspherical nanoparticles. Because of this fact, several theoretical and stochastic models of nonspherical nanoparticles have been proposed. To deal with the appropriate shape of nanoparticles, the 'shape factor' has attracted the attention of many researchers [62, 177, 218, 225]. This is because of the reason that the corresponding constitutive equation is comparatively less complicated and one can hope for the analytical and numerical solutions. In view of these facts, we consider the 'shape factor' of nonspherical nanoparticles in this thesis.

In lung mechanics, one can use two types of elastic model i.e. linear or nonlinear. Many of the earlier studies have considered nonlinear elastic model, but some of the living tissues and cells are very soft and followed the linear postulate of elasticity that the stress tensor is directly proportional to the deformation tensor. When working on the pulmonary region of lung the elasticity is controlled by viscosity and named as viscoelasticity. In the pulmonary region, the gas is transferred not only by fluid movement but also by the mechanical movement of tissues. Several models [52, 139, 164] of viscoelasticity have been proposed in the literature. However, the simplest forms of the viscoelastic material are defined by Kelvin-Voigt which has attracted the attention of several researchers. So, the effect of viscoelasticity has been studied in the present work in order to show its effect on the flow of fluid through parenchymal tissues.

Another way to makes the mathematical model more realistic is the use of the variable porous medium. Alveoli, tiny bubbles with an interconnected void, are supplies a porous region (alveolar region and parenchyma), where gas exchanges with the blood take place [42]. A few studies focused on the variable porosity of lungs. The interest in this topic has been stimulated, due to its three specifications: first, structural change in alveoli and lung volume during breathing; second, a number of alveoli changes with respect to age. Third, the irregular motion of the nonspherical nanoparticle around the individual alveoli responsible for deposition inside alveoli more effectively. So, variable porosity has an obvious influence on the flow pattern. Thus in the present work, studies are conducted involving variable porous media.

Many researchers have focused on capillary flow by using conventional Krogh cylinder model [195, 204, 247] while a few have considered exchange of species in between capillary blood and surrounding tissue or intercapillary flow. For better understanding, the process of gas exchange from alveolar capillary to pulmonary capillary inclusion of intercapillary process is needed.

Finally, the motivation behind the thesis is to make the mathematical model of lung mechanics more realistic, by incorporating the idea of variable porosity of lung, shape factor of nonspherical nanoparticle, viscoelasticity of parenchymal tissue, inter capillary gas transfer from alveoli to the pulmonary capillary.

Numerical simulation of the problems is carried out by using conventional explicit finite difference method [188]. Results are displayed in the form of graphs in Origin (8.0) and behavior of fluid particles are visualized by images generated in MATLAB R2013 and R2016. The whole work of the thesis is divided into nine chapters and chapter-wise summary of the thesis is as follows:

Chapter 1 is introductory in nature and gives a brief account of the general theory of lung mechanics, disease, human respiratory system, air flow in capillaries, deposition mechanism of various sizes and shapes nanoparticles, mathematical modeling and numerical solutions in biology. It presents the current status of the field, motivation to the investigations, a review of the available literature and tools/techniques used in the study. It also includes objective and brief ideas about various concepts used in the forthcoming chapters.

In **Chapter 2**, we investigate the flow dynamics of needle prolate nanoparticle from generations 5-16 under periodic permeability of airways with oscillatory boundary conditions. An appropriate one-dimensional unsteady momentum equation in the cylindrical polar coordinate system is used by incorporating the idea of the shape factor of needle prolate nanoparticles. Filtration efficiency of the lung from generations 5-16 is also calculated using appropriate biofilter model. The effect of various physical parameters, such as mean permeability of media (K_0), the aspect ratio of particle (β), the orientation of particle with respect to the flow stream, Reynolds number (Re), and frequency of oscillation (f) are analyzed on the flow dynamics of air, particles and filtration efficiency of lung. Results show that the aspect ratio of a particle causes an increment in drag force and decrement in pressure gradient; and for parallel orientation velocity of particles increases than perpendicular orientation. Additionally, we obtained that the filtration efficiency of lung varies inversely with the value of mean permeability.

In **Chapter 3**, we presented an age-based study of the human lung from childhood to the age of 30 by considering the growth of lung is caused by a progressive increment in a number of alveoli and calculated its effect on airflow dynamics and filtration efficiency of the human lung. Incorporating the idea of filtration through lung with respect to age biofilter model is extended for variable porous media by assuming that the porosity of lung varies with the number of alveoli and their surface area. Additionally, transportation and filtration properties of nanoparticles of various shapes during inhalation are calculated by using particle shape factor with and without orientation of the particles. Generalized Navier Stokes' equation is used for flow dynamics of viscous air and Newton second law of motion is applied to study the flow of particles. Effect of aspect ratio (β), the orientation of particles with respect to the flow stream, Darcy number (Da), and porosity (ϵ) are studied. Results indicate that the filtration efficiency of lung decreases as age increases from childhood to 30 years; additionally, nonspherical nanoparticles with high aspect ratio's will take a longer time to be filtered from the lung as compared to spherical nanoparticles.

In **Chapter 4**, we use a mathematical model to study the effect of homogeneous porosity of the alveolar region on the flow dynamics of viscous air by considering a pulsatile pressure gradient due to periodic breathing of respiratory system. Two-dimensional momentum equations are used with Darcy law to show the flow through porous media. An extensive quantitative study is performed through a finite difference technique to solve the governing equation. Effect of Reynolds number (Re), Darcy number (Da), porosity (ϵ) are studied on air and particle velocities inside the alveolar region. Results show that porosity is an active factor for deposition of nanoparticles and the fraction of particles trapped in the alveolus increases by decreasing the Darcy number.

In **Chapter 5**, we consider lung as a porous permeable medium to build a mathematical model of early-stage emphysema. The computational geometry utilized in this study spans one generation of alveolar duct attached with alveoli. Two-dimensional generalized equation of momentum is used to study the flow of air and equation of motion for elongated shaped nanoparticles. Variable porosity is used by incorporating the idea of change in volume during ventilation together with a shape factor of elongated shaped nanoparticles. Various parameters such as inlet Reynolds number (Re), media porosity (ϵ), Darcy number (Da), breathing rate (f), and particle shape factor (S_f) are varied to study the condition of the emphysematous lung. Results demonstrated that during inhalation, breathing stress increases and the deposition of particles is smaller due to the rupture alveoli in an emphysematous lung as compared to a healthy lung.

In **Chapter 6**, we focused on the flow through an axisymmetric constricted artery of the pulmonary region to study the condition of stenosis. Theory of dust particles suspended in gas is applied on blood flow through the artery, where the 'particles' represent 'cells' suspended in plasma. The flow is governed by two dimensional Navier-Stokes' equations by including Darcy-Forchheimer drag force caused by non-Darcian effect. The material of the artery is approximated as a linear elastic and simplest rheological equation that includes viscosity and elasticity (considered lung as a Voigt body) is used. Effect of various parameters, such as Reynolds number (Re), Forchheimer number

(F_s), Darcy number (Da), aspect ratio (β), shape factor (S_f), porosity (ϵ), aerodynamic diameter (d_p), bulk compression (ϕ) of elasticity, shear (η) and bulk (ζ) coefficients of parenchymal viscosity are obtained on the radial and axial velocities of blood and particles graphically. We found that the fluid (blood) and particle (cells suspended in plasma) velocities along both the axes (axial and radial) increase by increasing Reynolds number, the pulsating amplitude, aspect ratio, and porosity of walls. While by increasing Forchheimer number, velocities of blood and particles in both the axes decreases gradually. The present analysis is also indicate that the viscoelasticity of walls are affected by the amplitude of pulsatile flow of blood and for a large value of amplitude, the viscoelastic effect decreases.

In **Chapter 7**, we analyzed the behavior of fluid flow through parallel walls, where both walls are porous and flow is induced by the oscillation of walls and sinusoidal pressure gradient. Concept of generalized Couette flow is applicable to model the flow of mucus through oscillatory walls, where porous walls are partially filled with fluid (mucus). Mathematical modeling of the flow of viscous fluid is done by using two-dimensional generalized momentum equations and flow of particle is done by using Newton equation of motion. Finite difference method is used to solve the problem numerically. Effect of wall oscillation frequency (f), wall porosity (ϵ), pressure (p), and particle aspect ratio (β) are calculated to make various hypotheses related to clearance of mucus. Result show that high frequency of breathing is applicable to clearance of mucus from the airways.

In **Chapter 8**, we worked on the effective area average concentration and dispersion coefficient associated with the unsteady flow, to understand the dispersion in the fibrosis-affected lung. We assumed that the tube wall (i.e. alveolar or pulmonary capillary wall) is thicker than its normal size due to fibrosis and chemical species may go through linear first-order kinetic reactions, one is reversible phase exchange with the wall material and other is irreversible absorption into the tube wall. By considering diffusivity as a function of thickness, the dispersion can be calculated by the distribution of concentration of gas along a tube. Mathematical modeling is done by using diffusion equation; and effects of various dimensionless parameters e.g., the Damkohler number (DA), phase partitioning number (α), dimensionless absorption number (Γ), thickness and permeability of wall are observed. Numerical simulation shows that the diffusion rate through the respiratory wall is decreased significantly as the thickness of wall increases, while it increased with the increment in the porosity of wall, the concentration of species increased when the tube wall thickness increases; which cause reduction in the spread of the species; additionally, the dispersion coefficient achieves the steady-state values in a very short time when $0 <$ Damkohlar number ≤ 1 and absorption rate < 1, while for $1 <$

Damkohlar number ≤ 20 and absorption rate =1 long time dispersion is achieved.

In the last **Chapter 9**, we present a mathematical model of spatial and temporal variations in inhaled gas partial pressure within the tissue and concentric blood capillary. Gas exchange between capillary blood and surrounding tissue is take place through the combined effect of convection and diffusion. We assumed capillary material is absorptive and reactive and the gas could bear linear first-order kinetic reactions, one is reversible among capillary material and other is irreversible into the surrounding tissue. Partial pressure distribution of gas between immobile (tissue) and mobile (blood) phase (through the interface) is calculated with the help of Aris method of moments. Effect of various non-dimensional parameters e.g., the Damkohler number (DA), phase partitioning number (α), dimensionless absorption number (Γ) are analyzed. The inferences we have drawn are (i) partial pressure of gas decreases inside tissue by increasing the value of porosity, (ii) by increasing breathing rate, partial pressure of gas first decreases and after some time it increases with breathing rate inside blood, (iii) under the consideration of tissue porosity or permeability, the convection speed does not change but the diffusion of gas increases from tissue, which causes increment in pressure gradient in mobile phase. Hence, these results can be helpful to optimize the reactive condition of excessive permeability of tissue due to aging, emphysema, asthma, and tuberculosis.

The thesis, finally, ends with the future research directions regarding studies done in this thesis, appendices, and bibliography.

List of Publications

Journal Papers

1. Kori, J. and Pratibha (2018). Numerical simulation of mucus clearance inside lung airways. *Journal of Applied Fluid Mechanics*, 11(5): 1163-1171.

2. Kori, J. and Pratibha (2019). Simulation and modeling for aging and particle shape effect on airflow dynamics and filtration efficiency of human lung. *Journal of Applied Fluid Mechanics*, 12(4):1273-1285.

3. Kori, J. and Pratibha (2019). Numerical simulation of dusty air flow and particle deposition inside permeable alveolar duct. *International Journal of Applied and Computational Mathematics*, 5(17):1-13.

4. Kori, J. and Pratibha (2019). Effect of periodic permeability of lung tissue on fluid velocity and nonspherical nanoparticle filtration. *International Journal of Applied and Computational Mathematics*, 5(49):1-15.

5. Kori, J. and Pratibha (2019). Effect of periodic permeability of lung airways on the flow dynamics of viscous fluid. *Nanosystems: Physics, Chemistry, Mathematics*, 10(3):235-242.

6. Kori, J. and Pratibha (2019). Mathematical modeling of pulsatile flow due to rhythmic breathing through emphysema affected lung. *Applications and Applied Mathematics: An International Journal*, 14(1):296-311.

7. Kori, J. and Pratibha (2019). Effect of dynamic shape factor in alveolar region as a filtration media. *World Journal of Modeling and Simulation*, 15(2):95-105.

Conferences

1. Jyoti, Km. and Pratibha (2014). Simulation and modeling of lung mechanics: critical roles of porosity and particle deposition-a review. *International Conference on Recent Trends in Mathematical Analysis and Its Applications*, Indian Institute of Technology Roorkee, Roorkee, India jointly organized with University of Central Florida, Orlando, USA, December 21-23.
2. Kori, J. and Pratibha (2016). A mathematical study on couette flow inside lung airways. *Recent Advances in Theoretical and Computational Partial Differential Equations with Applications*, Punjab University, Chandigarh, India, December 05-09.
3. Kori, J. and Pratibha (2018). Two dimensional mathematical modeling of viscous air flow inside pulmonary region. *Fourth International Conference on Mathematics and Computing 2018*, Indian Institute of Technology BHU, Varanasi India, January 09-11.
4. Kori, J. and Pratibha (2018). Numerical simulation of dusty air flow and particle deposition inside permeable alveolar duct. *International Conference in Conjunction with 14th Biennial Conference of ISIAM*, Guru Nanak Dev University Amritsar, Punjab, India, Feb 2-4.
5. Kori, J. and Pratibha (2018). Mathematical modeling of nanoparticle removal efficiency of different age group lung. *International Conference On Mathematical Modelling And Computations In Biosystems*, Indian Institute of Technology Roorkee, Roorkee, India, March 12-14.
6. Kori, J. and Pratibha (2018). Numerical study of deposition and clearance of inhaled elongated nano particles through alveolar region. *International Conference on Frontiers in Industrial and Applied Mathematics*, National Institute of Technology Hamirpur, Himachal Pradesh, India, April 26-27.
7. Kori, J. and Pratibha (2018), Analysis of wall shear stress of stenosis affected artery by mathematical modeling and simulation, *International Conference on Mathematical Methods and Models in Biosciences (Biomath)*, Sofia, Bulgaria, June 24-29, abstracted in: Biomath Communications Supplement, 5(1).
8. Pratibha and Kori, J. (2018). Effect of particle aspect ratio and shape factor on air flow inside pulmonary region. *20th International Conference on Applied Mathematics and Engineering Mathematics*, Toronto, Canada, June 21-22, abstracted in: International Journal of Mathematical and Computational Sciences, 12(6).

9. Kori, J. and Pratibha (2018). A study of movement of mucus inside lung airways through generalized couette flow. *National Conference on Modeling, Optimization and Computing for Engineering Problems: Use of Technical Hindi Terminology*, Indian Institute of Technology Roorkee, Roorkee, India, October 12-14.

10. Pratibha and Kori, J. (2018). A study of particle deposition in emphysema affected lung. *National Conference on Modeling, Optimization and Computing for Engineering Problems: Use of Technical Hindi Terminology*, Indian Institute of Technology Roorkee, Roorkee, India, October 12-14.

Communicated Papers

1. Kori, J. and Pratibha. Mathematical modeling and simulation of viscous fluid flowing through porous and viscoelastic artery affected by stenosis. *Journal of Computational Science (Elsevier Publication).*

2. Kori, J. and Pratibha. A mathematical study of first order chemical reactions in the fibrosis affected lung. *Computational and Applied Mathematics (Springer Publication).*

3. Kori, J. and Pratibha. Mathematical modeling of partial pressure distribution of inhaled gas through tissue-blood interface. *Journal of Applied Mathematics and Computing (Springer Publication).*

Acknowledgements

This Ph.D. thesis had been difficult to reach the final stage without the support and encouragement of numerous people including my well-wishers, my friends, and family. It is a pleasing task to precise my gratitude to each one of the individuals, who contributed in one manner or the other to offer the final shape of the thesis which is a memorable experience for me.

First and foremost I would like to thank the **Almighty God** for being my strength and guide me to write this thesis. Without Him, I would not have had the wisdom of the physical ability to do so.

It gives me immense pleasure to have the privilege of extending my heartfelt appreciation and sincere gratitude to my esteemed supervisor, **Dr. Pratibha**, Associate Professor, The Department of Mathematics, Indian Institute of Technology Roorkee, Uttarakhand, India. Being my supervisor, her involvement with this work goes right from the begin with the choice of the topic and the suggestions of the resource materials to the significant sources of info, checking and corrections of the initial and subsequent drafts. I have learned extensively from her, including how to raise new possibilities, how to regard an old question from a new perspective, how to approach a problem by systematic thinking, and data-driven decision making. In every meeting, her positive and spiritual behavior gave me confidence in myself to improve my work according to her suggestions. This thesis would not have been possible without her valuable guidance, advise, constant encouragement, and support which she has given me all through my Ph.D. work. Thank you for believing in me when I found it difficult.

I am highly obliged to Department of Mathematics, Indian Institute of Technology Roorkee, India and all faculties for providing the departmental facilities for carrying out my research work. I sincerely thankful to Prof. Kusum Deep, DRC and my Student Research Committee (SRC) members Prof. Rama Bhargava and Prof. Kusum Deep from the Department of Mathematics and Prof. M. Parida from the Department of Civil Engineering, IIT Roorkee for their insightful comments and encouragement that helped me in improving the quality of my research work. I express my earnest regard to Dr. R. C. Mittal and Dr. V. K. Katiyar, the ex Heads and Dr. Nagrajan Sukavanam, Head and Professor, Department of Mathematics, IIT Roorkee, Roorkee, India for providing computational and other infrastructural facilities during my thesis work. I am indebted to the 'Ministry of

Human Resource Development, Government of India' for providing me financial support to carry out my research work.
The administrative staff in the department has been continuously helpful. I especially thank Mr. Ved Prakash Verma, Mr. Lekhraj, Mr. Kshitij Yadav, Mr. Rahul, Miss Ritu, Mrs. Pooja, Mr. Islam, Mr. Javed for all their assistance.

Certainly, I would miss the company of my friends, colleagues and many others who had been in my contact during my research. I would like to acknowledge my sincere thanks to my lab colleagues including seniors and juniors Dr. Anju Saini, Dr. Dev Datta, Mr. Amit Kumar, Mr. Rahul, Miss Manisha, Dr. Mania Goyal, Dr. Renu Rana, and Mr. Tajender have all extended their support in a very special way and I gained a lot from them, through their personal and scholarly interactions, their suggestions at various points of my research programme. I am also thankful for encouragement, support and co-operation which I have received from my friends Alka, Neha Singhal, Sumit Malik, Sumita, Ruchi Panwar, Kalu Ram, Avinash, Vanita, Rangoli, Anil Kori, Arshi, Rahul Saini and Pooja Gupta are beyond the scope of my acknowledgment, yet I would like to express my heartfelt gratitude to them for their help and moral support.

Last but not least, I feel a deep sense of gratitude for my grandparents Late **Shri. Sita Ram and Smt. Shyama Devi**, my father **Shri. Sahadev Prasad**, mother **Smt. Daya Devi**, my uncle (Chacha Ji) **Shri. Suresh Kumar** who formed part of my vision, taught me good things and always provided me a constant source of joy, moral support, love, encouragement, and aim throughout my study. The time they spent, the opportunities they provided and the instructions they gave continuously to bless my life. Their patience and sacrifice will remain my inspiration throughout my life. I am also very much thankful to my brothers Umesh and Yash together-with my sister Chanchal for their impatience that pushes me through and guides me to do work with positive thinking.

I cannot found words to express my love towards my uncle (Chacha Ji). His struggle and patients always motivate me to do something better than today. This thesis is heartily dedicated to my Chacha Ji, who has been the stirring source behind this research work. I find myself very lucky and heartily thankful to God that I have an uncle like him.
At last, I am thankful to everyone including those whose name might have missed unknowingly.

Km. Jyoti
IIT Roorkee, Roorkee
May , 2019.

Table of Contents

Chapter 3 Mathematical study of various shapes nonspherical nanoparticle deposition and filtration through alveolar region of human lungs of age 1-30 55

List of Figures

List of Tables

Nomencleture

Roman Symbol	**Notation**
a	radius of duct
a_0	pulsatile amplitude
b	Forchheimer inertial resistance parameter
b_1	biological degradation constant
$c(z, r, t)$	concentration of the species dissolved per unit volume in the mobile phase of fluid
$c_s(z, r, t)$	concentration of the species in immobile phase preserved per unit area of tube wall.
c	local concentration of solute
C	Cunningham slip correction factor
d	diameter of spherical particle
d_i	inner diameter of alveolus
d_o	outer diameter of alveolus
d_p	diameter of nonspherical particle
D	Diffusion coefficient in blood
Da	Darcy number
DA	Damkohler number
D_C	diffusion coefficient in plasma
D_T	diffusion coefficient in tissue
f	frequency
F_d	drag force on nonspherical particle
F_s	Forchheimer number
F	drag force on spherical particle
g_r	axial component of gravity
g_z	radial component of gravity

k	the reversible reaction rate
k_f	Stokes drag force
k_m	partitioning coefficient
K_0	mean permeability of media
m	mass concentration of dust particle
N_0	number density of the dust particles
N_a	number of alveoli in human lung
p	fluid pressure
$p(r, z, t)$	partial pressure inside blood
$p_t(r, z, t)$	partial pressure inside tissue
$P(x, z, t)$	Partial pressure of air
P_0	atmospheric pressure
Pe	Peclet number
P_l	particle load
$P_t(X, Z, t)$	Partial pressure of blood
r	radial axis
r'	radius of lung
r_o	radius of alveoli
Re	Reynolds number
R_C	radius of the capillary
R_T	radius of the tissue
S	surface area of spherical particle
S'	surface area of nonspherical particle
s_k	Stockeian coefficient
$S_{\parallel}$	parallel orientation of particle
$S_{\perp}$	perpendicular orientation of particle
S_f	dynamic shape factor
S_t	Strouhal number
t	stands for time
t'	dimensionless traveling time
u	velocity of air or blood
u_0	velocity of the flow at the center of the tube

u_r	velocity in radial direction
u_z	velocity in axial direction
v	velocity of dust particles
v_r	particle velocity in radial direction
v_z	particle velocity in axial direction
z	axial axis
z_s	initial slug length
Greek Symbol	**Notation**
α	the partition coefficient
α_c	Solubility of oxygen in plasma
α_t	Solubility of oxygen in tissue
β	particle aspect ratio
ϵ	porosity of media
f	breathing rate or oscillation frequency
Γ	irreversible absorption rate
λ	mean free path of the gas
λ'	first order reaction rate constants for the mobile phase
μ	coefficient of dynamic viscosity of the fluid
ν	kinematic viscosity
ρ_0	unit density
ρ	air density
τ_e	stress due to emphysema
τ_v	stress due to viscoelasticity

Chapter 1: Introduction

1.1 Biomechanics

The motion and function of lifeless and biological systems are governed by mechanics. Many scientist-philosophers (such as Leonardo da Vinci (1452-1519), Galileo Galilei (1564-1642), Johannes Kepler (1571-1630), Rene Descartes (1596-1650), and Isaac Newton (1642-1726)) had focused on the mechanical interactions between biological systems and the environment. The discovery of these mechanical interactions has come to create a discipline of analysis known as biomechanics. Biomechanics is the study of mechanics that manages the flow of fluid in biological systems together with the mechanical consequences of the body's movement, with respect to size, shape, and structure [142]. To demonstrate the inner mechanics of cells and the mechanical properties of soft or hard tissue's science of mechanics [83], engineering principles, and biological methods, physical laws are applied and constitutive equations are derived which have their applications in physiology, medicine, surgery, materials, and many others. Thus, biomechanics is the basic science for the advancement in biomedical engineering.

Biomechanics has been defined in many different ways but according to Fung et al. [65], research in biomechanics needs knowledge of:

- The geometry of the system such as anatomical, morphological and histological studies
- The materials of the system and their mechanical properties
- The basic laws governing the system, and
- The boundary conditions

1.1.1 Classification of biomechanics

Biofluid mechanics

Biofluid mechanics is a combined study of the flow of gas and liquid in or around biological system [134] by using fundamental principles of fluid mechanics [145]. It is a conjunction of mechanical engineering and biological engineering that varies from cells to organs and covering various aspects of the functionality of general physiology such as blood flow within the human circulatory system, air flow in human respiration, reproductive, urinary, musculoskeletal and neurological systems, etc. To boot biofluid mechanics and its simulations, the concept of fluid dynamics are applied in internal as well as external flow.

- **Internal biofluid mechanics**-Internal biofluid mechanics is basically concerned with fluid flow, transport of mass and heat, blood flow in veins and arteries, peristaltic pumping flow, urine, interstitial flows [136], within a living being flow of air in the respiratory system.
- **External biofluid mechanics**-External biofluid mechanics, however, concern with the flow of fluids viz. air and water outside the living beings, e.g. flights of birds in the air and aquatic locomotion such as swimming of fish in water [135].

Biosolid mechanics

Biosolid mechanics is the study of the mechanics of biological solid material such as bones and tissues. For solid materials, the stress-strain curve is used which give information about their strength, extensibility, and work of fracture. In general, biological tissues behave like a viscoelastic material but a few biological materials (stress-strain relation may be linear or nonlinear), such as bones, the linear elasticity is not applicable as long as the deformation is not small.

The range of biomechanics is too wide so we blend it into two sciences, i.e. physiology and mechanics. The major physiological areas, which carries major difficulties are covered by the cardiovascular system, the pulmonary system, muscle mechanics, nervous system, digestive tract, and endocrine system.

1.2 Human Respiratory System

The human respiratory system extracts oxygen from the air and transfers it into the bloodstream, and in return, release carbon dioxide from the bloodstream into the air. Respiratory system (Figure 1.1) includes nose, pharynx, larynx, trachea, and lungs (bronchi, bronchioles and their smaller branches or duct), which contain the terminal air sacs, or alveoli. The respiratory system can be separated into the following regions based on its functions and anatomy [21].

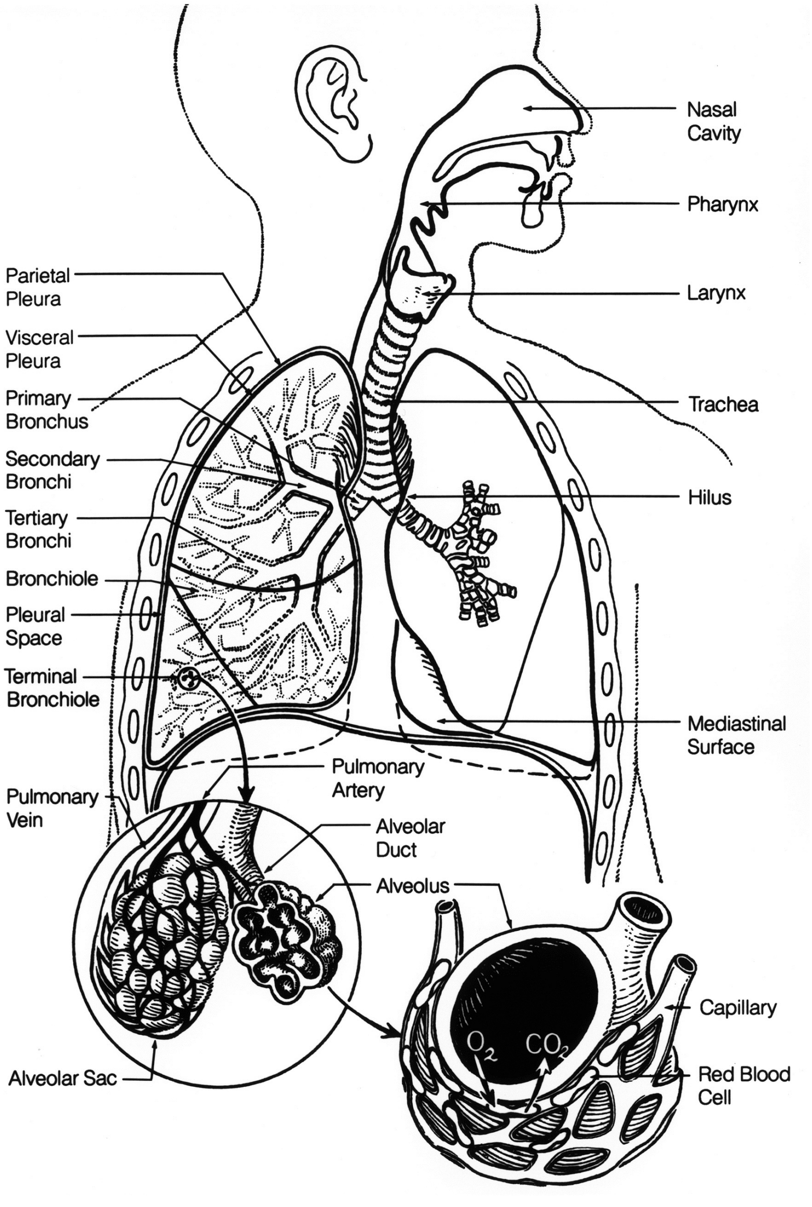

Figure 1.1: Anatomy of human respiratory system [21].

- **Conducting zone**-The conducting zone includes nose, trachea, upper respiratory system 0 to 16 and all those passageways, which are helpful in reaching the air to the gas exchange sites but not in direct contact with the pulmonary capillaries. The passageways of conducting zone clean, warm, and humidify the incoming air; so that very fewer particles of dust, bacteria, and other irritants are reaches in the deep lung generations as compare to initial inhaled air.

- **Respiratory zone**-The respiratory zone includes bronchioles, alveolar duct, alveolar sac and alveoli (forms the end of the respiratory tract), through which air reaches to gas exchange area, i.e. gas-blood barrier (pulmonary capillary network in their walls), where the process of gas exchange takes place.

- **The intermediate or transition zone**-The transition zone of tubes very closely associated with alveoli and forming a link between respiratory and conducting zones.

1.2.1 Process of respiration or mechanics of breathing

In the human body, the respiratory system provides oxygen to the tissues and removes carbon dioxide from the blood. The lung is a main muscleless organ which is responsible for respiration [173]. Respiration is a process of inspiration and expiration. Inspiration and expiration are initiated by the contraction and extraction of the diaphragm. The diaphragm lines the lower part of the thorax, sealing it off air-tight from the abdominal cavity below. To perform the task of respiration some sub-processes, which are collectively called respiration must be happened (Figure 1.2), such as:

- **Pulmonary ventilation**- Movement of air from the atmosphere to lung and lung to atmosphere so that the gases (oxygen and carbon dioxide) are consistently exchanged and refreshed is generally called breathing.

- **Inspiration**- During inspiration diaphragm contracts and descends from 10 cm to 1 cm, Its contraction causes muscles in the thorax to pull the anterior end of each rib up and outwards enlarging its volume, and the contents of the abdomen are pushed downward. This results in a larger thoracic volume and negative pressure (with respect to the atmospheric pressure) inside the thorax. The pressure inside the thorax, i.e. intrathoracic pressure, and inside the lungs, i.e. intrapulmonary pressure, decreases relative to the atmospheric air pressure. Consequently, decrement in the pressure of the chest is responsible for the movement of air into the upper respiratory tract, where the air is filtered, warmed, and humidified.

- **Transport of respiratory gases**- Inhaled air includes, 78 % nitrogen, 21 % oxygen, 0.965 % argon, 0.04 % carbon dioxide, helium, water droplets, and other gases, which reaches to the alveoli, where oxygen diffuses into the capillaries, while carbon dioxide diffuses back into the air. This transport is accomplished by the cardiovascular system using blood as the transporting fluid.

- **Expiration**- The lungs have a natural elasticity, as they recoil from the stretch of inhalation, air flows back out until the pressure in the chest and the pressure in the atmosphere reach equilibrium. Expiration is generally a passive process, in which the lung and chest wall returns to its equilibrium position and shape. During slow breathing, only the elastic recoil of the lung and chest walls is needed to return the thorax to equilibrium, while in forceful expiration additional muscles (intercostals) in the thorax and abdomen are also used for further increment in the pressure.

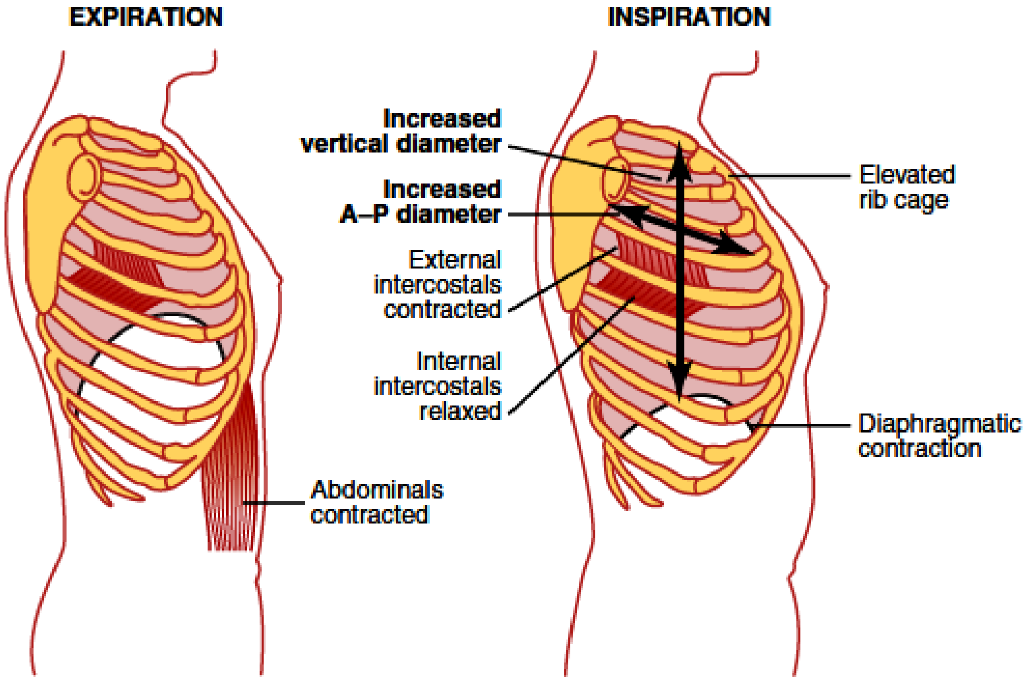

Figure 1.2: Function of respiration during expiration and inspiration [78].

1.2.2 Amount of oxygen and carbon dioxide used during alveolar ventilation

Exchange of oxygen and carbon dioxide takes place all along the 2800 km length and 70 m^2 of the surface area of the pulmonary capillaries. The exchange is governed by the partial pressures of oxygen and carbon dioxide in the alveoli and in the pulmonary capillaries, the diffusivity of the walls and those areas of walls which are in contact with one another. The inspired air is at about 760 mm of Hg pressure and it contains about 20.95 % of oxygen so that the partial pressure of oxygen in inspired air is (20.95/100) x 760 mm of Hg $\approx$ 159 mm of Hg. Similarly, the partial pressure of carbon dioxide in inspired air is (0.04/100) x 760 mm of Hg = 0.30 mm of Hg. A pressure difference of 60 mm of Hg drives oxygen from alveolar space to pulmonary capillaries [212]. Similarly, a pressure difference of 6-7 mm of Hg drives carbon dioxide from pulmonary space to alveolar space. Though the pressure difference for carbon dioxide is much smaller than that for oxygen, yet its diffusivity is equally important since the solubility of carbon dioxide in blood plasma is about 20 times that of oxygen.

1.2.3 Effect of dead space on ventilation

A portion of the air an individual inhales never achieves the gas exchange areas but simply fills conducting respiratory passages where gas exchange does not occur [104] is called dead space. In the process of inspiration, a normal person takes about 0.5 litres or 500 ccs of air, of which about 350 ccs go to the alveoli and the remaining to dead space of airway segments and conducting proximal air channels. On expiration, the air in the dead space is expired first, before any of the air from the alveoli reaches the atmosphere. Hence, the dead space is very harmful to removing the expelling gases from the lungs.

1.2.4 Inert gases

In nature, inert gases are found primarily in the atmosphere. Atmospheric nitrogen is the most common example. Helium and argon are the other inert gases commonly used in breathing mixtures for divers. Specific physiological processes inside the human body may be indicated by trace gases originating from the lung. The mixing of inspired air with gas in the lungs is the initial step in the procedure of gas exchange between the atmosphere and the tissues. It is a step which is critically damaged by a wide range of pulmonary diseases. Inert gases have been shown to be useful for quantitative analysis of gas exchange both in lungs and tissues.

1.2.5 Function of respiratory system

The major functions of respiration are [78]:

- The respiratory system is responsible for the first two steps in oxygen transport from inspired air to muscle mitochondria: the bulk transport of oxygen from atmospheric air to alveoli and the transfer of oxygen from alveolar gas to pulmonary capillaries.

- The respiratory system is also responsible for regulating carbon dioxide levels in the body and for much of the regulation of pH.

- Importantly, arterial blood gas homeostasis maintained at a minimum energy expense to the organism by the respiratory system.

- Pulmonary vascular resistance and vascular pressures maintained low to limit the load on the right heart and prevent trauma to the delicate alveolar-capillary interface.
- The ultimate importance of the respiratory system is to continually renew the air or regulate ventilation in the gas exchange areas (air-blood barrier) of the lungs.

1.3 Human Lung

The lung is an important part of the respiratory system. Human lung is branched in two parts, left and right. The lungs are enclosed within the pleural sac, which divides each lung into sections called lobes. Pleural sac also protects the lungs and allows the lungs to expand and deflate, without much friction. The right lung composed of three lobes whereas the left lung is slightly smaller consisting of only two lobes. The right lung accounts for 55% of overall gas volume and the left lung for 45%. The lung itself also consists of two parts: the leading air passages and the respiratory air passages.

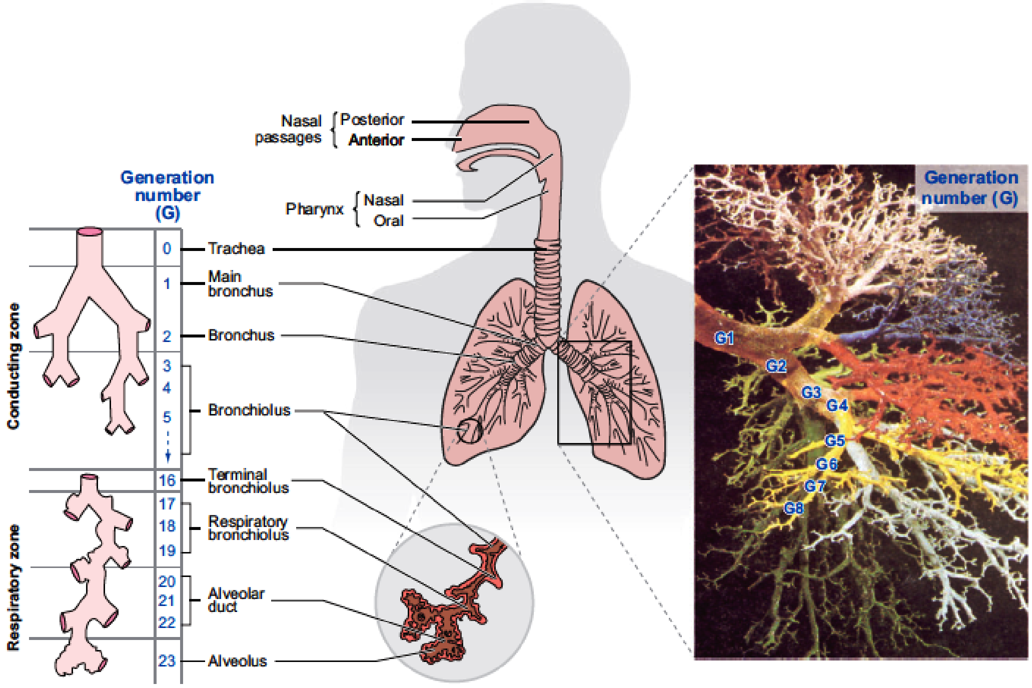

Figure 1.3: Human lung as a branched network [114].

The leading air passages only transport the air deeper into the lungs and consist of the trachea and its main branches, which is subdivided into secondary lobar bronchi. The lobar bronchi branch into tertiary bronchi, which divide repeatedly into fourth-order, fifth-order, bronchi, etc. This process continues for 20-23 generations, as shown in Figure 1.3. A perfect bifurcating system can be produced by 2n airway tubes at generation n.The generations $0 \leq n \leq 16$, conduct the gas flow in and out, without having any special equipment to exchange oxygen and carbon dioxide between air-blood barrier, named as conducting zone. However, from generations, $17 \leq n \leq 19$, visibility of small air sacs or alveoli (alveoli are thin-walled and compliant with rich capillary blood supply) start to appear on the airway walls which participate in the gas exchange process, named as a respiratory zone. Airways smaller than 1 millimeter in diameter are called bronchioles, and the tiniest of these, the terminal bronchioles, have a diameter between 75-300 micrometer [21] and named as alveoli. These alveoli in the lungs account for most of the lung volume and provide a tremendous surface area for gas exchange. Altogether, a healthy lung (both lungs) generally have about 2800 km of airways and about 300-480 millions alveolar sacs or alveoli. So, the total surface area of both lungs is about 70 square meters.

1.3.1 Lung volumes and capacities

In Figure 1.4 left part is listed with four pulmonary lung volumes, which are accumulatively equal to the maximum volume and are responsible for the expansion of the lungs. The significance of each of these pulmonary lung volumes are as follows:

1. **The tidal volume**-The volume of air inspired or expired with each normal breath is known as tidal volume and its amount for an adult lung is about 500 millilitres.
2. **The inspiratory reserve volume**-The amount of extra volume of air when a person inspires with full force over and above the normal tidal volume is called inspiratory reserve volume and normally equal to 3000 millilitres.
3. **The expiratory reserve volume**-The maximum amount of extra volume of air when a person expires with full force after the end of normal tidal expiration is called expiratory reserve volume and usually equal to 1100 millilitres.
4. **The residual volume**-The amount of volume of air remaining in the lungs after the most forceful expiration is called the residual volume and averages 1200 millilitres.

The lung capacities are estimations of at least two volumes.

1. **Inspiratory capacity**-Sum of the tidal volume and inspiratory reserve volume is equal to inspiratory capacity.
2. **Functional residual capacity**-Sum of the expiratory reserve volume and residual volume is equal to functional residual capacity.

3. **Vital capacity**-Sum of the inspiratory reserve volume, the tidal volume, and the expiratory reserve volume are equal to vital capacity.

4. **Total lung capacity**-Sum of vital capacity and the residual volume is equal to the total capacity of the lung.

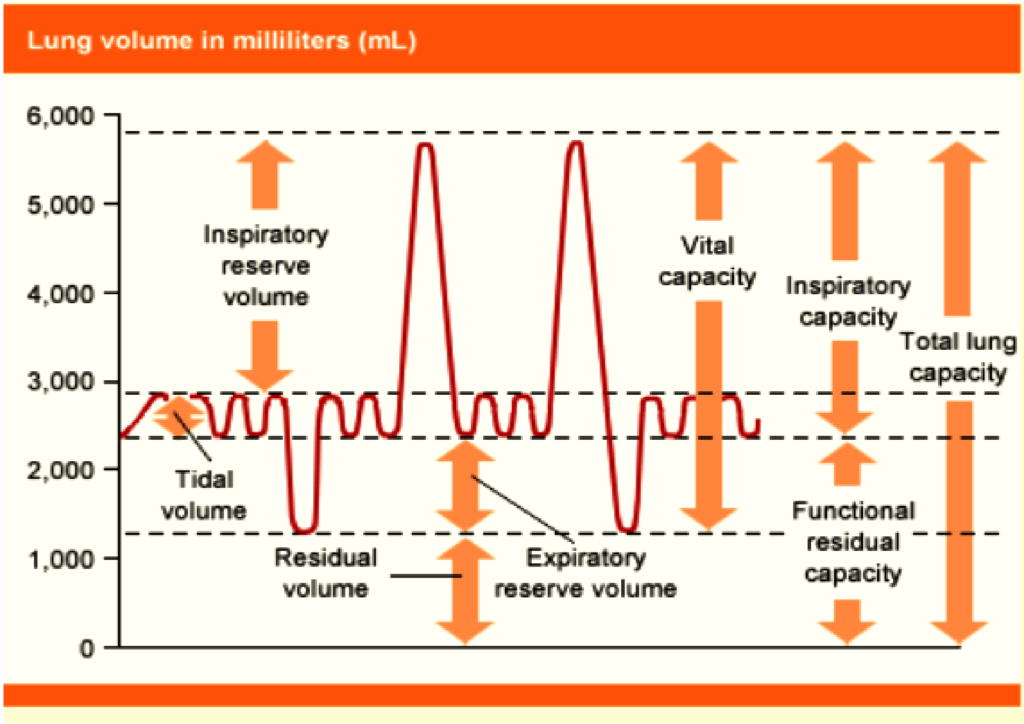

Figure 1.4: The pulmonary volumes and pulmonary capacities [78].

1.4 Lung Mechanics

Mechanical changes in lung structure during respiration, termed as lung mechanics [135], have been usually talked about in the literature e.g. [14, 52, 131]. However, no established unifying theory currently exists. Much of the uncertainty has been due to the difficulties in documenting alveolar and capillary mechanics, given the small size and large movement during breathing. It describes all those things that determine the relationships between pressure, flow, and volumes in the study.

1.4.1 Anatomical characteristics of lung

Porosity

The quantitative measurement of voids or emptiness in a material is named as porosity, which can be calculated for biological tissues by the ratio of the volume of voids to the total volume. Porosity varies between the limit of 0-1 or 0%-100%.

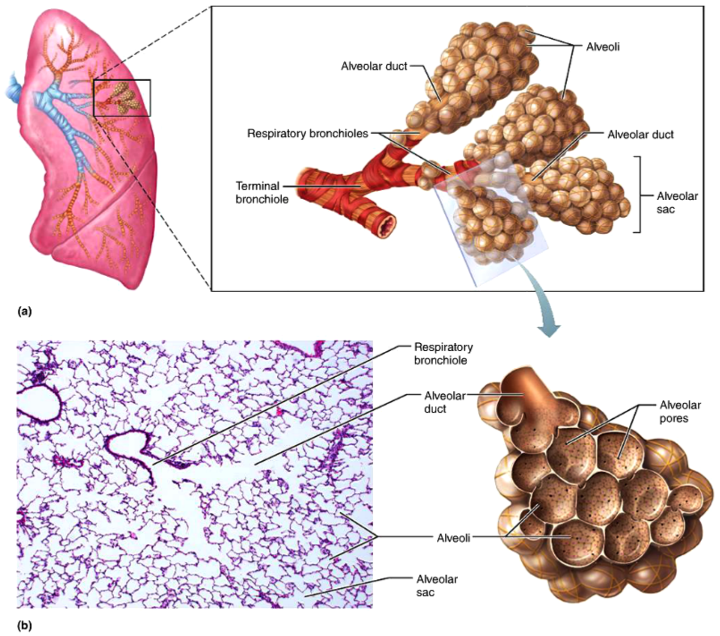

Figure 1.5: (a) The cross-sectional view of human lung, and (b) the microscopic view of alveolar region (https://antranik.org/the-respiratory-system/)

There are distinct holes inside alveoli and in between adjacent alveoli in the alveolar region of the human respiratory system, which are entitled as pores of Kohn [116]. These pore of Kohn are very helpful in collateral ventilation to some extent during the partial deflation of the human lung. In addition, they equalize the pressure in adjacent alveoli or play an important role in the prevention of collapse of the lung and provide a passage of other materials (fluid and bacteria). Overall, the pore of Kohn is responsible for the porosity of lung [150] and play a significant role in cell survival and gas exchange process. We can notice the thinness of the alveolar walls in Figure 3.4.

Permeability

Another important factor, responsible for tissue characteristic is its permeability. Permeability is the measurement of the ability of a material to transmit the fluid. Tissue may be extremely porous but if the pores are not connected, it will have no permeability. Likewise, a tissue has a few continuous voids, it allows ease in fluid flow or obtains more permeability but does not seem very porous.

Biofilter

Biofiltration is an emerging technology to control pollution by using a bioreactor, which contains living material to capture and biologically degrade pollutants. Biofilter commonly used in wastewater, drinking water treatment. A biofilter is usually a porous media [206] through which flow of fluid is studied by established models, such as the Darcy model [37]. In human lung, the alveolar region contains alveolar sacs, which can be considered as an internal biofilter media that capture dust particles from the inspired air [196].

Elasticity and viscoelasticity of lung tissue

Elasticity is the tendency of an organ to return to its normal position or shape, while viscoelasticity is the property of materials that exhibit both viscous and elastic characteristics when undergoing deformation. Human lung have both properties i.e. elasticity and viscoelasticity. The aptitude of the lung elastic tissues to retreat through expiration form elasticity and when exhibiting time-dependent strain due to mucus or other biological fluid (periciliary liquid and blood), it forms viscoelasticity.

No slip

No slip is a condition for viscous fluids relative to the solid boundary of material, where the assumption of zero velocity of the fluid can be applied. A boundary condition for viscous fluids at such a wall is that there be no relative motion between the wall and the fluid immediately in contact with the wall when there is no tangential motion of the fluid relative to the wall is called no-slip condition [41].

1.4.2 Factors affecting the lung mechanics

Airway resistance

Resistance to flow in the airways confide, either the flow is laminar or turbulent with respect to the dimensions of the airway, and viscosity of the gas. Airway resistance is the conflict to flow due to a nonelastic source of resistance such as friction or drag encountered in the respiratory passageways. It is described as the ratio of the driving pressure to the rate of air flow and represented in centimeter water per litre per second as

$$R = \frac{\Delta P}{\dot{V}}, \tag{1.1}$$

where $\dot{V}$ is volumetric airflow change constantly during the respiratory cycle, P is pressure, and R is resistance. This equation shows that the flow of gas is reciprocal to the resistance or we can say that the flow of gas decreases with respect to the resistance.

Resistance in the respiratory system also depends on the diameter of the conducting tubes. Initially, the diameter of the conducting zone is very large for the primer branches, which causes low resistance, while deep inside lung generations, the diameter of branches become small and the resistance on flow increases. Hence, maximum resistance is found in the medium-sized bronchi, because at the terminal bronchioles also known as alveoli the process of gas exchange occurs through molecular diffusion, which is not affected by resistance.

Alveolar surface tension

Due to the molecular attraction between liquid and gas a state of tension is ingrown at the liquid surface of alveoli, this tension is termed as alveolar surface tension. So, alveolar surface tension is the smallest edge between the liquid-gas boundary in the alveoli. The oxygen in the air must go through the membrane to be absorbed by the blood vessels in the alveoli. The greater the surface tension, the harder it is for the blood vessels to obtain oxygen from the air which causes lower the pulmonary ventilation.

Lung compliance

Breathing is a mechanical process in which the muscles of the thorax and abdomen, functioning jointly, generate the pressures necessary to inflate the lung [217]. These pressures must be enough to overcome the inclinations of the lung and chest wall tissues to recoil. A pressure-volume curve is a tool to monitor the deformation of the lung during breathing [4, 10]. It demonstrates the mechanical behavior (elasticity, distensibility) of lung and chest walls during inflation and deflation. It is also responsible for lung compliance (CL). The extent to which the lungs will expand for each unit increase in transpulmonary pressure (if enough time is allowed to reach equilibrium) is called the lung compliance. Specifically, lung compliance (CL) is the measurement of the change in lung volume (ΔV_L) that occurs with a given change in the transpulmonary pressure (ΔP_L). This relationship is stated as

$$C_L = \frac{\Delta V_L}{\Delta P_L}. \tag{1.2}$$

For lower compliance values, lung inflates stiffly, while for a greater compliance values lung expands easily.

1.5 Diseases Affecting the Lung

Lung diseases are some of the most common medical conditions in the world, affecting millions of people every year. Smoking, infections, genetics, and accidents are responsible for most lung diseases and injuries. The lungs can be affected by a number of diseases, including pneumonia, chronic obstructive pulmonary disease (COPD), acute respiratory distress syndrome (ARDS), and lung cancer [105]. Some of these diseases can lead to lung failure caused by the collapse of a lung or parts of it, especially the alveoli.

1.5.1 Emphysema

Emphysema is a disease caused by cigarette smoke, deposition of irritants and dust particles. In emphysema, lung loses its elasticity and require more energy to breath (15-20% vs 5% normal). In complex situations, the bronchioles open during inspiration but collapse during expiration and trap huge volumes of air in the alveoli, which make hyperinflation or permanent expansion of barrel chest and flattens the diaphragm, consequently reducing ventilation efficiency. The physiologic effects of chronic emphysema (Figure 1.6) are variable, depending on the severity of the disease and can are described as below:

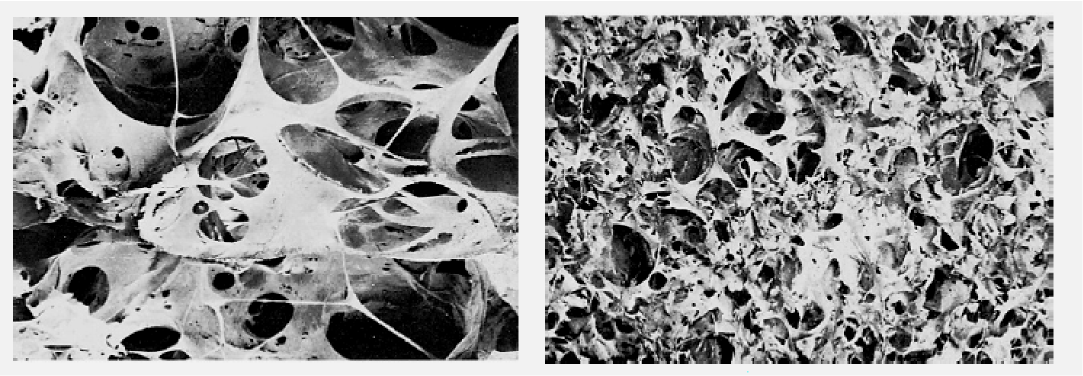

Figure 1.6: Diagrammatic view of the emphysema affected lung (on the left side) and normal lung (on the right side) in the figure (https://www.mcw.edu/).

- Emphysema affects the normal protective mechanisms of the airways, such as partial paralysis of the cilia of the respiratory epithelium which cause difficulty in movement out of the passageways.

- The bronchiolar obstruction increases the airway resistance due to which some portions of the lungs are well ventilated, whereas other portions are poorly ventilated.

- The marked loss of alveolar walls greatly decreases the number of pulmonary capillaries together-with diffusing capacity of the lung, which reduces the ability of the lungs to oxygenate the blood and remove carbon dioxide from the blood.

1.5.2 Chronic bronchitis

Chronic bronchitis is a lower respiratory disease, which occurs due to the inhalation of irritants, cigarette smoking, environmental pollution, etc. and lead to excessive production of mucus, ibnflammation, and fibrosis in the lower part of the respiratory system. These response obstructions in the airways or severely impair lung ventilation and gas exchange process [137].

1.5.3 Chronic obstructive pulmonary disease

Chronic obstructive pulmonary diseases (COPD), is a combination of emphysema and chronic bronchitis, which is a chronic disease that makes breathing harder eventually. Due to COPD, the airways and air sacs lose their elastic quality, the walls between several of the air sacs are damaged, and the walls of the airways turn out to be thick and inflamed. Usually, bronchodilators and corticosteroids in aerosol form (inhalers) are used to heal this disease.

1.5.4 Asthma

Asthma is characterized by episodes of coughing, dyspnea, wheezing, and chest tightness alone or in combination. The cause of asthma has been hard to pin down. Initially, it was viewed as a consequence of bronchospasm triggered by various factors such as cold air, exercise, allergens, and deposition of foreign substances. In asthma, the functional residual capacity and residual volume of the lung become especially increased during the acute asthmatic attack because of the difficulty in expiring air from the lungs.

1.5.5 Fibrosis

Fibrosis or scarring of the lungs describes a group of lung diseases in which scars are formed in the lung tissues, leading to serious breathing problems [81]. Scar formation, the accumulation of excess fibrous connective tissue, leads to thickening of the walls and causes a reduction in oxygen supply in the blood. As consequence patients suffer from perpetual shortness of breath. Other effects of fibrosis are given below:

- Breathing problem during expiration
- Chronic dry, hacking coughing
- Weakness
- Chest distress because of chest pain
- Loss of appetite and rapid weight loss

- Reduction in lung volume and compliance
- Alterations in pulmonary hemodynamics and gas exchange
- Change in the shape and performance of the conducting airways in the gas exchange process

Idiopathic pulmonary fibrosis is the most common idiopathic interstitial [1] pneumonia and one of the most frequently diagnosed interstitial lung diseases characterized by chronic, progressive scarring accumulation of fibrotic tissue in the lung parenchyma, associated with significant morbidity and poor prognosis [180].

1.5.6 Stenosis

In stenosis pulmonary valve (the valve that lets the blood flow from the heart to the lungs via the pulmonary artery) become narrow due to abnormal constriction [207, 240]. Patients with significant stenosis may present with dyspnea, wheezing, or stridor. Stenosis may occur in airway, pulmonary, trachea which leads to the obstruction of the breathing airflow.

1.6 Mathematical Modeling

According to Stephen Smale (1930) "Good mathematical model do not start with the mathematics, but with a deep study of certain natural phenomena".

Mathematics is a very precise language, which helps us to formulate ideas and identify underlying assumptions by using mathematical concepts and languages such as equations, inequalities, functions, variables, and constraints. It is a concise language, with well-defined rules for manipulations. A mathematician can divide the universe into two parts: mathematics, and everything else or the rest of the world, also called 'the real world' [170]. To describe the function of real world mathematical modeling is a powerful tool. Modeling is an abstraction of reality to present a simplified version of something. It basically consists of transforming real-world problems into mathematical problems, solving the mathematical problems either by hand or using computers and deducing these solutions in the language of the real world [104].

1.6.1 Stages of modeling

Mathematical modeling is helpful to divide the process of modeling into four broad categories of activity, such as building, studying, testing and use. In general, it is difficult to model a real-world

---

[1] Interstitial means the disease affects the interstitium, the lace-like network of tissue that supports the air sacs in the lungs.

problem from the first step to the last without any mistake. Defects found at any stage will affect the other stages. So, it is necessary to correct the defect by returning back to that stage and repeat the process for the other stages. A diagrammatic view of the modeling process is shown in Figure 1.7. In 'Mathematical Biosciences', we study the applications of mathematical modeling and mathematical techniques to get an insight into the problems of biosciences. A mathematical modeling of the brain, conduction of current in nerve cells [205], exchange of oxygen and carbon dioxide in the human respiratory system and the functioning of various sense organs (eyes and ears), kidneys, blood flow through heart and flow of gases in lung airways, plays a dominant role in control of diseases of the above systems [79, 145, 157].

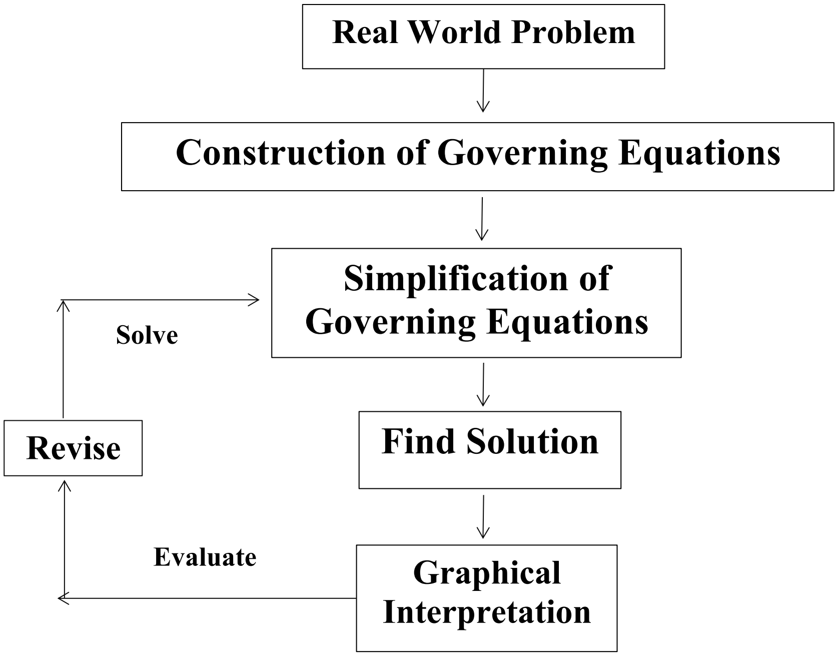

Figure 1.7: Diagrammatic view of mathematical modeling process.

1.6.2 Classification of model

Mathematical models in the mathematical biosciences may be classified according to their nature as follows:

1. **Linear or nonlinear**-Depending on the nature of operator used in basic equations mathematical models may either be linear or nonlinear. If all the operators in a mathematical model exhibit linearity, then the model is linear otherwise nonlinear.

2. **Static or dynamic**-Depending on the time-variations in the system mathematical models may be either static or dynamics. The dynamic model considered time-dependent changes, while the static model does not consider time-dependent changes in the working system.

3. **Explicit or implicit**-In explicit scheme input parameters are familiar and output parameters can be calculated by a finite series of computations, while such a case where the output parameters are familiar, respective inputs must be solved by an iterative procedure is known as an implicit method.

4. **Deterministic or stochastic**-Depending on the chance factors mathematical models are considered as deterministic or stochastic.

5. **Discrete or continuous**- Depending on the variables involved mathematical models may be discrete or continuous.

Linear, static and deterministic models are usually easier to handle than non-linear, dynamic and stochastic models and in general, in any discipline, these are the first to be considered. Essentially most realistic models are non-linear, dynamic and stochastic. Generally, linear, static or deterministic models are used because these are easier to handle and give good approximate answers to the problems.

1.7 Fluid Dynamics in Lung

Fluid dynamics is a sub-discipline of fluid mechanics that deal with transactions of fluid either liquids or gases inside or around the human body [145]. Fluid dynamics has a broad area of applications, such as calculating the forces and moments on aircraft, formative the mass flow rate of petroleum through pipelines, forecasting weather patterns, etc. Fluid dynamics propose a methodical arrangement that motivates these practical regulations and holds empirical and semi-empirical laws resulting from flow measurement and used to explain practical problems. The solution to a fluid dynamics problem usually occupies calculating a variety of properties of the fluid, for example, velocity, pressure, density, and temperature, as functions of space and time. Various flows used in fluid dynamics are as follows.

1.7.1 Compressible and incompressible flow

When a change in pressure or temperature cause changes in density then the fluid is said to be compressible, while in many situations the change in pressure and temperature are sufficiently small so that the change in density can be negligible; in this case, the flow can be modeled as an incompressible flow. Gases are compressible with respect to change in temperature and density.

1.7.2 Steady and unsteady flow

Steady-state flow refers to the condition where the fluid properties at a point in the system do not change over time or flow that is not a function of time is called steady flow. While time-dependent flow is known as unsteady.

1.7.3 Laminar, transitional and turbulent flow

A flow can be laminar, turbulent or transitional in nature. This classification depends on the Reynolds number. For low Reynolds number ≤ 2000, the flow seemed to follow a straight line in which each particle of the fluid follows a smooth path (paths which never interfere with one another) and flow is known as laminar flow. In laminar flow, the velocity of the fluid is constant at any point in the fluid. Additionally, the flow between $2000 <$ Reynolds number ≤ 4000 is known as transition. While, the flow of fluid for higher Reynolds number ≥ 4000 is known as turbulent flow, in which recirculation, eddies, and apparent randomness occur. In the respiratory system during inhalation flow is turbulent, while in the smaller airway (bronchi and even bronchioles), the small diameters will essentially damp out the inertial effects and contribute towards a laminar flow.

1.7.4 Pulsatile flow

Several studies on unsteady viscous flows in either rigid or compliant tubes for identified periodic function for the pressure gradient along the pipe axis have been made and the time-dependent flow rate through the pipe has been obtained [122]. In fluid dynamics, a flow with periodic variations is known as pulsatile flow or as Womersley flow [248]. Cardiovascular system, engines, and hydraulic systems are a good example of pulsatile flow. Blood flow is pulsatile on account of the periodic nature of heart action [194].

1.7.5 Couette flow

Couette flow, named in honor of Maurice Couette, is a flow of viscous fluid between two surfaces or two parallel plates, one of which is moving tangentially relative to the other. The flow is driven by the help of viscous drag force acting on the fluid and pressure gradient applied in the direction of flow. The designing of journal bearings is a case, where Couette flow is applicable.

1.7.6 Convection

The intensive, shared movement of ensembles of molecules within fluids (e.g., liquids, gases) is called convection. Convection of mass cannot occur in solids, because neither bulk current flows nor considerable diffusion occurs in solids. Process of inhalation and movement of air in conducting zone performed by the virtue of convection [159, 206].

1.7.7 Diffusion of gas

Diffusion is an essential process for the respiratory system, which provides oxygen to and removes carbon dioxide from the blood. The net movement of gas molecules moves from the region of higher partial pressure to the region of lower partial pressure [85] (Figure 1.8). Since the process is at the molecular level, the gas moves randomly in the direction of the partial pressure gradient until there is an equilibrium condition. Diffusion process can be defined by Fick's law. The rate of gas diffusion is affected by several factors such as:

- Gas solubility in fluid
- Effect of the cross-sectional area
- Distance of gas diffusion
- Molecular weight of the gas
- Temperature

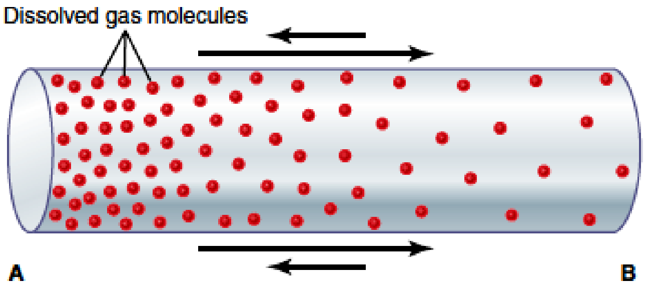

Figure 1.8: Diffusion of oxygen from the region of higher concentration, A, toward the lower concentration, B. [78]

However, the temperature remains reasonably constant and usually need not be considered. So, a combined mathematical relation incorporating all the above factors is defined as

$$D \propto \frac{\Delta p A S}{d\sqrt{MW}}, \tag{1.3}$$

where D represents the rate of diffusion, Δp represents partial pressure difference between two regions, A represents the cross-sectional area of the region, S represents the gas solubility, d represents the distance of diffusion, and MW represents the molecular weight of the gas [78].

According to Fick's law, diffusion of gas directly proportional to surface area, and difference of gas partial pressure, and inversely proportional to the thickness (l) of the boundary [78] as follows

$$D \propto \frac{\Delta p A}{l}. \tag{1.4}$$

1.7.8 Dispersion

In fluid dynamics, dispersion is an effect named after G. I. Taylor [232], in which a shear flow can increase the effective diffusivity of a species. In Taylor dispersion, when a nanoliter-scale sample pulse is injected into the laminar flow of run buffer inside a microcapillary it then spreads out axially due to the combined actions of convection and radial diffusion. Basically, the shear demonstrations to spread out the concentration distribution toward the stream, improving the rate at which it spreads toward that direction.

1.8 Nanoparticle and Need of Shape Factor

Nanoparticles are ultra small objects with dimensions measured in nanometers (nm). Nanoparticles typically have at least one dimension less than 100 nm in size [129] and come in a range of different types. Nanoparticles are found in the industries (cloth, wood, cosmetic, food etc.), atmosphere (in form of dust and incomplete combustion) [140, 221], coal mines, harvesting, mammals hair, several kinds of indoor activities such as smoking, cooking, candle-burning, etc. Major characteristics of nanoparticles are selfly reassembling, high conduction, reliability, and sustainability. Nanoparticles have many useful applications in the commercial, industrial and technological sectors, chemistry, biology, computer and fiction sciences, mathematics, mechanical engineering, artificial intelligence, garments, wear and tear, electronics, fertilization, purification and many more, while these particles cause several kinds of health issues if inhaled. The principal parameters of nanoparticles are not only their size but their morphological sub-structure characteristics, defined by their different shapes, aspect ratios. Depending on the shape related characteristics, nanoparticles can be zero, one, two or three dimensional [234]. While in respect of aspect ratio's particles are classified as high and low aspect ratio's particles. Nanoparticles of high aspect ratio's can be in carbon nanotubes [220], nanorods, nanocrystals, nanowires, nanoribbons, polyhedral, disk-like, helices, zigzags, belts, nanotubes or perhaps nanowires shapes, while low aspect ratio's can be in spherical, oval, cubic, prism, octal, hexagonal, tetrahedral, quantum dots, and pillar shapes. Different models have been used to explain the shape-dependent properties [224, 225], where the nanoparticles are assumed as ideal spheres. To characterize the nanoparticles with respect to their different shapes one quantitative parameter is used named as ‘shape factor’. Shape factor (S_f), the ratio of the surface area of a nonspherical nanoparticle S' to the spherical nanoparticle (S), in the identical volume, was defined by Qi et al. [177] as

$$S_f = \frac{S'}{S}. \tag{1.5}$$

Computation of the particle shape factor does not solely depend on particle shape but is also influenced by the coordination of a particle relative to the direction of air flow. So, the dynamic shape factor is defined by [90, 218]

$$S_f = \frac{1}{3}\left[\frac{1}{S_\perp} + \frac{2}{S_\|}\right], \tag{1.6}$$

where $S_\|$ represents the parallel orientation of particles and $S_\perp$ represents the perpendicular orientation of particles with respect to the direction of flow. Both factors are defined by the equations for the respective particles. In term of drag force, shape factor can be defined by the ratio of drag force of nonspherical particle (F_d) to the drag force of spherical particles (F) in the equivalent volume, which is defined as [90, 218] follows,

$$F_d = S_f F. \tag{1.7}$$

1.8.1 Aerodynamic diameter

The aerodynamic diameter of an irregular particle [119], introduced in the 1990s [62], is defined as the diameter of the spherical particle with a density of 1000 kg/m^3 and the same settling velocity as the irregular particle. Aerodynamic diameter is applied for particulate pollutants or inhaled drugs to predict the place of deposition in the respiratory tract. Different shape particles will make different drag forces with different particle terminal settling velocities; which might successively have an effect on the aerodynamic behavior of particles [35]. In continuation, the aerodynamic diameter determines how well the particles enter and how far they go in the lungs. Nonspherical nanoparticle geometries are most reliably approximated with the help of the aerodynamic diameter (d_p), which is defined as [90, 218]

$$d_p = d\sqrt{\frac{\rho}{S_f \rho_0}}. \tag{1.8}$$

where d is the diameter of spherical particle d and ρ_0 is the unit density of particle.

1.8.2 Cunningham slip correction factor

Cunningham slip correction factor (C), named after Ebenezer Cunningham [36], is applicable on the continuum regime and free molecular flow to predict the drag force on the smaller and irregular particles moving in a fluid.

$$C = 1 - \frac{\lambda}{d_p}\left[2.514 + 0.800 exp\left(\frac{-0.55 d_p}{\lambda}\right)\right]. \tag{1.9}$$

When particles become smaller than 15 micrometers, this factor becomes very significant.

1.9 Deposition Mechanism

Few irritants, for example, smoke, dust, sulfur dioxide and some of the acidic elements in smog frequently act directly on the lung tissues to initiate local, non-nervous reactions that cause obstructive narrowness in the airways. During inhalation velocity of air is very high (Reynold number is greater than 4000), so that the flow field come under the turbulent flow range. Resultantly, particles having size ≤ 6 μm may enter through the nose (inertial impaction), while remaining are catch by the cilia of the nose. After getting entry from nose particle of size range 1-5 micrometers may settle down in the smaller bronchioles by the mechanism of gravitational precipitation or sedimentation. The best example found for this kind of deposition in coal mines. Those particles which have a diameter < 1 micrometer, deposit inside alveolar fluid by the mechanism of diffusion. However, most of the particles having a diameter less than 0.5 micrometers left suspended in the alveolar air and are expelled out during expiration. Particles of cigarette smoke come in this range. Instead of expelling out all the smoke particles, unfortunately, approximately one-third of them do deposit in the alveoli by the process of diffusion. Most of the deposited particles in the alveolar region are cleared by coughing, alveolar macrophages, and remaining are removed by the lung lymphatics. While, excess of particles become the cause of scars and growth of tissues, also known as fibrosis along the wall of alveolar septa, which leads shortness of breath.

There are four major deposition mechanisms: impaction, interception, sedimentation, and diffusion, which contribute to fiber deposition with respect to fiber's dimensions, the inspiration flow rate, and the lungs' geometry. In general, deposition occurs with the combination of these mechanisms.

1.9.1 Inertial impaction

Inertial impaction happens when airflow changes its direction then the particles, which are close to the airway wall, follow it's original direction instead of adjusting to the airflow.

1.9.2 Gravitational settling

Settling or sedimentation is driven by the influence of gravity, which makes particles to depart their original air stream. The probability of a particle to deposit due to gravitational settling depends on the ratio of particle settling distance to airway dimensions at air stream's velocity.

1.9.3 Diffusion

Diffusion is a disperse mass transfer that is caused by random molecular motions also called Brownian motion. Small particles displace when they collide with air molecules. Diffusion is inversely proportional to the particle diameter.

1.9.4 Interception

Interception is the result of physical contact of a particle with the airway surface because of geometrical features. For pure interception particles follow the air stream and thus have negligible inertia, settling and Brownian motion. The particle does not depart its original air streamline but makes contact due to its physical size. Interception depends on the ratio of particle size to airway diameter which means that interception is the most important for elongated particles, like fibers, which are long in one dimension but have small enough diameters to reach the small airways.

1.10 Some Dimensionless Numbers

1.10.1 Reynolds number

The flow of air in the human respiratory system can be characterized in term of laminar, transition or turbulent flow by the use of Reynolds number. Reynold number is the ratio of inertial force to viscous force and can be defined as

$$Re = \frac{\rho d u}{\mu}, \tag{1.10}$$

where ρ is the density, d is the hydraulic diameter, u is the average velocity, and μ is the dynamic viscosity of air. For a low Reynolds number, i.e. Re <<2300, viscous force is stronger than inertial force. In such cases, inertial forces can be neglected and flow behavior is named as Stokes or creeping flow. While, at high Reynolds numbers, i.e. Re >>4000, where inertial force is more effective than viscous (friction) force, the flow is often modeled as transitional or turbulent or inviscid.

1. laminar when $Re \leq 2300$

2. transient when $2300 < Re < 4000$

3. turbulent when $4000 \leq Re$

1.10.2 Peclet number

Peclet number (Pe), named after the French physicist Jean Claude Eugene Peclet, is applicable in fluid flow or transport phenomena. The peclet number can be defined as a similar quantity driven by an appropriate gradient as

$$Pe = \frac{Lu}{D}, \tag{1.11}$$

where L is the characteristic length, u is the flow velocity, and D is the mass diffusion coefficient.

1.10.3 Darcy number

The Darcy number, named after Henry Darcy, generally used for mass transfer through porous media and defined as the ratio of the permeability of medium over the cross-sectional area or diameter as

$$Da = \frac{K}{d^2}, \tag{1.12}$$

where K is the permeability of media and d is the diameter of the particle.

1.10.4 Womersley number

The Womersley number (w_0), named after John R. Womersley, is applicable in the pulsatile flow of blood and air in biofluid mechanics. It can be defined as the multiplication of Reynold number (Re) and Strouhal number (S_t, is a dimensionless number use in oscillatory flow mechanisms).

$$w_0 = \sqrt{2\pi Re S_t}. \tag{1.13}$$

1.11 Conservation Equation of Momentum and Mass Transport

For the momentum balance over a thin shell of fluid and for steady state flow, the equations are as follows:

Momentum transfer

$$[\text{rate of momentum in}] - [\text{rate of momentum out}] + [\text{sum of forces acting on system}] = 0 \tag{1.14}$$

Mass transfer

$$\begin{aligned}&[\text{rate of mass of a substance in}] - [\text{rate of mass of a substance out}]\\&+ [\text{rate of production of mass of a substance by homogeneous chemical reaction}] = 0\end{aligned} \tag{1.15}$$

Navier-Stokes equation (for incompressible fluid) or Equation of Motion (conservation of momentum)

Cartesian coordinate system are as follows:

$$\rho\left[\frac{\partial u}{\partial t}+u\frac{\partial u}{\partial x}+v\frac{\partial u}{\partial y}+w\frac{\partial u}{\partial z}\right]=X-\frac{\partial p}{\partial x}+\mu\left[\frac{\partial^2 u}{\partial x^2}+\frac{\partial^2 u}{\partial y^2}+\frac{\partial^2 u}{\partial z^2}\right], \tag{1.16}$$

$$\rho\left[\frac{\partial v}{\partial t}+u\frac{\partial v}{\partial x}+v\frac{\partial v}{\partial y}+w\frac{\partial v}{\partial z}\right]=Y-\frac{\partial p}{\partial y}+\mu\left[\frac{\partial^2 v}{\partial x^2}+\frac{\partial^2 v}{\partial y^2}+\frac{\partial^2 v}{\partial z^2}\right], \tag{1.17}$$

$$\rho\left[\frac{\partial w}{\partial t}+u\frac{\partial w}{\partial x}+v\frac{\partial w}{\partial y}+w\frac{\partial w}{\partial z}\right]=Z-\frac{\partial p}{\partial z}+\mu\left[\frac{\partial^2 w}{\partial x^2}+\frac{\partial^2 w}{\partial y^2}+\frac{\partial^2 w}{\partial z^2}\right]. \tag{1.18}$$

Conservation of mass or equation of continuity

$$\frac{\partial u}{\partial x}+\frac{\partial u}{\partial y}+\frac{\partial u}{\partial z}=0, \tag{1.19}$$

where u, v and w are the velocity components along x, y and z axes respectively, p is pressure, ρ is density, μ is viscosity, t is time and X, Y, Z are body forces along x, y, and z axes respectively.

Navier-Stokes equation (for incompressible fluid) or Equation of Motion (conservation of momentum)

Cylindrical polar coordinate system are as follows:

$$\begin{aligned}\rho\left[\frac{\partial v_r}{\partial t}+v_r\frac{\partial v_r}{\partial x}+\frac{v_\theta}{r}\frac{\partial v_r}{\partial \theta}-\frac{v_\theta^2}{r}+v_z\frac{\partial v_r}{\partial z}\right]&=F_r-\frac{\partial p}{\partial r}\\&+\mu\left[\frac{\partial^2 v_r}{\partial r^2}+\frac{1}{r}\frac{\partial v_r}{\partial r}-\frac{v_r}{r^2}+\frac{1}{r^2}\frac{\partial^2 v_r}{\partial \theta^2}-\frac{2}{r^2}\frac{\partial v_\theta}{\partial \theta}+\frac{\partial^2 v_r}{\partial z^2}\right],\end{aligned} \tag{1.20}$$

$$\begin{aligned}\rho\left[\frac{\partial v_\theta}{\partial t}+v_r\frac{\partial v_\theta}{\partial x}+\frac{v_\theta}{r}\frac{\partial v_\theta}{\partial \theta}-\frac{v_\theta^2}{r}+v_z\frac{\partial v_\theta}{\partial z}\right]&=F_\theta-\frac{\partial p}{\partial \theta}\\&+\mu\left[\frac{\partial^2 v_r}{\partial r^2}+\frac{1}{r}\frac{\partial v_\theta}{\partial r}-\frac{v_\theta}{r^2}+\frac{1}{r^2}\frac{\partial^2 v_\theta}{\partial \theta^2}-\frac{2}{r^2}\frac{\partial v_\theta}{\partial \theta}+\frac{\partial^2 v_\theta}{\partial z^2}\right],\end{aligned} \tag{1.21}$$

$$\rho\left[\frac{\partial v_z}{\partial t}+v_r\frac{\partial v_z}{\partial x}+\frac{v_\theta}{r}\frac{\partial v_z}{\partial \theta}-\frac{v_\theta^2}{r}+v_z\frac{\partial v_z}{\partial z}\right]=F_z-\frac{\partial p}{\partial z}$$

$$+\mu\left[\frac{\partial^2 v_z}{\partial r^2}+\frac{1}{r}\frac{\partial v_z}{\partial r}+\frac{1}{r^2}\frac{\partial^2 v_z}{\partial \theta^2}+\frac{\partial^2 v_z}{\partial z^2}\right], \tag{1.22}$$

where v_r, v_θ and v_z denote the velocity component in radial (r), azimuthal (θ), and axial (z) directions respectively.

Conservation of mass or equation of continuity

$$\frac{\partial v_r}{\partial r}+\frac{v_r}{r}+\frac{1}{r}\frac{\partial v_\theta}{\partial \theta}+\frac{\partial v_z}{\partial z}=0. \tag{1.23}$$

1.11.1 Conservation equation in porous media

Using Darcy model, momentum equation can be extended for porous medium [42, 160, 196]. Let ϵ denotes the porosity of the material and K is the permeability of media then following conservation of momentum equation in generalized form is used for porous media regime.

$$\frac{\partial u}{\partial t}+\frac{u}{\epsilon}\frac{\partial u}{\partial z}=-\frac{\epsilon}{\rho}\frac{\partial p}{\partial z}+\nu\left(\frac{\partial^2 u}{\partial z^2}+\frac{1}{z}\frac{\partial u}{\partial z}\right)-\frac{\epsilon\nu}{K}u+F, \tag{1.24}$$

where, u is velocity of fluid and external forces acting in the porous medium is represented by F.

1.12 Mathematical Method

1.12.1 Numerical method

Numerical method is a mechanism of solution, which give solution closer and closer with each iteration toward the exact solution. A number of problems related to the field of science and engineering remain unsolved because it is impossible to get analytical solution of those problems. Moreover, analytical approaches are suitable for linear problems but the governing equations related to air flow, blood flow and heat transfer are mostly nonlinear in nature. Numerical methods are commonly used to solve the nonlinear partial differential equations subject to the initial and boundary conditions. Additionally, advancements in computer technology have enabled many in science and engineering to apply numerical methods to simulate physical phenomena. Although there are various numerical techniques. The most popular numerical methods used are as follows:

1. Finite Difference Method

2. Finite Element Method

3. Finite Volume Method
4. Boundary Element Method
5. Spectral Element Method

To find the solution of problems related to air flow, blood flow and heat transfer different methods are used [192, 237, 238]. Some researchers obtained theoretical, experimental and analytical solutions [39, 46, 95, 219] and some of them used numerical methods i.e. finite difference method (FDM) [44, 139, 210], finite element method (FEM) [2, 5, 56] and finite volume method (FVM) [123]. Many commercial softwares are also available based on the finite element method and used by many authors for the analysis of blood flow in complicated geometries [179].

Moreover, the problem is related to the flow dynamics of air and particles in a circular cylinder, with regular geometry. Among other methods, FDM is the most suitable technique for regular geometry. So, we applied a finite difference technique to solve the present problems (see Appendix-A 9.6).

1.12.2 Method of moment

The method of the moment is probably the oldest method for constructing an estimator, which was introduced by Pafnuty Chebyshev in 1887. The method of moments is a technique to estimate population parameters, like the population mean or population standard deviation. The basic idea is taking the known facts about the population, and extend those ideas to a sample. The advantage of the method of the moment is that it is quite easy to use. Within a population, m^{th} moment of a distribution for a random variable X is defined as μ_m = E(X^m) and if X_1, X_2, X_3,..., X_n be random variables from the distribution then the m^{th} sample moment is defined by following formula,

$$M_m = \bar{x} = \frac{1}{N}\sum_{i=1}^{N} x_i^m. \tag{1.25}$$

We can use M_m as an estimator (Poisson, Normal, Gamma Distributions) for μ_m and get sample mean named as the first moment, $\bar{x}$, while for the second moment we have to find the variance, Var(x) = σ^2, which is defined as follows,

$$\sigma^2 = E(x - M_m)^2 = \frac{1}{N}\sum_{i=1}^{N}(x_i - M_m)^2. \tag{1.26}$$

1.13 Literature Survey

Anatomy of the human respiratory system is an important aspect to analyze the applicability of flow dynamics [149]. The human respiratory system is a control system [151] of body. The main organ of the respiratory system is lung, whose function is to take fresh oxygen from the air and remove waste carbon dioxide from the blood. Human lung has a tree-like structure which facilitates gas exchange. A quantitative morphological analysis of the architecture of the human lung presented by Weible in 1963 [245]. Lung volume, dead space volume, cardiac output, pressure, airway opening, and cerebral blood flow vary with breathing rate. Lung constrains air and blood to isolate compartments or channels to lead air to and fro lung airways, and allow blood to move through pulmonary capillaries [246].

In the literature, many approaches have been adopted to investigate the flow dynamics of vicious air, gas transfer mechanism, deposition characteristics of particles through the respiratory system. Some studies have utilized experimental approach to understand the mechanism of branching morphogenesis, such as, Guo et al. [71], who experimentally described an elegant pattern of branching (including side branching and tip bifurcation) in the development of the lung. Miller et al. [152] have been used three-dimensional reconstruction techniques, from individual cells, conducting airway and alveolar duct branching systems, to examine various aspects of lung structure. An image-based model has been developed via image registration and soft tissue mechanics by Tawhai and Lin [231] to analyze the airflow pattern from mouth to the terminal bronchiole associated with physiological boundary conditions. Also, a three-dimensional model is presented by Rosati et al. [186] which include whole human respiratory system and found that the model is applicable in various states of lung disease. However, some researchers developed mathematical models, which are reliable enough to make experimental predictions, for example, Peterman and Longtin [167] simulated the function of the lungs by using multi-compartment model and stated that the model predicts the buildup of gases in the lungs and the washout of gases from the lungs. Rozanek and Roubik [190] studied lung morphology using an electro-acoustic analogy to deal with development, design and implementation of the human respiratory system and simulated distribution of important intrapulmonary parameters along the bronchial tree such as pressure amplitude, tidal volume, and regional mechanical lung properties. Xu et al. [252] and Varnera et al. [239] studied mammalian lung development using turing instability analysis and found that wavelength affects the branching structure. The dynamics and thermodynamics of gas flow in the human respiratory system discussed by Abrahamyan [1] to approximate the time dependence changes of intrapulmonary pressure including the breathing process.

Every day billions of particles are inhaled with the ambient air flow by each human being [89]. The flow of various types of particles are different have different characteristics for individual lung generations. The particle size [27], number density [96], airway geometry, inspiratory flow rate, breathing pattern, particle complex movement and Reynold number [6] are the controlling parameters to predict the location of deposition of a particle in the lung generations [90]. Deposition of particles with diameters of 0.1 μ m - 10 μ m varies with flow rate from mouth to oropharynx [117] and particles of range 10 μ m - 20 μ m are very likely to deposit in nasal cavity by combined action of facial features [202], while particles of range 4.9 μ m - 44.3 μ m are deposited inside extrathoracic (i.e., in the head and throat) region [213]. Nanoparticles are very small size particles and may reach almost any region of human body [163]. Due to their small size and extremely high surface area to volume ratio, these particles are very toxic for human lung and the toxicity of these particle depends not only on its chemical composition but also on the quantity and position of the deposition [178].

Most of the aerosol particles are hygroscopic and nonspherical, such as fibers, droplets, and vapors, and categorized as unconventional with respect to solid spheres [59]. Determination of the behavior of inhaled unconventional particles in the human respiratory system has challenged the scientists for the last few years. The complex movement of the particles makes it more difficult to predict the pattern of their deposition in human airways than conventional spherical particles [225]. Furthermore, non-spherical particle deposition is enhanced as the breathing rate increases [59]. Asbestos is a famous example of the dangerous nonspherical nanoparticle. Some kind of metallic nanoparticles demonstrate prolonged tissue retention and presents serious concerns for toxicity [141]. Chena et al. [31] experimentally carried out a study on lung model subjected to a single horizontal bifurcation with different steady inhalation conditions and found that deposition of the fibrous particle was affected by different body positions. Hussan [82] investigated the effect of different dry particle shapes on flowability, aerosolization, and deposition properties and found that pollen-shaped particles exhibit higher emitted dose, better flowability, and higher fine particle fraction than sphere, needle, cube and plate particles in same size ranges. Also, Sturm [220] investigated the behavior of single-walled and multiwalled carbon nanotubes of diameter ranges 10 to 100 nm by considering dynamic shape factors of nanotubes with Monte Carlo method through the lung airways and concluded that multiwalled carbon nanotubes have the tendency to be deposited in more distal lung regions than single-walled carbon nanotubes. Balashazy et al. [11] presented the analysis on man-made mineral fibers by a stochastic lung deposition model subjected to different flow rates and equivalent diameters and found that thick and long fibers have the probability to penetrate central airways at low flow rates and particles with parallel orientation have highest deposition efficiency. Recently, Feng et al. [59] stated that nonspherical particles with higher aspect ratios are very hazardous as compared to thicker particles and have the ability to penetrate lower lung generations if aligned with the flow stream. In continuation, Su and Cheng [226] experimentally observed that due to impaction, a particle with lower inertia are more likely to be transported to deeper lung airways, while particle with higher inertia is more likely to be deposited at the oropharynx wall. They also reported that the particle deposition efficiency was generally lower than those of spherical particle.

Moreover, age is another factor that affects lung behavior in respect of both airway structure and respiratory conditions. Pruthi and Multani [175] studied the effect of age on pulmonary function on 50 subjects under the age group of 25-75 years and found that the lung functions significantly decline with age. Sharma et al. [203] stated that respiratory system undergoes various anatomical, physiological and immunological changes with age. A study by Xu and Yu [251] found that deposition in the head region is higher for children than that for adults. Recently, Kim et al. [108] presented a study on human tracheobronchial (G1-G9), bronchioles (G10-G22) and alveolar sacs (G23) geometric models for subjects of age 50 and 80 years old and found a 38% decrease in pressure drop, 41% increase in lung compliance and a 35% to 50% change occur in airway mechanical component for the age of 80 as compared to age 50.

Lung disease refers to any disease or disorder in which lung do not function properly. Deposition of various particles initiates numerous lung diseases, such as chronic obstructive pulmonary disease, cystic fibrosis, tuberculosis, asthma, asbestosis, emphysema, and many more, which results in poor air flow. Excess of mucus either due to aging or particle deposition is another reason for poor air flow. Coughing [109] is a primary innate clearance (either deposited particles or mucus) mechanism in the human airways, however in literature [88], some more airway clearance techniques are mentioned i.e. nebulized medications, antibiotics [125], chest physical therapy or postural drainage, percussion, oscillating positive expiratory pressure, active cycle of breathing technique and autogenic drainage that help people stay healthy and breathe easily. Airway clearance techniques loosen thick and sticky lung mucus, generates a burst of airflow, which creates shear stress at the air-mucus interface and provide an expiratory bias in airflow helped for effective mucus propulsion, so that mucus can be cleared by coughing or huffing. A theoretical study was done by Sturm [223] on different ages from 1-20 years to find the clearance efficiency of lung of biogenic particles in four phases such as bronchial clearance, slow bronchial clearance, fast alveolar clearance, and slow alveolar clearance associated with stochastic modeling and concept of projective-diameter and found that very fine ($<0.01\ \mu$ m) and very coarse particles ($>5\ \mu$ m) obtained highest clearance rates, while particles having large size accumulated in the alveoli for a long time. Clearance and toxicity of iron oxide nanoparticles of different sizes and coatings studied by Feng et al. [59] and found that 10 nm particles showed higher cellular uptake than 30 nm, and clearance of these particles from tissues will take a long time (>2 weeks). Also, Saini et al. [196] worked on a removal efficiency model for human lung and found that the clearance of nanoparticle is low at lower Darcy numbers but very strong at higher Darcy numbers. Clearance efficiency of teflon particles for 46 healthy subjects of age ranging from 19 to 81 years was studied by Svartengren et al. [229] to find that clearance efficiency decreases with aging. Moreover, Haik et al. [77] developed a filter for automotive exhausts and found that the synthesized carbon nanotubes of the diameter of 20-50 nm and a length of 1-10 micrometers are purified using ionic liquid solution up to 95%.

Some diseases are caused by loss of elasticity of lung tissues, which produce decrement in the total volume of air including pulmonary fibrosis, pneumonia, and lung cancer. Idiopathic pulmonary fibrosis (IPF) is a disease of unknown etiology and life expectancy. The disease is characterized by repeated injury to the alveolar epithelium, resulting in inflammation and deregulated repair, leading to scarring of the lung tissue resulting in progressive dyspnea and hypoxemia [81]. To simulates the effects of tissue elasticity and surfactant on the stability of human alveoli a mathematical model was presented by Andreassen et al. [7] to demonstrate that due to a loss in surfactant and elasticity, lung tissue always stayed at an unstable equilibrium state. Fung [64] has observed that alveolar geometry, the elastic property of the alveolar walls (sheets, septa) and the surface tension characteristics of the lung parenchymal tissue are related to each other with a nonlinear stress-strain relationship. Also, by using contact impact analysis model, Ilegbusi et al. [98] presented a breathing-induced spatially dependent lung deformation in association with the nonlinear elastic property of lung.

Moreover, atherosclerosis [133] is a disease, which creates constriction in lung airways or pulmonary capillaries and arteries and significantly alter the local blood flow dynamics and sometimes becomes a reason for stenosis. A number of literatures [24] are there on this disease such as a three dimensional mathematical model of arteries structure with atherosclerosis is studied by Wong et al. [249]. Haghigh [76] presented a two dimensional mathematical model of pulsatile blood flow through overlapped constricted tapered vessels and found that by increasing the taper angle, the axial velocity and volumetric flow rate increase and the micro rotational velocity and resistive impedance reduce.

Preceding respiratory diseases significantly affect the process of gas transfer. A number of studies are concerned about the oxygen content of blood flowing along capillaries, intravascular resistance to oxygen diffusion, and myoglobin facilitated diffusion. Goldman [70] presented a theoretical study of oxygen transport in microvessels subjected to intravascular resistance between blood-tissue by considering Krogh tissue cylinder model in a single capillary. Roy and Aleksander [189] developed a steady-state model to predict the minimum end capillary pressure of oxygen from the erythrocyte to the mitochondrion by taking account the effects of oxyhemoglobin dissociation kinetics and diffusion of hemoglobin and myoglobin. To investigate the binding and buffering effects, a model of blood-tissue gas exchange is used by Carlson et al. [22] and it was stated that velocities of red blood cells are higher than plasma in the flowing blood.

Aforementioned studies concern long time convection and diffusion process to formulate the gas transfer process in association with conventional Krogh cylinder model [118]. However, some researches [146] characterize the transport of oxygen in the intrinsic capillaries enclosing around the tissue, the convective effect of the blood, the nonlinear effects of oxyhemoglobin, and the depletion of oxygen within the biological process under consideration of dispersion. In dispersion, the chemical species may spread out axially along the tube at a rate much larger than that given by the molecular diffusion [168, 232]. When the dispersion has been developing on a time scale that is shorter than or comparable to the diffusion time scale across the tube section then it is known as short-time dispersion. Aris [8] extended Taylor dispersion theory by introducing the method of moments, in which moments at different orders contain accurate information on the evolution of the concentration distribution statistically. Based on the method of moments, Vedel et al. [241] presented a theoretical expression for time-dependent dispersion of an initial point concentration in steady and unsteady laminar flows via a long straight channel for a constant cross-section and found time-dependent diffusion criteria before reaching steady Taylor-Aris limit. Salathe et al. [198] used radial mixing between gas and fluid.

1.14 Objective and Scope of the Thesis

Lung mechanics is an important area of research due to its wide demand in biology, biotechnology, medicine and many more. From the above literature review it is clear that problems, related to particle shape factor with media porosity, age-based study of particle filtration, flow of mucus through airways using theory of Couette flow, effect of viscoelasticity on the flow of air and particles, flow of chemical spices from fibrosis-affected lung and inter capillary gas transfer through pulmonary region (tissue-blood barrier) are not considered yet. Therefore, the aim of the present study is to investigate the effect of nonspherical nanoparticles on the flow dynamics of air from healthy lung as well as diseased lung (emphysema, asthma, atherosclerosis, stenosis, fibrosis) by taking account variable porosity and different boundary conditions.

The objective of the present thesis is planned under the following points.

- To examine the effect of periodic permeability of lung and find filtration efficiency for needle prolate nanoparticle through upper generations (Chapter 2).
- To examine the age-based filtration efficiency of the lung for various shapes nanoparticles (Chapter 3).
- To study the flow of viscous air through homogeneous porous alveolar region of human lung (Chapter 4).
- To study the nanoparticle deposition through emphysema affected lung (Chapter 5).
- To study the blood flow dynamics through stenosis affected viscoelastic artery (Chapter 6).
- To study the mucus clearance mechanism from human lung airways by using generalized Couette flow (Chapter 7).
- To find the effect of first-order chemical reactions on the dispersion coefficient associated with laminar flow through the fibrosis-affected lung by using the method of moment (Chapter 8).
- To analyze inter capillary gas flow by using the theory of dispersion from the pulmonary region by using the method of moment (Chapter 9).

Chapter 2: Mathematical study of needle prolate nanoparticle flow, deposition and filtration through upper generation of periodically permeable lungs

2.1 Introduction

Most of the air particulate (ozone, sulphur dioxide, nitrogen dioxide, carbon monoxide, lead, etc.), industrial particles (such as cosmetic, textile, pulp and paper, timber industries, etc.), mines particles are nano-sized particles. Nanoparticles are frequently used in material design to enabling the development of better products upon the existing ones, but these extremely small size particles can be toxic and extremely hazardous to human health [47, 169] because there smaller size helps them to easily suspend in the surrounding environment for a long time so the chances of inhalation of these particles with the air stream increases and after inhalation they easily flow through the airways and deposit in lung generations [93, 113].

Lung morphometry and its finite boundary condition make it more important to study particle deposition in different lung airways [245]. Mina et al. [153] stated that nanoparticle of range 10 nm to 52 nm deposited in the upper portion of the human respiratory system. A study by Tian et al. [233] described that the nanoparticles of range 5.52-98.2 nm are very risky for occupational workers and developed various respiratory, cardiovascular, and neurological disorders. Rissler [184] studied the adverse effect of nanoparticles of diameters 15-5000 nm and stated that particles less than 3500 nm have the highest deposition capability.

While it is not necessary that nanoparticles are spherical in shape, asbestos [228], carbon nanotube, a particle of gold, silver, titanium dioxide, etc. are some nonspherical shape nanoparticles used in the most of the industries from the last few years. These particles have the capacity to deposit different places of lung generations [225]. An experimented study investigated that the effect of particle dimension and fiber inertia affect the deposition pattern of nonspherical particles in the human airway replica [179]. Chena [31] et al. developed a lung model with a single horizontal bifurcated tube under different steady inhalation conditions and explored the effect of fiber length, flow rate, orientations, and body positions affect the deposition of carbon nanoparticles. In a theoretical study Sturm [224] studied the deposition behavior for platelets ranging in thickness from 10 nm to 1 μ m with diameter from 1 to 30 μ m for different breathing scenarios and found that during sitting position platelets with a thickness of 10 nm deposited in the airways by 21% to 40%, and have potential to act as serious health hazard. A study by Su and Cheng [226] demonstrated that most of the high inertia carbon fibers deposited in the oropharynx and the carina ridges of the bifurcations in tracheobronchial airways. Also, Belkaa et al. [15] stated fractional deposition of glass fibers was higher in the first few generations (up to 7) of the tracheobronchial tree.

However, deposition of various size and shapes nanoparticles make inflammation or looseness of airways, ruptures the alveoli and become a cause of various kind of lung diseases such as bronchitis, emphysema, fibrosis, chronic obstructive pulmonary disease, asthma, etc. To analyze various conditions of the lung due to diseases a number of researchers worked either mathematically or theoretically on lungs, such as Kuwahara et al. [126], DeGroot and Straatman [43] considered the lung as a sponge or porous media due to multiple bifurcations and microscopic cavities. Siddiqui and Siddiqa [208] presented the effect of constant wall permeability and porous media on the creeping flow passing through the rounded vessel and observed that low permeability of porous medium slow down the velocity of the fluid, while constant wall permeability shows the opposite behavior on the same properties. Kumari and Goyal [124] studied the effect of the oscillatory flow of a viscous fluid between two vertical parallel plates with a porous medium. Chitra and Karthikeyan [32] studied oscillatory blood flow in an inclined tapered stenosed artery with the permeable wall. A three-dimensional study of a viscous, incompressible fluid for the highly porous medium is done by Singh et al. [211] for time-dependent oscillation of velocity.

So, clearance of deposited nanoparticles is very necessary. Conventional filters are working well against spherical the nanoparticle but filtration of non-spherical nanomaterials, such as carbon nanotubes and nanoparticle agglomerates, possesses different filtration characteristics compared to spherical particles. In the bronchial airways and alveoli clearance partly takes place via transepithelial routes, disintegration, mucociliary clearance, etc. but particles like asbestos and other nonsoluble fibers are often difficult to remove by phagocytosis because the macrophage is unable to engulf the entire fiber. Feng et al. [59] found that 10 nm size ion particles showed higher cellular uptake than 30 nm ones but biodegradation and clearance of these particles from tissues taking a larger amount of time. Sturm [220] simulated clearance of single and multi-walled carbon nanotubes and found that single-walled carbon nanotubes reside significantly longer time in the lungs than multi-walled carbon nanotubes. In some study, Wang [243] studied that the filtration efficiency of fibers increases as the size of fiber decreases down to 2-3 nm. Additionally, Yan et al. [253] considered lung as biofilter media to filter air pollutants by comparing three biofilter models numerically by using lattice Boltzmann method and stated that due to porous media there exists a strong flow heterogeneity that degrades the removal efficiency of biofilters. After that Saini et al. [196] extended this model and modeled alveolar sacs as a biofilter with constant porosity to filter inhaled spherical nanoparticles and found that higher removal efficiency required a larger amount of traveling time.

We observed from the present state of the above studies that-(i) mathematical model dealing with the effect of porous media with dynamic shape factor on breathing capacity of human lung is not considered yet, (ii) permeability of media either depends on the porosity or taken as constant (iii) reliable studies to find the filtration efficiency of deposited nonspherical nanoparticles is not available. So, the objective of this study is to comprehend the effect of media permeability together-with particle shape on flow dynamics of fluid flowing through airway generations 5-16. The permeability of media is defined as periodic due to an oscillation of velocity about a nonzero constant mean. The resulting governing equations are solved subject to physically realistic oscillatory boundary conditions with the finite difference method. Non-dimensionalized boundary value problem is shown to controlled by various physical parameters, namely mean permeability of media, the aspect ratio of particle, the orientation of particle with respect to the flow stream, Reynolds number, and frequency of oscillation. Effect of these parameters are found on velocity of air and particle. Filtration efficiency of the lung is also analyzed for needle prolate nonspherical nanoparticles with respect to traveling time at different values of mean permeability using biofilter model. A comparative study is also shown with the published study.

2.2 Mathematical Formulation

2.2.1 Governing equations

An incompressible fully-developed, steady, laminar, and Newtonian fluid [1] is flowing along the axis of the circular tube (airways of lung generations 5-16) of radius 'a'. Axial axis measured along

---

[1] combines air and particles

the tube and radial axis is normal to the flow direction, as shown in Figure 2.1. It is assumed that the optimal particles are nonspherical needle prolate nanoparticle and are distributed homogeneously throughout the inhaled volume. Due to various deposition mechanism, particles can be deposited and accumulated either on the sides and turns of the airways or inside alveoli, which can be filtered by the mechanism of mucociliary clearance or coughing. The possible orientations of particles before the deposition are considered as parallel $\|$ and perpendicular $\perp$ with velocity 'v'.

Also, we consider human lung as an internal biofilter [2] and periodic permeability of medium due to an oscillation of velocity about a nonzero constant mean under oscillatory boundary conditions is used. Mathematical equations proposed by Saini et al. [196] are extended by including periodic permeability of porous media and shape factor of particle to analyze the flow dynamics of vicious air and filtration efficiency during upper generations (from 5-16) of lung. The boundary value flow governing equations in cylindrical polar coordinate system (r, z, θ=constant for axi-symmetry flow) are defined as follows:

$$\frac{\partial u}{\partial t}+\frac{u}{\epsilon}\frac{\partial u}{\partial r}=-\frac{\epsilon}{\rho}\frac{\partial p}{\partial r}+\nu\left(\frac{\partial^2 u}{\partial r^2}+\frac{1}{r}\frac{\partial u}{\partial r}\right)+\left(-\frac{\epsilon\nu}{K}u+s_k\frac{N_0}{\rho}\left(v-u\right)\right), \tag{2.1}$$

$$m\frac{\partial v}{\partial t}=S_f s_k\left(u-v\right). \tag{2.2}$$

Equation 2.1 represents the momentum equation of air and equation 2.2 represents the motion equation of particles. The first term in the left hand side of the equation 2.1 is for unsteady flow and the second term is for convection. First, second and third terms in the right hand side of equation 2.1 are the pressure gradient, diffusion and the entire body force because of the existence of porous media and additional external force fields respectively. The term in the left hand side of equation 2.2 represents the product of the mass times the acceleration and right hand side of this equation represents the drag force on nonspherical needle prolate nanoparticle.

In equation 2.1, ϵ, denotes the porosity and K, denotes the periodic permeability of the media, which is defined as

$$K=\frac{K_0}{1-a_0\,\cos(\frac{\pi r}{a})}, \tag{2.3}$$

where K_0 is the mean permeability of porous medium, a_0 is the amplitude of oscillation. Also, in equation 2.1, $s_k=3\pi\mu d_p/C$ is the drag force coefficient for nonspherical particles and C is the

---

[2] Biofilter is defined in Chapter 1, Subsection 1.4.1

Cunningham slip correction factor, which is used for free molecular flow regime and defined as follows,

$$C = 1 - \frac{\lambda}{d_p}\left[2.514 + 0.800\exp\left(\frac{-0.55d_p}{\lambda}\right)\right]. \tag{2.4}$$

here d_p denotes aerodynamic diameter of nonspherical nanoparticle and defined [62] as follows

$$d_p = d\sqrt{\frac{\rho}{S_f\rho_0}}. \tag{2.5}$$

In equation 2.2, S_f is the dynamic shape factor of particle, which can be written in terms of drag force, as the ratio of the drag force on the nonspherical nanoparticle (F_d) to the drag force on the equivalent spherical nanoparticle (F) in the same volume and defined as [90]

$$S_f = \frac{F_d}{F}, \tag{2.6}$$

while, in terms of particle orientation shape factor is defined by Stober [218] as follows,

$$S_f = \frac{1}{3}\left[\frac{1}{S_\perp} + \frac{2}{S_\parallel}\right], \tag{2.7}$$

where $S_\perp$ represents the perpendicular orientation of particle and $S_\parallel$ represents the parallel orientation of particle with respect to the air stream. In the present study, we used needle prolate nonspherical nanoparticles, so the form of $S_\perp$ and $S_\parallel$ can be described by the following formulation [113].

$$\left.\begin{aligned} S_\perp &= \frac{(2/3)\beta^{2/3}}{ln(2\beta) - 1/2},\\ S_\parallel &= \frac{(4/3)\beta^{2/3}}{ln(2\beta) - 1/2},\end{aligned}\right\}\beta > 6, \tag{2.8}$$

where β is the aspect ratio of particle length to particle width or diameter.

2.2.2 Initial and boundary conditions

Initial conditions at $t = 0,\;\; 0 \le r \le a$ are as

$$u(r,t) = v(r,t) = 0. \tag{2.9}$$

Due to rhythmic breathing walls are oscillating along their own axis, so oscillatory boundary conditions are used at $t > 0$, for $r = 0$ and $r = a$ as

$$\left(\frac{\partial u}{\partial r}\right)_{r,t} = \frac{u_0^2}{a}\,\sin(2\pi f t a/u_0), \tag{2.10}$$

where f is the frequency of breathing and u_0 is the initial velocity of viscous air.

2.3 Methodology

2.3.1 Transformation of the governing equations

To solve the governing equations 2.1-2.2 numerically we have to make them dimensionless, so we used the following quantities:

$$x^* = \frac{r}{a}, P^* = \frac{pa^2}{\rho u_0^2}, T^* = \frac{tu_0}{a}, U^* = \frac{au}{\nu}, V^* = \frac{v}{u_0},$$

$$\frac{\partial U}{\partial T} + \frac{U}{\epsilon}\frac{\partial U}{\partial x} = -\epsilon\frac{\partial P}{\partial x} + \frac{1}{Re}\left(\frac{\partial^2 U}{\partial x^2} + \frac{1}{x}\frac{\partial U}{\partial x}\right) + B\left(V - U\right) - \frac{\epsilon}{DaRe}U, \tag{2.11}$$

$$\frac{\partial V}{\partial T} = \frac{S_f\left(U - V\right)}{\tau}, \tag{2.12}$$

where

$$Da = \frac{K}{a^2}, Re = \frac{au_0}{\nu}, B = \frac{M}{\tau} = \frac{N_0 s_k a}{\rho u_0}, M = \frac{N_0 am}{\rho}, \tau = \frac{mu_0}{as_k},$$

where Da is Darcy number, Re is Reynolds number and B, M, τ are used for simplification. Transformed initial conditions from equation 2.9, at $T \leq 0,\ \ 0 \leq x \leq 1$ are as follows:

$$U(x,T) = V(x,T) = 0, \tag{2.13}$$

Transformed boundary conditions from equation 2.10, at $T > 0$, for $x = 0$ and $x = 1$ are as follows,

$$\left(\frac{\partial U}{\partial x}\right)_{x,T} = u_0\ \sin\ (2\pi fT). \tag{2.14}$$

In equation 2.1, due to the periodic breathing the pressure gradient is assumed in the non-dimensional form as

$$-\frac{\partial P}{\partial x} = P_0\ \sin(\pi fT) + S_f, \tag{2.15}$$

where f is the frequency of breathing.

2.4 Numerical Scheme

Finite difference method [214] is the most suitable technique for nonlinear problems related to regular geometries so, to find the solution of the non-dimensional governing equations 2.11-2.12 subject to the initial and boundary conditions 2.13-2.15 we used this method. The computational grid are defined in the following form where the discretization of air velocity $U(x,T)$ is written as $U(x_i,t_j)$ or $U(i,j)$ and similarly the particle velocity $V(x,T)$ is written as $V(x_i,t_j)$ or $V(i,j)$.

$$x_i = i\Delta x,\ (i = 0,1,2,3,...,N),\ \text{where } x_N = 1.0,$$
$$t_j = (j-1)\Delta t, (j = 1,2,..),$$

where i and j are the space and time indexes; Δx and Δt are the increments in axial direction and time respectively.

We used central difference approximation at point (x_i,t_j) for all the spatial derivatives as follows:

$$\frac{\partial U}{\partial x} = \frac{U_{i+1,j} - U_{i-1,j}}{2\Delta x}, \tag{2.16}$$

$$\frac{\partial^2 U}{\partial x^2} = \frac{U_{i+1,j} - 2U_{i,j} + U_{i-1,j}}{(\Delta x)^2}, \tag{2.17}$$

and forward difference approximation for all the time derivatives as

$$\frac{\partial U}{\partial T} = \frac{U_{i,j+1} - U_{i,j}}{\Delta t}. \tag{2.18}$$

Additionally, at $x = 0$, following approximation is applicable in equation 2.11, [3]

$$\lim_{x\to 0} \frac{1}{x}\frac{\partial U}{\partial x} = \lim_{x\to 0} \frac{\partial^2 U}{\partial x^2}, \tag{2.19}$$

so, the equation 2.11 at $x = 0$ becomes,

$$\begin{aligned} U_{i,j+1} = &\left(1 - B\Delta t - \left(\frac{\epsilon}{DaRe}\right)\Delta t - \frac{4r_1}{Re}\right)U_{i,j} + \left(\frac{2r_1}{Re} - \frac{U_{i,j}r_1\Delta x}{2\epsilon}\right)U_{i+1,j} \\ &+ \left(\frac{2r_1}{Re} + \frac{U_{i,j}r_1\Delta x}{2\epsilon}\right)U_{i-1,j} + B\Delta t V_{i,j} + \left(P_0 \sin(\pi f j\Delta t) + S_f\right)\epsilon\Delta t, \end{aligned} \tag{2.20}$$

---

[3] When $x \to 0$, we found that the denominator is also approaching to zero and make the term indeterminate, which is inappropriate for the physical state of the respiratory system. Therefore, to remove this kind of inconsistency we used L'hospital rule of limit here.

and at $0 < x \leqslant 1$,

$$U_{i,j+1} = \left(1 - B\Delta t - \left(\frac{\epsilon}{DaRe}\right)\Delta t - \frac{2r_1}{Re}\right)U_{i,j} + \left(\frac{r_1}{Re} - r_1\Delta x\frac{U_{i,j}}{2\epsilon} + \frac{r_1}{2iRe}\right)U_{i+1,j}$$
$$+ \left(\frac{r_1}{Re} + \frac{r_1\Delta x U_{i,j}}{2\epsilon} - \frac{r_1}{2iRe}\right)U_{i-1,j} + B\Delta t V_{i,j} + \left(P_0\sin\left(\pi f j\Delta t\right) + S_f\right)\epsilon\Delta t, \tag{2.21}$$

where $\left(\frac{\Delta t}{\Delta x^2}\right) = r_1$.

The equation 2.12 transforms as

$$V_{i,j+1} = \left(1 - \frac{S_f\Delta t}{\tau}\right)V_{i,j} + \frac{S_f\Delta t}{\tau}U_{i,j}, \tag{2.22}$$

and the initial and boundary conditions from equation 2.13-2.14 are transform as follows:

$$U_{i,1} = V_{i,1} = 0,$$
$$U_{2,j} = 2u_0\sin(2\pi f j\Delta t)\Delta x + U_{0,j};\;\; U_{N+1,j} = 2u_0\sin(2\pi f j\Delta t)\Delta x + U_{N-1,j}. \tag{2.23}$$

So, we got velocity profiles from equations 2.20-2.22 at the $(j+1)^{th}$ time level in terms of j^{th} time level.

2.5 Results and Discussion

In this section the effect of various physical parameters such as particle aspect ratio (β), orientation ($S_\perp$, $S_\|$), diameter (d), Reynolds number (Re), periodic permeability (K), frequency of breathing (f), effect of shape factor (S_f) are analyzed on the velocity profile of air and particles, pressure of air, filtration efficiency of lung, and shown in Figure 2.4 - 2.11 by using the values defined in Table 2.2 [23, 38, 80, 115, 187, 211, 251].

To estimate the accuracy of the solution the grid independence test is performed at each time level by varying the grid points between 10x10^5 - 25x10^5, using the following stability criteria for finite difference explicit scheme so that less error occurred in the numerical computation, as shown in Table 2.1 (Figure 2.2).

$$\max\left(\frac{\Delta t}{\Delta x^2}\right) \leq 0.5. \tag{2.24}$$

and observed that no significant change is found beyond the grid points 20x10^5. Therefore, all the computations are done by using the grid size 20x10^5 with the accuracy of 10^{-5}.

Before discussing the results of the present problem a numerical code validation and predictive accuracy of the model are checked by comparing output data produced by the present model with respective results generated by the model of Saini et al. [196] for air velocity at Da = 0.1, ϵ = 0.6 with the exponential pressure gradient and represented in Figure 2.3. Saini et al. [196] studied the flow of viscous air through a circular tube by considering the alveolar region as a biofilter media with constant porous media and exponential pressure gradient. Filtration of the spherical particle of d = 100 nm with ϵ = 0.6 of the lung by using removal efficiency model was calculated. In Figure 2.3, a comparison of the present result with Saini et al. is shown and found that our result is very much closer ($\approx$ 99.9 %) with their result. So, we can say, our model is in excellent agreement with Saini et al. [196].

2.5.1 Effect of aspect ratio (β) on the velocity profile of air and particles

Figure 2.4(a) - 2.4(b) show the effect of aspect ratio (β = 7 - 10000) on the velocity profile of air and particles of spherical and needle prolate shapes at porosity (ϵ) = 0.6, mean permeability (K_0) = 0.1, Reynolds number Re = 1, and diameter (d) = 10 nm. From Figure 2.4(a) we found the velocity of the spherical particle is less than the velocity of needle prolate particle and by increasing value of β from 7 to 10000, the velocity of needle prolate particle increases gradually with time. While in Figure 2.4(b) air velocity due to spherical and needle prolate particles (β = 7 to 10000) first increase and attain their maximum value at t = 0.6 and then decrease gradually with time. In this Figure, we found that due to spherical and lower aspect ratio's particle air velocity obtained its high values but due to increment in aspect ratio velocity of air tends to its lower values. Overall from Figure 2.4, we observed that high aspect ratio particles retain in the air stream for a longer time. which cause decrement in air flow, while lower aspect ratio or spherical particles either deposited inside earlier airway or generations and cause an increment in airflow. Hence, particles with high aspect ratio's ($>$100) have a tendency to go inside deep lung generations, however, particles with low aspect ratio's ($<$100) and spherical particles may be deposited in the primer or earlier airway generations.

2.5.2 Effect of Reynolds number (Re) on the velocity of air and particle

It has been known that the Reynolds number (Re) has a great influence on the flow field inside the respiratory system because from the trachea to alveoli value of Re decreases from 4000 to 0.001 with respect to lung generations. In this study we focused on airway generations 5-16 and we chose Re = 1 - 10, K_0 = 0.1 to 5, d = 10 nm, ϵ = 0.6, and β = 10, to study the flow dynamics of air and particles during these generations. From Figure 2.5(a), we found that velocity profile of air at generation 5 (at Re = 10) is highest due to the convection effect, which tends to decrease due to the diffusion effect as the air flow down to the lung generations (at generation 16, Re = 0.1). Similar behavior is found for the velocity of a particle in Figure 2.5(b), where the velocity of particles tends to decrease from generation 5 to 16 by decreasing value of Re from 10 to 0.1. Consequently, we observed from these figures that with respect to the time flow of air inside the lung generations decreases due to the domination of the viscous effect over the inertial effect.

2.5.3 Effect of periodic permeability (K) on the velocity of air and particle

To find the effect of periodic permeability of media on air and particle velocity we varying the mean permeability, K_0, of the porous medium from 0.1 - 5 and fixed Re = 1, d = 10 nm, ϵ = 0.6 and β = 10. We found from Figure 2.6(a), at K_0 = 0.1 velocity of air is lesser than velocity of air at K_0 = 5. By increasing value of K_0 = 0.1 - 5, periodic permeability of airway walls increased and due to highly permeable walls, level of pressure inside airway tubes reduces, which increases the velocity of air periodically. Similar behavior is obtained for the velocity of particles in Figure 2.6(b). So, we can conclude from Figure 2.6 that the increment in permeability (K), increases the flow of viscous air inside the lung airways.

2.5.4 Effect of orientations of particle on the velocity profile of air and particle

In Figure 2.7, we plotted the effect of different orientations of needle prolate nanoparticles on velocity of air and particles at K_0 = 0.1, Re = 1, d = 10 nm, ϵ = 0.6 and β = 10. From Figure 2.7(a), we found that the velocity of particle increases for parallel orientation and from Figure 2.7(b), we found that the velocity of air decreases for parallel orientation. Similarly, from Figure 2.7(a), we found that the velocity of the particle decreases for perpendicular orientation and from Figure 2.7(b), we found that the velocity of air increases for perpendicular orientation. Overall, Figure 2.7 shows that particle with perpendicular orientation gets deposited in former airway generations which causes an increment in the velocity of air, while particles with parallel orientation flow with air and make the air more viscous. Therefore, we can conclude, if particles are in parallel orientation then they may have a tendency to go deep inside the lung generations with the air stream and have the possibility to deposit there.

2.5.5 Effect of diameter (d) of particle on the velocity profile of air and particle

Figure 2.8 shows the effect of particle diameter (d = 1 - 100 nm) on flow dynamics of air and particles at aspect ratio (β) = 10, K_0 = 0.1 - 5, Re = 1, ϵ = 0.6, and β = 10. From Figure 2.8(a), we obtained that at d = 100 nm velocity of the particle is very low and it increases as the diameter of particle decreases (up to 1 nm). Similarly, the velocity of air in Figure 2.8(b) obtained its higher values, at d = 100 nm and tends to decrease by decreasing the value of d (up to 1 nm). So, from these Figures, we found that particle with smaller diameter makes the air stream very slow as compare to larger diameter.

2.5.6 Effect of breathing frequency (f) on the velocity of air and particle

In Figure 2.9, we found the effect of breathing frequency ($0.2 \leq f \leq 0.5$) on the flow profile of air and particles at d = 1 nm, β =10, K_0 = 0.1, Re = 1 and ϵ = 0.6 with respect to time.
Figure 2.9(a) shows that due to a sinusoidal oscillation of wall, the velocity of air first increases and attain its maximum values at t = 0.5 and then decreases with time gradually with time, however by increasing frequency of breathing from 0.2 to 0.5 we obtained that velocity of air increased rapidly. Also from Figure 2.9(b), we found that by increasing the value of breathing frequency velocity of a particle increases gradually. Hence from these Figures, we concluded that when the frequency of breathing increases from normal lung breathing frequency (12 - 20 breath per minute) to diseased lung breathing frequency (21 - 30) then the velocity of particle increases and a chance of particles deposition inside lung generations are also increases.

2.5.7 Effect of particle shape factor (S_f) on pressure of air

Effect of particle shape factor (S_f) on air pressure is shown in Figure 2.10 at d = 1 nm, β =7-1000, K_0 = 0.1, Re = 1, f = 0.2, and ϵ = 0.6. In Figure 2.10 level of pressure is visible on the whole length of air velocity. By increasing the value of aspect ratio β from 7 - 1000 air pressure decreases with respect to time, because higher aspect ratio applied a higher drag force on particles, which causes decrement in pressure gradient and makes the process of breathing very difficult.

2.5.8 Biofilter model for porous media

In the biofilters, the traveling time of viscous air passing through lung (porous media) is an important parameter to evaluate the filtration efficiency (F.E.) of lung. If the traveling time is too short, the biofilter cannot filter the deposited particles effectively, and if the traveling time is too long, the efficiency of biofilter would be too low. To calculate the traveling time, the porous media is divided uniformly into N nodes, and the path-lines passing through the N nodes are traced to determine the traveling time of each deposited particle. To analyze the performance of biofilter one of the main parameter is finding its efficiency. For this purpose we used a steady-state first-order degradation rate model, which was defined and used by [33, 92, 196, 254] in dimensionless form as follows

$$F.E. = 1 - \exp[-b_1 k_m t']. \tag{2.25}$$

In above equation 2.25, b_1 is the biological degradation constant, k_m is the partitioning coefficient and t' is the dimensionless average traveling time of viscous air. The product of b_1 and k_m is constant.

Effect of periodic permeability (K) on filtration efficiency of lung

In this study we choose, ϵ = 0.6, Re = 1, K_0 = 0.1, f = 0.5, and d = 100 nm, so, that we can found the filtration efficiency of lung up to 90$\%$. The time of travel of each particle is placed into equation 2.25 and the resultant F.E. is averaged. The average F.E. of the particles has been taken as the total biofilter F.E. for this simulation. Figure 2.11 shows the variation in the F.E. of the lung to filter needle prolate nanoparticle of aspect ratio (β) = 1000 by varying mean permeability (K_0) from 0.1 to 5. Following observations can be made:

1. We obtained that the traveling time of particles increases when the value of mean permeability (K_0) decreases from 5 - 0.1 as shown in Table 2.3.
2. For a high value of mean permeability, traveling time is less and it increases by decreasing the value of mean permeability.
3. High filtration efficiency costs a large amount of traveling time.
4. For K_0 = 0.1, F.E. of needle prolate at aspect ratio = 1000 took much more traveling time as compared to K_0 = 5.
5. Thus we found that filtration efficiency of the lung under oscillatory boundary condition depends on periodic permeability and is effective to filter deposited nonspherical nanoparticles.

2.6 Conclusion

To analyze the flow dynamics of viscous air and filtration efficiency of the lung to filter needle prolate shaped nanoparticles from generations 5 to 16, we modeled lung as a porous media with periodic permeability under oscillatory boundary conditions. Effect of various parameters such as aspect ratio (β), particle orientation ($\|, \perp$), periodic permeability (K), frequency (f), shape factor (S_f) and Reynolds number (Re) are studied. The results can be summarized as follows:

1. The aspect ratio of particles causes an increment in drag force and decrement in the pressure gradient of air. Additionally, for parallel orientation of particles velocity of fluid increases.
2. Particles with smaller diameter obtained higher aspect ratio, which easily flows with the air stream and has a tendency to deposit deep generations of the lung.
3. Filtration efficiency and traveling time of particles varies inversely with the value of mean permeability for needle prolate nanoparticles from generation 5 to 16.
4. It is found that by increasing the breathing frequency of lung, the velocity of air and particles increases.
5. At low Reynolds number, the increase in the viscosity of fluid decreases the particle velocity and causes the deposition of particles.

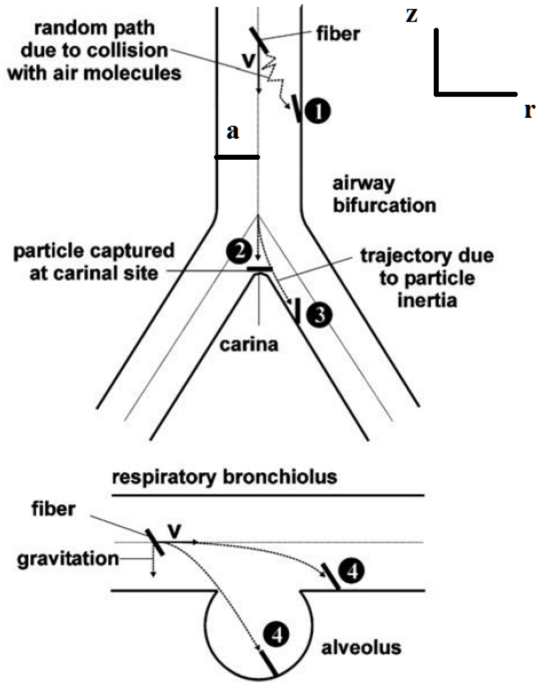

Figure 2.1: Various mechanisms of fiber deposition ((1) Brownian diffusion, (2) interception, (3) inertial impaction, and (4) gravitational settling (sedimentation)) on airways walls of the human respiratory system, where v is the velocity of particle [225].

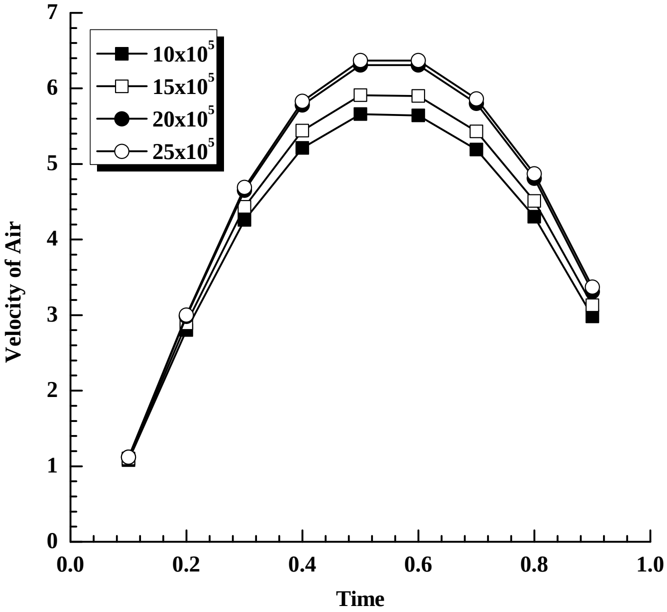

Figure 2.2: Grid independency test when Re = 1, ϵ = 0.6, d = 10 nm, and β = 10.

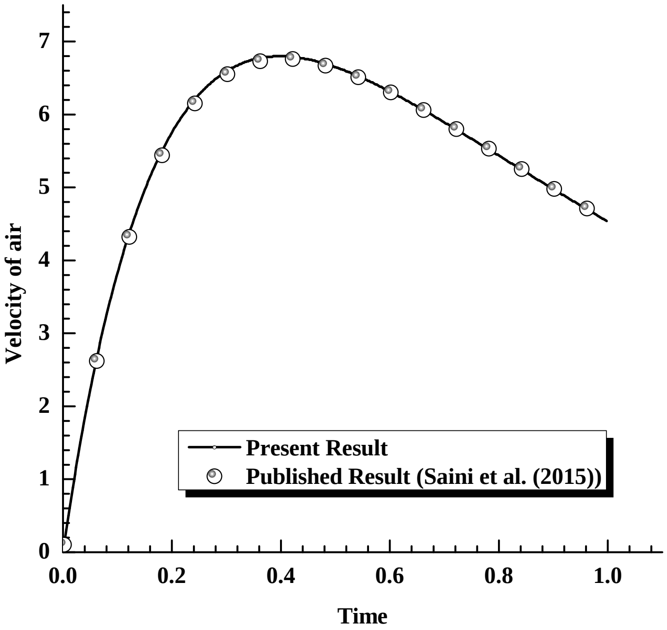

Figure 2.3: Comparison between published (Saini et al. [196]) and present results for air velocity at Da = 0.1, d = 100 nm, and ϵ = 0.6.

Table 2.1: Grid independency test when Re = 1, ϵ = 0.6, d = 10 nm, and β = 10.

	Grid points			
Time	10x10^5	15x10^5	20x10^5	25x10^5
0.1	1.08	1.1	1.12	1.12
0.2	2.8	2.89	2.98	3
0.3	4.26	4.43	4.65	4.69
0.4	5.21	5.44	5.78	5.83
0.5	5.66	5.91	6.31	6.37
0.6	5.64	5.9	6.31	6.37
0.7	5.19	5.43	5.8	5.86
0.8	4.3	4.51	4.81	4.87
0.9	2.98	3.13	3.31	3.37

Table 2.2: Values for numerical calculation.

Variable	Value	Variable	Value
a	0.5μ m	ρ	1.145 kg/m^3
ν	1.52*$10^{-5}m^2$/s	ϵ	0.6
m	0.00002 Kg/l	K_0	0.1 - 5
a_0	0.1 Kg/m^2s^2	N_0	0.02504*$10^{12}/m3$
d	1 - 100 nm	β	7 - 10000
P_0	101.325 k Pa	ρ_0	1 kg/m^3
λ	0.066 μm	f	0.2 - 0.5 per minute
Re	0.1 - 10	-	-

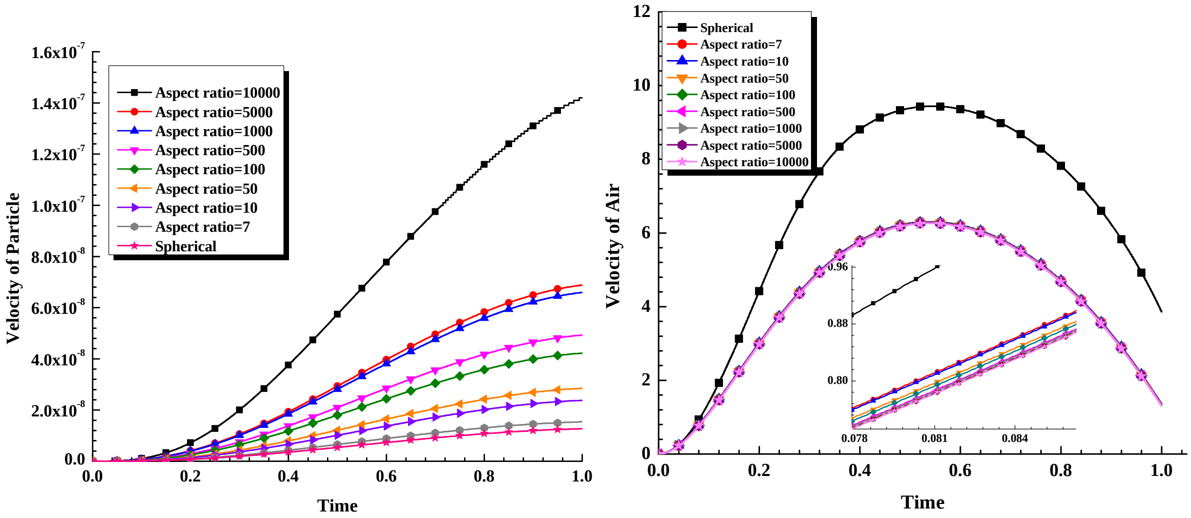

(a)

(b)

Figure 2.4: Effect of shape and aspect ratio (β) on the velocity profiles of (a) particle and (b) air at porosity (ϵ) = 0.6, K_0 = 0.1, Re = 1, and d = 10 nm.

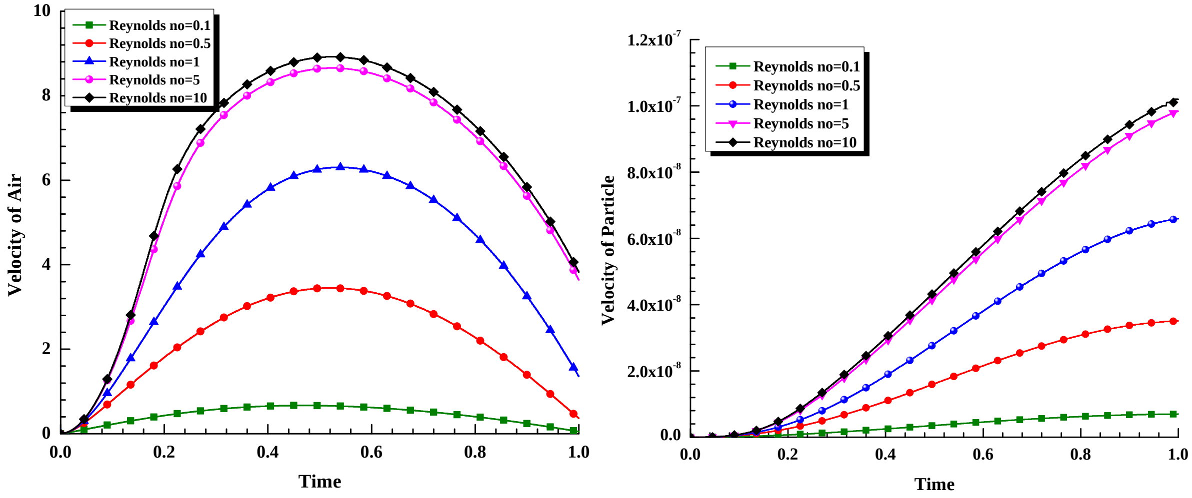

(a) (b)

Figure 2.5: Effect of Reynolds number (Re) on the flow dynamics of (a) air and (b) particles during generations 5 - 16 at K_0 = 0.1, d = 10 nm, ϵ = 0.6, and β = 10.

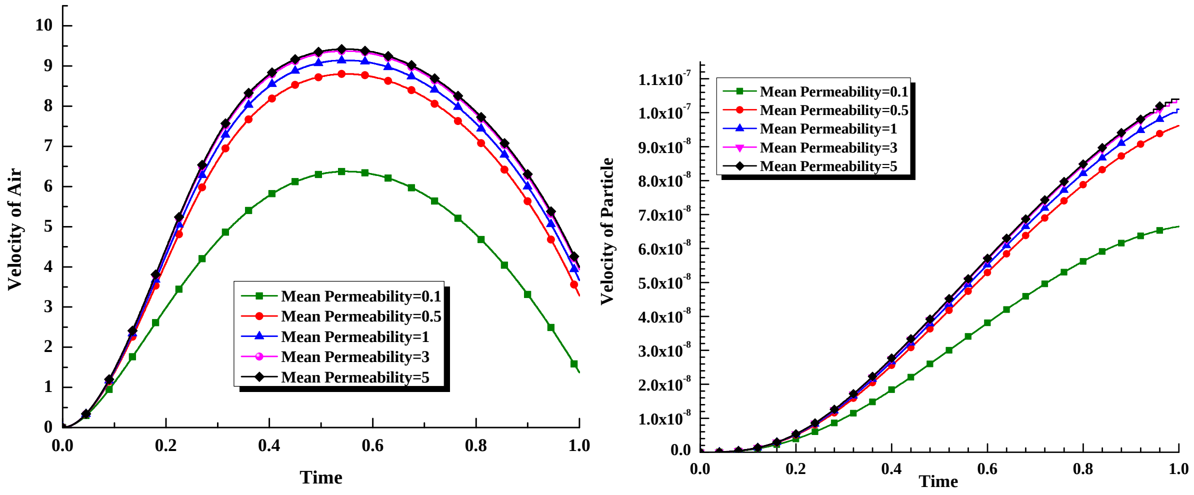

(a) (b)

Figure 2.6: Effect of periodic permeability (K) of media on (a) air and (b) particle by varying mean permeability K_0 of porous medium from 0.1 to 5 at Re = 1, d = 10 nm, ϵ = 0.6, and β = 10.

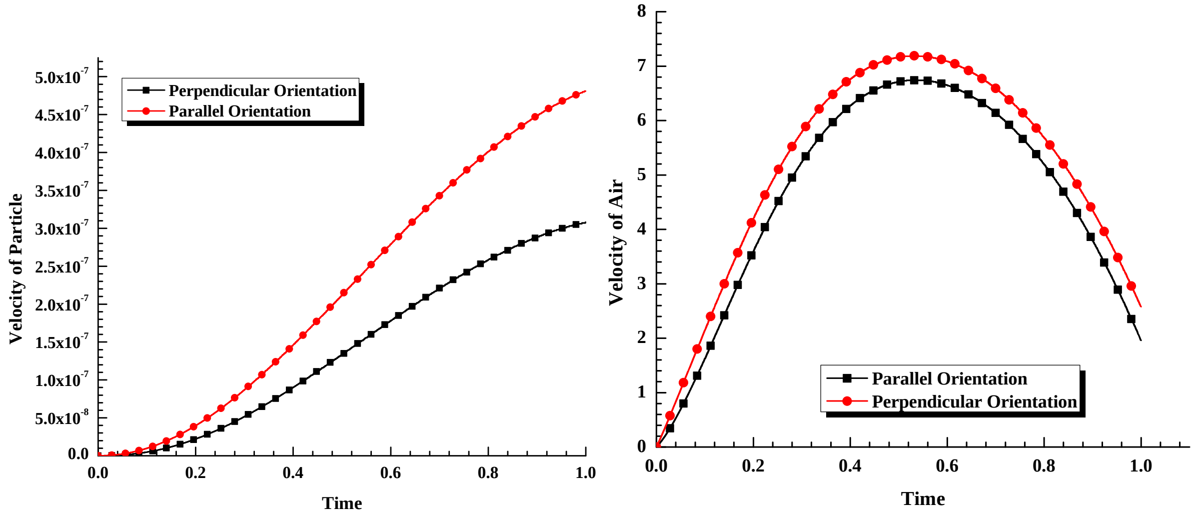

(a) (b)

Figure 2.7: Effect of different orientations (∥, ⊥) of needle prolate nanoparticles on velocity of (a) air and (b) particle at K_0 = 0.1, Re = 1, d = 10 nm, ϵ = 0.6, and β = 10.

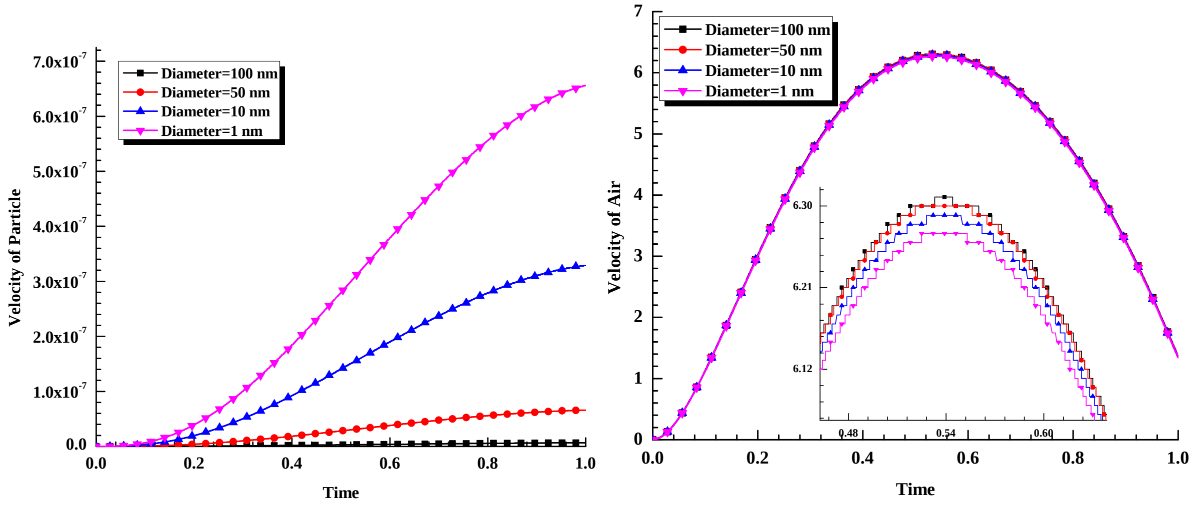

(a) (b)

Figure 2.8: Effect of particle diameter (d = 1 - 100 nm) on (a) air and (b) particle at K_0 = 0.1, Re = 1, ϵ = 0.6, and β = 10.

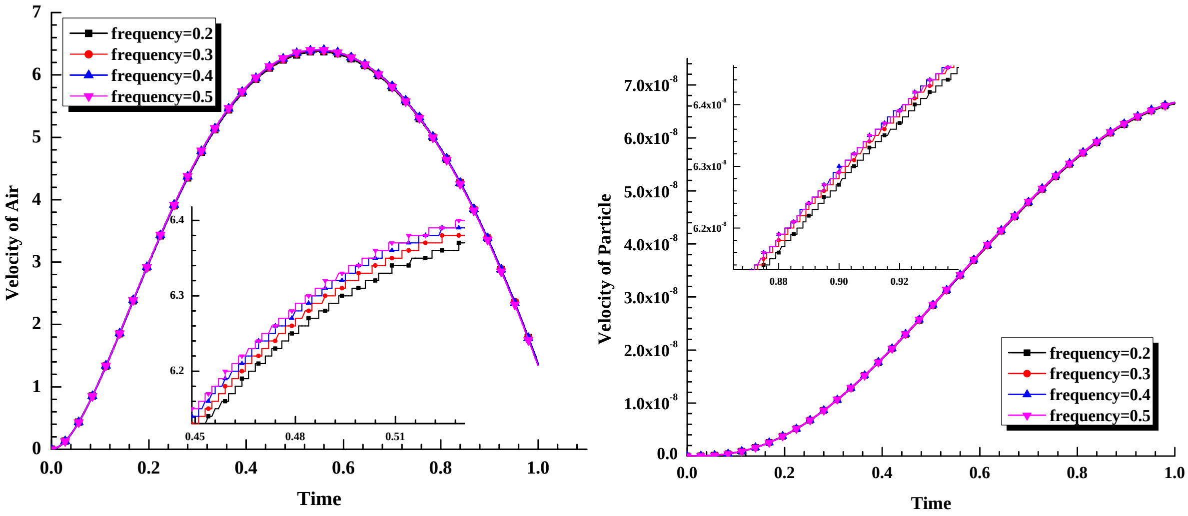

(a) (b)

Figure 2.9: Effect of frequency ($0.2 \leq f \leq 0.5$) on the flow profile of (a) air and (b) particle at d = 1 nm, β = 10, K_0 = 0.1, Re = 1, and ϵ = 0.6.

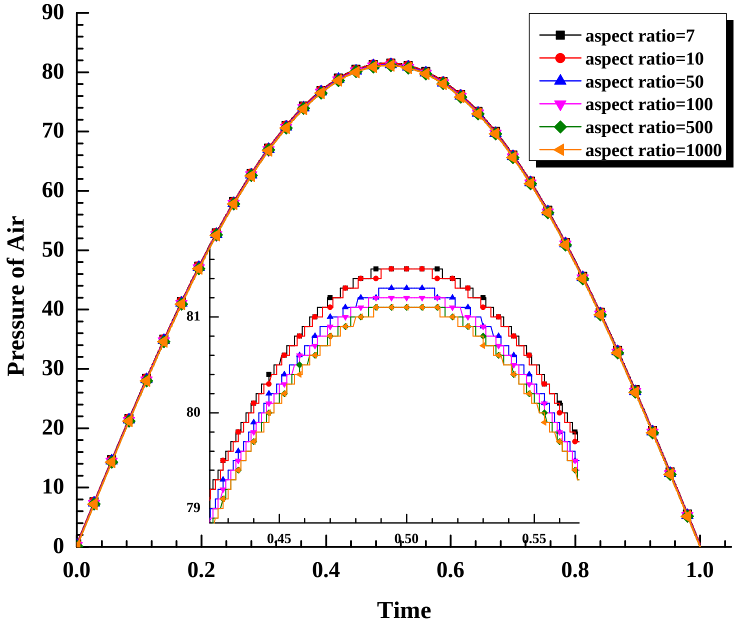

Figure 2.10: Effect of particle shape factor (S_f) on air pressure at d = 1 nm, β = 7-1000, K_0 = 0.1, Re = 1, f = 0.2, and ϵ = 0.6.

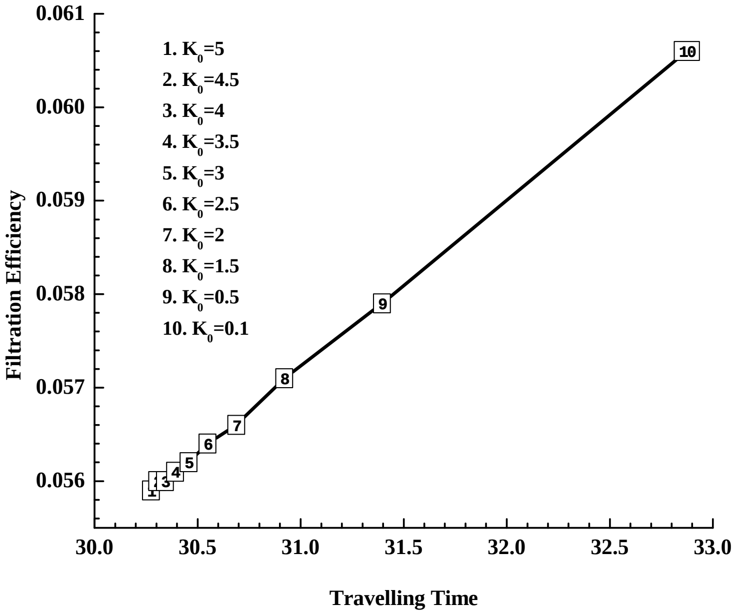

Figure 2.11: Overall filtration efficiency at average traveling time for mean permeability K_0=0.1-5.

Table 2.3: Filtration efficiency of lung at different value of mean permeability K_0 = 0.1 - 5.

Mean permeability K_0	Traveling time	Filtration efficiency of lung
5	30.2739	0.0559
4.5	30.3043	0.056
4	30.3423	0.056
3.5	30.3914	0.0561
3	30.4569	0.0562
2.5	30.549	0.0564
2	30.6879	0.0566
1.5	30.9213	0.0571
1	31.3951	0.0579
0.5	32.8741	0.0606
0.1	33	0.061

Chapter 3: Mathematical study of various shapes non-spherical nanoparticle deposition and filtration through alveolar region of human lungs of age 1-30

3.1 Introduction

Fiber is the most prominent and notorious nanoparticle which is an exposure of a different kind of asbestos and found in irregular shapes such as curl stretched spheroid, elongated or oblate; one of the best examples of this range is multi-walled carbon nanotubes [54, 95]. These fibers are responsible for occupational hazards for asbestos workers and increase the incidence of lung cancer because these kinds of particles have a high probability to reach in the vulnerable gas exchange region in deep lung generations. The structure and dimensions of airways, tidal volume of lung, breathing frequency, fiber shapes and sizes, etc. [69, 192] are the most prominent parameters, which are responsible for penetration and deposition of particles in various generations (0-23, trachea to alveoli) of the lung.

There are various studies [9, 49, 149, 185, 244, 251] suggesting that the deposition of particles as well as human lung architecture and tissue parameters are varied with respect to age. Age is allied to the development of the lung. In 1970, Davidson and Schroter [40] give age based study of human alveoli, in which they stated that a number of alveoli are closely related to total lung volume with larger lungs having considerably more alveoli. Hislop et al. [91] suggested that at birth 24 million alveoli are present, and by the age of 8 years, these are increases up to 300 million. By using design-based stereological approach Ochs et al. [162] calculated the mean alveolar number like 480 million. So, reconstruction would seem to indicate that the development of lung is due to increment in a number of alveoli along with alveolar ducts. By using computational fluid dynamics DeGroot and Straatman [42] developed an approach based on the theory of volume-averaging by considering smaller scale airways and alveoli as a porous domain. Consequently, for the structural determinant of lung architecture number of alveoli, which varies with age, is a key parameter [55]. In addition, aging causes variation in respiratory condition, due to which accurate information of aerosol deposition and clearance in the growing lung is critical not only for infants and children but also in adults. According to Hofmann [94], total deposition inside human lung decreases with increasing age from 7 months to 30 years. In 2016, Sturm [222] presented work on the deposition of bioaerosols with various shapes and sizes in the tracheobronchial tree of probands with different ages (1-20 yr) and stated that bioparticles have higher possibility to reach and deposit in the alveoli of adults than in infant's and deposition of bioparticle is correlated positively with age. In the same year a numerical prediction which was in support with vivo findings [13] given by Henry and Tsuda [86] on postnatal development and particle deposition, according to the study, in humans, major structural change occurs over the first 2 years of life and during this postnatal development the shape of alveolar affects the rate of deposition of nanoparticles deep in the lung.

Moreover, Svartengren and Tsuda [229] observed 46 healthy subjects from 19-81 years and stated that the clearance of deposited particles decreases with age. Sturm [220] simulated clearance of single and multi-walled carbon nanotubes by using a mathematical approach and found that single-walled carbon nanotubes reside significantly longer time in the lungs than multi-walled carbon nanotubes because for single-walled carbon nanotubes mucociliary clearance takes 24 hours after exposure, compared to multi-walled carbon nanotubes, additionally, long size single-walled carbon nanotubes have a higher probability of alveolar deposition than multi-walled carbon nanotubes. In 2017, Sturm [223] presented age (1-20 years) based theoretical study to clear biogenic particles and found that very fine ($<0.01\ \mu$ m) particles cost highest clearance rates than very coarse particles (>5 μ m).

So, from the literature review, we observed that there are various theoretical and experimental studies on the effect of aging on particle deposition, clearance, and lung structure, while there are only a few mathematical studies which observed the effect of nanoparticle deposition and clearance with respect to aging. By considering lung as a variable porous media to calculate filtration efficiency using a biofilter model to remove inhaled nonspherical nanoparticles with respect to aging is still unsolved. The motivation behind this study is to comprehend the effect of age on flow, deposition and filtration efficiency through alveolar region of lung. In this chapter, we present an age-based study of the human lung from childhood to age of 30 by considering the growth of lung is caused by a progressive increment in a number of alveoli and calculated its effect on airflow dynamics together-with filtration efficiency of the human lung. Incorporating the idea of filtration through lung with respect to age biofilter model is extended for variable porous media by assuming that the porosity of lung varies with the number of alveoli and their surface area. Additionally, transportation and filtration properties of nanoparticles of various shapes during inhalation are calculated by using particle shape factor with and without orientation of the particles. Generalized Navier Stokes' equation is used for flow dynamics of viscous air and Newton second law of motion is applied to study the flow of particles. Finite difference numerical method is used to get simple discretized equations and computational work is performed by using user-defined code at very fine grid. Effect of various parameters such as aspect ratio (β), the orientation of particles with respect to the flow stream, Darcy number (Da), porosity (ϵ) is analyzed. To validate the mathematical model a comparative study is also presented.

3.2 Mathematical Formulation

3.2.1 Governing equations

An incompressible fully-developed, steady, laminar, and Newtonian fluid is flowing along the axial axis of the circular tube (alveolar duct) of radius 'a' with terminal alveoli of radius 'r_0'. Axial axis measured along the tube and radial axis is normal to the flow direction, as shown in Figure 3.1. We assumed various shapes and sizes of nonspherical nanoparticles are distributed homogeneously throughout the inhaled volume. Dirt can be accumulated either on the sides and turns of the ducts or inside alveolies, which can be filtered by the mechanism of mucocillary clearance or coughing. Consequently, we considered alveolar region as an internal biofilter media [1]. Since number of alveoli change with respect to age, therefore, we assumed porosity of lung is also change with aging and is a function of number of alveoli or age. A mathematical model proposed by [196, 253] is extended by including variable porosity and particle shape factor terms to find the filtration efficiency of lung at different ages (1-30 years) subject to no slip boundary condition and time dependent sinusoidal pressure gradient. One dimensional flow governing equations in cylindrical polar coordinate system (r, z, θ) are given below:

$$\frac{\partial u}{\partial t} + \frac{u}{\epsilon}\frac{\partial u}{\partial r} = -\frac{\epsilon}{\rho}\frac{\partial p}{\partial r} + \nu\left(\frac{\partial^2 u}{\partial r^2} + \frac{1}{r}\frac{\partial u}{\partial r}\right) + \left(-\frac{\epsilon\nu}{K}u + s_k\frac{N_0}{\rho}(v-u)\right), \tag{3.1}$$

$$m\frac{\partial v}{\partial t} = S_f s_k (u - v). \tag{3.2}$$

---

[1] Biofilter is defined in Chapter 1, Subsection 1.4.1

Equation 3.1 represents the momentum equation of air and equation 3.2 represents the motion equation of particles. The first term in the left hand side of the equation 3.1 is for unsteady flow and the second term is for convection. First, second and third terms in the right hand side of equation 3.1 are the pressure gradient, diffusion and the entire body force because of the existence of porous media and additional external force fields respectively. The term in the left hand side of equation 3.2 represents the product of the mass times the acceleration and right hand side of this equation represents the drag force on nonspherical nanoparticles.

According to Weibel [245] each of the structural components such as airways, alveoli, and blood vessels have different growth patterns in number as well as in size. After using Weibel model, Hofmann [94] defined an age dependent lung geometry from birth to adulthood in which the total number of alveoli N_a increase with age as follows,

$$N_a = [37.6 + (1 - e^{-0.4\tau})286.21]10^6, \quad \tau = 1, 2, ...23..., 30 \text{ year}. \tag{3.3}$$

Since porosity is the measurement of vacant spaces and alveolies are the void spaces inside lung, they can be approximated as spherical bubble and responsible for porousness an growth of lung [42]. Moreover there are theoretical, experimental and vivo studies [49, 108, 179] which showed that, not only number of alveoli but their surface area also linearly associated with aging. So, by utilizing equation 3.3 we modeled porosity (ϵ, in equation 3.1) of lung $\approx$ as the product of number of alveoli and ratio of surface area of single alveoli to total surface area of lung as

$$\epsilon = N_a \left(\frac{r_0}{r'}\right)^2, \tag{3.4}$$

also, in equation 3.1, K, denotes the permeability of media, which is defined [57] in terms of ϵ as follows

$$K = \frac{\epsilon^3 d_p^2}{150\,(1-\epsilon)^2}, \tag{3.5}$$

and s_k, denotes the drag force coefficient for nonspherical particles and C is the Cunningham slip correction factors used for free molecular flow regime [2]. Additionally, in equation 3.5, d_p, denotes, aerodynamic diameter, which determines how well the particle enter and how far it go in the lungs [3]. In continuation, to analyse the filtration/clearance efficiency of lung the property of nanoparticles such as size and shape [101] are also very important factors. There are different models in which

---

[2] see Chapter 2, Subsection 2.2.1, and equation 2.4

[3] see Chapter 2, Subsection 2.2.1, and equation 2.5.

size dependent properties are explained, some assumed nanoparticles as ideal spheres [158] while some model reported particle shape as an important property and worked on polyhedral, disk like nanoparticles [209]. In equation 3.2, S_f is the particle shape factor, which is defined as the ratio of the surface area of a nonspherical nanoparticle (S') to the surface area of spherical nanoparticle (S), where both of the nanoparticle have identical volume [177]

$$S_f = \frac{S'}{S}, \tag{3.6}$$

generally, for polyhedral shape nanoparticle surface is composed of different planes. So, the surface area of a nanoparticle is the sum of area of all the planes as

$$S' = \sum_i S_i, \tag{3.7}$$

where S_i is the area of the plane i.

In terms of drag force the dynamic shape factor can be described as shown in Chapter 2 [4]. However, some authors [218, 225] mentioned the concept of particle orientation (parallel and perpendicular) in their study [5]. In the present study we used elongated particles, so the formulation for parallel $S_{\|}$ and perpendicular $S_{\perp}$ orientations can be described by following formulation [225]

$$\left.\begin{aligned} S_{\perp} &= \frac{\frac{8}{3}\left(\beta^2-1\right)\beta^{\frac{-1}{3}}}{\left(\frac{(2\beta^2-3)}{(\beta^2-1)^{\frac{1}{2}}}\right)\ln\left(\beta+(\beta^2-1)^{\frac{1}{2}}\right)+\beta}, \\ S_{\|} &= \frac{\frac{4}{3}\left(\beta^2-1\right)\beta^{-\frac{1}{3}}}{\left(\frac{(2\beta^2-1)}{(\beta^2-1)^{\frac{1}{2}}}\right)\ln\left(\beta+(\beta^2-1)^{\frac{1}{2}}\right)-\beta}, \end{aligned}\right\}\beta > 1, \tag{3.8}$$

where, β is the aspect ratio of particle length to particle width/diameter. For extremely long fibers, $\beta >> 1$ and for extremely thin disks, $\beta << 1$. In the case of oblate particle, the following equations are commonly used

$$\left.\begin{aligned} S_{\perp} &= \frac{\frac{8}{3}\left(\beta^2-1\right)\beta^{\frac{-1}{3}}}{\left(\frac{(2\beta^2-3)}{(1-\beta^2)^{\frac{1}{2}}}\right)\arccos\beta+\beta}, \\ S_{\|} &= \frac{\frac{4}{3}\left(\beta^2-1\right)\beta^{-\frac{1}{3}}}{\left(\frac{(2\beta^2-1)}{(1-\beta^2)^{\frac{1}{2}}}\right)\arccos\beta-\beta}, \end{aligned}\right\}\beta > 1. \tag{3.9}$$

---

[4] Subsection 2.2.1 and equation 2.6

[5] see Chapter 2, Subsection 2.2.1, and equation 2.7

3.2.2 Initial and boundary conditions

Initial conditions at $t \leq 0, \ \ 0 \leq r \leq a$ are as follows:

$$u(r,t) = v(r,t) = 0, \tag{3.10}$$

Boundary conditions at $t > 0$, for $r = 0$ and a as

$$\left(\frac{\partial u}{\partial r}\right)_{r,t} = 0. \tag{3.11}$$

3.3 Methodology

3.3.1 Transformation of the governing equations

To solve the governing equations 3.1-3.2 numerically we have to make them dimensionless, so we used the following quantities:

$$x^* = \frac{r}{a}, P^* = \frac{pa^2}{\rho\nu^2}, T^* = \frac{t\nu}{a^2}, U^* = \frac{au}{\nu}, V^* = \frac{av}{\nu},$$

$$\frac{\partial U}{\partial T} + \frac{U}{\epsilon}\frac{\partial U}{\partial x} = -\epsilon\frac{\partial P}{\partial x} + \left(\frac{\partial^2 U}{\partial x^2} + \frac{1}{x}\frac{\partial U}{\partial x}\right) + B\left(V - U\right) - \frac{\epsilon}{Da}U, \tag{3.12}$$

$$\frac{\partial V}{\partial T} = \frac{S_f\left(U - V\right)}{\tau}, \tag{3.13}$$

where

$$Da = \frac{K}{a^2}, B = \frac{M}{\tau} = \frac{N_0 s_k a^2}{\mu}, M = \frac{N_0 m}{\rho}, \tau = \frac{m\nu}{a^2 s_k}$$

where, Da is Darcy number and B, M, τ are used for simplification.

Transformed initial conditions from equation 3.10, at $T \leq 0, \ \ 0 \leq x \leq 1$ are as follows:

$$u(x,T) = v(x,T) = 0, \tag{3.14}$$

Transform boundary conditions from equation 3.11, at $T > 0$, for $x = 0$ and 1 are as follows:

$$\left(\frac{\partial u}{\partial x}\right)_{x,T} = 0. \tag{3.15}$$

In equation 3.1, the pressure gradient due to periodic breathing in non-dimensional form is assumed as

$$-\frac{\partial P}{\partial x} = P_0 \sin(\pi f T) + S_f, \tag{3.16}$$

where f is the frequency of breathing.

3.4 Numerical Scheme

Finite difference method [214] is the most suitable technique for nonlinear problems related to regular geometries so, to find the solution of the non-dimensional governing equations 3.12-3.13 subject to the initial and boundary conditions 3.14-3.16 we used this method. The computational grid are defined in the following form where the discretization of air velocity $U(x, T)$ is written as $U(x_i, t_j)$ or $U(i, j)$ and similarly the particle velocity $V(x, T)$ is written as $V(x_i, t_j)$ or $V(i, j)$.

$$x_i = i\Delta x,\ (i = 0, 1, 2, 3, ..., N),\ \text{where } x_N = 1.0,$$
$$t_j = (j - 1)\Delta t, (j = 1, 2, ..),$$

where i and j are the space and time indexes; Δx and Δt are the increments in axial direction and time respectively.
We used central difference approximation at point (x_i, t_j) for all the spatial derivatives as follows:

$$\frac{\partial U}{\partial x} = \frac{U_{i+1,j} - U_{i-1,j}}{2\Delta x}, \tag{3.17}$$

$$\frac{\partial^2 U}{\partial x^2} = \frac{U_{i+1,j} - 2U_{i,j} + U_{i-1,j}}{(\Delta x)^2}, \tag{3.18}$$

and forward difference approximation for all the time derivatives as

$$\frac{\partial U}{\partial T} = \frac{U_{i,j+1} - U_{i,j}}{\Delta t}. \tag{3.19}$$

Additionally, at $x = 0$, following approximation is applicable in equation 3.12, [6]

$$\lim_{x\to 0} \frac{1}{x}\frac{\partial U}{\partial x} = \lim_{x\to 0} \frac{\partial^2 U}{\partial x^2}, \tag{3.20}$$

so, the equation 3.12 at $x = 0$ becomes,

$$U_{i,j+1} = \left(1 - B\Delta t - \left(\frac{\epsilon}{Da}\right)\Delta t - 4r_1\right)U_{i,j} + \left(2r_1 - \frac{U_{i,j}r_1\Delta x}{2\epsilon}\right)U_{i+1,j}$$
$$+ \left(2r_1 + \frac{U_{i,j}r_1\Delta x}{2\epsilon}\right)U_{i-1,j} + B\Delta t V_{i,j} + \left(P_0 \sin\left(\pi f j\Delta t\right) + S_f\right)\epsilon\Delta t, \tag{3.21}$$

---

[6] When $x \to 0$, we found that the denominator is also approaching to zero and make the term indeterminate, which is inappropriate for the physical state of the respiratory system. Therefore, to remove this kind of inconsistency we used L'hospital rule of limit here.

and at $0 < x \leqslant 1$,

$$U_{i,j+1} = \left(1 - B\Delta t - \left(\frac{\epsilon}{Da}\right)\Delta t - 2r_1\right)U_{i,j} + \left(r_1 - r_1\Delta x\frac{U_{i,j}}{2\epsilon} + \frac{r_1}{2i}\right)U_{i+1,j}$$
$$+ \left(r_1 + \frac{r_1\Delta x U_{i,j}}{2\epsilon} - \frac{r_1}{2i}\right)U_{i-1,j} + B\Delta t V_{i,j} + \left(P_0 \sin\left(\pi f j \Delta t\right) + S_f\right)\epsilon\Delta t, \tag{3.22}$$

where $\left(\frac{\Delta t}{\Delta x^2}\right) = r_1$.
The equation 3.13 transforms as

$$V_{i,j+1} = \left(1 - \frac{S_f\Delta t}{\tau}\right)V_{i,j} + \frac{S_f\Delta t}{\tau}U_{i,j}, \tag{3.23}$$

and the initial and boundary conditions from equation 3.14-3.16 are transform as follows:

$$U_{i,1} = V_{i,1} = 0,$$
$$U_{2,j} = U_{0,j} = 0;\ \ U_{N+1,j} = 0. \tag{3.24}$$

After applying above mentioned discretization technique we got velocity profiles at the $(j+1)^{th}$ time level in terms of the velocity at j^{th} time level for equations 3.21-3.24 respectively.

3.5 Results and Discussion

The numerical computations have been carried out by using the values defined in Table 3.1 and 3.2 to analyze the effect of particle aspect ratio (β), orientation ($S_{\perp}$, $S_{\parallel}$), diameter (d), effect of variable porosity (ϵ), Darcy number (Da), effect of shape factor (S_f) on the velocity profile of air and particles, pressure of air, filtration efficiency of alveolar region, and shown in Figure 3.3-3.10. In addition, we calculated the effect of particle shape and variable porosity on the filtration efficiency of the human lung with respect to age. To estimate the accuracy of the solution the grid independence test is performed at each time level by varying the grid points $\Delta x \geq$ 0.0014 and $\Delta t \geq 10^{-6}$ by using the following stability criteria so that less error occurred in the numerical computation

$$\max\left(\frac{\Delta t}{\Delta x^2}\right) \leq 0.5 \tag{3.25}$$

and found result remains consistent beyond the grid points Δx = 0.01 and $\Delta t = 10^{-5}$ in axial and radial directions respectively. Therefore, all the computations are done by using the grid size 100x10^5 with the accuracy of 10^{-5}.

Before discussing the analysis of the present problem a numerical code validation and predictive accuracy of the model are checked by comparing output data produced by present model with respective results generated by model of Saini et al. [196] for air velocity at Da = 0.1, d = 100 nm, ϵ = 0.6 with exponential pressure gradient and represented in Figure 3.2 (see in Table 3.3).

Saini et al. [196] studied flow of viscous air through a circular tube by considering alveolar region as a biofilter media with constant porous media and exponential pressure gradient. Filtration efficiency of spherical particles of d = 100 nm was calculated using biofilter model at constant porosity (ϵ = 0.6) of filtration media. In Figure 3.2, comparison is shown between present result with published results (Saini et al. [196]) and found that our result is quite similar ($\approx$ 99.9 %) with the published result. So, we can say, our model is in excellent agreement with Saini et al. [196].

3.5.1 Effect of aspect ratio (β) on the velocity of air and particle

In this study we used regular octahedral, regular hexahedral, regular tetrahedral particles without orientations and prolate particles at diameter (d) = 50 nm and aspect ratio (β) = 3 - 1000 or disk shaped particles at diameter (d) = 50 nm and aspect ratio (β) = 0.1 - 0.001 with orientation effect. From Figure 3.3(a)- 3.3(d), we analyze the effect of various shapes and aspect ratios on the velocity of air and particles at age 15. We found, from Figure 3.3(a), the velocity of regular tetrahedral particles is higher than octahedral particles, which cause decrement in the velocity of air (see Figure 3.3(b)). Additionally, in Figure 3.3(c), at β = 3, the velocity of the particle is very low correspondingly velocity of air in Figure 3.3(d) is very high, while by increasing the value of aspect ratio velocity of particle increases and the velocity of air decreases with time. So, from Fig 3.3, we observed that particle with high aspect ratio remain in the air for a longer time and causes decrement in air velocity or consequently, we can say that nonspherical nanoparticle with high aspect ratio slows down the air flow and have the probability to trigger pro - inflammatory effects.

3.5.2 Effect of lung porosity (ϵ) on the flow dynamics of air and particle

From equation 3.4, we found that porosity of lung varying from 0.2 to 0.7 due to aging 1 - 30. Effect of porosity (ϵ) on flow dynamics of air and particles are shown in Figure 3.4(a) - 3.4(b) at β = 10, d = 50 nm, Da = 0.1. From these figure we found that at ϵ = 0.2 (age = 1) velocity of air and particle are lesser than ϵ = 0.7 (age = 30) and with the increment in age (1 to 30 years) the porosity of lung increases, therefore, velocity of air and particle increases gradually with time. Since, porous media with higher porosity have large number of alveolies, which allow flow of air more freely as compare to lower porous media. Consequently, we can say people with less porous lungs are face difficulty in the process of breathing.

3.5.3 Effect of particle orientations on the flow dynamics of air and particle

In Figure 3.5(a) - 3.5(b) we present the effect of different orientations of particles for aspect ratio's 10 and 1000 on the velocity of air and particle at the age = 15, Da = 0.1, and d = 50 nm. At β = 10, from Figure 3.5(b), we observed that velocity of parallel oriented particle is higher than perpendicular oriented, while from Figure 3.5(a), we found velocity of air due to parallel orientation of particle is lower than perpendicular orientation. As well as by increasing the value of β from 10 to 1000, we found similar effect of aspect ratio on air and particle velocities but value of velocities are increases as compare to previous one. So, from these figures, we obtained that velocity of air and particles are increases in parallel orientation by increasing aspect ratio from 10 - 1000. While, velocity of air and particles are decreases in perpendicular orientation by increasing aspect ratios from 10 - 1000. It may happen due to the alignment of parallel orientated particles with the direction of flow stream, which cause increment in the drag force on flow stream. Consequently, the particles with parallel orientation have tendency to flow with air stream deep inside the lung.

3.5.4 Effect of Darcy number (Da) on air and particle velocity

Darcy number (Da) is very important for flow in porous media. We observed the effect of Da from 0.001 to 0.5 on flow dynamics of air and particles at aspect ratio (β) =10, d = 50 nm, at age 15 in Figure 3.6(a)-3.6(b). We found from these, figures that by decreasing the value of Da from 0.5 - 0.001, velocity of air and particles through porous media are decreases significantly. For smaller values of Da, the porous layer is considered low permeable for penetration and the fluid experiences pronouncedly larger resistance and hindrance through the porous matrix and the velocity of air and particle decreases, while for large value of Da media become highly permeable to allow the fluid to pass easily, which causes increment in the flow of air and particle. Additionally, due to increment in Da media pressure will be decreased; which cause increment in velocity of air and particles gradually with time through porous region. So, Darcy number affect the flow-ability of fluid in a great extent.

3.5.5 Effect of porosity (ϵ) on pressure gradient

In Figure 3.7 effect of lung porosity ($0.2 \leq \epsilon \leq 0.7$) is found on the pressure gradient of airflow. From this figure we found that at ϵ = 0.2868 pressure is very high (for infant of 1 year = 346 Kpa), while for ϵ = 0.7037 (for adult of 30 years), it is very low (i.e.142 Kpa) and with the increment in age (or porosity) it decreases gradually with time. So, from this figure, we concluded that aging cause gradually increments in an air pressure gradient inside the human lung.

3.5.6 Filtration efficiency of lung in respect of age

To analyze the performance of biofilter one of the main parameter is finding its efficiency. For this purpose we used a steady-state first-order degradation rate model, which is defined in Chapter 2 [7]. We aimed to find the F.E. of the lung from age 1-30. For this purpose, we first calculated the porosity of lung by Equation 3.4 associated with age 3, 8, 13, 30. As the traveling time of each particle is identical, we try to optimize the biofilter model (equation 2.25) at β=10, $10^{-1} \leq Da \leq 10^{-3}$ in respect of age, as shown in Figure 3.8(a)-3.8(d) (Table 3.4). From these figures we can see, for a particular age (3, 8, 13, 30) there is discernible variation in the F.E. and traveling time of particles. As age increases from 1 to 30 traveling time increases and F.E. decreases with a decrement in Darcy number from 0.1 to 0.001. These results are compatible with the theoretical and physiological results by Sturm [223] and can be useful to calculate F.E. of the growing lung.

3.5.7 Filtration efficiency of lung in respect of shape factor

In Figure 3.9, we show F.E. of lung for spherical (d = 100 nm) and nonspherical nanoparticles ($10 \leq \beta \leq 1000$) by varying Darcy number ($10^{-1} \leq Da \leq 10^{-3}$) in respect of age 15. For each graph we found that at the same aspect ratio, the traveling time of particle increases when the Darcy number is decrease from 0.1 to 0.001. As shown in Figure 3.9(a)- 3.9(d) (Table 3.5), traveling time of particle and F.E. of lung increases by increasing β from 10 to 1000 and decreasing Darcy number from 0.1 to 0.001. After analysis following observations can be drawn:

1. For spherical shape particles traveling time is less and it increases by increasing particle aspect ratio from 10 to 1000.
2. High filtration efficiency costs a large amount of traveling time for nonspherical nanoparticle of aspect ratio 1000.
3. For $Da = 0.1$ (in Figure 3.10), we found F.E. of nonspherical nanoparticle of aspect ratio = 1000 costs much more traveling time compared to the spherical nanoparticle.

3.6 Conclusion

Human lung goes through various anatomical changes from birth to adulthood. Development of alveoli with age is one of the main factors of growth of lung. In this study, we carried out an

---

[7] Subsection 2.5.8 and equation 2.25

age based study of nonspherical nanoparticle deposition and filtration effect of growing lung from age 1 to 30. For this purpose, we model the lung as a variable porous media and porosity depend on a number of alveoli. In addition, we analyzed the efficiency of the lung to filter nonspherical nanoparticle of different aspect ratio with diameter = 50 nm. Computational study is done by using various physical parameters such as: Effect of aspect ratio (β), the orientation of particle with respect to flow stream, Darcy number (Da), porosity (ϵ) graphically. The important concluding remarks of the conducted study are as follows:

1. In respect of shape factor, the velocity of particles related with this inequality, regular octahedral $<$ regular hexahedral $<$ regular tetrahedral and velocity of air-related with this inequality, regular octahedral $>$ regular hexahedral $>$ regular tetrahedral.
2. It is noticed that the air and particle velocity of elongated nanoparticles are affected by increasing their aspect ratio from 3 to 1000.
3. Due to parallel orientation of particles we found an increase in the velocity of fluid was increased.
4. Increment in Darcy number causes an increment in the velocity of fluid and decrement in pressure gradient.
5. High porosity (during adulthood) will reduce the pressure gradient of the lung.
6. It is found that the fraction of particles trapped in the alveolus increase by decreasing the Darcy number.
7. Due to aging, filtration efficiency of lung decreases and traveling time of particles increases.
8. Nonspherical nanoparticle of aspect ratio 1000 cost a large amount of time to filter from lung as compared to the spherical nanoparticle of the same diameter. By this, we conclude that the nonspherical nanoparticle with a high aspect ratio has the feasibility to hang in the air stream and take a long time to deposit in deeper lung generations.

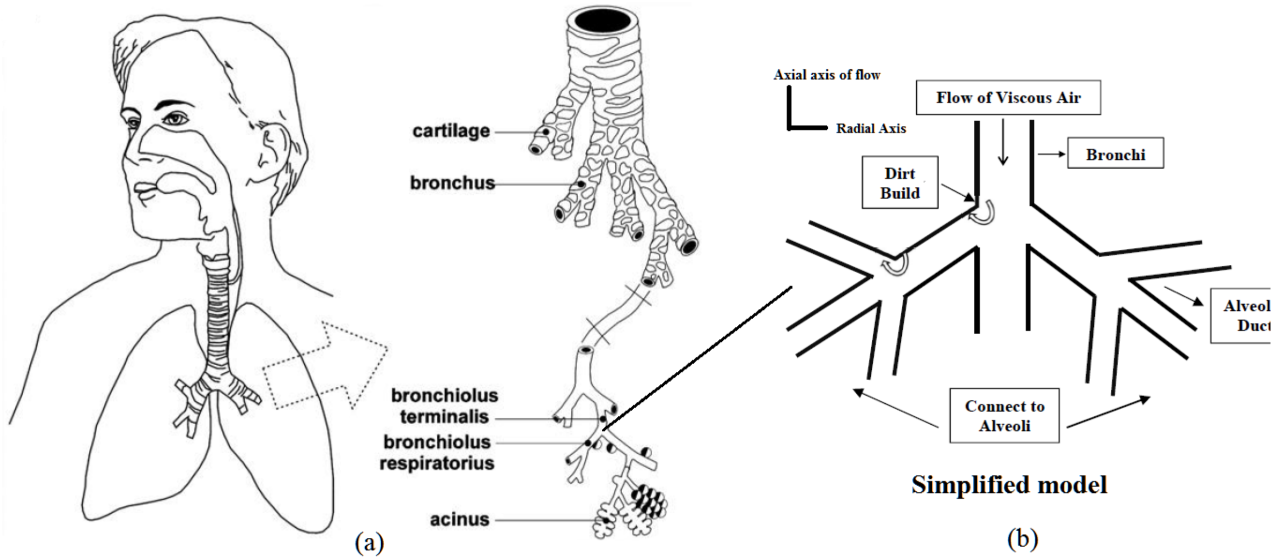

Figure 3.1: (a) Architecture of the tracheobronchial tree and the alveolar region [225] and (b) simplified model of alveolar region for viscous air flow.

Table 3.1: Shape factors for special shapes [177].

S.N.	Particle Shape	Shape factor (s_f)
1.	Regular tetrahedral	1.49
2.	Regular hexahedral	1.24
3.	Regular octahedral	1.18

Table 3.2: Values for numerical calculation.

Variable	Value	Reference
a	0.5μ m	Saini et al. [196]
ρ	1.145 kg/m^3	Saini et al. [196]
ν	1.52*$10^{-5}m^2/s$	Saini et al. [196]
m	0.0002 Kg/l	Saini et al. [196]
r_o	0.11 mm	-
N_0	0.02504*$10^{12}/m3$	Saini et al. [196]
d	50 nm	Rissler et al. [184]
β	10 - 1000 for elongated and 0.1 - 0.001 for oblate	Sturm [221]
P_0	101.325 k Pa	Saini et al. [196]
b_1	0.0061	Hodge et al. [92]
ρ_0	$1kg/m^3$	-
λ	0.066 μm	Sturm [221]

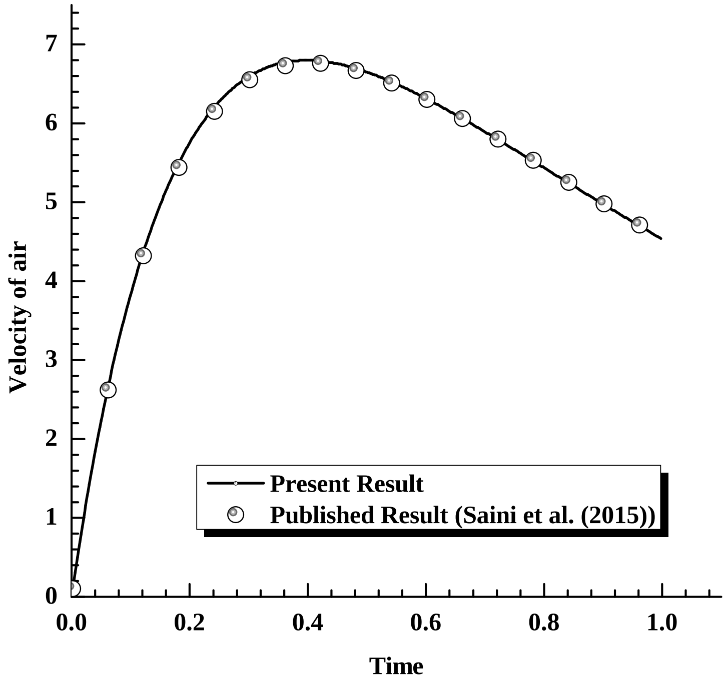

Figure 3.2: Comparison between published (Saini et al. [196]) and present work for air velocity at Da = 0.1, d = 100 nm, and ϵ = 0.6.

Table 3.3: Comparison between published (Saini et al.[196]) and present result.

	Velocity of Air	
Time	Present Result	Published Result (Saini et al. [196])
0.1	3.83	3.77
0.2	5.75	5.69
0.3	6.59	6.54
0.4	6.8	6.76
0.5	6.65	6.63
0.6	6.32	6.31
0.7	5.89	5.9
0.8	5.44	5.45
0.9	4.98	4.99
0.998	4.54	4.56

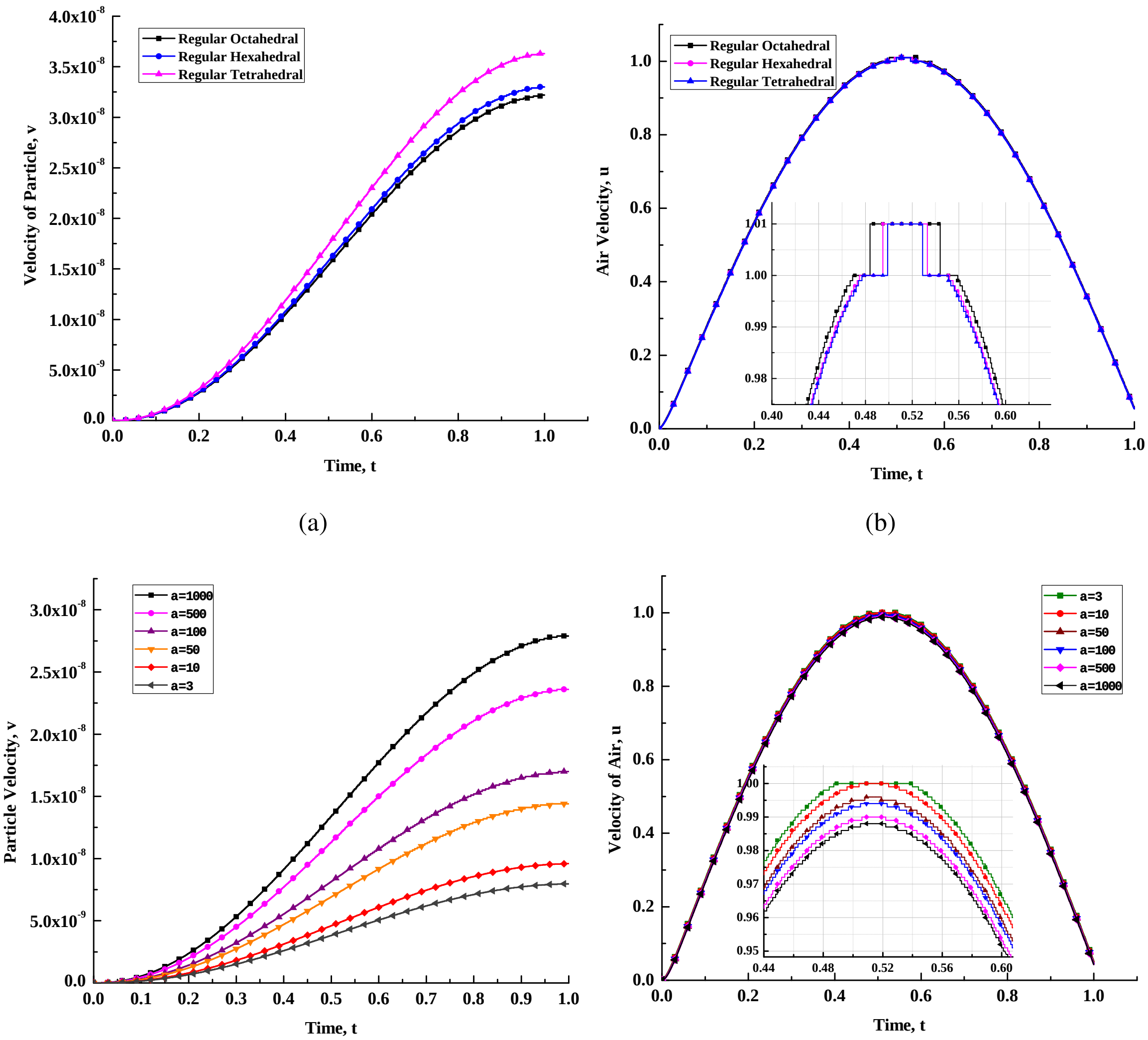

(a) (b)

(c) (d)

Figure 3.3: Influence of aspect ratio (β) without orientation of particle at age = 15 on (a) particle velocity, (b) air velocity and influence of shape factor with orientation of particle at $3 \leq \beta \leq 1000$, age = 15 on (c) particle velocity, (d) air velocity.

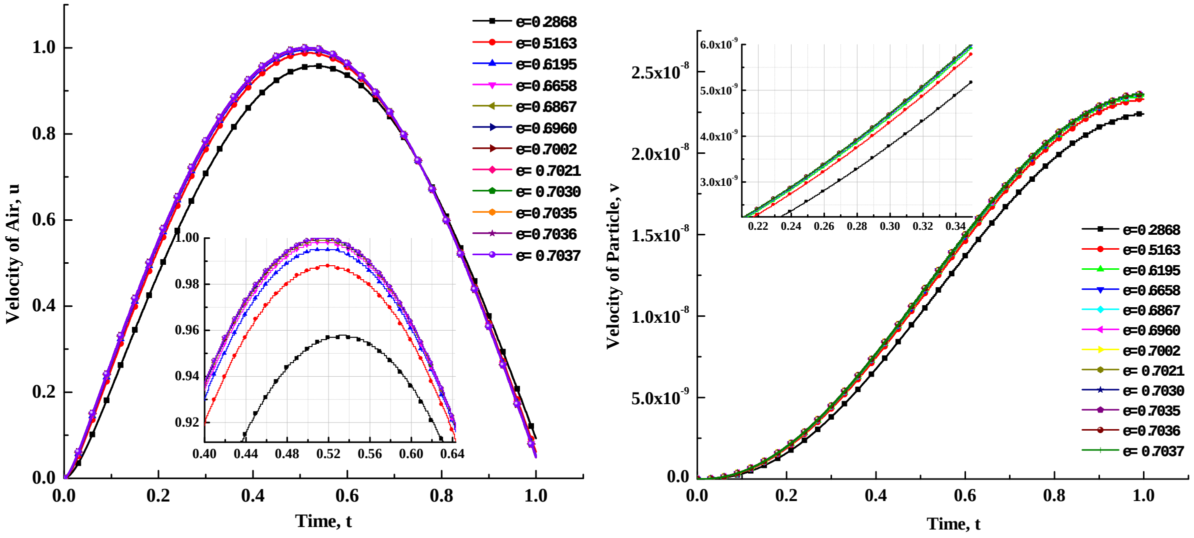

(a) (b)

Figure 3.4: Effect of lung porosity on flow dynamics of (a) air and (b) particle at β = 10, d = 50 nm, and Da = 0.1.

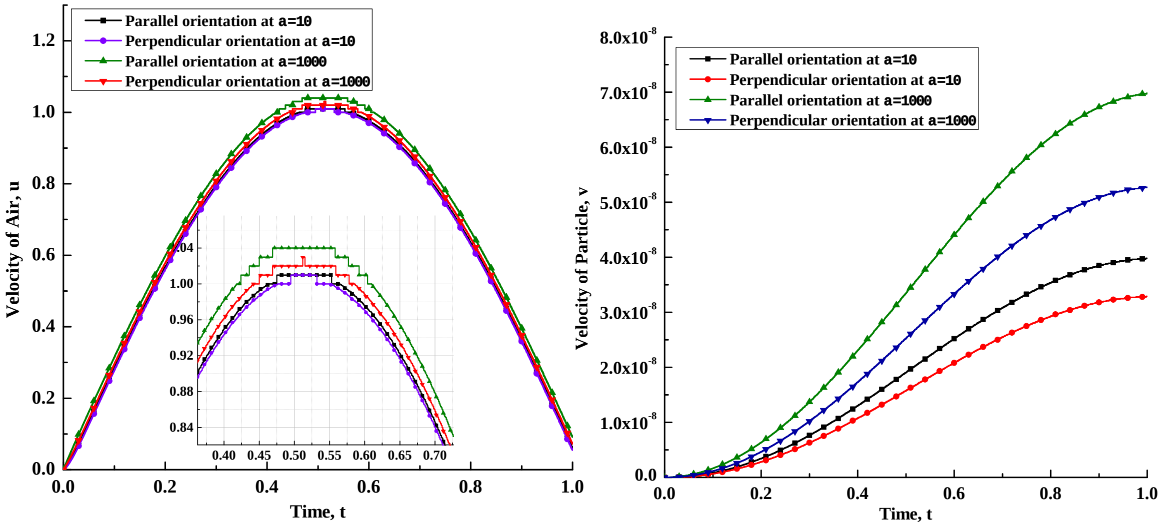

(a) (b)

Figure 3.5: Significance of parallel and perpendicular orientation of particle at the age = 15, β = 10 & 1000, Da = 0.1, and d = 50 nm on (a) air velocity and (b) particle velocity.

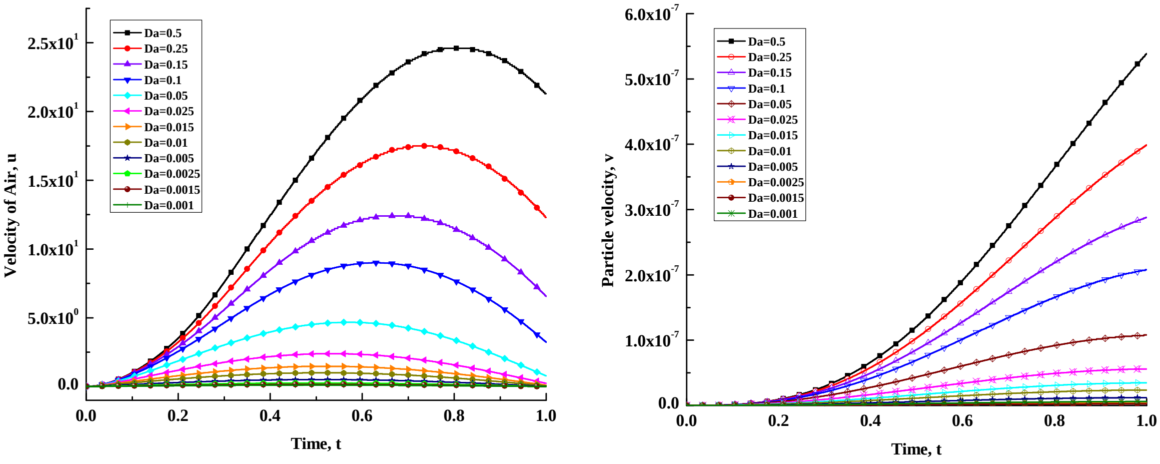

(a) (b)

Figure 3.6: Effect of Darcy number ($0.001 \leq \mathrm{Da} \leq 0.5$) on flow dynamics at β = 10, d = 50 nm at age=15 on (a) air velocity and (b) particle velocity.

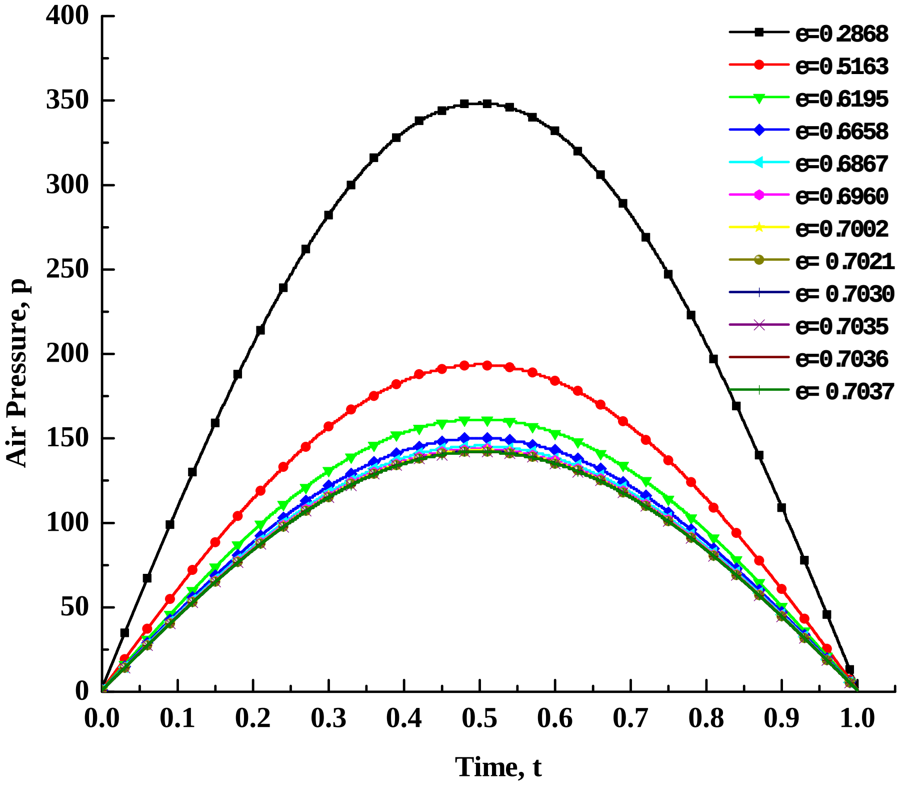

Figure 3.7: Effect of porosity ($0.2 \leq \epsilon \leq 0.7$) with respect to age on air pressure.

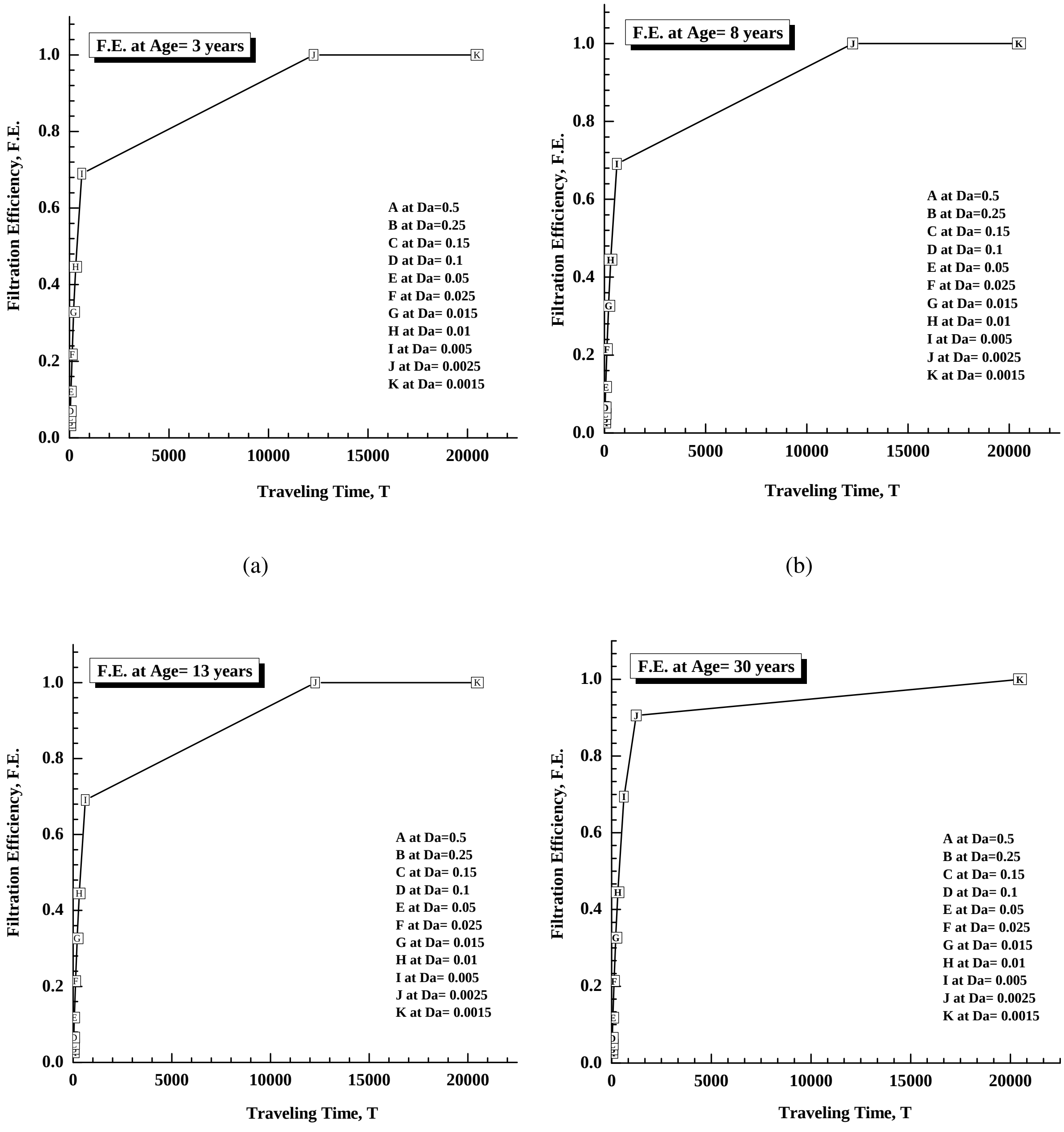

(a) (b)

(c) (d)

Figure 3.8: Traveling time and filtration efficiency of lung for (a) age of 3, (b) age of 8, (c) age of 13, (d) age of 30 at β = 10, d = 50 nm, and $10^{-1} \leq Da \leq 10^{-3}$.

Table 3.4: Correlation between traveling time (t') and filtration efficiency (F.E.) of lung from age 3 - 30.

	Age = 3		Age = 8		Age = 13		Age = 30	
Da	t'	F.E.	t'	F.E.	t'	F.E.	t'	F.E.
0.5	17.5439	0.0328	14.3885	0.027	14.0845	0.0264	14.0845	0.0264
0.25	21.2766	0.0396	19.2308	0.0359	18.8679	0.0352	18.8679	0.0352
0.15	28.86	0.0534	26.2467	0.0486	26.0078	0.0482	26.0078	0.0482
0.1	37.9507	0.0696	35.7143	0.0656	35.461	0.0652	35.461	0.0652
0.05	67.5676	0.1205	66.0066	0.1179	66.0066	0.1179	66.0066	0.1179
0.025	129.0323	0.2174	127.3885	0.215	126.58237	0.2138	126.5823	0.2138
0.015	209.6436	0.3286	207.9002	0.3263	207.9002	0.3263	207.9002	0.3263
0.01	311.042	0.4462	309.5975	0.4447	309.5975	0.4447	309.5975	0.4447
0.005	615.3846	0.6894	617.284	0.6905	617.284	0.6905	623.053	0.6939
0.0025	12270	1	12270	1	12270	1	1242.2	0.9056
0.0015	20492	1	20492	1	20492	1	20492	1

Table 3.5: Traveling time (t') and filtration efficiency (F.E.) of lung for different shape particles at the age of 15 and $10^{-1} \leq Da \leq 10^{-3}$.

	Spherical Particle [196]		Aspect Ratio = 100		Aspect Ratio = 1000		Aspect Ratio = 10	
Da	t'	F.E.	t'	F.E.	t'	F.E.	t'	F.E.
0.5	13.4228	0.0252	14.0845	0.0264	14.7059	0.0276	15.748	0.0295
0.25	18.3486	0.0343	18.8679	0.0352	19.6078	0.0366	20.8333	0.0388
0.15	25.7069	0.0477	26.0078	0.0482	26.738	0.0495	28.1294	0.052
0.1	35.5872	0.0654	35.461	0.0652	36.3636	0.0668	37.8072	0.0693
0.05	67.3401	0.1201	66.0066	0.1179	67.1141	0.1197	68.7285	0.1224
0.025	129.0323	0.2174	126.5823	0.2138	128.2051	0.2162	129.8701	0.2187
0.015	210.5263	0.3297	207.9002	0.3263	209.8636	0.3288	211.6402	0.3311
0.01	312.5	0.4477	309.5975	0.4447	312.0125	0.4472	314.4654	0.4498
0.005	621.118	0.6928	621.118	0.6928	623.053	0.6939	623.053	0.6939
0.0025	1234.6	0.9042	1227.0	1	1242.2	0.9056	1242.2	0.9056
0.0015	2061.9	0.9801	2049.2	1	2064	0.9802	2070.4	0.9804

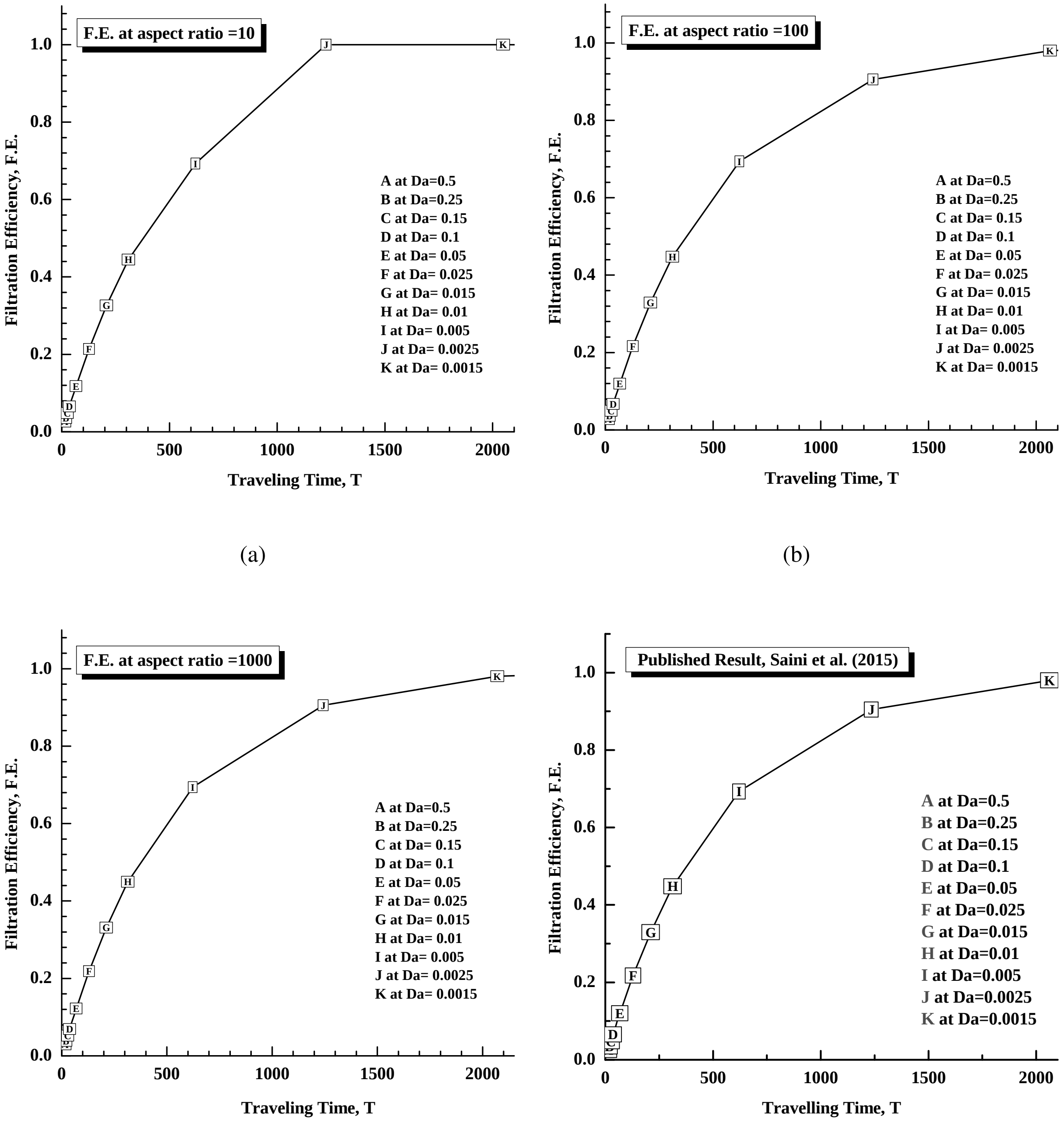

(a) (b)

(c) (d)

Figure 3.9: Traveling time and filtration efficiency of spherical and nonspherical $(10 \leq \beta \leq 1000)$ nanoparticle at (a) β = 10, (b) β = 100, (c) β = 1000, (d) spherical particle at age = 15, and $10^{-1} \leq Da \leq 10^{-3}$.

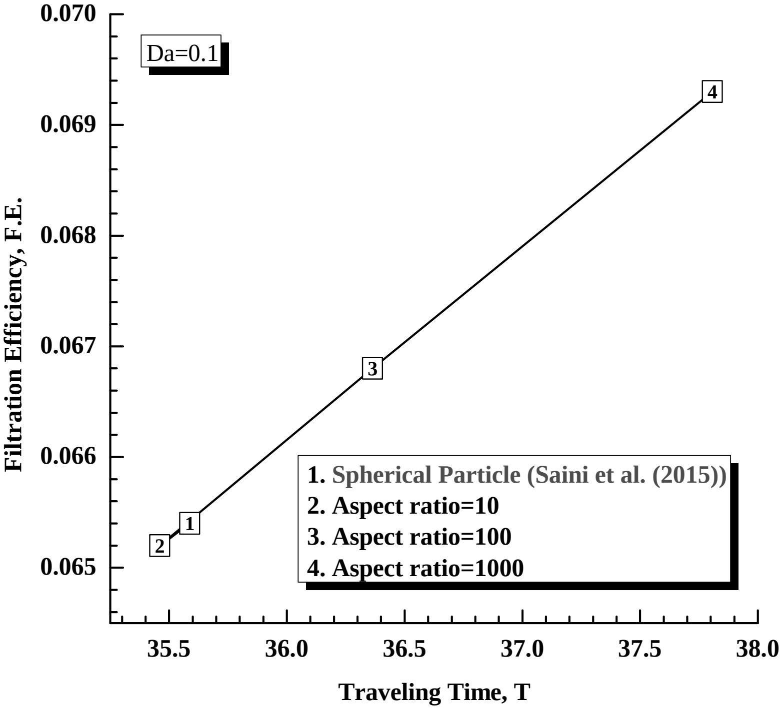

Figure 3.10: Comparison between F.E. of spherical and nonspherical nanoparticle at Da = 0.1, age = 15, and $10^{-1} \leq Da \leq 10^{-3}$.

Chapter 4: Simulation and modeling of the flow of viscous air through homogeneously porous alveolar region of human lung

4.1 Introduction

The deposition is a joint action of biological and physical aspects, which depends on some physiological factors such as particle density, porosity, breathing frequency, lung morphology, respiratory physiology [178], and Reynolds number [11] etc. Concerning the effect of inhaled nanoparticles on different regions of the human lung, a number of studies are done. Tian et al. [233] stated that nanoparticles of ranges 5.52 - 98.2 nm are very risky for occupational workers can develop various respiratory, cardiovascular, and neurological disorders. A CT scanned images based study done by Debo et al. [132] to find the effect of micron particles (1-10 μ m) and nanoparticles (1-100 nm) in the nasal cavity to upper six-generation of lung observed that deposition efficiency of micron particles are much higher than nanoparticles in the nasal region. A theoretical study done by Sturm [221] stated that due to very small size, nanoparticles are aggregates with highly irregular shape (chain-like, loose, compact) and after inhalation these particles are taken up into the respiratory tract by the mechanism of Brownian diffusion, sedimentation and being stored in epithelial cells for a longer time span, which causes formation of cancerous cells. Chuang et al. [34] studied biomass burning, which significantly affects the air quality and found its potential effect on the alveolar region of human lungs. Also, Seraa et al. [200] hypothesized that the particle deposition can be much influenced by the complex acinar geometry. Recently, Saini et al. [197] studied the deposition of nanoparticles of diameter 100 nm and found that nanoparticles have the capacity to go deeper in the lung generations and ultimately deposit in the alveolar ducts of the human lung.

Many researchers [42, 107] defined lung as a sponge or porous media, according to Haber et al. [75] deposition of particles also depends on media porosity due to a large number of alveoli inside human lung, Vafai and Tien [237] developed a set of governing equations utilizing the local volume-averaging technique for the depth analysis of transport through porous media. By using the theory of homogenization, Markus et al. [131] derived macroscopic equations for average air flows and solid tissue displacements in respiratory lung tissue and considered full lung as a porous medium due to a number of alveoli. Also, Kuwahara et al. [126] obtained mass transfer resistance between the inlet of the trachea and blood in the capillaries using porous media approach. Khanafer et al. [107] studied the flow of fluid within hollow fiber membranes of the artificial lungs by using Brinkman-extended Darcy model and found that pressure drop across the artificial lung device increased with an increment in the Reynolds number and decrement in the Darcy numbers. Saini et al. [196] assumed the alveolar region as a biofilter and found removal efficiency of the lung for nanoparticles by using generalized Navier-Stokes equations. Recently, DeGroot and Straatman [42] worked on expansion and contraction of the alveolar duct and assumed lung as a porous medium by using the theory of volume-averaging technique for the unit cell of an alveolated duct to predict permeability of human lung.

From literature review we found that there are various studies which stated the effect of nanoparticle deposition on lung, however, there are a few studies which considered lung as a homogeneous porous media. So, in this chapter, we used a mathematical model to study the effect of homogeneous porosity of the alveolar region on the flow dynamics of viscous air flowing through circular tube subject to pulsatile pressure gradient due to rhythmic breathing. To investigate the flow characteristics of air, Navier Stokes' equation with Darcy law of porous media and flow of nonspherical nanoparticle, Newton equation of motion in two-dimensional system are used. Numerical solutions have been computed via finite difference method. A comparative study between present study and published study is also presented. After performing computational work graphs are drawn to examine the behavior of various physical parameters such as effect of Reynolds number, Darcy number, porosity on flow and deposition of viscous air through alveolar region.

4.2 Mathematical Formulation

4.2.1 Governing equations

To understand the flow dynamics of an incompressible fully-developed laminar, Newtonian, viscous air through alveolar region an extended horizontal cylindrical tube (representing alveolar duct) is considered whose radius is ‘a’ and which is placed perpendicular to the incoming flow [11]. Schematic diagram is shown in Figure 4.1, where, z is the axial direction of flow along the tube and r is the radial direction of flow. We approximated alveolar region of lung as a porous medium because it is viewed as a continuum which is homogeneous, and saturated with an incompressible fluid. So, the porous medium has a unique or homogeneous porosity and permeability values. A mathematical model proposed by Saini et al. [197] is extended by including Darcy law of porous media and Newton second equation of motion used to find the adverse effect of nanoparticles on alveolar region. The pressure gradient ia assumed as time dependent sinusoidal. Two dimensional conservation equations of mass, momentum together with particle motion in the cylindrical polar coordinates system (r, z, θ) are given below:

$$\frac{\partial u_r}{\partial r} + \frac{u_r}{r} + \frac{\partial u_z}{\partial z} = 0, \tag{4.1}$$

$$\frac{\partial v_r}{\partial r} + \frac{v_r}{r} + \frac{\partial v_z}{\partial z} = 0, \tag{4.2}$$

$$\begin{aligned}\frac{\partial u_r}{\partial t} + \frac{u_r}{\epsilon}\frac{\partial u_r}{\partial r} + \frac{u_z}{\epsilon}\frac{\partial u_r}{\partial z} = -\frac{\epsilon}{\rho}\frac{\partial p}{\partial r} + \nu\left(\frac{\partial^2 u_r}{\partial r^2} + \frac{1}{r}\frac{\partial u_r}{\partial r} + \frac{\partial^2 u_r}{\partial z^2}\right)\\ + \left(k_f\frac{N_0}{\rho}(v_r - u_r) - \frac{\epsilon\nu}{K}u_r\right),\end{aligned} \tag{4.3}$$

$$\begin{aligned}\frac{\partial u_z}{\partial t} + \frac{u_r}{\epsilon}\frac{\partial u_z}{\partial r} + \frac{u_z}{\epsilon}\frac{\partial u_z}{\partial z} = -\frac{\epsilon}{\rho}\frac{\partial p}{\partial z} + \nu\left(\frac{\partial^2 u_z}{\partial r^2} + \frac{1}{r}\frac{\partial u_z}{\partial r} + \frac{\partial^2 u_z}{\partial z^2}\right)\\ + \left(k_f\frac{N_0}{\rho}(v_z - u_z) - \frac{\epsilon\nu}{K}u_z\right),\end{aligned} \tag{4.4}$$

$$m\left(\frac{\partial v_r}{\partial t} + v_z\frac{\partial v_r}{\partial z} + v_r\frac{\partial v_r}{\partial r}\right) = k_f(u_r - v_r), \tag{4.5}$$

$$m\left(\frac{\partial v_z}{\partial t} + v_z\frac{\partial v_z}{\partial y} + v_r\frac{\partial v_z}{\partial r}\right) = k_f(u_z - v_z). \tag{4.6}$$

Equations 4.1 - 4.2 represent the continuity equation for air and particle respectively. Equations 4.3 - 4.4 represent the momentum equation of air in radial and axial direction respectively. Equations 4.5 - 4.6 represent the motion equation of particles in radial and axial direction respectively. The first term in the left hand side of the equations 4.3 - 4.4 is for unsteady flow and the second-third terms are for convection. First, second, third, and forth terms in the right hand side of equations 4.3 - 4.4 are the pressure gradient, diffusion, and the entire body force because of the existence of porous

media and additional external force fields respectively. The term in the left hand side of equations 4.5 - 4.6 represents the product of the mass times the acceleration and right hand side of this equation represents the drag force on the nanoparticles.
In equation 4.3-4.4, K is the permeability that depends on media porosity (ϵ), and defined [57] as follows

$$K = \frac{\epsilon^3 d^2}{150\left(1-\epsilon\right)^2}. \tag{4.7}$$

In equation 4.5-4.6, k_f, denotes the Stokes resistance coefficient for spherical particles and defined as follows

$$k_f = 3\pi\mu d.$$

4.2.2 Initial and boundary conditions

Initial conditions at $t \leq 0$ are as follows:

- At rest, no flow takes place therefore

$$u_r = v_r = u_z = v_z = 0. \tag{4.8}$$

Boundary conditions at $t > 0$, for $r = 0$ and $r = a$ are as follows:

- The axial velocity gradient is equal to zero due to the assumption of no radial flow along the axis of the alveolar sac

$$u_r = 0; v_r = 0; \frac{\partial u_z}{\partial r} = 0; \frac{\partial v_z}{\partial r} = 0. \tag{4.9}$$

- Due to periciliary liquid layer, no-slip condition is applicable at the inner surface of the wall.

4.3 Methodology

4.3.1 Transformation of the governing equations

To solve the governing equations 4.1-4.6 numerically we have to make them dimensionless, so we used the following quantities:

$$R^* = \frac{r}{a}, Z^* = \frac{z}{a}, P^* = \frac{p}{\rho U_0^2}, \tau^* = \frac{tU_0}{a}, U_r^* = \frac{u_r}{U_0}, U_z^* = \frac{u_z}{U_0}, V_r^* = \frac{v_r}{U_0}, V_z^* = \frac{v_z}{U_0},$$
$$Da = \frac{K}{a^2}, P_l = \frac{N_0}{\rho}, S_m = \frac{ak}{U_0}, Re = \frac{aU_0}{\nu},$$

$$\frac{\partial U_r}{\partial R} + \frac{U_r}{R} + \frac{\partial U_z}{\partial Z} = 0, \tag{4.10}$$

$$\frac{\partial V_r}{\partial R} + \frac{V_r}{R} + \frac{\partial V_z}{\partial Z} = 0, \tag{4.11}$$

$$\begin{aligned} \frac{\partial U_z}{\partial \tau} + \frac{U_r}{\epsilon}\frac{\partial U_z}{\partial R} + \frac{U_z}{\epsilon}\frac{\partial U_z}{\partial Z} &= -\epsilon\frac{\partial P}{\partial Z} + \frac{1}{Re}\left(\frac{\partial^2 U_z}{\partial R^2} + \frac{1}{R}\frac{\partial U_z}{\partial R} + \frac{\partial^2 U_z}{\partial Z^2}\right) \\ &\quad + S_m P_l\left(V_z - U_z\right) - \frac{\epsilon}{DaRe}U_z, \end{aligned} \tag{4.12}$$

$$\frac{\partial V_z}{\partial \tau} + V_r\frac{\partial V_z}{\partial R} + V_z\frac{\partial V_z}{\partial Z} = \frac{S_m\left(U_z - V_z\right)}{m}. \tag{4.13}$$

Transformed initial conditions from equation 4.8, at $\tau = 0$ are as follows:

$$U_r = 0; U_z = 0; V_r = 0; V_z = 0, \tag{4.14}$$

and boundary conditions from equation 4.9, at $\tau > 0$, for $R = 0$ and $R = a$ are as follows:

$$U_r = 0; \frac{\partial U_z}{\partial R} = 0; V_r = 0; \frac{\partial V_z}{\partial R} = 0; U_z = 0; V_z = 0. \tag{4.15}$$

In equation 4.3, due to the expansion and contraction of alveolar duct and right heart pressure we assumed time dependent pressure gradient within the alveolus in non-dimensional form as follows

$$-\frac{\partial P}{\partial Z} = a_0 \sin\omega\tau, \quad \omega = 2\pi f \tag{4.16}$$

where a_0 is the amplitude and f is the frequency of breathing.

4.4 Numerical Scheme

To solve the non-dimensional equations 4.10-4.13 subject to two point boundary conditions (equation 4.14-4.15) we used finite difference numerical technique [214], which is the most suitable method for nonlinear problems related to regular geometries. The computational grid are defined in the following form where the discretization of air velocity $U(R, T, \tau)$ is written as $U_z(R_i, Z_j, \tau_k)$ or ${(U_z)_{i,j}}^k$.

$$\begin{aligned} &R_i = i\Delta R,\ (i = 0, 1, 2, ..., M),\ R_N = 1.0, \\ &Z_j = j\Delta Z,\ (j = 0, 1, 2, ..., N), \\ &\tau_k = k\Delta\tau\ (k = 0, 1, 2, ...), \end{aligned}$$

where i, j and k are the space and time indices; Δx, Δy, and $\Delta\tau$ are the increments in axial, radial directions and time respectively.

We used central difference approximation at point (x_i, t_j) for all the spatial derivatives, as

$$\frac{\partial U_z}{\partial Z} = \frac{(U_z)^k_{i,j+1} - (U_z)^k_{i,j-1}}{2\Delta Z}, \tag{4.17}$$

$$\frac{\partial^2 U_z}{\partial Z^2} = \frac{(U_z)^k_{i,j+1} - 2(U_z)^k_{i,j} + (U_z)^k_{i,j-1}}{(\Delta Z)^2}, \tag{4.18}$$

and forward difference approximation for all the time derivatives, as

$$\frac{\partial(U_z)}{\partial\tau} = \frac{(U_z)^{k+1}_{i,j} - (U_z)^k_{i,j}}{2\Delta\tau} \tag{4.19}$$

Additionally, at $R = 0$, following simplifications are applicable in equations 4.10-4.13, [1]

$$\lim_{R\to 0} \frac{1}{R}\frac{\partial U_z}{\partial R} = \lim_{R\to 0} \frac{\partial^2 U_z}{\partial R^2}, \tag{4.20}$$

$$\lim_{R\to 0} \frac{U_r}{R} = \lim_{R\to 0} \frac{\partial U_r}{\partial R}, \tag{4.21}$$

$$\lim_{R\to 0} \frac{V_r}{R} = \lim_{R\to 0} \frac{\partial V_r}{\partial R}, \tag{4.22}$$

so, the equation 4.10 at $R = 0$ becomes,

$$(U_r)^{k+1}_{i+1,j} = (U_r)^{k+1}_{i,j} - \frac{\Delta R}{2\Delta Z}\left((U_z)^{k+1}_{i,j+1} - (U_z)^{k+1}_{i,j}\right), \tag{4.23}$$

and at $0 < R \leqslant 1$,

$$(U_r)^{k+1}_{i+1,j} = (U_r)^{k+1}_{i,j}\left(1 - \frac{1}{i}\right) - \frac{\Delta R}{\Delta Z}\left((U_z)^{k+1}_{i,j+1} - (U_z)^{k+1}_{i,j}\right), \tag{4.24}$$

equation 4.11 at $R = 0$ transforms as,

$$(V_r)^{k+1}_{i+1,j} = (V_r)^{k+1}_{i,j} - \frac{\Delta R}{2\Delta Z}\left((V_z)^{k+1}_{i,j+1} - (V_z)^{k+1}_{i,j}\right), \tag{4.25}$$

and at $0 < R \leqslant 1$,

$$(V_r)^{k+1}_{i+1,j} = (V_r)^{k+1}_{i,j}\left(1 - \frac{1}{i}\right) - \frac{\Delta R}{\Delta Z}\left((V_z)^{k+1}_{i,j+1} - (V_z)^{k+1}_{i,j}\right), \tag{4.26}$$

---

[1] When $R \to 0$, we found that the denominator is also approaching to zero and make the term indeterminate, which is inappropriate for the physical state of the respiratory system. Therefore, to remove this kind of inconsistency we used L'hospital rule of limit here.

equation 4.12 at $R = 0$ becomes,

$$\begin{aligned}
\left(U_z\right)_{i,j}^{k+1} &= \left(1 - S_m P_l \Delta\tau - \left(\frac{\epsilon}{DaRe}\right)\Delta\tau - \frac{2r_1}{Re} - \frac{4r_2}{Re}\right)\left(U_z\right)_{i,j}^{k} \\
&- \frac{r_2 \Delta R}{2\epsilon}\left(\left(U_z\right)_{i+1,j}^{k} - \left(U_z\right)_{i-1,j}^{k}\right)\left(U_r\right)_{i,j}^{k} - \frac{r_1 \Delta Z}{2\epsilon}\left(\left(U_z\right)_{i,j+1}^{k} - \left(U_z\right)_{i,j-1}^{k}\right)\left(U_z\right)_{i,j}^{k} \\
&+ \frac{2r_2}{Re}\left(\left(U_z\right)_{i+1,j}^{k} + \left(U_z\right)_{i-1,j}^{k}\right) + \frac{r_1}{Re}\left(\left(U_z\right)_{i,j+1}^{k} + \left(U_z\right)_{i,j-1}^{k}\right) \\
&+ S_m P_l \Delta\tau \left(V_z\right)_{i,j}^{k} - \epsilon\Delta\tau\frac{\partial P}{\partial Z},
\end{aligned} \tag{4.27}$$

and at $0 < R \leqslant 1$,

$$\begin{aligned}
\left(U_z\right)_{i,j}^{k+1} &= \left(1 - S_m P_l \Delta\tau - \left(\frac{\epsilon}{DaRe}\right)\Delta\tau - \frac{2r_1}{Re} - \frac{2r_2}{Re}\right)\left(U_z\right)_{i,j}^{k} \\
&- \frac{r_2 \Delta R}{2\epsilon}\left(\left(U_z\right)_{i+1,j}^{k} - \left(U_z\right)_{i-1,j}^{k}\right)\left(U_r\right)_{i,j}^{k} - \frac{r_1 \Delta Z}{2\epsilon}\left(\left(U_z\right)_{i,j+1}^{k} - \left(U_z\right)_{i,j-1}^{k}\right)\left(U_z\right)_{i,j}^{k} \\
&+ \frac{2r_2}{Re}\left(\left(U_z\right)_{i+1,j}^{k} + \left(U_z\right)_{i-1,j}^{k}\right) + \frac{r_1}{Re}\left(\left(U_z\right)_{i,j+1}^{k} + \left(U_z\right)_{i,j-1}^{k}\right) \\
&+ \frac{r_2}{2iRe}\left(\left(U_z\right)_{i+1,j}^{k} - \left(U_z\right)_{i-1,j}^{k}\right) + S_m P_l \Delta\tau \left(V_z\right)_{i,j}^{k} - \epsilon\Delta\tau\frac{\partial P}{\partial Z},
\end{aligned} \tag{4.28}$$

while, equation 4.13 transforms as follows,

$$\begin{aligned}
\left(V_z\right)_{i,j+1}^{k+1} &= \left(1 - \frac{S_m \Delta\tau}{m}\right)\left(V_z\right)_{i,j}^{k} - \frac{\Delta\tau}{\Delta Z}\left(V_z\right)_{i,j}^{k}\left(\left(V_z\right)_{i,j+1}^{k} - \left(V_z\right)_{i,j-1}^{k}\right) \\
&- \frac{\Delta\tau}{\Delta R}\left(V_r\right)_{i,j}^{k}\left(\left(V_z\right)_{i+1,j}^{k} - \left(V_z\right)_{i-1,j}^{k}\right) + \frac{S_m \Delta\tau}{m}\left(U_z\right)_{i,j}^{k},
\end{aligned} \tag{4.29}$$

and initial and boundary conditions from equations 4.14-4.15 are transformed as follows,

$$\begin{aligned}
&\left(U_r\right)_{1,j}^{k} = 0, \quad \left(U_z\right)_{0,j}^{k} = \left(U_z\right)_{2,j}^{k}, \quad \left(U_r\right)_{N+1,j}^{k} = 0, \quad \left(U_z\right)_{N+1,j}^{k} = 0, \\
&\left(V_r\right)_{1,j}^{k} = 0, \quad \left(V_z\right)_{0,j}^{k} = \left(V_z\right)_{2,j}^{k}, \quad \left(V_r\right)_{N+1,j}^{k} = 0, \quad \left(V_z\right)_{N+1,j}^{k} = 0, \\
&\left(U_r\right)_{i,j}^{1} = 0, \quad \left(U_z\right)_{i,j}^{1} = 0, \quad \left(V_r\right)_{i,j}^{1} = 0, \quad \left(V_z\right)_{i,j}^{1} = 0.
\end{aligned} \tag{4.30}$$

After applying above mentioned discretization technique we got velocity profiles at the $(j+1)^{th}$ time level in terms of the velocity at j^{th} time level for equations 4.23-4.30 respectively.

4.5 Results and Discussion

In this work we analysed the effect of homogeneous porosity of lung on the flow of viscous air by using two dimensional pulsatile flow regime at different number of parameters involving, Darcy number (Da), Reynold number (Re), and porosity (ϵ). To solve the governing equations 4.23-4.29

subject to two point boundary conditions (equation 4.30) following default values of the parameters [99, 104, 197] are used.

$m = 0.0002\text{Kg/l}, d = 50\text{nm}, \rho = 1.145\text{Kg}/m^3, N_0 = 0.02504 * 10^{12}/m^3, Da = 0.1 - 0.001,$

$r = 140\mu\text{m}, a_0 = 1\text{Kg}/m^2s^2, \nu = 1.71 * 10^{-5}m^2/s, Re = 10 - 30, \epsilon = 0.2 - 1, f = 1.2\text{hz}.$

Before analysing the present problem, a grid independency test and numerical code validation is done to find the predictive accuracy of the model by comparing outcomes produced by present model with published model (Saini et al. [197]) as shown in Fig. 4.5 (Table 4.1) at grid sizes 10x10, 50x50 and 100x100.

Saini et al. [197] studied the flow of viscous air and found location of deposition of nanoparticles (diameter = 100nm) inside alveolar duct of the human lung without considering the porosity of lung. The present study is compared with the results of Saini et al. [197] in Figure 2.8 for velocity of air with respect to axial distance after removing Darcy term (porosity) at Re = 30, d = 100 nm, and a = 125 μ m. After comparison we found that our results for grid size 100x100 is compatible with their results up to 99.8 %. Hence, a grid size of 100x100 is chosen for all the computations of this study. The accuracy of the numerical method is also checked in each time level and found that results are convergent of oder of 10^{-5} with following stability criteria so that less error occurred in the numerical computation

$$\max\left(\frac{\Delta\tau}{\Delta R^2}\right) \leq 0.5,$$
$$\max\left(\frac{\Delta\tau}{\Delta Z^2}\right) \leq 0.5. \tag{4.31}$$

4.5.1 Effect of porosity (ϵ)

In human lung alveolies are the vacant spaces, which increase with age. In Figure 4.3, we obtained the effect of porosity (ϵ) by varying it from 0.2 to 1 on air and particle velocities at Re = 10, d = 50 nm, and a = 140 μ m in axial and radial directions respectively. We found from figures 4.3(a)-4.3(d), at ϵ = 0.2 velocity of air and particle in axial and radial directions are lesser than velocities at ϵ = 1. By increasing value of porosity (ϵ) from 0.2 to 1 permeability of terminal airways increase and due to highly permeable walls level of pressure gradient of air inside the ducts reduces, which increase the possibility of flow and deposition of nanoparticles deep inside the respiratory system. Therefore, we observed by increasing the porosity of media fluid velocity increases with respect to distance or more porous lung allow air to flow more freely.

4.5.2 Effect of Darcy number (Da)

In porous media Darcy number (Da) is inversely proportional to media pressure. In figure 4.4, we found the effect of Darcy number (Da = 0.001 to 0.1) on air and particle velocities at ϵ = 0.6, Re = 10, d = 50 nm, and a = 140 μm in axial and radial directions respectively. From figures 4.4(a) - 4.4(d), we observed that velocity of air and particle in axial and radial directions show parabolic profile for each value of Da and increases by increasing the value of Da from 0.001 to 0.1. For smaller values of Da, the porous layer is viewed as less penetrable or less permeable for fluid entrance and encounters pronouncedly substantial obstruction as it moves through the porous matrix, which cause hindrance in the stream activities. Additionally, due to the decrement the value of Darcy number, pressure gradient increases, which also causes decrement in the velocity of air and particles through porous region. However, with the increment in the value of Da media pressure decreases and permeability increases; consequently, the velocity of air and nanoparticle increases gradually with distance and allow particles to deposit deep inside the lung generations.

4.5.3 Effect of Reynolds number (Re)

It has been known that the Reynolds number (Re) has a great influence on the flow regime. The effect of the Reynolds number on the unsteady pulsating flow are discussed in this study. The Reynolds number (Re) of ranges 10 - 30 are considered here to show the flow of fluid inside the alveolar region, with ϵ = 0.6, Da = 0.1, d = 50 nm, and a = 140 μm. The instantaneous streamlines for sinusoidal pulsatile flow at Re 10 - 30 inside circular tube are shown in Figure 4.5(a)- 4.5(d) respectively. At Re = 30, we found velocity profiles for air and particle in axial and radial directions show parabolic profiles and these profiles are decreases by a decreasing Re up to 10 gradually with distance either due to the random movement of nanoparticles and fluid viscosity or due to pulsatile nature of the fluid. Hence, in alveolar region flow of viscous air decreases by decreasing value of Re.

4.6 Conclusion

The present work is dealing with the flow and deposition of nanoparticles through a circular tube of alveolar region, with homogeneous porosity under pulsatile pressure gradient. Two dimensional momentum equation with Darcy law of porosity together with Newton's second equation of motion are used for the flow of air and nanoparticles respectively. Effect of Reynolds number, Darcy number, and porosity are found on velocity of air and particle. After solving the governing equations following conclusions are made.

1. The physical flow parameter, Reynolds number (Re), is the most important factor affecting the fluid velocity. When Re = 10, the results show that the fluid velocity is dominated by viscous effect and when Re = 30, the fluid velocity is dominated by the inertial effect.
2. The Darcy number is found to be the most effective factor in flow through porous media as the increment in the Darcy number is found to be the best for flow regime because the maximum number of particles flow towards the alveolar region, where they can stuck or deposit and clear either by simple exhalation process or coughing.
3. It is found that the fraction of particles trapped in the alveolus increase by decreasing the Darcy number. However, by increasing the value of Darcy number flow become very smooth and freely.
4. Increment in the homogeneous porosity decreases the pressure gradient of the lung.

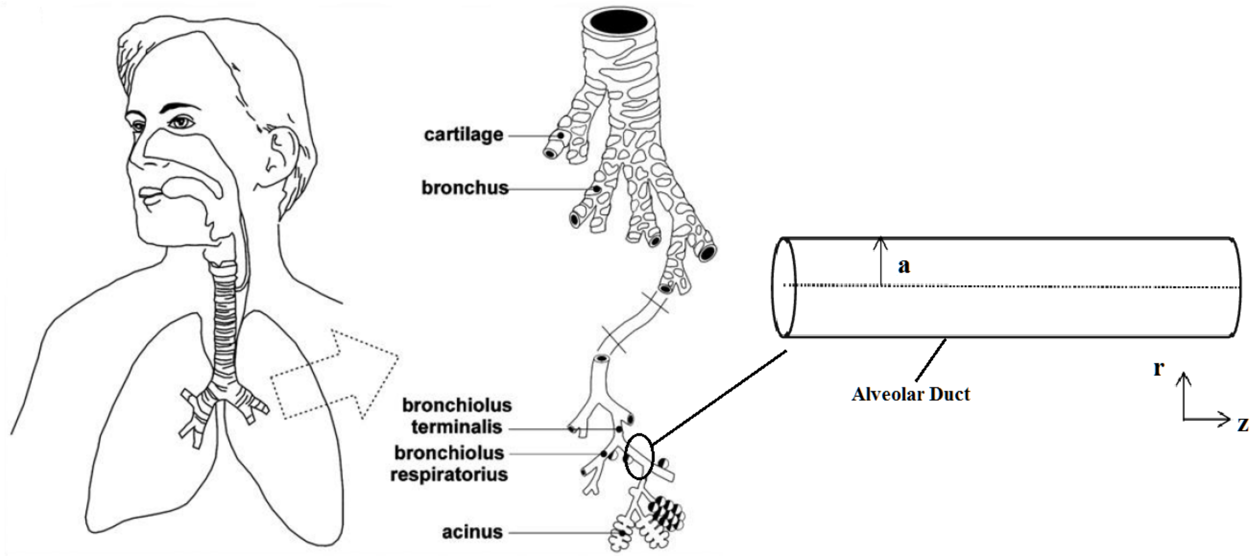

Figure 4.1: Architecture of the tracheobronchial tree [225] and alveolar duct.

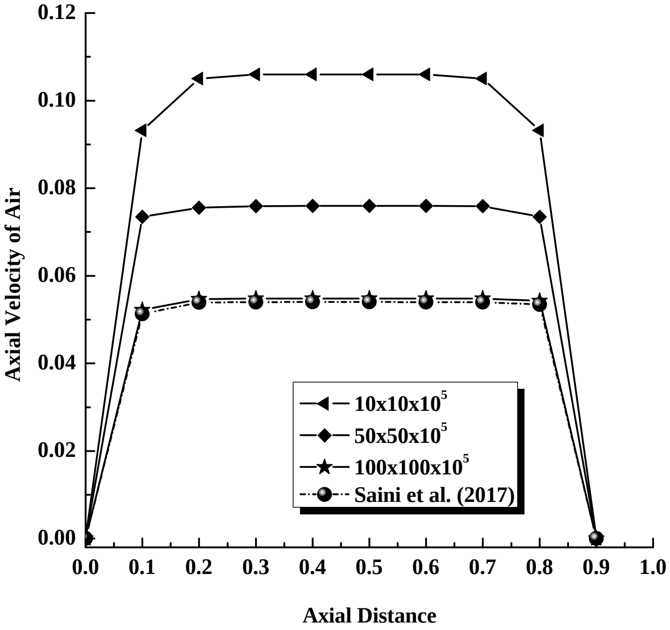

Figure 4.2: Comparison between present and published (Saini et al. [197]) results at Re = 30, d = 100 nm, and a = 125 μ m.

Table 4.1: Comparison between present and published (Saini et al. [197]) results for axial velocity of air with respect to axial distance.

	Present result at grid			Published result (Saini et al. [197]) at grid
Axial distance	10x10	50x50	100x100	100x100
0	0	0	0	0
0.1	0.0932	0.07347	0.05217	0.05129
0.2	0.105	0.07556	0.05472	0.0539
0.3	0.106	0.07591	0.05482	0.05401
0.4	0.106	0.07598	0.05482	0.05401
0.5	0.106	0.07598	0.05482	0.05401
0.6	0.106	0.07597	0.05482	0.05401
0.7	0.105	0.07591	0.0548	0.05399
0.8	0.0932	0.07347	0.05428	0.05345
0.9	0	0	0	0

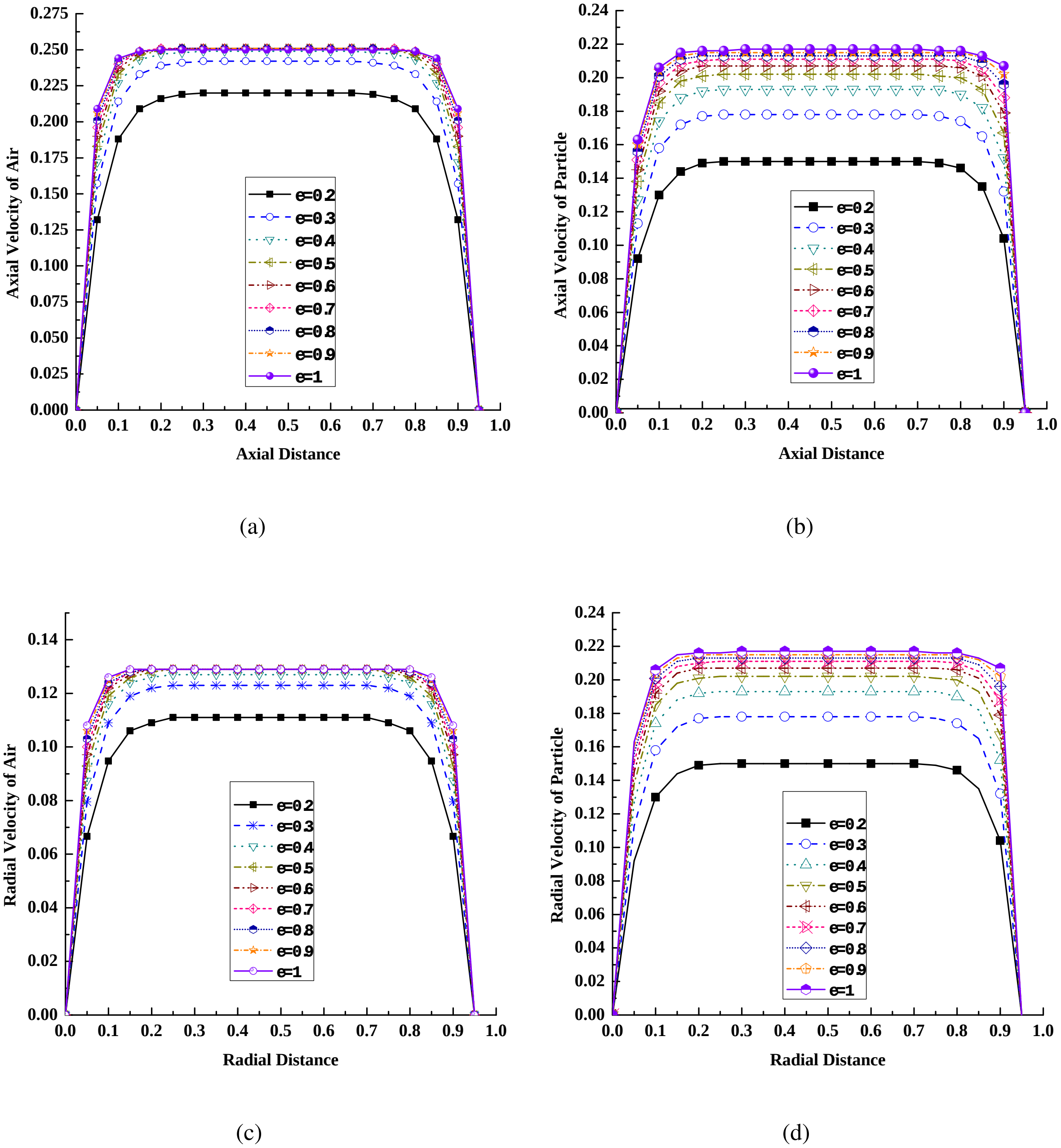

(a)

(b)

(c)

(d)

Figure 4.3: Effect of porosity on axial velocity of (a) air and (b) particles; and radial velocity of (c) air and (d) particles at Re = 10, d = 50 nm, and a = 140 μ m.

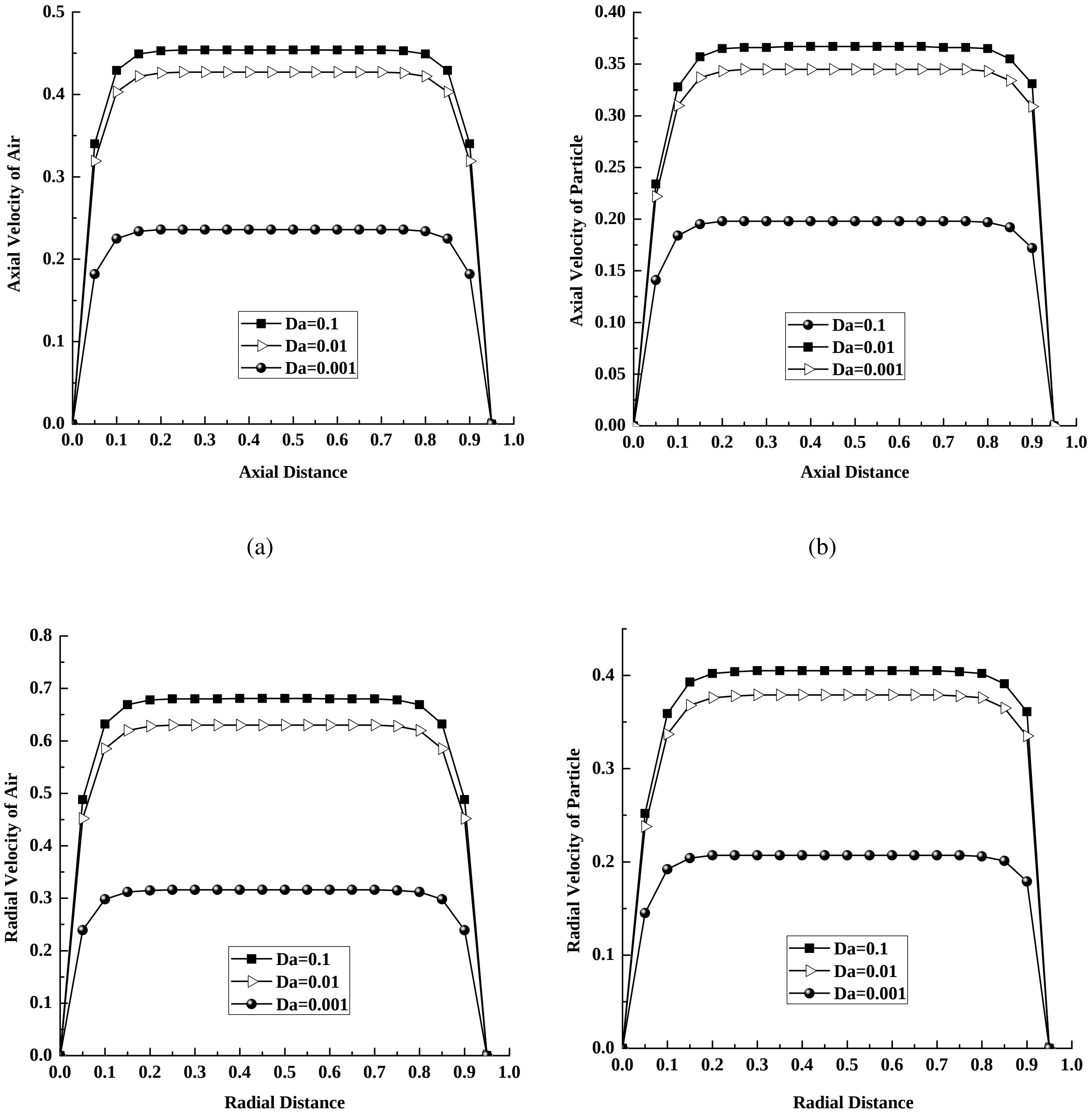

(a)

(b)

(c)

(d)

Figure 4.4: Effect of Darcy number on axial velocity of (a) air and (b) particles; and radial velocity of (c) air and (d) particles at Re = 10, d = 50 nm, and a = 140 μm.

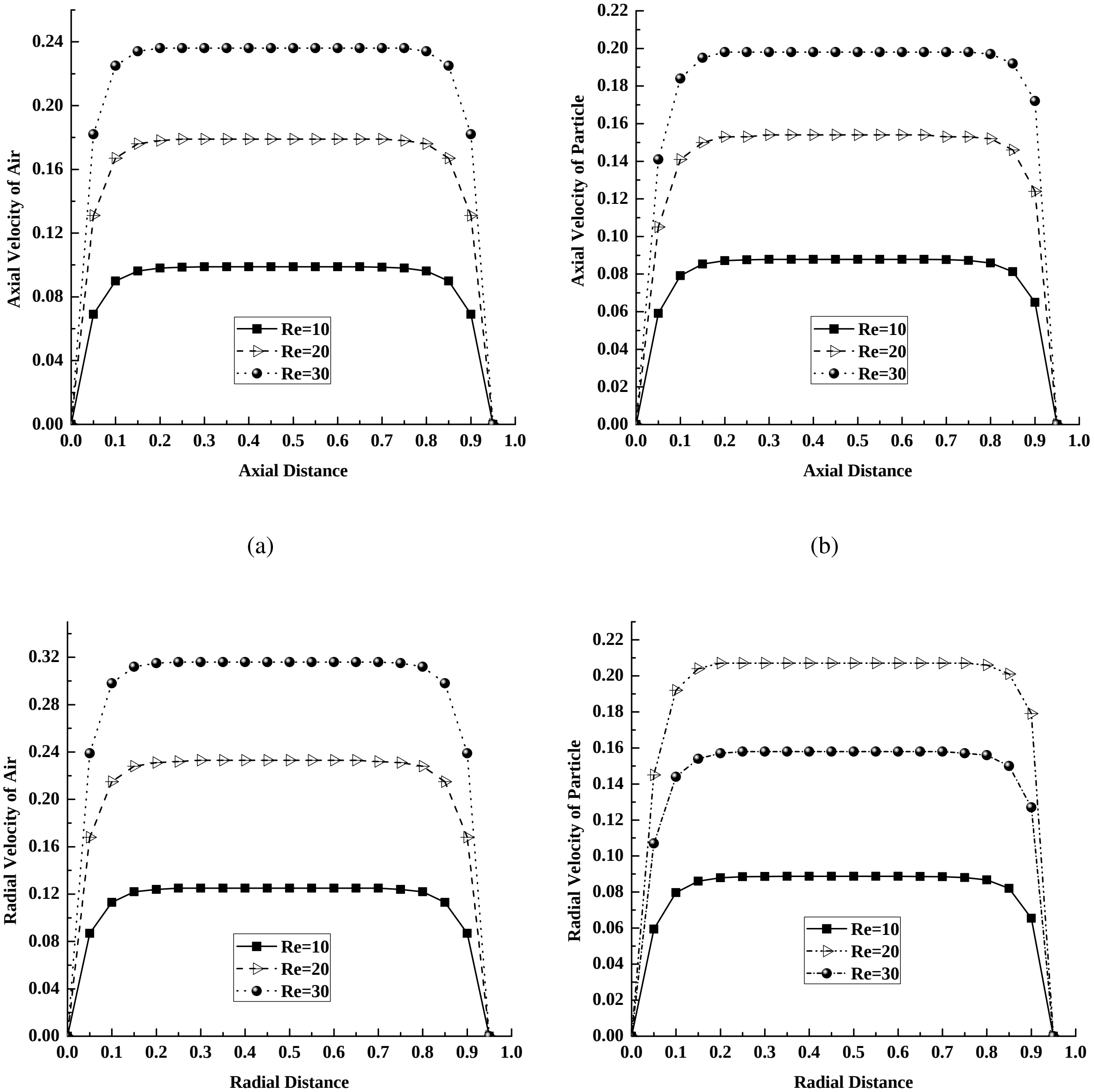

(a) (b)

(c) (d)

Figure 4.5: Effect of Reynold number on axial velocity of (a) air and (b) particles; and radial velocity of (c) air and (d) particles at Da = 0.1, d = 50 nm, and a = 140 μm.

Chapter 5: Two dimensional numerical study of the flow of viscous air from emphysema affected lung

5.1 Introduction

With ever-increasing environmental pollution, the first and the most important organ being affected and afflicted is the lung. There are many common conditions that can affect the lung. Some make breathing harder and some damages the lung's ability to exchange carbon dioxide with oxygen. Emphysema, along with chronic bronchitis, is one of the major obstructive lung diseases that fall under the category of chronic obstructive pulmonary disease. It gradually destroys the air sacs (alveoli) or forms holes in the inner walls of the air sacs in the lungs and makes it difficult to take enough oxygen so that it can be delivered to the bloodstream. Over the time, it also destroys the elasticity of lung airways, which cause a collapse of the air sacs and trap oxygen in the alveolar region (we cannot fully exhale air from our lungs if we can not fully inhale air either). The main cause of emphysema is the long-term exposure of airborne irritants and pollutants, such as tobacco smoke, air pollution, chemical fumes and manufacturing fumes, and cooking fires. It is believed that the most airborne particles were derived from fossil, biomass, and solid fuels combustion [34, 67], traffic exhausts [112]. The particles emitted by engines have a high proportion of nanoparticles, though most of them are in accumulation mode [110]. Epidemiological studies have confirmed that air pollution makes adverse health effect, especially the pollutant in nanoscale [111]. After deposition nano-sized particles have the potential to migrate through the alveolar wall and into the bloodstream. Thus, nowadays most attention is paid to airborne pollutants lies under nanoparticles and ultrafine particles range.

Due to very small size, nanoparticle adopts the ability to penetrate the lung epithelium and enter the blood circulation within a rather short time span [67]. Besides particles with spherical or close-to-spherical shape, there are also ones adopting the shapes of cylinders and platelets or disks [224].

According to numerous experimental and theoretical studies [221, 225] transport of non-spherical particles within the inspired air stream may significantly differ from ideal, spherical particles. It has been seen in a theoretical work by Balashazy et al. [11] that wall motion is a vital element because it drives alveolar flow. A study by Dutta et al. [50] found that alveolar deformation may ease the flow of fluid but become a cause of circulatory flow behavior inside alveoli of a human lung. Tsuda and Henry [236] investigated the effect of tidal breathing on particle deposition in an alveolated duct model and demonstrated that due to tidal breathing and rhythmical movement there was a highly complex and irreversible flow pattern inside the alveolated duct. Oakes et al. [161] and later Berg and Robinson [16] measured flow fields in idealized and replica models, respectively, by particle image velocimetry and found that flow of fluid tends to decrease the deposition of a particle in emphysema lung than the healthy lung. Gefen et al. [66] presented an alveolar sac model for numerical analysis of the internal stress distribution and septal displacement inside alveoli of both normal and emphysematic saline-filled lungs and found that stress sites and cyclic loading of breathing explained the observed progressive damage to elastin fibers in emphysematic patients.

In literature, most of the studies are based on the flow behavior of emphysema affected lung by considering the ruptured septal wall, while some studies are centered on the deposition of spherical particles inside emphysema affected lung. No attention has been paid to the porous characteristic of emphysemic lung together with particle shape on the flow and deposition behavior of nanoparticles. These fundamental facts are still very poorly understood. Therefore, in this study, we examined the flow of viscous air through, emphysemic and healthy lung under the pulsatile flow of fluid due to rhythmic breathing condition. The generalized Navier Stokes' equations for variable porous media in the two-dimensional system are used to describe the flow condition of an emphysema affected lung and Newton second equation of motion is used to demonstrate the motion of nonspherical nanoparticles. The effects of the embedded flow controlling parameters namely, Reynolds number, aspect ratio, and breathing rate are analyzed graphically. Additionally, a comparison between normal to emphysema affected lung is done in term of stress analysis.

5.2 Mathematical Formulation

5.2.1 Governing equations

To understand the flow dynamics of viscous air inside the alveolar region, an extended horizontal cylindrical tube with radius 'a' hooked with a single alveolus of diameter 'd_i' placed perpendicular to the incoming pulsatile flow [11]. The schematic of the problem is shown in Figure 5.1, where, z

is the axial direction of flow and r is the radial direction of flow. The impedance effect generated by emphysema lung is simulated by Darcy regime. We assumed that the fluid is Newtonian and viscous with constant density and the flow is fully-developed, unsteady and laminar. So, the conservation equations together with mass (continuity), momentum and motion in cylindrical polar coordinates system (r, z, θ) are given below:

Equation of continuity for air,

$$\frac{\partial u_r}{\partial r} + \frac{u_r}{r} + \frac{\partial u_z}{\partial z} = 0, \tag{5.1}$$

equation of continuity for particle,

$$\frac{\partial v_r}{\partial r} + \frac{v_r}{r} + \frac{\partial v_z}{\partial z} = 0, \tag{5.2}$$

equation of radial momentum for air,

$$\begin{aligned}\frac{\partial u_r}{\partial t} + \frac{u_r}{\epsilon}\frac{\partial u_r}{\partial r} + \frac{u_z}{\epsilon}\frac{\partial u_r}{\partial z} = -\frac{\epsilon}{\rho}\frac{\partial p}{\partial r} + \nu\left(\frac{\partial^2 u_r}{\partial r^2} + \frac{1}{r}\frac{\partial u_r}{\partial r} + \frac{\partial^2 u_r}{\partial z^2}\right) + \\ \left(-\frac{\epsilon\nu}{K}u_r + k_f\frac{N_0}{\rho}(v_r - u_r)\right),\end{aligned} \tag{5.3}$$

equation of axial momentum for air,

$$\begin{aligned}\frac{\partial u_z}{\partial t} + \frac{u_r}{\epsilon}\frac{\partial u_z}{\partial r} + \frac{u_z}{\epsilon}\frac{\partial u_z}{\partial z} = -\frac{\epsilon}{\rho}\frac{\partial p}{\partial z} + \nu\left(\frac{\partial^2 u_z}{\partial r^2} + \frac{1}{r}\frac{\partial u_z}{\partial r} + \frac{\partial^2 u_z}{\partial z^2}\right) + \\ \left(-\frac{\epsilon\nu}{K}u_z + k_f\frac{N_0}{\rho}(v_z - u_z)\right).\end{aligned} \tag{5.4}$$

equation of motion for particles in the radial direction,

$$m\left(\frac{\partial v_r}{\partial t} + v_z\frac{\partial v_r}{\partial y} + v_z\frac{\partial v_r}{\partial r}\right) = F_{d_1}, \tag{5.5}$$

and the equation of motion for particles in the axial direction,

$$m\left(\frac{\partial v_z}{\partial t} + v_z\frac{\partial v_z}{\partial z} + v_r\frac{\partial v_z}{\partial r}\right) = F_d. \tag{5.6}$$

The first term in the left hand side of the equations 5.3-5.4 is for unsteady flow and the second-third terms are for convection. First, second, third, and forth terms in the right hand side of equations 5.3-5.4 are the pressure gradient, diffusion, and the entire body force because of the existence of porous media and additional external force fields respectively. The term in the left hand side of equations 5.5 - 5.6 represents the product of the mass times the acceleration and right hand side of this equation represents the drag force on the nanoparticles.

In equation 5.3 - 5.4, K is the permeability of media, which depends on the porosity (ϵ) [57] as follows

$$K = \frac{\epsilon^3 d_p^2}{150\left(1-\epsilon\right)^2}, \tag{5.7}$$

The lung volume at the maximum inspiration level is the total lung capacity (TLC) of normal lung, while the volume of air inspire/expire normally is known as tidal volume. An emphysemic lung is not able to inhale or exhale normally, which affect the tidal volume of the lung. In emphysema, victim's lungs are expanded and fill the chest before the required volume of air is inhaled and when the victim exhales, he is not able to exhale properly because of the higher residual volume in his/her lungs. So, in this study we assumed lung as variable porous media, which is a function of lung volume and defined as follows

$$\text{Porosity}(\epsilon) = \frac{\text{Tidal lung volume}}{\text{Total lung volume}}. \tag{5.8}$$

Additionally, in equation 5.5 - 5.6, F_d and F_{d_1} are drag forces on nonspherical nanoparticles, and S_f is the dynamic shape factor (see Chapter 2 [1] and Chapter 3 [2] with respect to particle orientation. Also, S_f can be defined in term of drag forces as the ratio of drag force on the nonspherical nanoparticles (F_d) and (F_{d_1}) to the drag force on the related spherical nanoparticles (f_d and f_{d_1}) with an equivalent volume [90]. The relations between F_d, F_{d_1} with S_f and f_d, f_{d_1} are shown below

$$\begin{aligned} F_d &= S_f f_d, \\ F_{d_1} &= S_f f_{d_1}, \end{aligned} \tag{5.9}$$

where

$$\left.\begin{aligned} f_d &= s_k\left(u_z - v_z\right), \\ f_{d_1} &= s_k\left(u_r - v_r\right), \end{aligned}\right\} s_k = 3\pi\mu C d_p, \tag{5.10}$$

where C represents the Cunningham slip correction factor for thin particles [3] and d_p is the diameter of elongated nanoparticle that depends upon the particle shape factor, which is described in Chapter 2 [4].

---

[1] Subsection 2.2.1, equation 2.7

[2] Subsection 3.2.1, equation 3.8

[3] see Chapter 2, Subsection 2.2.1, and equation 2.4

[4] Subsection 2.2.1, and equation 2.5

Stress due to emphysema is defined as

$$\tau_e = \mu \left(\frac{\partial U_z}{\partial r} + \frac{\partial U_r}{\partial z} \right). \tag{5.11}$$

5.2.2 Initial and boundary conditions

Following initial and boundary conditions are subjected to equation 5.1 - 5.6:

- At rest ($t = 0$) there is no flow takes places therefore

$$u_r = v_r = u_z = v_z = 0. \tag{5.12}$$

- We assumed that there is no radial flow along the axis of the alveolar tube so the axial velocity gradient adequate to zero

$$u_r = 0; v_r = 0; \frac{\partial u_z}{\partial r} = 0; \frac{\partial v_z}{\partial r} = 0. \tag{5.13}$$

- The no-slip condition is applicable at the inner surface of the wall.

5.3 Methodology

5.3.1 Transformation of the governing equations

To solve the governing equations 5.1 - 5.6 numerically we have to make them dimensionless, so we used the following quantities:

$$R^* = \frac{r}{a}, Z^* = \frac{z}{a}, P^* = \frac{p}{\rho U_0^2}, \tau^* = \frac{t}{t_0}, U_r^* = \frac{u_r}{U_0}, U_z^* = \frac{u_z}{U_0}, V_r^* = \frac{v_r}{U_o}, V_z^* = \frac{v_z}{U_o},$$
$$Da = \frac{K}{r^2}, P_l = \frac{N_0}{\rho}, S_m = \frac{ak}{U_0}, Re = \frac{aU_0}{\nu}, S_t = \frac{a}{U_0 t_0},$$

where, a is the radius of circular tube, t_0 is the initial time, U_0 initial velocity, Re is the Reynolds number and S_t is the Strouhal number.

By using the above quantities, together with our assumptions, we got the following dimensionless equations

$$\frac{\partial U_r}{\partial R} + \frac{U_r}{R} + \frac{\partial U_z}{\partial Z} = 0, \tag{5.14}$$

$$\frac{\partial V_r}{\partial R} + \frac{V_r}{R} + \frac{\partial V_z}{\partial Z} = 0, \tag{5.15}$$

$$S_t \frac{\partial U_z}{\partial \tau} + \frac{U_r}{\epsilon}\frac{\partial U_z}{\partial R} + \frac{U_z}{\epsilon}\frac{\partial U_z}{\partial Z} = -\epsilon \frac{\partial P}{\partial Z} + \frac{1}{Re}\left(\frac{\partial^2 U_z}{\partial X^2} + \frac{1}{R}\frac{\partial U_z}{\partial R} + \frac{\partial^2 U_z}{\partial Y^2}\right) + S_m P_l \left(V_z - U_z\right)$$
$$- \frac{\epsilon}{DaRe} U_z, \tag{5.16}$$

$$S_t \frac{\partial V_z}{\partial \tau} + V_r \frac{\partial V_z}{\partial R} + V_r \frac{\partial V_z}{\partial Z} = \frac{S_f S_m \left(U_z - V_z\right)}{m}. \tag{5.17}$$

Transformed initial and boundary conditions from equation 5.12 - 5.13 are as follows:

$$U_r = 0; U_z = 0; V_r = 0; V_z = 0, \tag{5.18}$$

$$U_r = 0; \frac{\partial U_z}{\partial R} = 0; V_r = 0; \frac{\partial V_z}{\partial R} = 0,$$
$$U_z = 0, V_z = 0. \tag{5.19}$$

The Womersley number is responsible for the frequency of pulsatile flow. It is related to the Reynolds number and is defines as

$$w_0 = \sqrt{2\pi Re S_t}. \tag{5.20}$$

The stress from equation 5.11 is transform as

$$\tau_e = \mu \frac{u_0}{a}\left(\frac{\partial U_z}{\partial r} + \frac{\partial U_r}{\partial z}\right). \tag{5.21}$$

In equation 5.3, due to the deformation of the alveolus wall and right heart pressure, we assumed a time-dependent pressure gradient inside the alveolar region as follows

$$-\frac{\partial p}{\partial z} = \exp(-fta/U_0) + S_f. \tag{5.22}$$

5.4 Numerical Scheme

To solve the non-dimensional equations 5.14 - 5.17 subject to two point boundary conditions (equation 5.18 - 5.19) we used finite difference numerical technique [214], which is the most suitable method for nonlinear problems related to regular geometries. The computational grid are defined in the following form where the discretization of air velocity $U(R, T, \tau)$ is written as $U_z(R_i, Z_j, \tau_k)$ or $(U_z)_{i,j}^k$.

$$R_i = i\Delta R, (i = 0, 1, 2, ..., M), R_N = 1.0,$$
$$Z_j = j\Delta Z, (j = 0, 1, 2, ..., N),$$
$$\tau_k = k\Delta \tau, (k = 0, 1, 2, ...),$$

where, i, j, and k are the space and time indices, Δx, Δy, and $\Delta\tau$ are the increments in axial, radial directions and time respectively.

We used central difference approximation at point (x_i, t_j, τ_k) for all the spatial derivatives, as follows:

$$\frac{\partial U_z}{\partial Z} = \frac{(U_z)^k_{i,j+1} - (U_z)^k_{i,j-1}}{2\Delta Z}, \tag{5.23}$$

$$\frac{\partial^2 U_z}{\partial Z^2} = \frac{(U_z)^k_{i,j+1} - 2(U_z)^k_{i,j} + (U_z)^k_{i,j-1}}{(\Delta Z)^2}, \tag{5.24}$$

and forward difference approximation is used for all the time derivatives, which is defined as follows:

$$\frac{\partial(U_z)}{\partial\tau} = \frac{(U_z)^{k+1}_{i,j} - (U_z)^k_{i,j}}{2\Delta\tau}. \tag{5.25}$$

Additionally, at $R = 0$, following simplification are applied in equations 5.14 - 5.17, [5]

$$\lim_{R\to 0} \frac{1}{R}\frac{\partial U_z}{\partial R} = \lim_{R\to 0} \frac{\partial^2 U_z}{\partial R^2}, \tag{5.26}$$

$$\lim_{R\to 0} \frac{U_r}{R} = \lim_{R\to 0} \frac{\partial U_r}{\partial R}, \tag{5.27}$$

$$\lim_{R\to 0} \frac{V_r}{R} = \lim_{R\to 0} \frac{\partial V_r}{\partial R}, \tag{5.28}$$

equation 5.14 in discretization form can be written as
at $x = 0$,

$$(U_r)^{k+1}_{i+1,j} = (U_r)^{k+1}_{i,j} - \frac{\Delta R}{2\Delta Z}\left((U_z)^{k+1}_{i,j+1} - (U_z)^{k+1}_{i,j}\right), \tag{5.29}$$

and at $0 < R \leqslant 1$,

$$(U_r)^{k+1}_{i+1,j} = (U_r)^{k+1}_{i,j}\left(1 - \frac{1}{i}\right) - \frac{\Delta R}{\Delta Z}\left((U_z)^{k+1}_{i,j+1} - (U_z)^{k+1}_{i,j}\right), \tag{5.30}$$

equation 5.15 at $R = 0$ transforms as,

$$(V_r)^{k+1}_{i+1,j} = (V_r)^{k+1}_{i,j} - \frac{\Delta R}{2\Delta Z}\left((V_z)^{k+1}_{i,j+1} - (V_z)^{k+1}_{i,j}\right), \tag{5.31}$$

---

[5] When $R \to 0$, we found that the denominator is also approaching to zero and make the term indeterminate, which is inappropriate for the physical state of the respiratory system. Therefore, to remove this kind of inconsistency we used L'hospital rule of limit here.

and at $0 < R \leqslant 1$,

$$(V_r)_{i+1,j}^{k+1} = (V_r)_{i,j}^{k+1}\left(1 - \frac{1}{i}\right) - \frac{\Delta R}{\Delta Z}\left((V_z)_{i,j+1}^{k+1} - (V_z)_{i,j}^{k+1}\right), \tag{5.32}$$

equation 5.16 at $R = 0$ is transforms as,

$$\begin{aligned}
(U_z)_{i,j}^{k+1} &= \left(1 - S_m P_l \frac{\Delta\tau}{S_t} - \left(\frac{\epsilon}{DaS_tRe}\right)\Delta\tau - \frac{2r_1}{ReS_t} - \frac{4r_2}{ReS_t}\right)(U_z)_{i,j}^{k}\\
&- \frac{r_2\Delta R}{2\epsilon S_t}\left((U_z)_{i+1,j}^{k} - (U_z)_{i-1,j}^{k}\right)(U_r)_{i,j}^{k} - \frac{r_1\Delta Z}{2\epsilon S_t}\left((U_z)_{i,j+1}^{k} - (U_z)_{i,j-1}^{k}\right)(U_z)_{i,j}^{k}\\
&+ \frac{2r_2}{ReS_t}\left((U_z)_{i+1,j}^{k} + (U_z)_{i-1,j}^{k}\right) + \frac{r_1}{ReS_t}\left((U_z)_{i,j+1}^{k} + (U_z)_{i,j-1}^{k}\right)\\
&+ \frac{\Delta\tau}{S_t} S_m P_l (V_z)_{i,j}^{k} - \epsilon\frac{\Delta\tau}{S_t}\frac{\partial P}{\partial Z},
\end{aligned} \tag{5.33}$$

and at $0 < R \leqslant 1$,

$$\begin{aligned}
(U_z)_{i,j}^{k+1} &= \left(1 - S_m P_l \frac{\Delta\tau}{S_t} - \left(\frac{\epsilon}{DaS_tRe}\right)\Delta\tau - \frac{2r_1}{ReS_t} - \frac{2r_2}{ReS_t}\right)(U_z)_{i,j}^{k}\\
&- \frac{r_2\Delta R}{2\epsilon S_t}\left((U_z)_{i+1,j}^{k} - (U_z)_{i-1,j}^{k}\right)(U_r)_{i,j}^{k} - \frac{r_1\Delta Z}{2\epsilon S_t}\left((U_z)_{i,j+1}^{k} - (U_z)_{i,j-1}^{k}\right)(U_z)_{i,j}^{k}\\
&+ \frac{2r_2}{ReS_t}\left((U_z)_{i+1,j}^{k} + (U_z)_{i-1,j}^{k}\right) + \frac{r_1}{ReS_t}\left((U_z)_{i,j+1}^{k} + (U_z)_{i,j-1}^{k}\right)\\
&+ \frac{r_2}{2iReS_t}\left((U_z)_{i+1,j}^{k} - (U_z)_{i-1,j}^{k}\right)\frac{\Delta\tau}{S_t} + S_m P_l \Delta\tau (V_z)_{i,j}^{k} - \epsilon\frac{\Delta\tau}{S_t}\frac{\partial P}{\partial Z},
\end{aligned} \tag{5.34}$$

equation 5.17 transforms as follows,

$$\begin{aligned}
(V_z)_{i,j+1}^{k+1} &= \left(1 - \frac{S_m S_f \Delta\tau}{mS_t}\right)(V_z)_{i,j}^{k} - \frac{\Delta\tau}{\Delta R S_t}(V_r)_{i,j}^{k}\left((V_z)_{i+1,j}^{k} - (V_z)_{i-1,j}^{k}\right)\\
&+ \frac{S_f S_m \Delta\tau}{mS_t}(U_z)_{i,j}^{k} - \frac{\Delta\tau}{\Delta Z S_t}(V_z)_{i,j}^{k}\left((V_z)_{i,j+1}^{k} - (V_z)_{i,j-1}^{k}\right),
\end{aligned} \tag{5.35}$$

and the equation 5.21 is converts as follows,

$$\tau_v = \frac{\mu U_0}{a}\left(\frac{(U_z)_{i+1,j}^{k} - (U_z)_{i-1,j}^{k}}{2\Delta R} + \frac{(U_r)_{i,j+1}^{k} - (U_r)_{i,j-1}^{k}}{2\Delta Z}\right), \tag{5.36}$$

The initial and boundary conditions from equation 5.18-5.19 in the discretized form are defined as follows:

$$\begin{aligned}
&(U_r)_{1,j}^{k} = 0, \quad (U_z)_{0,j}^{k} = (U_z)_{2,j}^{k}, \quad (U_r)_{N+1,j}^{k} = 0, \quad (U_z)_{N+1,j}^{k} = 0,\\
&(V_r)_{1,j}^{k} = 0, \quad (V_z)_{0,j}^{k} = (V_z)_{2,j}^{k}, \quad (V_r)_{N+1,j}^{k} = 0, \quad (V_z)_{N+1,j}^{k} = 0,\\
&(U_r)_{i,j}^{1} = 0, \quad (U_z)_{i,j}^{1} = 0, \quad (V_r)_{i,j}^{1} = 0, \quad (V_z)_{i,j}^{1} = 0.
\end{aligned} \tag{5.37}$$

Equation 5.29 - 5.36 gives air and particle velocities at the $(k+1)^{th}$ time level in terms of velocities k^{th} time level.

5.5 Results and Discussion

The two-point boundary value problem, defined by equations 5.29- 5.36, is controlled by Reynolds number (Re), Strouhal number (S_t), Womersley number (w_0), Darcy number (Da), aspect ratio (β), breathing rate (f), and porosity (ϵ). Additionally, the effect of emphysema disease has been analyzed on the lung and result is shown via graph. To calculate the effects of the above parameters, the numerical values defined in Table 5.1 are used [18, 197, 245] and following graphs 5.2 - 5.7 are obtained. Firstly, before performing the numerical computation we chose time step $\Delta\tau = 0.001$, grid spaces $\Delta R = 0.01$, and $\Delta Z = 0.01$ in radial and axial directions, respectively and check the stability in each time level as follows

$$\begin{aligned} &\max\left(\frac{\Delta\tau}{\Delta R^2}\right) \leq 0.5, \\ &\max\left(\frac{\Delta\tau}{\Delta Z^2}\right) \leq 0.5. \end{aligned} \tag{5.38}$$

We found that the results of the present study appear to converge with the accuracy of order 10^{-3}. So, all the computation are performed at 100x100x1000 uniform grid points.

5.5.1 Importance of aspect ratio (β) and comparison with published work

In the environment, it is not necessary that all the particles are perfectly spherical in shape, hence to keep account of nonspherical nanoparticles, the aspect ratio is a key factor. We used elongated nanoparticles from aspect ratio $3 \leq \beta \leq 1000$, which covers a wide range of an inhalable nonspherical nanoparticles [222] and compared our result with (Saini et al. [197]) with spherical nanoparticles at Re = 10, d = 100nm, and ϵ = 0.84.

We found that the axial velocity of the particle, in Figure 5.2(a), is very low for spherical nanoparticles (Saini et al. [197]) and it increases due to increment in the aspect ratio from 3 to 1000. While, axial velocity of air, in Figure 5.2(b), is very high for spherical nanoparticles and it decreases due to increment in aspect ratio from 3 to 1000. From these figures, we observed that particles with high aspect ratio applies a high drag force on the air stream, which causes decrement in the velocity of air, however, spherical particle and low aspect ratio's particles applies a low drag force on air stream, which causes an increment in the velocity of air. Additionally, a comparison between spherical and nonspherical nanoparticles shows that nonspherical nanoparticles affect the air stream to a great extent.

5.5.2 Effect of Reynolds number (Re) on velocity

In Figure 5.3, we found the effect of Reynolds number (10 - 30) at $\beta = 10$, d = 100 nm, and ϵ = 0.84 on the axial velocity of air and particles. From Figure 5.3(a), we found by increasing the Reynolds number from 10 - 30, axial velocity of air and particle increases gradually with time (Figure 5.3(b)). Since, a large value of Reynolds number results in the thinner concentration boundary layer on the walls of airways, which promotes overall gas transfer while a lower value of Reynolds number causes high concentration on the walls of airways and affect the gas transfer. So, at Reynolds number = 30, the viscosity of the fluid is higher than at Reynold number = 10, which causes an increment in the flow of fluid.

5.5.3 Effect of porosity (ϵ)

In Figure 5.4, we found the effect of porosity ϵ on normal as compared to emphysema affected lung. In this study, we used porosity as a function of lung volume to analyze the impact of emphysema on the flow of viscous air at β = 10, d = 100 nm and Re = 10.

From Figure 5.4(a) - 5.4(b), we found that the velocity of a normal lung is lesser than emphysema affected lung because large pore size or highly permeable medium allows fluid to pass more easily. Therefore, emphysema affected lung allows air to flow more easily as compared to a normal lung but physiologically this behavior of an emphysema affected lung create a problem, since air is trapped in the alveolar sac and a person is unable to exhale properly so in the cyclic breathing person face breathing problem.

5.5.4 Effect of Darcy number (Da)

In Figure 5.5, we found the effect of the Darcy number on the flow regime at β = 10, d = 100 nm, ϵ = 0.84, and Re = 10. We found from Figure 5.5(a) - 5.5(b) that by increasing the value of the Darcy number from 0.001 to 0.1, velocity of air U_y and particle V_y due to emphysema are increased gradually with time. Highly porous media or ruptured alveoli applies a high drag force on fluid and lower pressure gradient on air as well as on particle, which cause increment in flow stream and most of the particles inside the air stream go toward various lung generations. From this behavior of ruptured alveoli inhalation become very easy but during exhalation a person face problem, because he/she not have enough pressure gradient to exhale properly.

5.5.5 Effect of breathing rate (f)

In Figure 5.6, we show the effect of breathing rate f from 12 to 30 breath per minute on the velocity of air and particles axially at aspect ratio (β) = 10, diameter (d) = 100 nm, porosity (ϵ) = 0.84 and Reynolds number (Re) = 10. We found for normal breathing rate (f=12/min), velocity of air (see Figure 5.6(a)) and particle (see Figure 5.6(b)) increases up to the axial distance z = 0.5 and after that it decreases with the axial distance down to zero but as we increase breathing rate in consideration with emphysemic lung (f = 25 - 30/min), there is a decrement in velocity of air and particles. So, we can conclude that due to emphysemic lung, a person can face breathing problem.

5.5.6 Analysis of stress on normal and emphysemic lung

We modeled the condition of the emphysemic lung by assuming lung as a porous media and porosity as a function of lung volume. By altering the volume for healthy lung (Saini et al. [197]) and emphysema affected lung results are analyzed. Typical breathing stress versus axial distance relationship for inhalation and exhalation is given in Figure 5.7. From this figure we found that the inspiratory breathing stress (in Table 5.2) depends on axial distance sinusoidally and increases linearly with the axial distance until it reaches maximum inspiration; after that, it falls linearly to zero and takes a pause during the elastic recoil, on axial distance = 0.5. It then starts decreasing and signaling the end of expiration at axial distance = 0. The figure also shows the comparison between stress on emphysemic lung and normal lung (Saini et al. [197]). We found due to the loss of elastic recoil of emphysemic lung airways do not inflate properly and obtain higher stress rate at the end of inspiration as compared to normal lung; while during expiration, due to the distortion in septal wall expiratory flow rate increases and simultaneous stress rate on the emphysemic lung decreased as compare to normal lung.

5.6 Conclusion

To study the effect of early - stage emphysema on flow dynamics of viscous air a numerical simulation is done. The computational geometry utilized in this study spans one generation of alveolar duct attaches with alveoli. The effects of emphysema consist of the destruction of alveolar septa and a reduction in airway flow rate. The gradual progression of these effects was investigated by comparing the results of a healthy lung with diseased lung. The concluding remarks are as follows:

1. It is found that the overall air velocity can be significantly increased by increasing the aspect ratio, alveoli size, Reynolds number, porosity, and breathing rate.

2. Increment in Darcy number causes high drag force on viscous air and low pressure gradient on lung.
3. We observed that emphysema produces decrement in oxygen transport through acinus. This is primarily due to the drop in generated pleural pressures which in turn lead to lower flow rates into the acinar branches.
4. In contrast, septal distortion has a notable effect on flow through acinus, where the loss of the alveolar septa tends to decrease the overall resistance to the flow, and hence lower inspiratory flow rates are observed in the ducts.
5. The particle deposition is smaller in the emphysematous lung as compared to healthy lungs and this, in turn, means particle deposition will occur more quickly when lungs are healthy.
6. Comparison between emphysema affected lung and normal lung shows higher stress rate at the end of the inspiration and lower expiratory rate due to septal destruction than the normal lung.

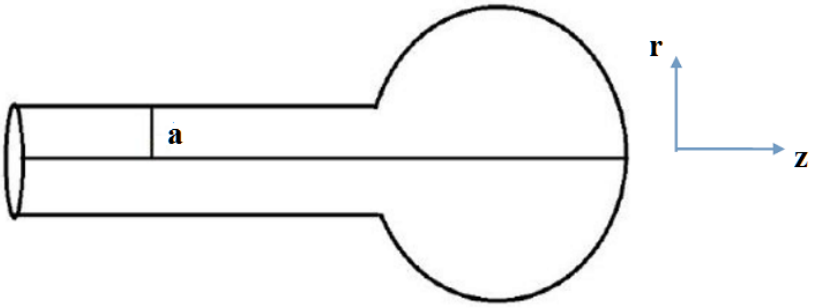

Figure 5.1: Schematic diagram of alveolar duct attached with a single alveoli.

Table 5.1: Numerical values used in the study

Variable	Value	Variable	Value
m	0.0002 Kg/l	d	100 nm
f_p	1.2 hz	ρ	1.145 kg/m^3
N_0	0.02504*$10^{12}/m^3$	r	125 μ m
a_2	0.5 Kg/m^2s^2	ν	1.71*$10^{-5}m^2/s$
u_{in}	0.3 m/s		

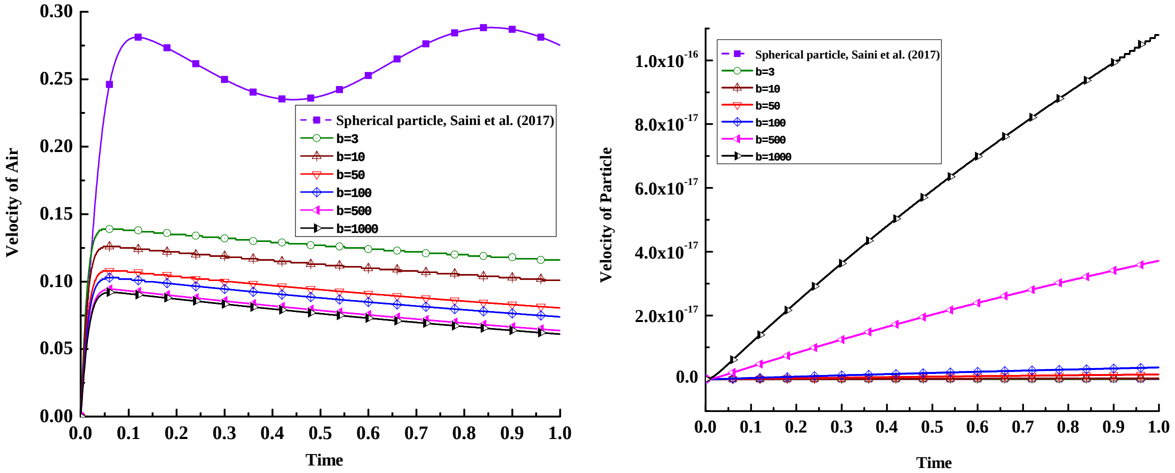

(a) (b)

Figure 5.2: Effect of spherical and nonspherical nanoparticles (3≤ β ≤ 1000) on the axial velocity of (a) air and (b) particle at Re = 10, d = 100 nm, and ϵ=0.84.

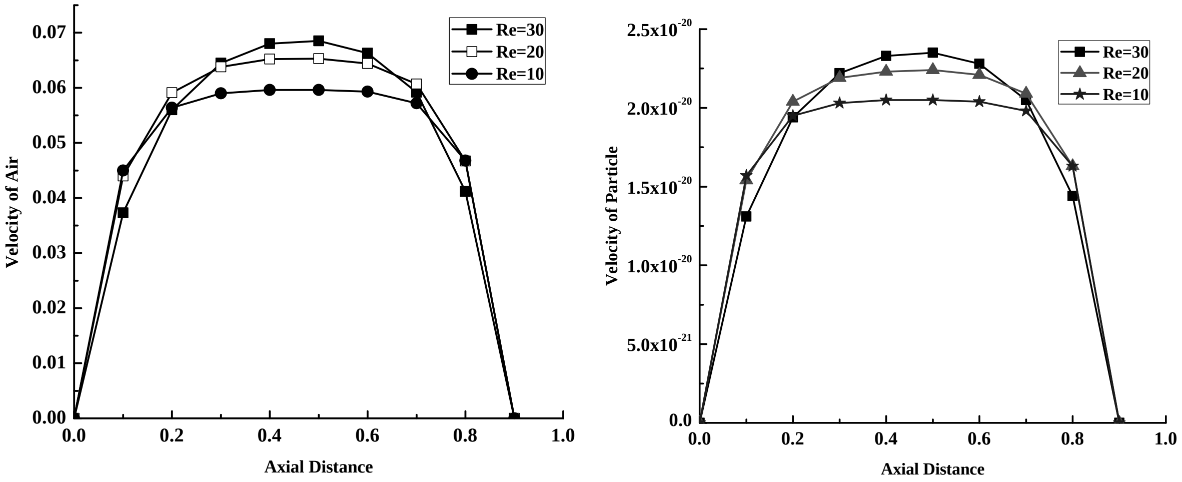

(a) (b)

Figure 5.3: Effect of Reynolds number on the axial velocity of (a) air and (b) particle at β = 10, d = 100 nm, and ϵ = 0.84.

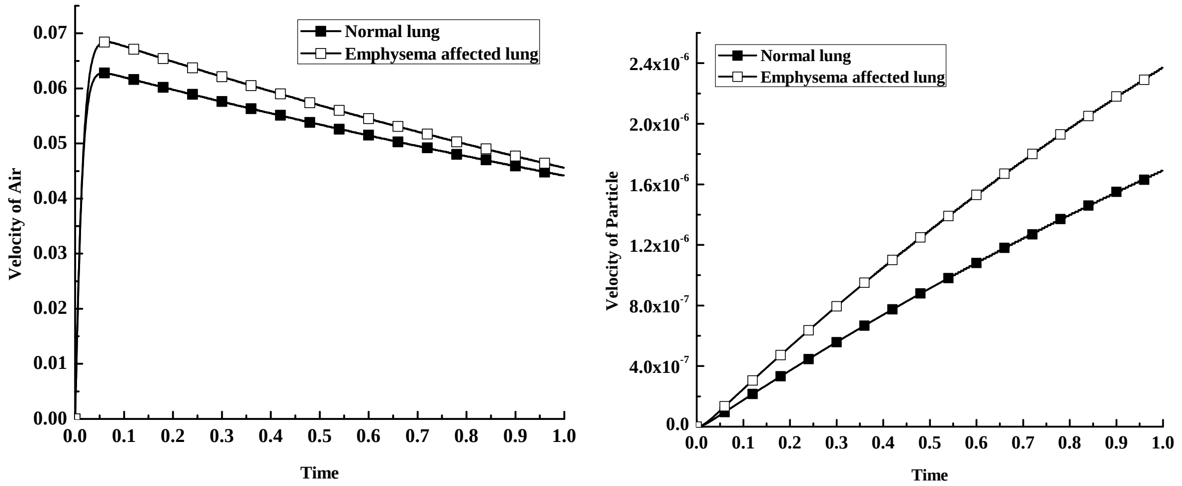

(a) (b)

Figure 5.4: Effect of porosity on the axial velocity of (a) air and (b) particle at β = 10, d = 100 nm, and Re = 10.

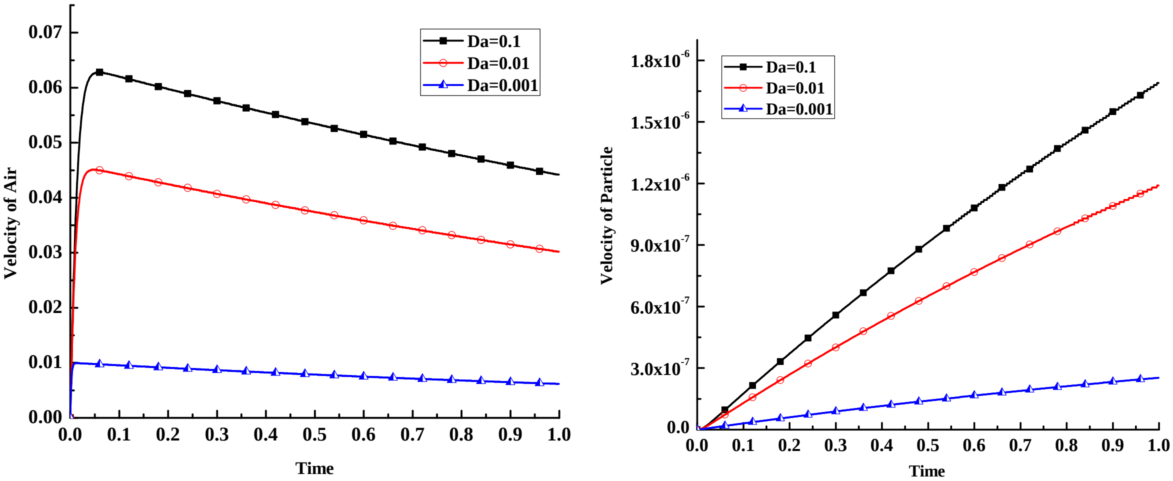

(a) (b)

Figure 5.5: Effect of Darcy number on the axial velocity of (a) air and (b) particle at β = 10, d = 100 nm, ϵ = 0.84, and Re = 10.

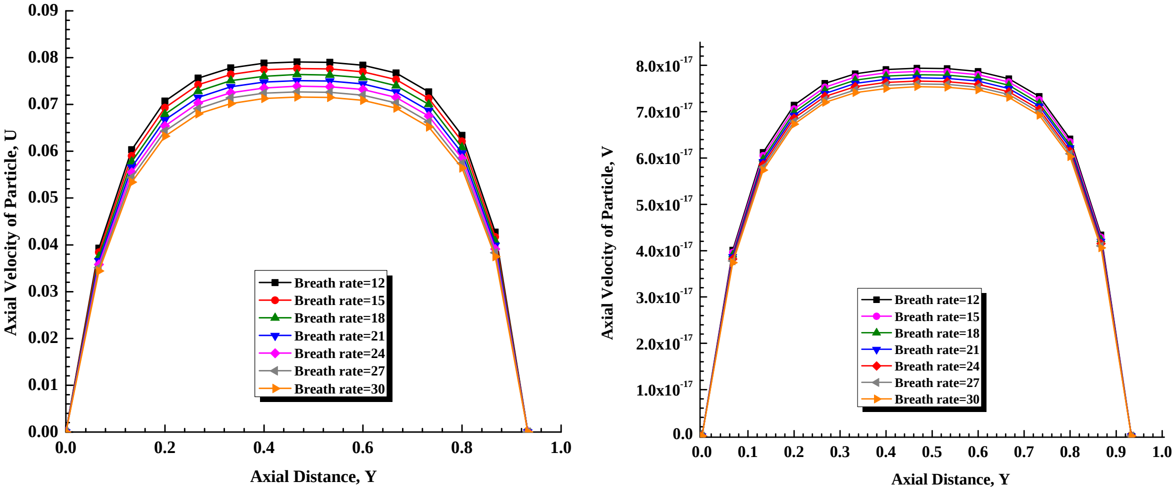

(a) (b)

Figure 5.6: Effect of breathing rate on the axial velocity of (a) air and (b) particle at f = 12 - 30/min, β = 10, and Re = 5.

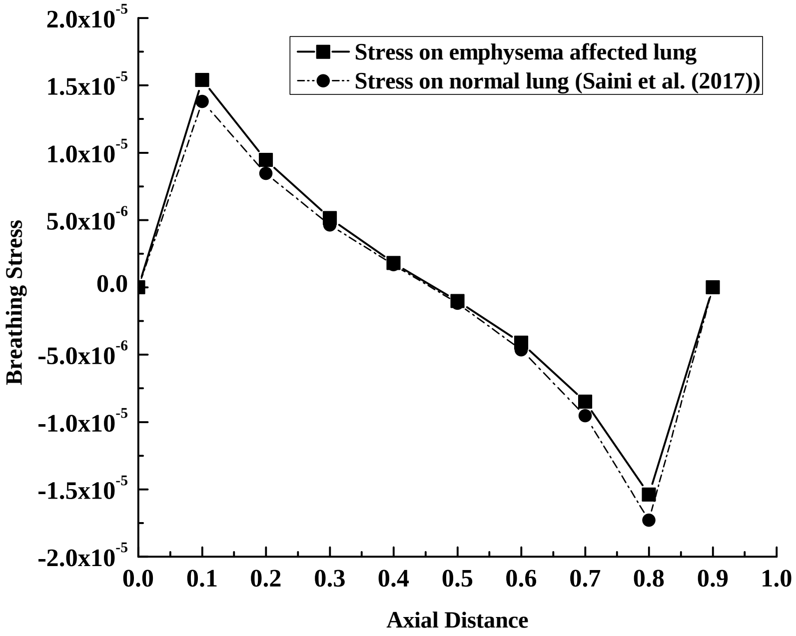

Figure 5.7: Analysis of stress on emphysemic lung and normal lung with respect to axial distance.

Table 5.2: Effect of emphysema on breathing.

Axial distance	Stress on emphysema affected lung	Stress on normal lung (Saini et al. [197])
0	0	0
0.1	1.54E-5	1.38E-5
0.2	9.45E-6	8.46E-6
0.3	5.13E-6	4.63E-6
0.4	1.81E-6	1.67E-6
0.5	-1.02E-6	-1.19E-6
0.6	-4.12E-6	-4.64E-6
0.7	-8.49E-6	-9.54E-6
0.8	-1.54E-5	-1.73E-5
0.9	0	0

Chapter 6: Mathematical study of the flow of blood through stenosis affect-ed viscoelastic artery in two dimensional system

6.1 Introduction

Biological tissue of lung is very soft or highly viscoelastic in nature that it exhibits a different type of stress-strain relationships [3]. The lungs have thin walls and endothelial cells, containing ultra-microscopic pores which makes the lung permeable and through which substances of various molecular sizes being penetrated can penetrate inside and pass into the lumen of the arteries from the surrounding tissues [106]. Moreover, lung contains several sources of viscoelasticity, namely the recoil nature of parenchyma [63], deformation of the membrane during respiration, etc.

The mathematical modeling of lung deformation is, however, challenging due to structural complexity, parenchymal heterogeneity, boundary conditions, and subject-specific breathing pattern [156]. Some study considered lung as a linear elastic substance [98] and some nonlinear hyperelastic [64] with one-phase continuum material [56]. Additionally, modeling the general permeability of media is not easy. In 1856, Sir Darcy [37] proposed a mathematical model, which applies to the permeability of tissue. The model is useful under some constraints, where the viscous effect dominated by inertial effect but due to high-pressure gradient or higher porous regimes, where inertial effect dominated by the viscous effect the Darcian model is not applicable. In literature significant work has been done by some authors considering mass exchange using an extended Darcy model [174], studying non-Darcian transportation of blood perfusion in tissue [238] and analyzing blood flow in cardiac vessels using Darcy-Forchheimer model [215]. However, Mehmood et al. [148] found that due to suspension of cholesterol, deposition of dead tissues, carbohydrates, and fats in the lumen, permeability, and elasticity of lung decreases, which causes various cardiovascular or arterial diseases such as thrombosis, erythrocytoses, atherosclerosis [138], and cancer, etc. Among these, disease atherosclerosis also known as stenosis is one of the dangerous disease, which causes constriction in blood vessels. It develops inward into the lumen at one or more locations of the cardiovascular system and reduces the regular blood flow and gas exchange in the pulmonary region.

There are various studies on tissue permeability, elasticity, deposition of nonspherical particles and stenosis [24, 53, 171, 182]. A mathematical study of oscillatory flow through thin-walled elastic tubes with small curvature is carried by Chandran et al. [25] and found that asymmetrical secondary flow pattern induced by centrifugal effects due to curvature. The effect of non-Newtonian blood and flow pulsatility stenosed tube have been studied by Chaturani and Samy [28] using perturbation method and they found that that the mean and steady flow rates decrease as the yield stress increases. Mathematical modeling of blood flow through an artery with multiple stenoses and poststenotic dilatations is carried out Wong et al. [250] and found that variation in arterial wall geometry has a great impact on the blood flow resistance. Alimohamadi and Imani [5] studied the effect of external magnetic field on the pulsatile blood flow patterns in a stenosis artery by considering the fatty deposited lump through porous arterial walls. Also, the study of suspension flow of smaller particles in a viscous fluid through constricted vessels have considerable significance in medical field [122]. Saffman [191] gave a simple analytical model for the motion of dusty fluid with a large number of dust particles suspended in a fluid. Saini et al. [194] carried out two-dimensional natural convection flow of a dusty fluid over a tube with axisymmetric constriction and found that stenosis affects the pressure of blood drastically in the upstream region of the stenotic artery.

From the above literature review, we noticed that the studies related to shape and orientation of particles and their effect on the flow dynamics of viscous air through porous, elastic and stenosed artery have not been considered yet. So, in this study, we include the shape factor of suspended particles together with tissue porosity and analyze their effect on flow pulsatility through a viscoelastic artery, which consists of axisymmetric stenoses of radius $R(z)$. Theory of dust particles suspended in gas on blood flow through the artery, where the ‘particles’ are cells suspended in ‘plasma’ is applied. The fluid is percolating through the stationary porous wall and particles tumble continuously in the bulk shear flow. In this way, the study will produce a more general description of the blood flow through a stenosed artery. The flow of air is governed by two dimensional Navier-Stokes’ equation by including drag force (Darcy-Forchheimer drag) caused by non-Darcian effect and flow of particle analyzed by Newton second equation of motion finite difference scheme is applicable to solve the governing equations and illustrations are presented through graphs in the form of radial and axial velocities by taking cyclic mean. Additionally, the material of the artery is approximated as a linear elastic or Voigt body. We used the simplest rheological equation that includes viscosity and elasticity and finds the effect of flow amplitude on the viscoelasticity of arterial walls.

6.2 Mathematical Formulation

6.2.1 Governing equations

Consider an unsteady, laminar, fully-developed, incompressible, viscous, Newtonian fluid is flowing through axisymmetrical arterial segment having mild stenosis due to deposition of nonspherical nanoparticles (cells suspended in plasma). The axial axis is along the tube and the radial axis is normal to the tube. To study the flow pulsatility a geometrical structure illustrated in Figure 6.2 in two dimensional cylindrical coordinate system (r, z, θ) is defined by following mathematical formulation

$$\begin{aligned} &R(z) = R_0 - \frac{C_1}{2}\exp(-fr)(1+cos(\pi\frac{z-l_c}{l_c}) \qquad 2|z-l_c| \leq l_s, \;\; 0 \leq z \leq L, \\ &R(z) = R_0, \;\; 2|z-l_c| > l_s, \qquad 0 \leq z \leq L, \end{aligned} \tag{6.1}$$

where C_1 is dimensionless constriction ratio, l_c is dimensionless distance to the centre of constriction, l_s is dimensionless length of the stenosis, R_0 is radius of artery, f is rate change parameter, L is length of arterial segment.

The wall of the artery is porous and viscoelastic and due to suspension of particles flow through permeable artery is modeled using non-Darcian regime. Dynamic shape factor is used to show the effect of nonspherical nano particles of shape elongated. We explored arterial wall dynamics for a short time when there is no mass exchange (blood flow) within the macroscales. So, density is changed only if there is a compression of medium as a whole. For this kind of condition arterial wall may be considered as homogeneous medium, which mean the velocities of all phases are equal. The continuity, motion, and Navier-Stokes' equations with Darcy-Forchheimer drag force in two dimensional cylindrical coordinate (r, z, θ) system are written as follows:

Equation of continuity for air,

$$\frac{\partial u_r}{\partial r} + \frac{u_r}{r} + \frac{\partial u_z}{\partial z} = 0, \tag{6.2}$$

equation of continuity for particle,

$$\frac{\partial v_r}{\partial r} + \frac{v_r}{r} + \frac{\partial v_z}{\partial z} = 0, \tag{6.3}$$

equation of radial momentum for air,

$$\frac{\partial u_r}{\partial t} + \frac{u_r}{\epsilon}\frac{\partial u_r}{\partial r} + \frac{u_r}{\epsilon}\frac{\partial u_r}{\partial z} = -\frac{\epsilon}{\rho}\frac{\partial p}{\partial r} + \nu\left(\frac{\partial^2 u_r}{\partial r^2} + \frac{1}{r}\frac{\partial u_r}{\partial r} + \frac{\partial^2 u_r}{\partial z^2}\right) + \left(-\frac{\epsilon\nu}{K}u_r - \frac{\epsilon b}{K}u_r^2\right)$$
$$+ s_k\frac{N_0}{\rho}\left(v_r - u_r\right), \tag{6.4}$$

equation of axial momentum for air,

$$\frac{\partial u_z}{\partial t} + \frac{u_z}{\epsilon}\frac{\partial u_z}{\partial r} + \frac{u_z}{\epsilon}\frac{\partial u_z}{\partial z} = -\frac{\epsilon}{\rho}\frac{\partial p}{\partial z} + \nu\left(\frac{\partial^2 u_z}{\partial r^2} + \frac{1}{r}\frac{\partial u_z}{\partial r} + \frac{\partial^2 u_z}{\partial z^2}\right) + \left(-\frac{\epsilon\nu}{K}u_z - \frac{\epsilon b}{K}u_z^2\right)$$
$$+ s_k\frac{N_0}{\rho}\left(v_z - u_z\right), \tag{6.5}$$

equation of motion of particle in radial direction,

$$m\left(\frac{\partial v_r}{\partial t} + v_z\frac{\partial v_r}{\partial z} + v_r\frac{\partial v_r}{\partial r}\right) = F_{d_1}, \tag{6.6}$$

equation of motion of particle in axial direction,

$$m\left(\frac{\partial v_z}{\partial t} + v_z\frac{\partial v_z}{\partial z} + v_r\frac{\partial v_z}{\partial r}\right) = F_d. \tag{6.7}$$

The first term in the left hand side of the equations 6.4 - 6.5 is for unsteady flow and the second-third terms are for convection. First, second, third, and forth terms in the right hand side of equations 6.4 - 6.5 are the pressure gradient, diffusion, and the entire body force because of the existence of non-Darcian effect together-with external force fields respectively. The term in the left hand side of equations 6.6 - 6.7 represents the product of the mass times the acceleration and right hand side of this equation represents the drag force on the nanoparticles.
In equation 6.4- 6.5, K is the permeability of media, which depends on the porosity (ϵ) [107] as follows

$$K = \frac{\epsilon^3 d_p^2}{150\left(1-\epsilon\right)^2}, \tag{6.8}$$

additionally, other variables, i.e. S_f, s_k, F_d, and F_{d_1}, from equation 6.4 - 7.6, have similar descriptions as defined in Chapter 5 [1].

---

[1] Section 5.2 and equation 5.9 - 5.10

Viscoelastic model

It is known that biological soft tissues demonstrate viscoelastic properties. Viscoelasticity is a combination of two words i.e. viscosity and elasticity. Viscosity, a characteristic of the fluid, which is used to calculate the resistance on flow. Besides this, elasticity is the characteristic of solid material, which calculates how material returns to its normal form after deformation. So, a material, which contains both properties (fluid and solid properties) is termed as viscoelastic material [164]. To study the flow dynamics of a viscous fluid through stenosed artery we analyzed the viscoelastic property of artery for small deformation and considered the medium as 'Voigt body' by applying the simplest rheological equation that includes both viscosity and elasticity [52]. The two-dimensional viscoelastic model introduced by the Kelvin-Voigt, which relates stress to strain and strain rate is used after extending for non-Darcian porous regime as follows

$$\tau_v = \left(\phi + \frac{4\mu}{3}\right)\left(\frac{\partial u_z}{\partial r} + \frac{\partial u_r}{\partial z}\right) + \left(\zeta + \frac{4\eta}{3}\right)\frac{\partial}{\partial t}\left(\frac{\partial u_z}{\partial r} + \frac{\partial u_r}{\partial z}\right), \tag{6.9}$$

where ϕ is used for bulk compression, μ is used for shear modules respectively due to elasticity and ζ is used for shear coefficients, η is used for bulk coefficient respectively due to parenchymal viscosity. $(\frac{\partial u_z}{\partial r} + \frac{\partial u_r}{\partial z})$ is strain and $\frac{\partial}{\partial t}(\frac{\partial u_z}{\partial r} + \frac{\partial u_r}{\partial z})$ is strain velocity.

6.2.2 Initial and boundary conditions

Following initial and boundary conditions are subjected to equation 6.2-6.7:

- At rest ($t = 0$) there is no flow takes places therefore

$$u_r = v_r = u_z = v_z = 0. \tag{6.10}$$

- We assumed that there is no radial flow along the axis of the alveolar tube so the axial velocity gradient adequate to zero

$$u_r = 0; v_r = 0; \frac{\partial u_z}{\partial r} = 0; \frac{\partial v_z}{\partial r} = 0. \tag{6.11}$$

- The no-slip condition is applicable at the inner surface of the wall.

6.3 Methodology

6.3.1 Transformation of the governing equations

To solve the governing equations 6.2-6.9 numerically we have to make them dimensionless, so we used the following quantities:

$$X^* = \frac{r}{R_0}, Y^* = \frac{z}{R_0}, p^* = \frac{P}{\rho U_0^2}, \tau^* = \frac{t}{t_0}, U_x^* = \frac{u_r}{U_0}, U_y^* = \frac{u_z}{U_0}, V_x^* = \frac{v_r}{U_o}, R' = R/R_0,$$
$$V_y^* = \frac{v_z}{U_o}, F_s = \frac{b}{R_0}, Da = \frac{K}{R_0^2}, P_l = \frac{N_0}{\rho}, S_m = \frac{R_0 k}{U_0}, Re = \frac{R_0 U_0}{\nu}, S_t = \frac{a}{U_0 t_0}.$$

P_l is particle load, Da is Darcy number, F_s is Forchheimer number, ρ_0 is unit density, Re Reynolds number, S_t Strouhal number, and S_m is used for simplification.

$$\frac{\partial U_x}{\partial X} + \frac{U_x}{X} + \frac{\partial U_y}{\partial Y} = 0, \tag{6.12}$$

$$\frac{\partial V_x}{\partial X} + \frac{V_x}{X} + \frac{\partial V_y}{\partial Y} = 0, \tag{6.13}$$

$$S_t \frac{\partial U_y}{\partial \tau} + \frac{U_x}{\epsilon}\frac{\partial U_y}{\partial X} + \frac{U_y}{\epsilon}\frac{\partial U_y}{\partial Y} = -\epsilon \frac{\partial P}{\partial Y} + \frac{1}{Re}\left(\frac{\partial^2 U_y}{\partial X^2} + \frac{1}{X}\frac{\partial U_y}{\partial X} + \frac{\partial^2 U_y}{\partial Y^2}\right)$$
$$+ S_m P_l \left(V_y - U_y\right) - \frac{\epsilon}{DaRe} U_y - \epsilon \frac{F_s}{Da} U_y^2, \tag{6.14}$$

$$S_t \frac{\partial V_y}{\partial \tau} + V_x \frac{\partial V_y}{\partial X} + V_y \frac{\partial V_y}{\partial Y} = \frac{S_f S_m \left(U_y - V_y\right)}{m}, \tag{6.15}$$

The Womersley number is responsible for the frequency of pulsatile flow. It is related to the Reynolds number and is defines as

$$w_0 = \sqrt{2\pi Re S_t}. \tag{6.16}$$

$$T = \frac{u_0}{R}\left[\left(\phi + 4\frac{\mu}{3}\right)\left(\frac{\partial U_y}{\partial X} + \frac{\partial U_x}{\partial y}\right)\right] + \frac{u_0}{R}\left[\left(\zeta + \frac{4\eta}{3}\right)\frac{\partial}{\partial \tau}\left(\frac{\partial U_y}{\partial X} + \frac{\partial U_x}{\partial y}\right)\right]. \tag{6.17}$$

Transformed initial and boundary conditions from equation 6.10 - 6.11 are as follows,

$$U_x = 0;\ U_y = 0;\ V_x = 0;\ V_y = 0, \tag{6.18}$$

$$
\begin{aligned}
&U_x = 0;\ \frac{\partial U_y}{\partial X} = 0;\ V_x = 0;\ \frac{\partial V_y}{\partial X} = 0,\\
&U_y = 0;\ V_y = 0.
\end{aligned} \tag{6.19}
$$

In equation 6.4 - 6.5, due to general physiological conditions flow properties of blood is based on the pumping action of the heart, which thus delivers a pulsatile pressure gradient over the cardiovascular system, so we assume pressure gradient as

$$
-\frac{\partial P}{\partial Z} = a_1 + a_2 \sin(\omega \tau t_0), \quad \omega = 2\pi f, \tag{6.20}
$$

where a_1 is the constant amplitude of the pressure gradient, a_2 is the amplitude of the pulsatile component, u_0 is reference velocity.

6.4 Numerical Scheme

The non - dimensional governing equations 6.12 - 6.17 subject to two point boundary conditions (equation 6.18 - 6.19) are solved by using finite difference numerical technique [214], which is the most suitable method for nonlinear problems related to regular geometries. The computational grid are defined in the following form where the discretization of air velocity $U(R, T, \tau)$ is written as $U_z(R_i, Z_j, \tau_k)$ or $(U_z)^k_{i,j}$.

$$
\begin{aligned}
&X_i = i\Delta x, (i = 0, 1, 2, 3, 4, ..., N), X_N = 1,\\
&Y_j = j\Delta y, (j = 0, 1, 2, 3, 4, ..., M,\\
&\tau_k = (k-1)\Delta\tau, (k = 1, 2, ...),
\end{aligned}
$$

where i, j, and n are radial, axial and time index; ΔX, ΔY, and $\Delta\tau$ are the increments in the radial, axial directions and time respectively.

We used central difference approximation at point (x_i, y_j, τ_k), for all the spatial derivatives, as follows:

$$
\frac{\partial U_y}{\partial Y} = \frac{(U_y)^k_{i,j+1} - (U_y)^k_{i,j-1}}{2\Delta Y}, \tag{6.21}
$$

$$
\frac{\partial^2 U_y}{\partial Y^2} = \frac{(U_y)^k_{i,j+1} - 2(U_y)^k_{i,j} + (U_y)^k_{i,j-1}}{(\Delta Y)^2}, \tag{6.22}
$$

and forward difference approximation for the first order time derivative as

$$
\frac{\partial (U_y)}{\partial \tau} = \frac{(U_y)^{k+1}_{i,j} - (U_y)^k_{i,j}}{2\Delta\tau}. \tag{6.23}
$$

Additionally, at $X = 0$, following simplification are applied in equations 6.12 - 6.17, [2]

$$\lim_{X\to 0}\frac{1}{X}\frac{\partial U_y}{\partial X} = \lim_{X\to 0}\frac{\partial^2 U_y}{\partial X^2},$$

$$\lim_{X\to 0}\frac{U_x}{X} = \lim_{X\to 0}\frac{\partial U_x}{\partial X},$$

$$\lim_{X\to 0}\frac{V_x}{X} = \lim_{X\to 0}\frac{\partial V_x}{\partial X},$$

In order to handle the nonlinearity of partial differential equations numerically, the method of Newton's linearization is applied as

$$(U_x)^{k+1}_{i,j} = (U_x)^{k}_{i,j} + \Delta(U_x)^{k}_{i,j}, \tag{6.24}$$

where, the first term of equation 6.24 represents the k^{th} iteration of the dependent variables, which is known and the second term represents the error at the k^{th} iteration at point (x_i, y_j, τ_k).

So, the equation 6.12 in discretization form can be written as, at $X = 0$,

$$(U_x)^{k+1}_{i+1,j} = (U_x)^{k+1}_{i,j} - \frac{\Delta X}{2\Delta Y}\left((U_y)^{k+1}_{i,j+1} - (U_y)^{k+1}_{i,j}\right), \tag{6.25}$$

and at $0 < X \leqslant 1$,

$$(U_x)^{k+1}_{i+1,j} = (U_x)^{k+1}_{i,j}\left(1 - \frac{1}{i}\right) - \frac{\Delta X}{\Delta Y}\left((U_y)^{k+1}_{i,j+1} - (U_y)^{k+1}_{i,j}\right), \tag{6.26}$$

equation 6.13 at $X = 0$ transforms as,

$$(V_x)^{k+1}_{i+1,j} = (V_x)^{k+1}_{i,j} - \frac{\Delta X}{2\Delta Y}\left((V_y)^{k+1}_{i,j+1} - (V_y)^{k+1}_{i,j}\right), \tag{6.27}$$

and at $0 < X \leqslant 1$,

$$(V_x)^{k+1}_{i+1,j} = (V_x)^{k+1}_{i,j}\left(1 - \frac{1}{i}\right) - \frac{\Delta X}{\Delta Y}\left((V_y)^{k+1}_{i,j+1} - (V_y)^{k+1}_{i,j}\right), \tag{6.28}$$

equation 6.14 at $X = 0$ converts as,

$$\begin{aligned}(U_y)^{k+1}_{i,j} &= \left(1 - S_m P_l\frac{\Delta\tau}{S_t} - \left(\frac{\epsilon}{DaS_tRe}\right)\Delta\tau - \frac{2r_1}{ReS_t} - \frac{4r_2}{ReS_t}\right)(U_y)^k_{i,j}\\ &- \frac{r_2\Delta X}{2\epsilon S_t}\big(U_y)^k_{i+1,j} - (U_y)^k_{i-1,j}\big)(U_x)^k_{i,j} - \frac{r_1\Delta Y}{2\epsilon S_t}\left((U_y)^k_{i,j+1} - (U_y)^k_{i,j-1}\right)(U_y)^k_{i,j}\\ &+ \frac{2r_2}{ReS_t}\left((U_y)^k_{i+1,j} + (U_y)^k_{i-1,j}\right) + \frac{r_1}{ReS_t}\left((U_y)^k_{i,j+1} + (U_y)^k_{i,j-1}\right)\\ &+ \frac{\Delta\tau}{S_t}S_m P_l(V_y)^k_{i,j} - \epsilon\frac{\Delta\tau}{S_t}\frac{\partial P}{\partial Y} - \epsilon\frac{F_s\Delta t}{Da}(U_y)^2_{i,j},\end{aligned} \tag{6.29}$$

---

[2] When $X \to 0$, we found that the denominator is also approaching to zero and make the term indeterminate, which is inappropriate for the physical state of the respiratory system. Therefore, to remove this kind of inconsistency we used L'hospital rule of limit here.

and at $0 < X \leqslant 1$,

$$\begin{aligned}
(U_y)_{i,j}^{k+1} &= \left(1 - S_m P_l \frac{\Delta\tau}{S_t} - \left(\frac{\epsilon}{DaS_tRe}\right)\Delta\tau - \frac{2r_1}{ReS_t} - \frac{2r_2}{ReS_t}\right)(U_y)_{i,j}^k \\
&- \frac{r_2\Delta X}{2\epsilon S_t}\left((U_y)_{i+1,j}^k - (U_y)_{i-1,j}^k\right)(U_x)_{i,j}^k - \frac{r_1\Delta Y}{2\epsilon S_t}\left((U_y)_{i,j+1}^k - (U_y)_{i,j-1}^k\right)(U_y)_{i,j}^k \\
&+ \frac{2r_2}{ReS_t}\left((U_y)_{i+1,j}^k + (U_y)_{i-1,j}^k\right) + \frac{r_1}{ReS_t}\left((U_y)_{i,j+1}^k + (U_y)_{i,j-1}^k\right) \\
&+ \frac{r_2}{2iReS_t}\left((U_y)_{i+1,j}^k - (U_y)_{i-1,j}^k\right) + \frac{\Delta\tau}{S_t}S_mP_l(V_y)_{i,j}^k - \epsilon\frac{\Delta\tau}{S_t}\frac{\partial P}{\partial Y} - \epsilon\frac{F_s\Delta t}{Da}(U_y)_{i,j}^2,
\end{aligned} \tag{6.30}$$

equation 6.15 converts as,

$$\begin{aligned}
(V_y)_{i,j+1}^{k+1} &= \left(1 - \frac{S_mS_f\Delta\tau}{mS_t}\right)(V_y)_{i,j}^k + S_f\Delta\tau(U_y)_{i,j}^k\frac{S_fS_m}{mS_t} - \frac{r_1\Delta Y}{S_t}(V_y)_{i,j}^k \\
&\left((V_y)_{i,j+1}^k - (V_y)_{i,j-1}^k\right) - \frac{r_2\Delta X}{S_t}(V_x)_{i,j}^k\left((V_y)_{i+1,j}^k - (V_y)_{i-1,j}^k\right),
\end{aligned} \tag{6.31}$$

also, equation 6.17 as follows,

$$\begin{aligned}
T &= \left(\phi + 4\frac{\mu}{3}\right)\left(\frac{(U_y)_{i+1,j}^k - (U_y)_{i-1,j}^k}{2\Delta X} + \frac{(U_x)_{i,j+1}^k - (U_x)_{i,j-1}^k}{2\Delta Y}\right) \\
&+ \left(\zeta + \frac{4\eta}{3}\right)\left(\frac{(U_y)_{i+1,j}^k + 1 - (U_y)_{i-1,j}^k + 1 - (U_y)_{i+1,j}^k + (U_y)_{i-1,j}^k}{2\Delta X\Delta\tau}\right) \\
&+ \left(\zeta + \frac{4\eta}{3}\right)\left(\frac{(U_x)_{i,j+1}^k + 1 - (U_x)_{i,j-1}^k + 1 - (U_x)_{i,j+1}^k + (U_x)_{i,j-1}^k}{2\Delta Y\Delta\tau}\right).
\end{aligned} \tag{6.32}$$

The initial and boundary conditions from equation 6.18 - 6.19 are found as follows,

$$\begin{aligned}
&(U_x)\,{}_{1,j}{}^k = 0, \quad (U_y)\,{}_{0,j}{}^k = (U_y)\,{}_{2,j}{}^k, \quad (U_x)\,{}_{N+1,j}{}^k = 0, \quad (U_y)\,{}_{N+1,j}{}^k = 0, \\
&(V_x)\,{}_{1,j}{}^k = 0, \quad (V_y)\,{}_{0,j}{}^k = (V_y)\,{}_{2,j}{}^k, \quad (V_x)\,{}_{N+1,j}{}^k = 0, \quad (V_y)\,{}_{N+1,j}{}^k = 0, \\
&(U_x)\,{}_{i,j}{}^1 = 0, \quad (U_y)\,{}_{i,j}{}^1 = 0, \quad (V_x)\,{}_{i,j}{}^1 = 0, \quad (V_y)\,{}_{i,j}{}^1 = 0.
\end{aligned} \tag{6.33}$$

6.5 Results and Discussion

The two dimensional boundary value problem defined by equations 6.25 - 6.32 under initial and boundary conditions (equation 6.33) are controlled by ten parameters, namely, Reynolds number (Re), Forchheimer number (F_s), Darcy number (Da), aspect ratio (β), shape factor (S_f), porosity (ϵ), aerodynamic diameter (d_p), bulk compression (ϕ) for elasticity, shear (η) and bulk (ζ) coefficients of parenchymal viscosity. Effect of these parameters are found on flow and viscoelastic characteristics and shown through graphs 6.3 - 6.8. For numerical computations values of parameters are defined in Table 6.3 [51, 100, 130, 194, 245, 255].

Before discussing the analysis of the present problem a numerical code validation and predictive accuracy of the model are checked by comparing output data produced by present model with respective results generated by model of Saini et al. [194]. The grid independence test is performed by varying grid sizes between 10x10x10^3 - 20x20x10^3 by using following stability criteria at each time level so that less error occurred in the numerical computation (shown in Figure 6.1(a) and Table 6.1).

$$\begin{aligned}&\max\left(\frac{\Delta\tau}{\Delta X^2}\right)\leq 0.5,\\ &\max\left(\frac{\Delta\tau}{\Delta Y^2}\right)\leq 0.5.\end{aligned}\tag{6.34}$$

From Table 6.1 it is observed that no significant change is found after the grid size 15x15x10^3. Therefore, all computations are made by using the grid size 20x20x10^3 as an optimal grid size.

For validation of model a comparative study is done between present study and Saini et al. [194] for radial velocity profile at ϵ = 0.7, F_s = 1, Da = 0.01, and Re = 10.

Saini et al. [194] studied two-dimensional natural convection flow of a dusty fluid over a tube with axisymmetric constriction. The present study is compared with the results of Saini et al. [194] in Figure 6.1(b) and Table 6.2 for the radial velocity of air with respect to radial distance at $z = 20$ mm. We found that our numerical result is validated with their result of up to 99.9%. So, we can say, our results are in excellent agreement with those of Saini et al. [194].

6.5.1 Effect of aspect ratio (β)

We used Re = 10, F_s = 1, ϵ = 0.4, Da = 0.05, A_2 = 2, the constriction ratio and the constriction length = 0.4, and 0.74 respectively and considered diameter of particles d = 50 nm, and aspect ratio 3 $\leq$ β $\leq$ 1000 which covers wide range of inhalable nonspherical nano particles. We found the effect of aspect ratio β on axial (V_x) and radial (V_y) velocity of particles in Figure 6.3(a) and Figure 6.3(b). The radial velocity profile increases from the origin on the axis with positive values and keeps moving away with the increase in aspect ratio. Due to the diastole (blood in), the radial velocity increases when β increases from 3 to 1000. It is due to the pumping action of heart creating the pulsatile pressure gradient which is directly responsible for the flow profiles and increases the radial velocity profile of particles. While, in axial velocity, due to systole (blood out) profile of particles the curve begins beyond the origin and decreases monotonically, at last, it reaches some finite value with respect to axial distance. The axial velocity profile increases in this manner by the increase in aspect ratio. Since particles with high aspect ratio are very thin so when we increase aspect ratio from 3 to 1000, it causes high drag force on fluid so there is an increase in particle velocity in both the directions. However, by comparing radial and axial velocity profiles we found that axially (Figure 6.3(b)) particles tend to deposit more rapidly in the axial direction than radially (Figure 6.3(a)) because the axial velocity of the particle is lesser than radial velocity profile.

6.5.2 Effect of Forchheimer number (F_s)

Forchheimer number (F_s) is used for the non-linear dependency of pressure drop on the velocity profile and Darcy-Forchheimer equation is used in high-velocity profile inside porous media. We used Re = 10, Da = 0.05, ϵ = 0.4, β = 10 with d = 50 nm, A_2 = 2, the constriction ratio and the constriction length being fixed to 0.4 and 0.74 respectively. In order to elucidate the effect of the Forchheimer number (F_s), the details of flow fields for different F_s = 1 - 18 shown in Figure 6.4(a) - Figure 6.4(d) respectively. The effect of F_s on the velocity of air and particle shown in radial (Figure 6.4(a) - Figure 6.4(b)) and axial directions (Figure 6.4(c) - Figure 6.4(d)). In axial velocity profile the curve begins beyond the origin and decreased monotonically and reaches some finite value while the radial velocity profile increases from the origin on the axis with positive values and move away with respect to distance; for both, air and particle. The higher F_s means higher drag values, which results in higher velocities. We noticed by the increment in F_s from 1 to 18, axial and radial, both velocity profiles for air and particles are increased.

6.5.3 Effect of Reynolds number (Re)

It has been known that the Reynolds number (Re) has a great influence on the flow field in the constricted or stenosis affected artery for unsteady flow. The effect of the Reynolds number on the unsteady pulsating flow is discussed in this study. Reynolds numbers (Re) ranging 10 - 200 is considered, with F_s = 1, Da = 0.05, ϵ = 0.4, A_2 is set to be 2, the constriction ratio and the constriction length being fixed to 0.4 and 0.74. So, the instantaneous streamlines for sinusoidal fluctuated flow at Re = 10 - 200 through constricted for small artery are shown in Figure 6.5(a) - Figure 6.5(d) respectively. We found that radial velocity profiles (for air and particles) increase up to the local peak by the increment in Re, and then decrease gradually with radial distance either due to the random movement of nonspherical nanoparticles or due to pulsatile nature of flow (see, Figure 6.5(a) - Figure 6.5(b)). While axial velocity profiles (for air and particles) start from the local peak values and increase by increasing the value of Re (see, Fig 6.5(c) - Figure 6.5(d)). Either due to stenosis inside a tube or due to suspension of nonspherical nanoparticles, fluid faced wall shear stress and hence the velocity of the fluid (air and particle) decreases with respect to axial distance gradually.

Consequently, by increasing the range of Reynolds number (Re) the flow pattern is affected to a high extent in both the directions axial and radial.

6.5.4 Effect of Darcy number (Da)

In Figure 6.6 graphs are obtained, for Re = 10, F_s = 1, ϵ = 0.4, β = 10 with d = 50 nm, A_2 = 2, constriction ratio = 0.4, constriction length = 0.74, and varying the Darcy Number (Da) from 0.05 to 1, between radial distance and radial velocity profile (see, Figure 6.6(a)- Figure 6.6(b)) as well as axial distance and axial velocity profile (see Figure 6.6(a)- Figure 6.6(b)). By increasing the value of Da from 0.05 to 1 medium becomes very porous or more fluidic increasingly. The fluid flow, therefore, is accelerated and velocity profiles are amplified for air and particles in radial and axial directions.

6.5.5 Effect of porosity (ϵ)

Figure 6.7 shows the effect of porosity (ϵ) on velocity profiles of air and particles by using Re = 10, F_s = 1, Da = 0.05, β = 10, d = 50 nm, A_2 = 2, the constriction ratio and the constriction length being fixed to 0.4, and 0.74 respectively. When porosity (ϵ) of the wall increases from 0.4 to 0.9, there is an increase in the velocity profile for both axial (Figure 6.6(c) - Figure 6.6(d)) and radial directions (Figure 6.7(a) - Figure 6.7(b)). We observed that for highly porous medium number of pores are increased which cause an increment in the fluidity of viscous fluid in both the directions, therefore by increasing porosity of walls velocity of air and particles increases.

6.5.6 Analysis of viscoelastic stress

In order to characterize the elastic and viscous stresses for small deformations, we adopted a two dimensional linear viscoelastic are model. Figure 6.8 shows the viscoelastic behavior of arterial wall at ϕ = 3000 Kg/(m s^2), μ = 400 Kg/(m s), ζ = 10, η = 0.039 Pascal second at room temperature, z = 20mm, Re = 10, F_s = 1, ϵ = 0.4, β = 10, d = 50 nm, A_2 = 2, constriction ratio = 0.4, and constriction length = 0.74. The figure shows that the viscoelasticity first exhibits stronger damping to zero in the transient, and then oscillate sinusoidally and produces pulsation. This behavior continues with the increasing amplitude of wave from 0.1 to 0.4. However, the value of viscoelasticity decreases by increasing the amplitude of the wave from 0.1 to 0.4. Therefore, it appears that the amplitude of oscillations is an intrinsic characteristic of the wall and is greatly influenced by the fluid properties. Nevertheless, the presence of fluid stain and stain velocity allows for a larger value of the amplitude decrement in viscoelasticity of the artery wall.

6.6 Conclusion

In the present investigation, two - dimensional viscous boundary layer flow is analyzed through a symmetrical constricted permeable and viscoelastic tube. Numerical results for two - dimensional pulsatile blood flow due to stenosed artery are analyzed using a finite difference scheme. Additionally, the effect of amplitude of flow on the viscoelasticity of arterial wall is obtained graphically and behavior of various parameters such as Reynolds number, Forchheimer number, the pulsatile amplitude, the aspect ratio of particle, porosity, and viscoelasticity of artery are investigated. After investigation following conclusions can be drawn:

1. Smaller permeability decreases the flow, while by increasing permeability, pressure drops and wall shear stress are decreases and flow velocity increases.

2. The variation in the Reynolds number affects the flow pattern of air and particles both the directions, in (axial and radial).

3. We analyzed the effect of Forchheimer number and found that axial and radial velocity profiles decrease for both air and particles.

4. It is found that the overall air velocity significantly increases through alterations in particle aspect ratio, media porosity, Reynold number, and oscillatory amplitude.

5. Viscoelasticity is affected by the amplitude of pulsatile flow and for a large value of amplitude, viscoelasticity decreases.

6. Our investigation is helpful to understand the flow condition of the lung, affected by stenosis, emphysema, and cancer.

Table 6.1: Grid independency test for radial velocity profile at ϵ = 0.7, F_s = 1, Da = 0.01, and Re = 10.

	Grid points		
t	10x10x10^3	15x15x10^3	20x20x10^3
0	0.341	0.148	0.221
0.1	0.0142	0.0134	0.015
0.2	0.0134	0.0134	0.0134
0.3	0.0134	0.0134	0.0134
0.4	0.0134	0.0134	0.0134
0.5	0.0134	0.0134	0.0134
0.6	0.0134	0.0134	0.0134
0.7	0.0134	0.0133	0.0134
0.8	0.0134	0.0133	0.0134
0.9	0.0133	0.0131	0.0134

Table 6.2: Comparison of present result with (Saini et al. [194]) at $z = 20$ mm.

t	Saini et al. [194]	Present Result
0	0	0
0.1	0.631	0.626
0.2	1.03	1.03
0.3	1.32	1.31
0.4	1.55	1.54
0.5	1.76	1.75
0.6	1.94	1.93
0.7	2.11	2.11
0.8	2.27	2.26
0.9	2.42	2.41

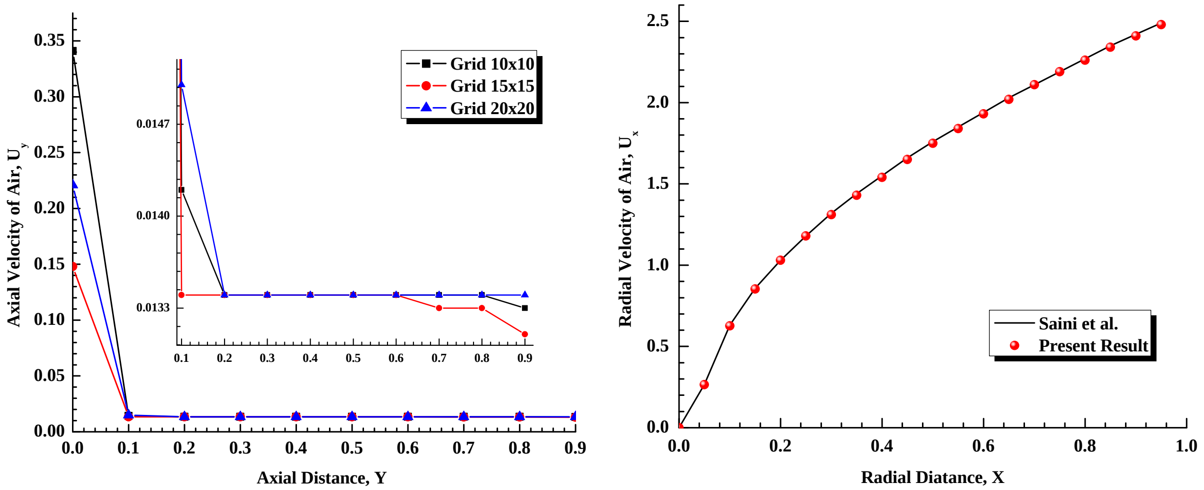

(a) (b)

Figure 6.1: (a) Axial velocity profile of particle through straight constricted tube at grid size 10x10x1000 to 20x20x1000 and (b) radial velocity profile at ϵ = 0.7, Da = 0.05, and Re = 10.

Table 6.3: Numerical values of variables used in computational analysis with their corresponding units

Abbreviation	Value	Abbreviation	Value
m	0.0002 Kg/l	d	50 nm
ρ	1.06 g/cm^3	N_0	0.02504*$10^6/cm3$
a_1	10 g/cm^2s^2	a_2	0.2*a_1
f	1.2 hz	ν	$1.71 * 10^{-5}m^2/s$
u_0	0.3 m/s	Re	10-250
F_s	1-15	Da	0.05-1
ϵ	0.4-0.9	β	3-1000
l_c	2*R_0	z	20 mm
R_0	370 μ m	λ	0.066 μm
ϕ	3000 Kg/(m s^2),	μ	400 Kg/(m s),
ζ	10 Kg/(m s),	η	0.039 Kg/(m s),

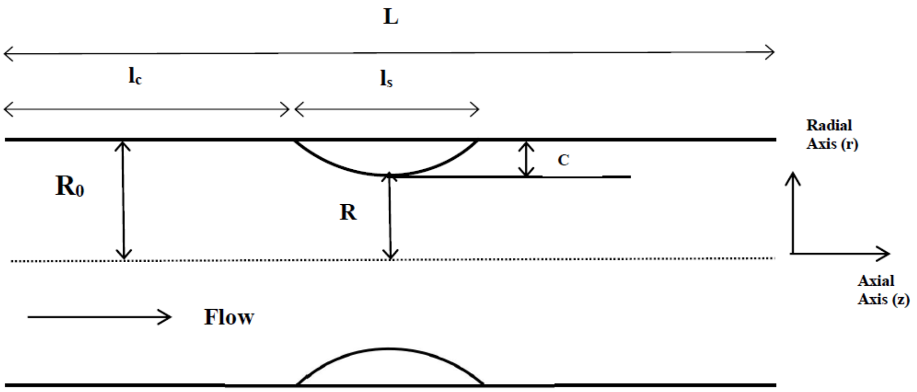

Figure 6.2: Physical model of the axi-symmetric stenosis affected artery.

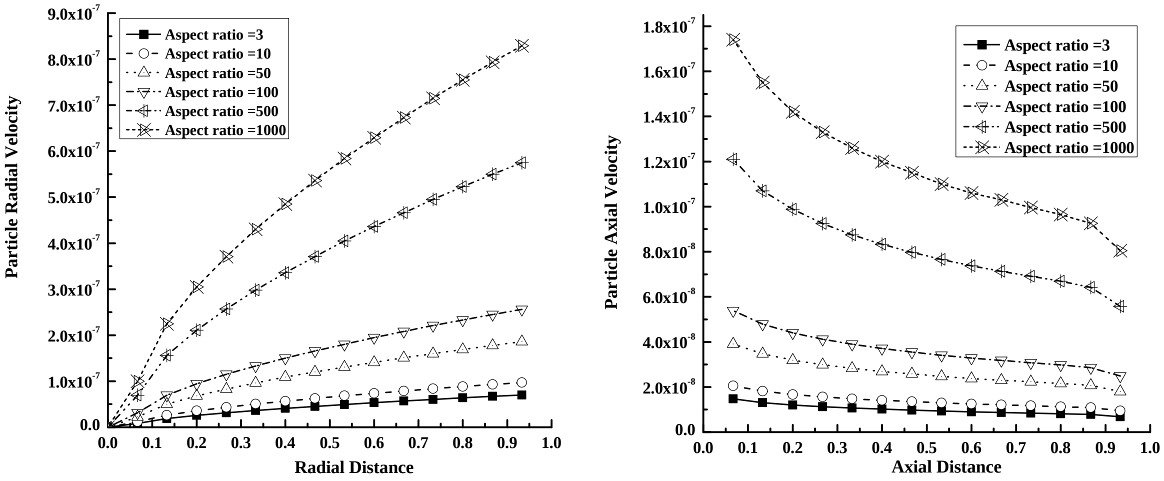

(a) (b)

Figure 6.3: (a) Radial velocity profile and (b) axial velocity profile of particle through straight constricted tube at ϵ = 0.7, F_s = 1, Da = 0.05, Re = 10, and β = 10 - 1000.

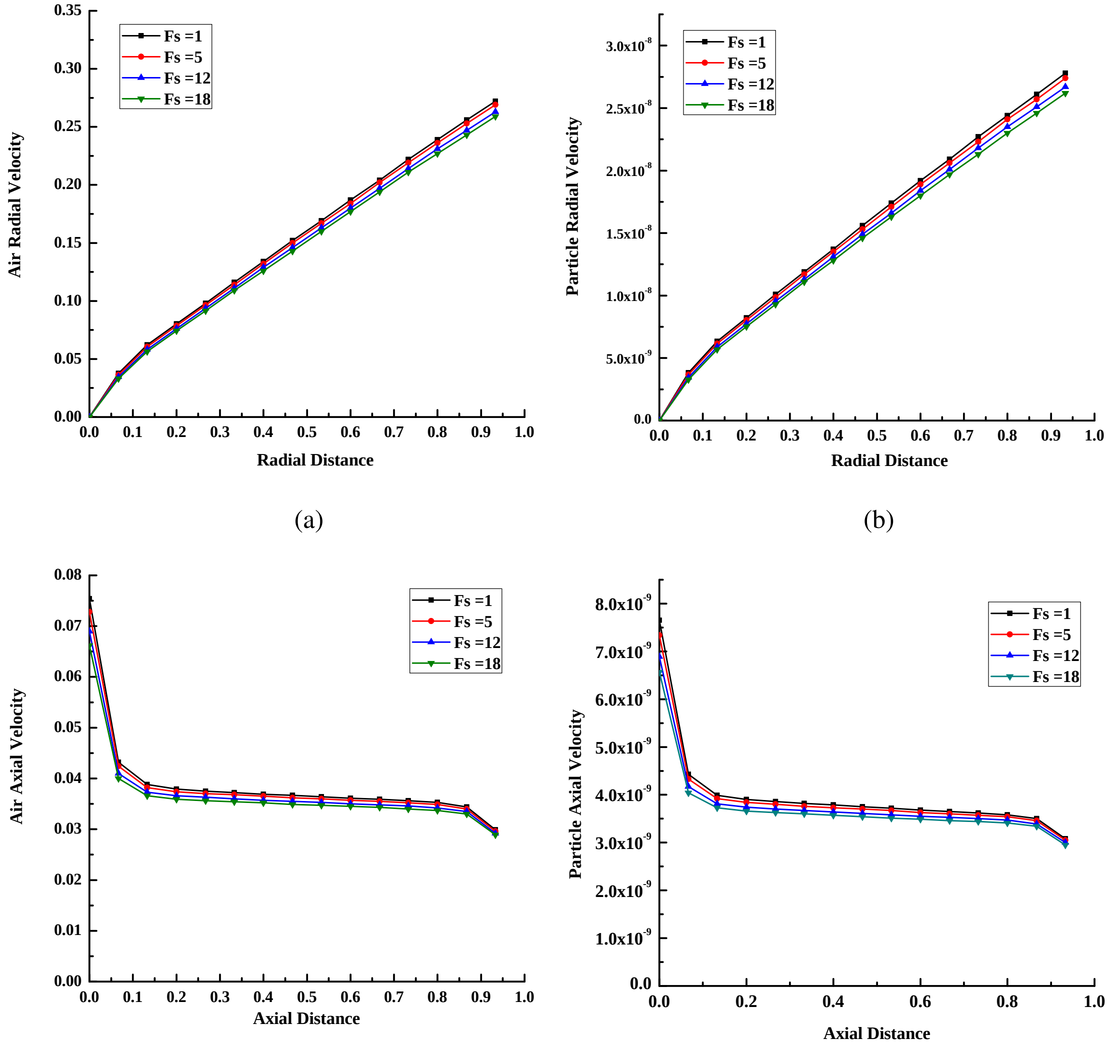

(a) (b)

(c) (d)

Figure 6.4: (a) &(b) Radial velocity profile, (c) & (d) axial velocity profile of air and particle respectively through straight constricted tube at ϵ = 0.7, Da = 0.05, Re = 10, β = 10, and F_s = 1 - 18.

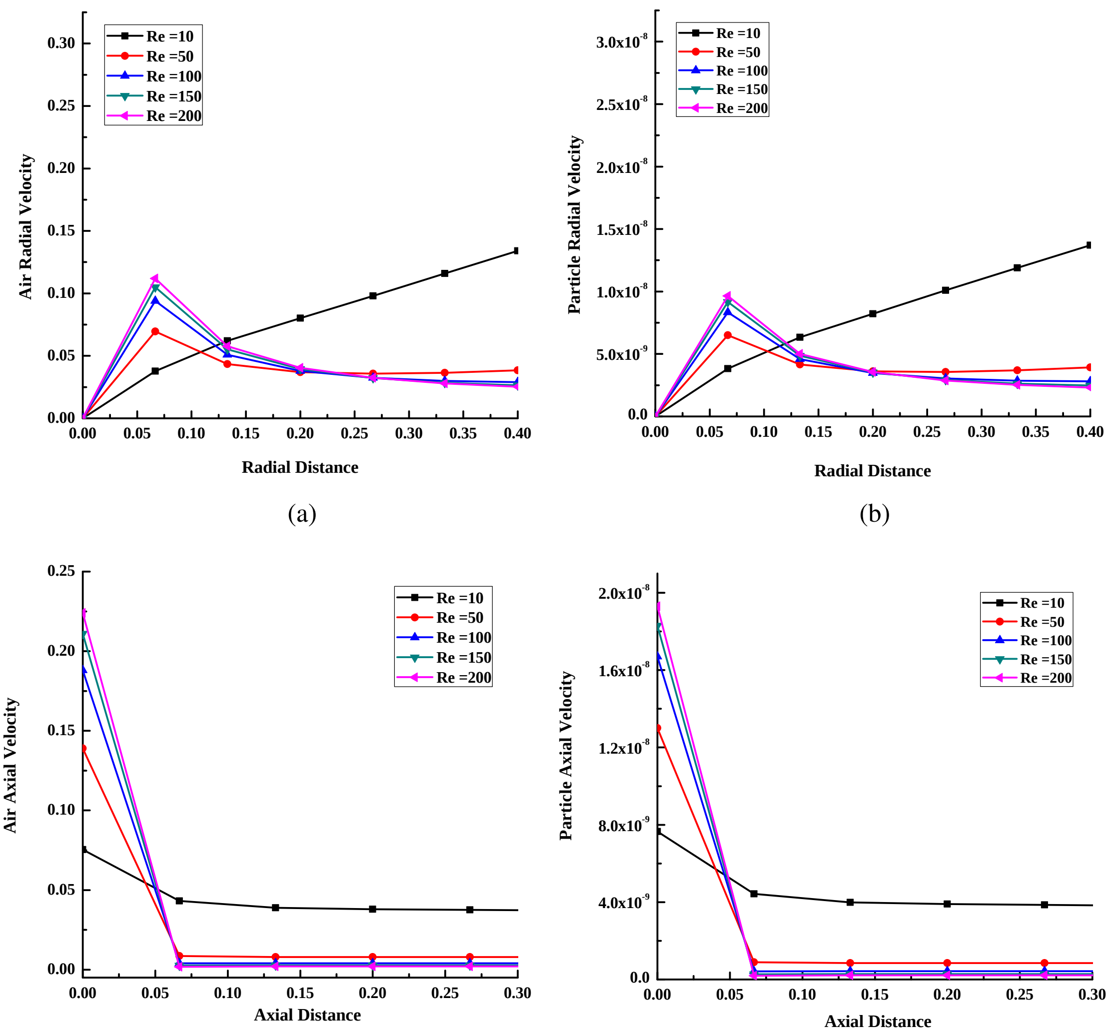

(a) (b)

(c) (d)

Figure 6.5: (a) &(b) Radial velocity profile, (c) & (d) axial velocity profile of air and particles respectively through straight constricted tube at ϵ = 0.7, Da = 0.05, β = 10, F_s = 1, and Re = 10 - 200.

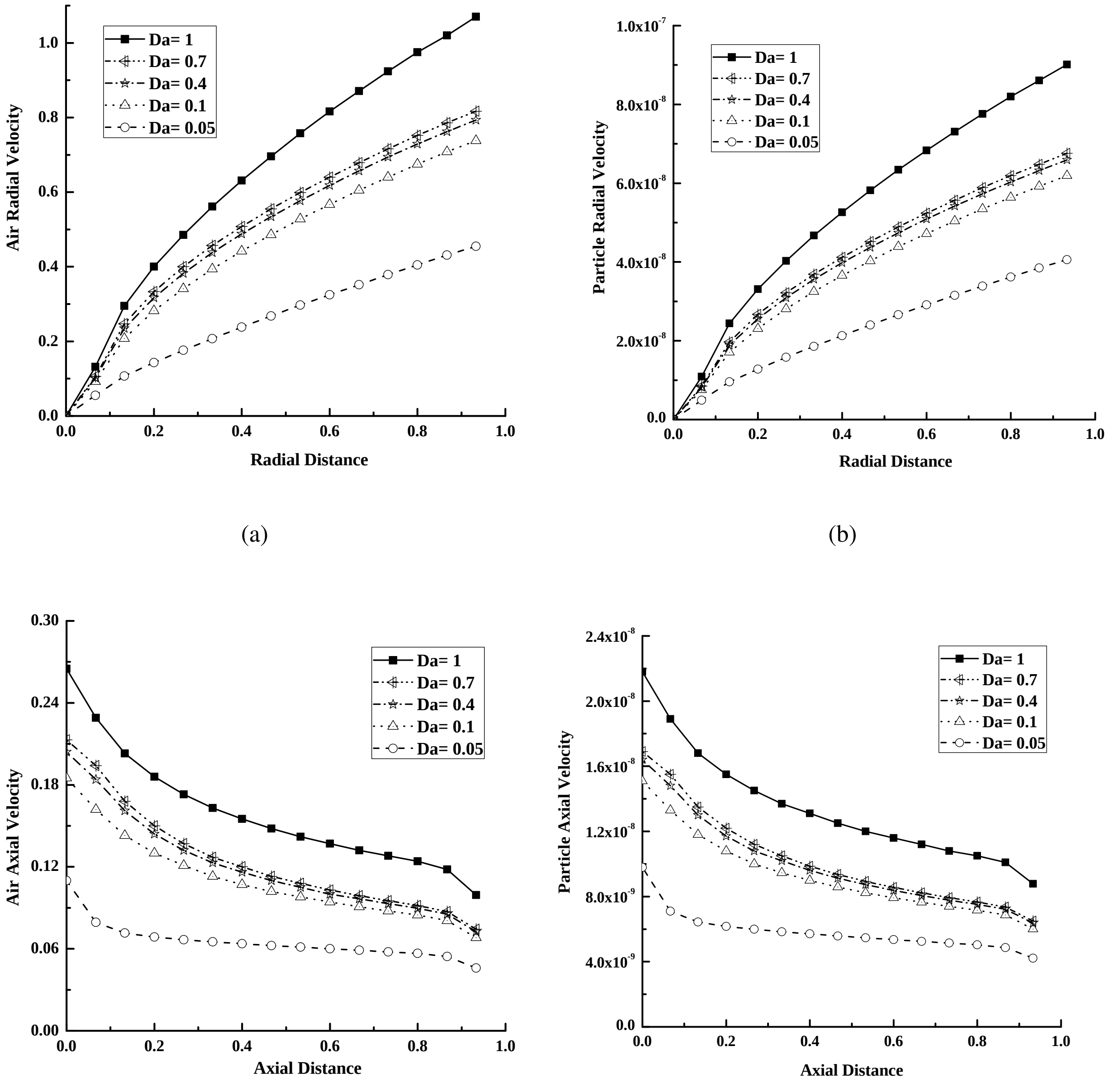

(a) (b)

(c) (d)

Figure 6.6: (a) &(b) Radial velocity profile, (c) & (d) axial velocity profile of air and particle respectively through straight constricted tube at ϵ = 0.7, β = 10, F_s = 1, Re = 10, and Da = 0.05 - 1.

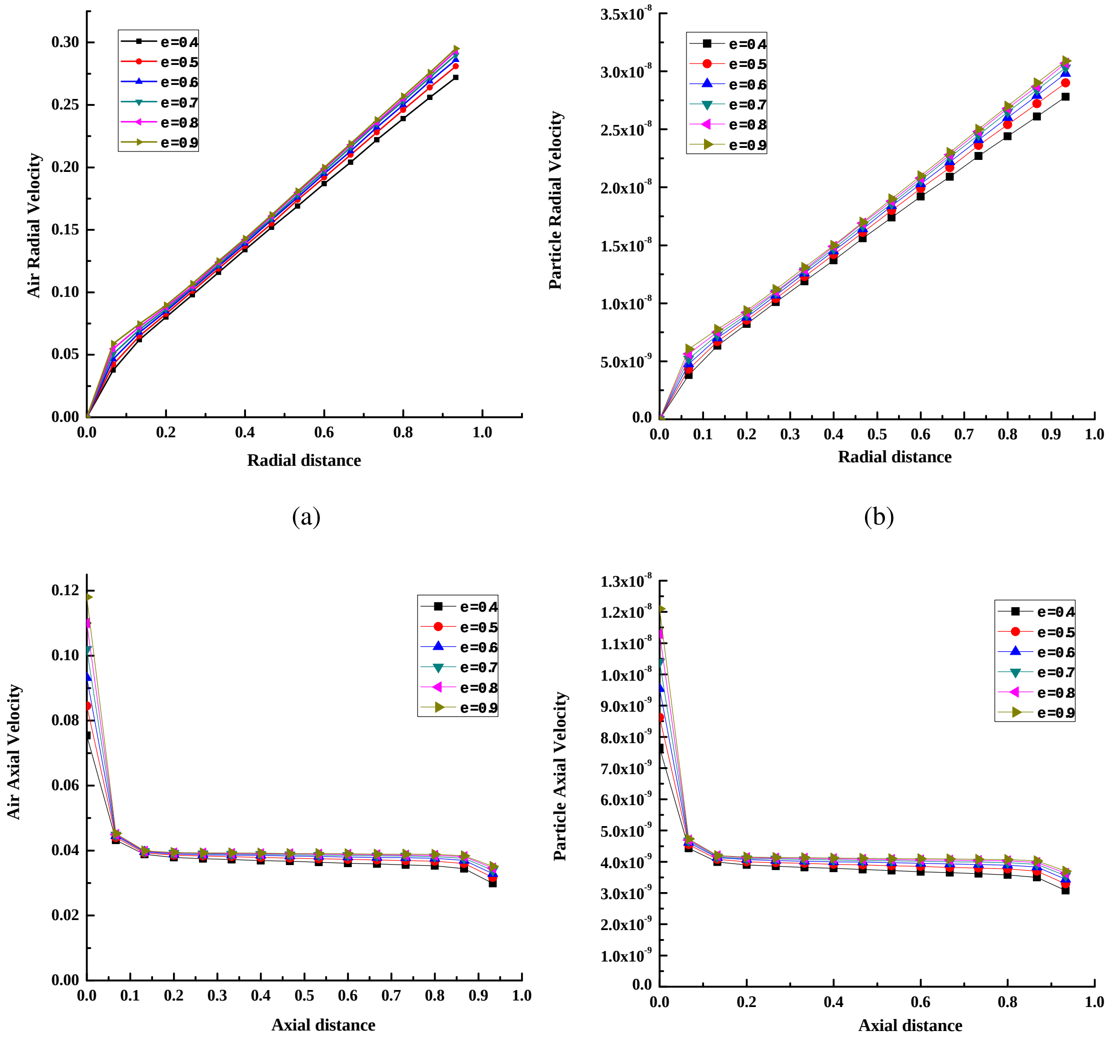

(a) (b)

(c) (d)

Figure 6.7: (a) &(b) Radial velocity profile, (c) & (d) axial velocity profile of air and particle respectively through straight constricted tube at β = 10, F_s = 1, Re = 10, Da = 0.05, and ϵ = 0.4 - 0.9.

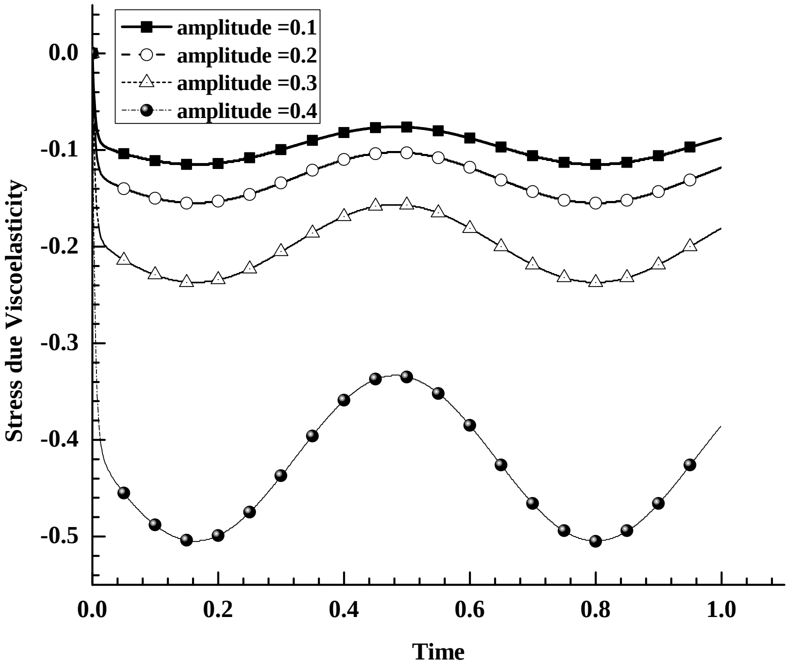

Figure 6.8: Effect of viscoelasticity at ϕ = 3000 Kg/(m s^2), μ = 400 Kg/(m s), ζ = 10 Kg/(m s), and η = 0.039 g/(cm s).

Chapter 7: Numerical study of the mucus clearance from human lung airways by using generalized couette flow

7.1 Introduction

Respiratory tract secretions consist of mucus [63], surfactant, and periciliary liquid. The mucus helps to humidify the passing inspired air and traps the dust particles, allergens, infectious agents, bacteria and other inhaled debris [137]. Once particles are deposited into the mucus layer, it is extremely necessary to flush out the mucus for airway integrity and pulmonary defense. Inside airways, there are tiny hairs, called cilia, which line the bronchi. Mucus is carried on the top of these cilia [63] and after capturing the aerocontaminers, mucus moves upward toward the oropharyngeal bifurcation with the motion the cilia [127]. This movement, against the force of gravity, is sometimes called mucus escalator. This event along with the continual movement of respiratory mucus layer toward the oropharynx, prevent small foreign objects from entering the lungs during breathing. However, to clear large particles and access of mucus of the respiratory system another mechanism such as coughing [109], high-frequency chest wall oscillation [61] and vibration, etc are used.

Particle deposition and hypersecretion of mucus cause many common illnesses, such as common cold, influenza, asthma, chronic bronchitis, and emphysema. Antibiotics treat infections and make a patient feel better but over the time damage builds again, therefore, effective mechanism to clear the pulmonary secretion and inhaled debris from the airways is needed.

There are some studies [26, 102, 199, 235] which are reported that tube wall oscillation may enhance displacement of mucus during coughing such as Singh et al. [211] presented an oscillatory flow of a viscous, incompressible fluid through a highly porous medium with periodic permeability and found that Jones [103] worked on studied isotope mucociliary clearance rates from cystic fibrosis subjects and found that the effective clearance occurred by increasing frequency of 10-15 Hz because at that frequency oscillatory flow was high. A study of the three-dimensional flow and heat transfer along with a flat plate by applying periodic suction is done by [68] and found that the components of the wall stress and the heat transfer depends on Prandtl number. A mathematical model is proposed by Manhas and Pardasani [144] on calcium oscillations in the pancreatic acinar cells and found that mitochondria uptakes calcium ion very fast to restrict calcium ion response on the pancreatic acinar cell.

However, the mechanics of clearance of mucus between two surfaces, one of which is moving tangentially relative to the other can be configured as two parallel plates, where the flow of fluid is driven by virtue of viscous drag force acting on the fluid by an applied pressure gradient in the flow direction. This kind of virtue is applicable in Couette flow models [84]. There are some studies related to Couette flow of such as Seth et al. [201] studied unsteady Couette flow of viscous incompressible electrically conducting fluid, in the presence of a transverse magnetic field, between two parallel porous plates, where fluid is flowing within the channel due to the impulsive and uniformly accelerated motion of the lower plate. Fang and Lee [58] worked on the transient incompressible Couette flow with and steady-state temperature profiles between two porous parallel plates for slightly rarefied gases and found that the slip parameters affect the temperature profiles and heat transfer greatly at the walls. Additionally, Verma et al. [242] carried out steady state fully developed flow of a viscous incompressible conducting fluid within a channel filled with a porous medium and bounded by two infinite walls and stated that injection has accelerating whereas suction has to retard effect on the flow. From the literature review, we found that there is no study done on lung airways by using phenomena of Couette flow.

To understand the mechanism of airway mucus clearance, where the inner walls of the long tube from the mouth to the alveoli are coated with a thin layer of mucus and flow of mucus is forced by the oscillation of both walls with sinusoidal pressure gradient. Two dimensional generalized Navier Stokes' equations are carried out to model the flow field and Newton second law of motion is used to study the movement of particles. Concept of generalized Couette flow is applicable to study the effect of media porosity together with a shape factor of nonspherical nanoparticles on flow dynamics of thin layer of mucus. Finite difference numerical scheme is used to solve the governing equations numerically and all the results are shown in the form of the graph after performing all the computational work on MATLAB. The present problem finds its application in clearance of mucus layer from lung airways.

7.2 Mathematical Formulation

7.2.1 Governing equations

The graphical model is shown in Figure 7.1, where we supposed, that the airways are subjected to oscillation due to periodic breathing or due to coughing and sinusoidal pressure gradient is applicable on both the boundary walls due to surrounding forces and porous media, which helps in the propulsion of mucus over the cilia. We consider the fluid as [1] incompressible, viscous, Newtonian; and flow is unsteady, laminar, fully-developed and along the axial direction of tube, while radial direction is perpendicular to the tube. In addition, cilia are assumed as a porous matrix which is covered by a thin layer of mucus. Fluid flow is modeled by the process of generalized unsteady Couette flow. Initially, there is no pressure gradient so we assumed that the velocities and stresses are zero at $t = 0$. The governing equations in polar coordinate system (r, z, θ) are given below:

Equation of continuity for air,

$$\nabla.u = 0, \tag{7.1}$$

equation of continuity for particle,

$$\nabla.v = 0, \tag{7.2}$$

equation of momentum in parallel (axial) direction for air,

$$\begin{aligned}\frac{\partial u_r}{\partial t} + \frac{u_r}{\epsilon}\frac{\partial u_r}{\partial r} + \frac{u_z}{\epsilon}\frac{\partial u_r}{\partial z} &= -\frac{\epsilon}{\rho}\frac{\partial p}{\partial r} + \nu\left(\frac{\partial^2 u_r}{\partial r^2} + \frac{1}{r}\frac{\partial u_r}{\partial r} + \frac{\partial^2 u_r}{\partial z^2}\right)\\ &+ \left(-\frac{\epsilon\nu}{K}u_r + s_k\frac{N_0}{\rho}(v_r - u_r) - \frac{\epsilon b}{K}u_r^2\right) + g_r\left(\frac{N_0 - \rho}{N_0}\right),\end{aligned} \tag{7.3}$$

equation of momentum in perpendicular (radial) direction for air,

$$\begin{aligned}\frac{\partial u_z}{\partial t} + \frac{u_r}{\epsilon}\frac{\partial u_z}{\partial r} + \frac{u_z}{\epsilon}\frac{\partial u_z}{\partial z} &= -\frac{\epsilon}{\rho}\frac{\partial p}{\partial z} + \nu\left(\frac{\partial^2 u_z}{\partial r^2} + \frac{1}{r}\frac{\partial u_z}{\partial r} + \frac{\partial^2 u_z}{\partial z^2}\right)\\ &+ \left(-\frac{\epsilon\nu}{K}u_z + s_k\frac{N_0}{\rho}(v_z - u_z) - \frac{\epsilon b}{K}u_z^2\right) + g_z\left(\frac{N_0 - \rho}{N_0}\right),\end{aligned} \tag{7.4}$$

the equation of motion for particle movement:

In axial direction,

$$m\left(\frac{\partial v_z}{\partial t} + v_z\frac{\partial v_z}{\partial z} + v_r\frac{\partial v_z}{\partial r}\right) = F_d, \tag{7.5}$$

---

[1] combines thin layer of mucus and nanoparticles

In radial direction,

$$m\left(\frac{\partial v_r}{\partial t}+v_z\frac{\partial v_r}{\partial z}+v_r\frac{\partial v_r}{\partial r}\right)=F_{d_1}. \tag{7.6}$$

The first term in the left hand side of the equations 7.3 - 7.4 is for unsteady flow and the second-third terms are for convection. First, second, third, and forth terms in the right hand side of equations 7.3 - 7.4 are the pressure gradient, diffusion, the entire body force because of the existence of non - Darcian effect and additional gravitational force fields respectively. The term in the left hand side of equations 7.5 - 7.6 represents the product of the mass times the acceleration and right hand side of this equation represents the drag force on the nanoparticles.

In equation 7.3 - 7.4, ϵ denotes the variable porosity of media and defined as [107] follows:

$$\epsilon=1-\frac{N_0 d_p^2}{(d_0^2-d_i^2)}, \tag{7.7}$$

and other variables, K, S_f, s_k, F_d, and F_{d_1}, from equation 7.3 - 7.6, have similar descriptions as defined in Chapter 5 [2].

7.2.2 Assumptions for Couette flow

To solve the governing equation by using generalized Couette flow we assumed following points:

1. For fully developed flow,

$$\frac{\partial u}{\partial r}=0, \tag{7.8}$$

2. For unsteady generalized couette flow,

$$\left.\begin{matrix}\frac{\partial}{\partial t}\\ u_r\\ v_r\\ \frac{\partial p}{\partial r}\end{matrix}\right\}\neq 0, \tag{7.9}$$

$$\left.\begin{matrix}u_z\\ v_z\end{matrix}\right\}=0. \tag{7.10}$$

---

[2] Section 5.2 and equation 5.9 - 5.10

7.2.3 Initial and boundary conditions

To solve the above defined equations following initial and boundary conditions are used:

1. Initial conditions at $t = 0$,

$$\left.\begin{array}{l} u_r \\ v_r \\ u_z \\ v_z \end{array}\right\} = 0, \tag{7.11}$$

2. Boundary conditions at $t > 0$,

   (a) Oscillation of top wall, when $r = a$:

$$u_r = \frac{u_0 \nu}{a}(1 + cos(2\pi f t)), \tag{7.12}$$

   (b) Oscillation of bottom wall, when $r = -a$:

$$u_r = \frac{u_0 \nu}{a}(1 + cos(2\pi f t)), \tag{7.13}$$

7.3 Methodology

7.3.1 Transformation of the governing equations

To solve the governing equations 7.1 - 7.6 numerically we have to make them dimensionless, so we used following quantities:

$$R^* = \frac{r}{a}, Z^* = \frac{z}{a}, P^* = \frac{pa^2}{\rho\nu^2}, \tau^* = \frac{t\nu}{a^2}, U^* = \frac{ua}{\nu},$$
$$V^* = \frac{va}{\nu}, F_s = \frac{b}{a}, P_l = \frac{N_0}{\rho}, Da = \frac{K}{a^2}, S_k = \frac{ka^2}{\nu},$$

By using above quantities together with our assumptions we got dimensionless equations, which are written after dropping the stars as follows:

$$\frac{\partial U_r}{\partial R} = 0, \tag{7.14}$$

$$\frac{\partial V_r}{\partial R} = 0, \tag{7.15}$$

$$\frac{\partial U_r}{\partial \tau} = -\epsilon \frac{\partial P}{\partial R} + \frac{\partial^2 U_r}{\partial Z^2} + S_k P_l \left(V_r - U_r \right) - \frac{\epsilon U_r}{Da} - \epsilon \frac{F_s}{Da} U_r^2, \tag{7.16}$$

$$\frac{\partial P}{\partial Z} = \frac{1}{\epsilon} \frac{a^3}{\nu^2} g_z \left(\frac{N_0 - \rho}{N_0} \right), \tag{7.17}$$

$$\frac{\partial V_r}{\partial t} = S_f S_k \frac{(U_r - V_r)}{m}, \tag{7.18}$$

$$U_r = V_r. \tag{7.19}$$

Transformed initial and boundary conditions from equation 7.11 - 7.13 are as:

1. Initial conditions at $\tau = 0$,

$$\left. \begin{matrix} U_r \\ V_r \\ U_z \\ V_z \end{matrix} \right\} = 0, \tag{7.20}$$

2. Boundary conditions at $\tau > 0$,
   (a) Oscillation of top wall, when $R = 1$:

$$U_r = u_0(1 + cos(2\pi f \tau)), \tag{7.21}$$

   (b) Oscillation of bottom wall, when $R = -1$:

$$U_r = u_0(1 + cos(2\pi f \tau)), \tag{7.22}$$

where u_0 is initial velocity.

The pressure gradient in equation 7.3 have following formulation,

$$-\frac{\partial P}{\partial R} = a_0 \sin \omega \tau, \quad \omega = 2\pi f, \tag{7.23}$$

7.4 Numerical Scheme

To solve the non - dimensional equations 7.14 - 7.19 subject to two point boundary conditions (equation 7.20 - 7.22) we used finite difference numerical technique [214], which is the most suitable method for nonlinear problems related to regular geometries. The computational grids used in a similar way as we defined in Chapter 6 [3], for both numerical computation and to tackle the nonlinearity of particle differential equations. So, the discretized form of the equations 7.14 - 7.19 are found as follows:

$$U_{i+1,j} = U_{i-1,j}, \tag{7.24}$$

$$V_{i+1,j} = V_{i-1,j}, \tag{7.25}$$

$$\begin{aligned}(U_r)^{k+1}_{i,j} &= -\epsilon\frac{\partial P}{\partial R}\Delta\tau + (U_r)^k_{i,j}\left[1 - 2\frac{\partial\tau}{\partial Z^2} - S_k P_l\Delta\tau - \frac{\epsilon}{Da}\Delta\tau\right] \\ &+ \frac{\Delta\tau}{\Delta Z^2}\left[(U_r)^K_{i,j+1} + (U_r)^k_{i,j-1}\right] + S_k.P_l(V_r)^k_{i,j}\Delta\tau - \frac{\epsilon F_s}{Da}((U_r)^2{}_{i,j-1})^k\Delta\tau,\end{aligned} \tag{7.26}$$

$$P_{i,j+1} = \frac{a^3}{\epsilon\nu^2}g_z\left[1 - P_l\right]\Delta z + P_{i,j-1}, \tag{7.27}$$

$$(v_r)^{k+1}_{i,j} = (v_r)_{i,j}\left[1 - \frac{S_f S_k}{m}\Delta t\right] + \frac{S_f S_k}{m}(u_r)_{i,j}\Delta\tau, \tag{7.28}$$

$$(u_r)_{i,j} = (v_r)_{i,j}, \tag{7.29}$$

The initial and boundary conditions from equation 7.20-7.22 in the discretized form are defined as follows:

$$\begin{aligned}&(U_r)\,^1_{i,j} = 0, \quad (U_z)\,^1_{i,j} = 0, \quad (V_r)\,^1_{i,j} = 0, \quad (V_z)\,^1_{i,j} = 0, \\ &(U_r)\,^k_{0,j} = u_0(1 + cos(2\pi f k * \tau)), \quad (U_r)\,^k_{N+1,j} = u_0(1 + cos(2\pi f k * \tau))\end{aligned} \tag{7.30}$$

Equations 7.24 - 7.29 gives the velocity profile at the $(k+1)^{th}$ time level in terms of velocity profile at k^{th} time level.

---

[3] Section 5.4

7.5 Results and Discussion

In this section we illustrated the influence of different values of aspect ratio of particle, porosity of media, frequency of oscillation graphically on velocity and pressure gradient by using following numerical values [197, 245].

$$\nu = 1.71 * 10^{-5} m^2/s, S_f = 1.54, \epsilon = 0.6, r = 0.5\mu m, m = 2 * 10^{-4} Kg/l,$$
$$d = 50nm, f_p \leq 1.2hz, F_s = 1, \rho = 1.145, N_0 = 2.504 * 10^{10}, a_2 = 0.25 Kg/m^2 s^2,$$
$$\beta = 10 - 1000, \epsilon = 0.6 - 1, f = 0.2 - 1.2,$$

In order to validate the computed numerical solutions and check the predictive accuracy of the model first, we did the mesh dependency test for various grid sizes, i.e. 10x10, 15x15, 20x20, 30x30, and 40x40, in the axial and radial directions to figure out the flow field, and we found that the results remain consistent when the grid size is set to 20x20 and above. So, we chose $\Delta t = 0.001$, $\Delta r = 0.05$, and $\Delta z = 0.05$ respectively throughout the study by using following stability criteria at each time level so that less error occurred in the numerical computation

$$\max\left(\frac{\Delta\tau}{\Delta R^2}\right) \leq 0.5,$$
$$\max\left(\frac{\Delta\tau}{\Delta Z^2}\right) \leq 0.5. \tag{7.31}$$

and then we performed comparison between output data produced by the present model (after removing the last term, media porosity and its respective terms) with published result [194] for radial velocity profile at ϵ = 0.7, F_s = 1, Da = 0.01, and Re = 10.

Saini et al. [194] studied two-dimensional natural convection flow of dusty fluid through an axisymmetric constricted tube. Comparison is shown in Figure 7.2 and Table 7.1. We found that our result is compatible to their result up to 99.9%. So, we can say, our results are in excellent agreement with the published result (Saini et al. [194]).

7.5.1 Effect of porosity (ϵ) on the clearance of mucus

Figure 7.3(a) - 7.3(b) depicted the behavior of transient velocity of air and particle for different value of porosity (0.6$\leq \epsilon \leq$1) at β = 10, F_s = 1, and f = 1.2 with respect to time. It can be seen from Figure 7.3(a) that velocity of air is very low at ϵ = 0.6 and it increases when we increase ϵ from 0.6 to 1.0 and attain its maximum value at ϵ = 1. Additionally, velocity of particle is also increased (as shown in Figure 7.3(b)) with the increment in ϵ from 0.6 to 1 with respect to time and attain its maximum value at ϵ = 1. Due to oscillation velocity of air, along with wall increases with the increment in ϵ and as we go far from wall, velocity values reaches its steady state values after $t = 1$. From these figures, we found that both velocities (for air, and particles) are affected by the increment in ϵ and it is interesting to observe that up to a particular time velocity of air increases and the time required to attain a steady state is unbiased on the value of porosity.

Also, it can be correlated physically, as the void size of porous media increases breathing capacity increases, which cause an increment in air velocity in either case, free flow allowed rise within the velocity of the fluid, which give propulsion and useful to clear thin layer of mucus.

7.5.2 Effect of aspect ratio (β) on particle deposition

Figure 7.4(a) - 7.4(b) show the effect of velocity at different level of aspect ratio (10$\leq \beta \leq$1000) at ϵ = 0.60, F_s = 1 and f = 1.2 with respect to time. It is evident in Figure 7.4(a) that velocity of air is low at β = 1000 and it increases when we decrease aspect ratio of particle β from 1000 to 10. While in Figure 7.4(b), velocity of particle increases with the increment in β from 10 to 1000 with respect to time monotonically. Physiologically, we can say that particles are oriented along the air and flow along with air stream in downward direction with time spherical particles and low aspect ratio particles are deposited in former airways while particles with high aspect ratio have tendency to go deep inside the lung airways with the air stream and affect the viscosity of airflow.

7.5.3 Effect of frequency (f) on wall oscillation and fluid velocity

In Figure 7.5(a) - 7.5(b), we found the effect of frequency ($0.2 \leq f \leq 1.2$) on velocity on air and particle at ϵ = 0.60, F_s = 1, and β = 10 with respect to time. From these figures we noticed that the magnitude of the fluid velocity between airway walls depends on the frequency of oscillation ($0.2 \leq f \leq 1.2$). In Figure 7.5(a), we observed that due to the increment in frequency from 0.2 to 1.2 velocity of air increases before $t = 0.1$ and after that it becomes steady. Also, from Figure 7.5(b), it is observed that the velocity of particle increases gradually as frequency increases from 0.2 to 1.2 and attain its maximum value at $f = 1.2$. We presented the numerical values obtained after computation in Table 7.2, which depicts the transient velocity for air and particle via time for different value of wall frequencies.

7.5.4 Effect of porosity (ϵ) on air pressure

The effect of wall porosity ($0.6 \leq \epsilon \leq 1$) on air pressure (P) is shown in Figure 7.6 with respect to time at β = 10, F_s = 1, and f = 1.2. From this figure we noticed that for all the cases, the air pressure increases by decreasing ϵ = 1.0 to 0.6 monotonically, because for low porosity pressure gradient is very high, which is responsible to remove thin mucus layer from airways and may improve the function of lung. Increase level of pressure can often be visible on the whole length of the wall. We can see the numerical values obtained after numerical computation in Table 7.3. In this table pressure variation for different values of porosity (ϵ) is shown with respect to time.

7.5.5 Comparison between air velocity obtained through oscillatory walls and non-oscillatory walls

Lung is one of the main organ in respiration and its airway walls are oscillate periodically during breathing. Thus, we used a time dependent function to the show the oscillation of walls. Each wall oscillates to and fro along its axis. The effect of wall oscillation on air velocity is depicted in Figure 7.7 with respect to time at $\beta = 10$, $F_s = 1$, $f = 1.2$, and $\epsilon = 0.60$. In this figure, the velocity of air is largely affected when walls are oscillating as compared to when walls are not oscillating along their own axis. In addition, we found that the steady state of the air velocity is attained much earlier with non-oscillatory walls than oscillatory walls.

7.6 Conclusion

The key findings of the present analysis are listed below.

1. It is observed that for high porosity ($\epsilon = 1$) fluidity along the airway walls increased, which is helpful to move the thin layer of mucus.
2. For small aspect ratio ($\beta = 10$) particles are deposited in former airways, while for high aspect ratio ($\beta = 1000$) particles have tendency to go lower lung generations with air stream.
3. Velocity of viscous fluid is proportional to the breathing frequency or oscillation of airway walls.
4. For all the cases, the air pressure increases by decreasing media porosity ϵ from 1 to 0.6 monotonically, which is responsible to remove mucus from airways and may improve lung function.
5. Comparison of oscillatory wall to nonoscillatory wall show that high frequency breathing can be applicable in the clearance of mucus.

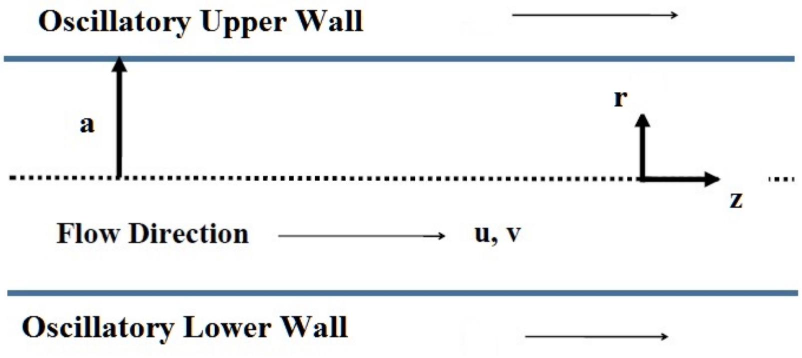

Figure 7.1: Schematic diagram for oscillatory walls applicable to clear thin layer of mucus.

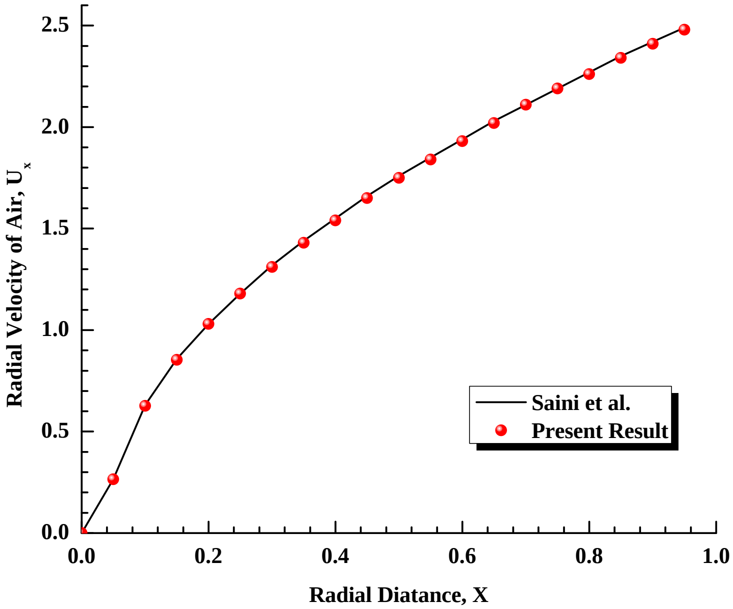

Figure 7.2: Radial velocity profile at ϵ = 0.7, F_s = 1, Da = 0.05, and Re = 10.

Table 7.1: Comparison between present and published result (Saini et al. [194]) at $z = 20$ mm.

time	Saini et al. [194]	Present Result
0	0	0
0.1	0.631	0.626
0.2	1.03	1.03
0.3	1.32	1.31
0.4	1.55	1.54
0.5	1.76	1.75
0.6	1.94	1.93
0.7	2.11	2.11
0.8	2.27	2.26
0.9	2.42	2.41

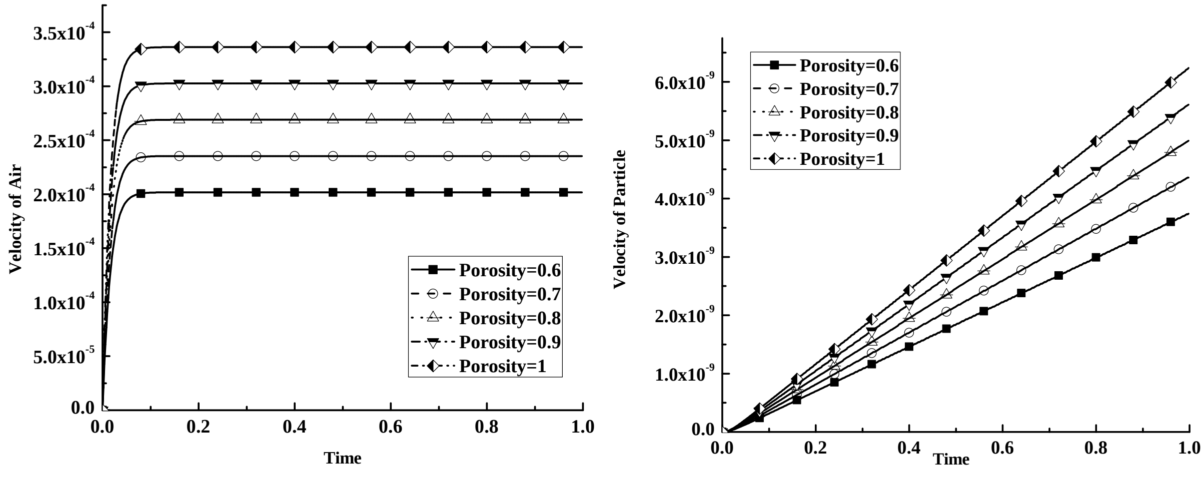

(a) (b)

Figure 7.3: Variation in (a) air velocity (u), and (b) particle velocity (v), with respect to porosity $(0.6 \leq \epsilon \leq 1)$.

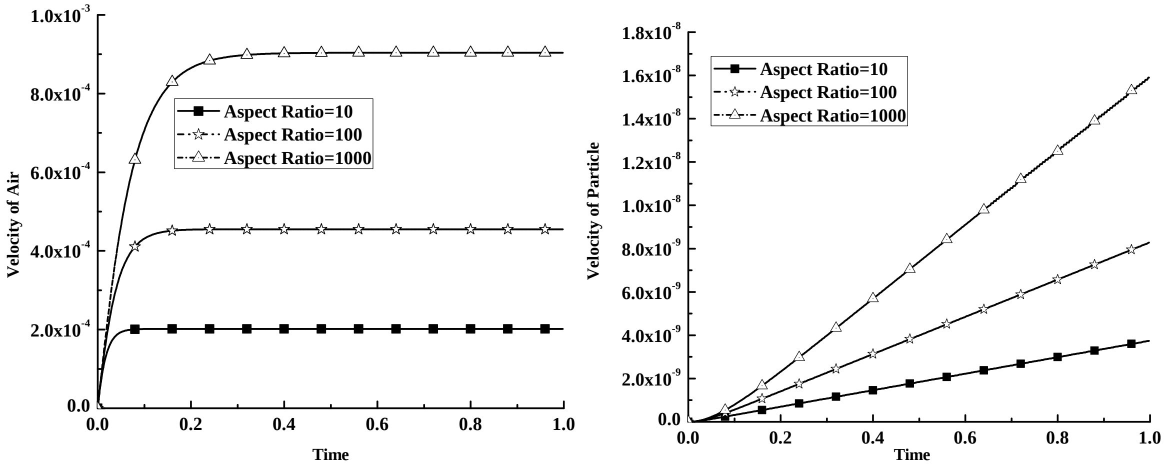

(a) (b)

Figure 7.4: Variation in (a) air velocity and (b) particle velocity with respect to aspect ratio ($10 \leq \beta \leq 1000$).

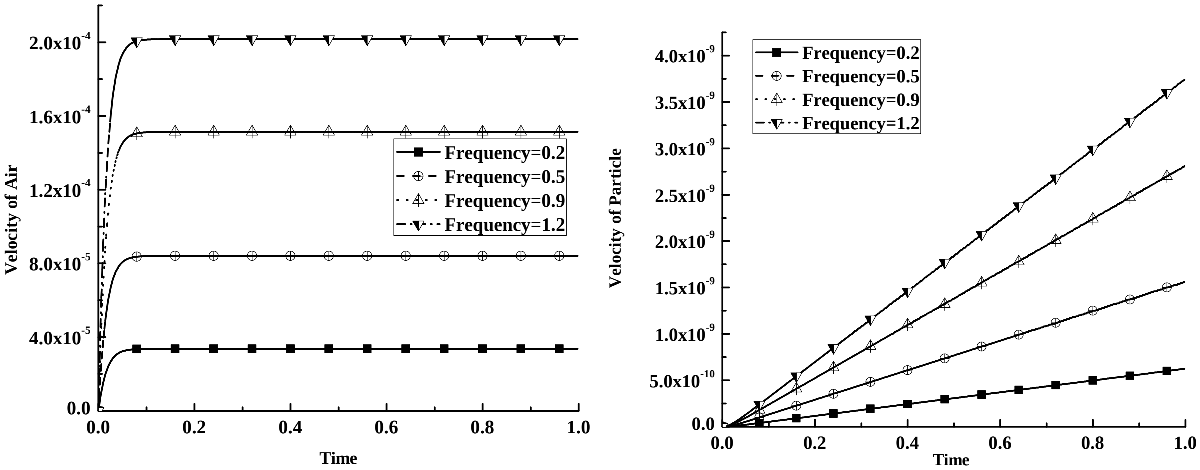

(a) (b)

Figure 7.5: Variation in (a) air velocity and (b) particle velocity with respect to frequency ($0.2 \leq f \leq 1.2$).

Table 7.2: Variation in velocities (air U, particle V)via time (t) for different values of wall frequency (f).

	f=0.2		f=0.5		f=0.9		f=1.2	
t	$U(10^{-5})$	$V\ (10^{-9})$	$U(10^{-5})$	$V\ (10^{-9})$	$U(10^{-4})$	$V\ (10^{-9})$	$U(10^{-4})$	$V(10^{-9})$
0.1	3.97423	0.626448	9.93324	0.156576	1.78686	0.281661	2.38078	0.375287
0.2	3.97930	0.137860	9.94590	0.344570	1.78913	0.619838	2.38382	0.825869
0.3	3.97931	0.213091	9.94593	0.532602	1.78914	0.958082	2.38383	0.127654
0.4	3.97932	0.288322	9.94595	0.720634	1.78914	0.129633	2.38383	0.172721
0.5	3.97933	0.363552	9.94597	0.908666	1.78915	0.163457	2.38384	0.217789
0.6	3.97933	4.38783	9.94598	1.09670	1.78915	1.97282	2.38384	2.62856
0.7	3.97934	5.14013	9.94600	1.28473	1.78915	2.31106	2.38384	3.07923
0.8	3.97935	5.89244	9.94602	1.47276	1.78915	2.64930	2.38385	3.52990
0.9	3.97935	6.64474	9.94603	1.66079	1.78916	2.98755	2.38385	3.98058
0.998	3.97936	7.38200	9.94605	1.84507	1.78916	3.31903	2.38386	4.42223

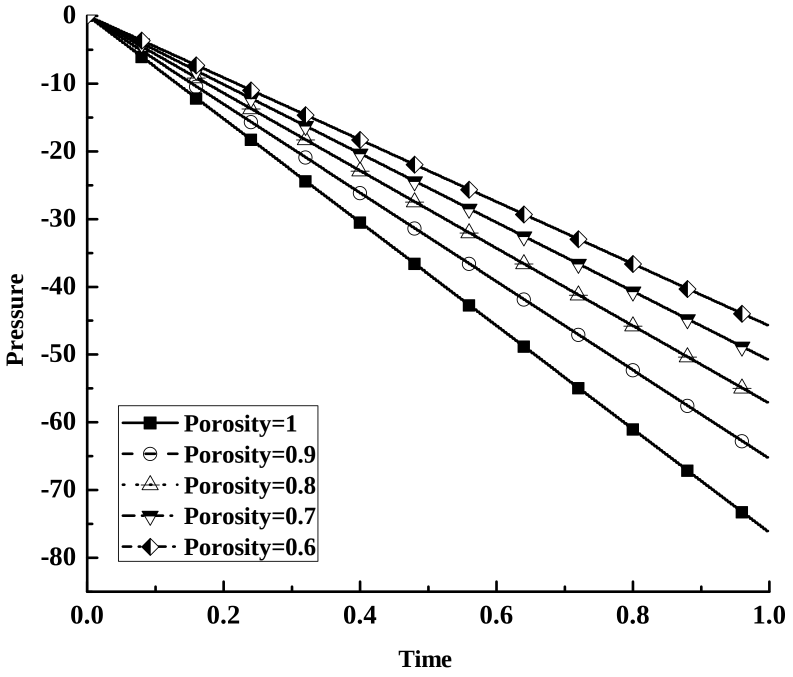

Figure 7.6: Effect of porosity ($0.6 \leq \epsilon \leq 1$) on air pressure.

Table 7.3: Variation in pressure via time for different values of wall porosity (ϵ).

	Value of Pressure				
time	ϵ=0.6	ϵ=0.7	ϵ=0.8	ϵ=0.9	ϵ=1
0.1	-7.6346909	-6.5440208	-5.7260182	-5.0897939	-4.5808145
0.2	15.269382	-13.088042	-11.452036	-10.179588	-9.1616291
0.3	-22.904073	-19.632062	-17.178055	-15.269382	-13.742444
0.4	-30.538764	-26.176083	-22.904073	-20.359176	-18.323258
0.5	-38.173455	-32.720104	-28.630091	-25.44897	-22.904073
0.6	-45.808145	-39.264125	-34.356109	-30.538764	-27.484887
0.7	-53.442836	-45.808145	-40.082127	-35.628558	-32.065702
0.8	-61.077527	-52.352166	-45.808145	-40.718352	-36.646516
0.9	-68.712218	-58.896187	-51.534164	-45.808145	-41.227331
0.998	-76.041522	-65.178447	-57.031141	-50.694348	-45.624913

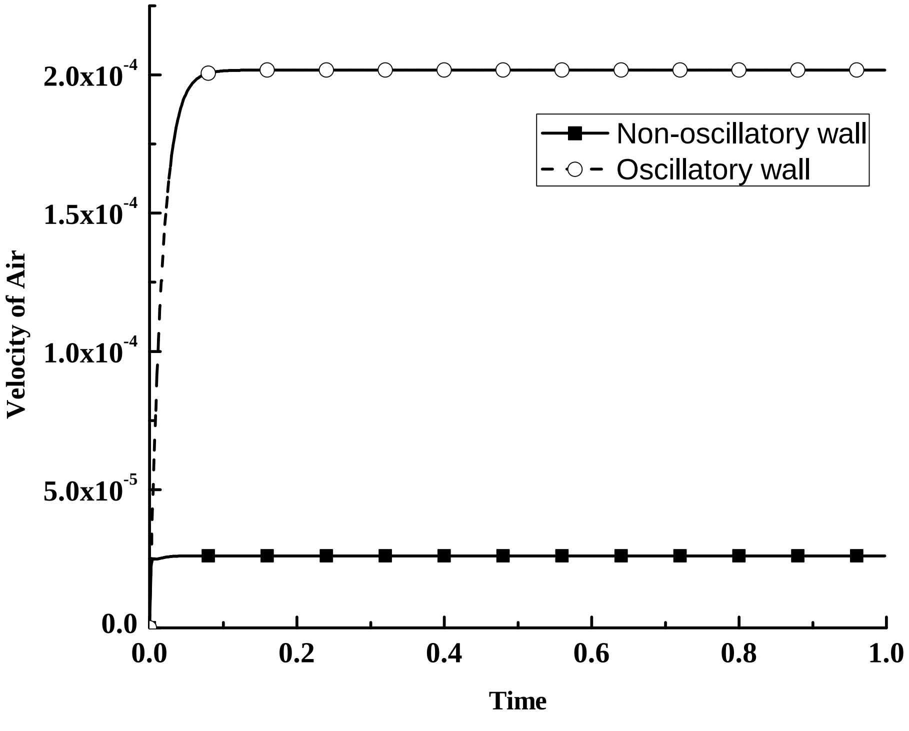

Figure 7.7: Comparison of air velocity between oscillatory walls and non-oscillatory walls at ϵ = 0.6, and β = 10.

Chapter 8: Effect of first order chemical reactions on the dispersion coefficient associated with laminar flow through fibrosis affected lung

8.1 Introduction

Human arteries, terminal airways, alveolar and pulmonary capillaries are thin tubes with small bores, through which dispersion of oxygen and other gases (carbon dioxide, nitrogen, etc.) occurs via a bridge known as a gas-blood barrier, lies between alveolar capillary and pulmonary capillary. These barrier are very thin through which absorption of the material from mobile phase (gas or blood) to immobile phase (tissue) be enriched, but some diseases such as chronic obstructive pulmonary disease, interstitial pulmonary diseases, edema, fibrosis, and lung surgeries distort the structure of capillary walls, which cause malfunction through gas-blood barriers. Among other diseases, fibrosis, an interstitial lung disease, is a physiological condition subjected to excessive production and accumulation of collagen, which makes the tissue of gas-blood barrier harder and affects the process of gas exchange [17].

In the gas exchange process, mass transport and reaction processes are more popular but the process of diffusion becomes more difficult when fluid is chemically reactive. In the human body, there are many reaction processes, which have broadly been attributed to biological or physiological transport [39, 168] such as phase exchange, partitioning, boundary uptake, the process of oxygen binding to hemoglobin [230], energy uptake by cells. These reaction process may occur in the bulk flow or at the boundary and may be reversible or irreversible, linear or nonlinear in nature of the fluid.

In 1953, Sir Geoffrey Taylor [232] studied the dispersion of fluid in a constricted long straight tube with a steady motion. Aris [8] include a method of moments and solved the equations partially for integral moments of the cloud of contaminant by using Taylor's explanation for the coefficient of dispersion. Later, there were various studies which used Taylor's long-time dispersion phenomena and various hypotheses. Chatwin [29] assumed that Taylor dispersion is eventually a Gaussian function of distance along the pipe axis and derived an asymptotic series based on the assumption that the diffusion of solute obeys Fick's law. Barton [12] modified Aris method of moments at short and moderate times for those parallel flows for which an associated eigenvalue problem has a discrete spectrum of eigenvalues. Purnama [176] applied Taylor dispersion of contaminant in association with reactions and retention at the boundaries, where mass is linearly related to the concentration and obtained that for homogeneous reaction effective Taylor diffusion coefficient reciprocally linked with the reaction rate constant.

When the dispersion has been developing only for a time scale that is shorter than or comparable to the diffusion time scale across the tube section then it is known as short-time dispersion. A number of studies focused their attention on short time dispersion and linear reversible or irreversible reactions at the boundary wall [74, 216]. Such as Davidson and Schroter [39] have used reversible phase exchange while Jiang and Grotberg [102] considered irreversible phase exchange, to deal with the problem of gas flow between the lumen and stationary bronchial wall tissue. A computational model has been developed by combining immunotherapy, radiation therapy, and estrogen inhibition to treat breast cancer using eight nonlinear reaction-diffusion equations and was solved numerically by [45] perturbed functional iterations. Lau and Ng [128] investigated the combined effect of the reversible and irreversible wall reactions on the early phase development of the dispersion coefficient by using flux-corrected transport algorithm and found that the dispersion coefficient may approach to its steady-state in a short time for Damkohler number $\geq$10 and absorption rate $\leq$ 0.5. Further, Ng and Rudraiah [159] reworked on Lau and Ng and generalized the dispersion model by using Damkohler number, absorption rate and phase partition number of any magnitude. Saini et al. [195] is also extended the work of Lau and Ng [128] by including first-order chemical reaction with linear reaction rate. Recently, Rana et al. [181] explored the transport of unsteady blood flow through small arteries of different radii with and without absorption at the wall by using the generalized dispersion model. We observed that the present state in the above studies have the following limitations - (i) the models do not permit changes in the structural properties of the tube wall, therefore incapable of simulating how the properties change with, e.g., wall thickness (fibrosis) and (ii) the models do not take into account the wall porosity effect on reaction parameter and dispersion by altering porosity. Therefore, in this study, we provide a correlation between the structural change occurs in the tube wall due to some disease like fibrosis or other interstitial pulmonary diseases and the simultaneous effect on the dispersion coefficient is obtained. It is assumed that the tube wall is coated with a thin liquid layer in which the solute may go through a first-order chemical reaction within the bulk flow and on the boundary. We discussed how the variations in the wall thickness and porosity affect the short time and short distance transient dispersion with the combined effects of kinetic reversible phase exchange and irreversible absorption by using method of Moments. Comparative study is also done with published result.

8.2 Mathematical Formulation

8.2.1 Governing equations

We considered the dispersion of a chemically reactive solute is initially distributed in a straight circular tube [1] of internal radius ‘a’, as shown in Figure 8.1 [159]. The thickness of the wall is, ‘l’ $\leq$ 3 radius/2 and is made of absorptive and reactive materials. The alveolar wall is semi-permeable so there is a constant permeability (K) and porosity (ϵ) through the wall. The transport of a completely soluble chemical species may undergo linear chemical reaction at the tube wall. Two types of first-order reactions occur on the tube wall; irreversible and reversible. The part of the solute consumed by the wall material is considered under irreversible reaction and the part engaged in the phase exchange process with the flowing fluid is considered under reversible reaction. The phase of the solute that flows with the fluid is called a mobile phase and that clings to the boundary is termed as an immobile phase. Initial description about boundary conditions can be seen in the study of Ng [159] and Lau and Ng [128]. Fluid is Newtonian and flow is unsteady, fully - developed, axisymmetric, laminar. In this study, we assumed that the alveolar wall is thicker than its normal size [2]. We updated the convection-diffusion model used by Saini et al. [195] by the inclusion of diffusion formula in terms of wall thickness and permeability, which was defined in Equation 8.3 to show the effect of wall thickness on diffusion and absorption. The transport of chemical species through this wall is defined by the two - dimensional unsteady convection - diffusion model as follows:

$$\frac{\partial c}{\partial t} + \frac{u}{\epsilon}\frac{\partial c}{\partial z} = D\frac{\partial^2 c}{\partial z^2} + \frac{D}{r}\frac{\partial}{\partial r}\left(r\frac{\partial c}{\partial r}\right) - \frac{\lambda' c}{\epsilon}, \quad -\infty < z < \infty,\ 0 < r < a, \tag{8.1}$$

for laminar flow velocity profile of air is taken as below:

$$u = u_0\left(1 - \frac{r^2}{a^2}\right), \tag{8.2}$$

---

[1] alveolar or pulmonary duct

[2] Fibrosis increases the thickness of airways/alveoli wall about two to three times of the normal size. It interferes significantly the normal respiratory gas exchange process of gases [78]. Hence the rate of diffusion through the wall is inversely proportional to the thickness of the wall.

where u_0 is the initial velocity of the flow at the center of the tube. Then, equation 8.1 becomes as

$$\frac{\partial c}{\partial t}+\frac{u_0}{\epsilon}\left(1-\frac{r^2}{a^2}\right)\frac{\partial c}{\partial z}=D\frac{\partial^2 c}{\partial z^2}+\frac{D}{r}\frac{\partial}{\partial r}\left(r\frac{\partial c}{\partial r}\right)-\frac{\lambda' c}{\epsilon}, \quad -\infty<z<\infty,\ 0<r<a. \tag{8.3}$$

Equation 8.3, represents the convection - diffusion equation for species. The first term in the left hand side of the equation is for unsteady flow and the second term is for convection. First, second and third terms in the right hand side of equation are diffusion, convection, and first order kinetics in porous media and D is the molecular diffusion coefficient of the chemical in the fluid. According to the Fick's law, diffusion is inversely proportional to the thickness of the wall and proportional to the permeability (K) of the wall so we assumed that the diffusion of the chemical is related to the thickness as follows,

$$D=\frac{Ku_0}{l}, \tag{8.4}$$

and permeability (K) depends on the porosity (ϵ) of the media as follows [57]

$$K=\frac{\epsilon^3 d^2}{150\left(1-\epsilon\right)^2}, \tag{8.5}$$

where d is the diameter of alveoli.

8.2.2 Initial and boundary conditions

We proceed with an initial condition of an impulse input in term of real part of e^{ir} at $t=0$, due to distribution of chemical species in between of mobile and immobile phases:

$$\begin{aligned}
&c(z,r,0)=cos(r) \quad |z|\le z_s, \quad 0<r<1,\\
&c(z,r,0)=0 \quad |z|>z_s, \quad 0<r<1,\\
&c_s(z,r)=0,\ \forall\ z,
\end{aligned} \tag{8.6}$$

where, z_s is the length of the slug input.

The following two boundary conditions are relevant for the present study:

For axial distribution,

$$c(z,r,t)=0, \quad z\to\pm\infty, \tag{8.7}$$

Condition for two reactions occurring on the tube wall are,

$$-D\frac{\partial c}{\partial r}-\Gamma c-K\left(\alpha c-c_s\right)=\frac{\partial c_s}{\partial t}=k\left(\alpha c-c_s\right)-\lambda_s c_s, \ \ r=a, \tag{8.8}$$

Condition due to symmetry at the tube center,

$$\frac{\partial c}{\partial r} = 0, \;\; r = 0, \tag{8.9}$$

In equation 8.8 - 8.9, λ' and λ_s are the first order reaction rate constants for the mobile and immobile phases respectively [166].

8.3 Methodology

8.3.1 Transformation of the governing equations

To solve the governing equations 8.3 numerically we have to make above equations dimensionless by using following quantities.

$$c^* = \frac{c}{c_0}, c_s^* = \frac{c_s}{ac_0}, r^* = \frac{r}{a}, z^* = \frac{z}{a^2u_0/D}, t^* = \frac{t}{a^2/D}, DA = \frac{ka^2}{D},$$
$$\alpha^* = \frac{\alpha}{a}, \Gamma^* = \frac{a\Gamma}{D}, Pe = \frac{au_0}{D}, \lambda* = \frac{\lambda' a^2}{D}, \lambda_s* = \frac{\lambda_s a^2}{D},$$

where c_0 is the initial concentration.
After dropping the star ($*$) above equation are written as follows:

$$\frac{\partial c}{\partial t} + \frac{(1-r^2)}{\epsilon}\frac{\partial c}{\partial z} = \frac{1}{Pe^2}\frac{\partial^2 c}{\partial z^2} + \frac{1}{r}\frac{\partial}{\partial r}\left(r\frac{\partial c}{\partial r}\right) - \frac{\lambda c}{\epsilon}, \tag{8.10}$$

$$-\frac{\partial c}{\partial r} - \Gamma c - \frac{Ka^2}{D}(\alpha c - c_s) = \frac{\partial c_s}{\partial t} = DA(\alpha c - c_s) - \lambda_s c_s, \;\; r = 1, \tag{8.11}$$

$$\frac{\partial c}{\partial r} = 0, \;\; r = 0, \tag{8.12}$$

In a convection controlled problem a fine gradient is required, otherwise the gradients will become contaminated by numerical dispersion errors. Therefore, we examined the corresponding curves based on the area average concentration. The mobile-phase concentration in terms of the area average concentration ($\bar{c}$) is defined by the function of axial coordinate as follows:

$$\bar{c}(z,t) = 2\int_0^1 crdr, \tag{8.13}$$

In equation 8.13 integral is calculated by Simpson's 1/3 rule. Based on $\bar{c}$, the spatial moments of the concentration distribution for the mobile phase are specified as follows

$$\mu_m = \int_{-\infty}^{\infty} z^m \bar{c}dz, \quad m = 0, 1, 2..., \tag{8.14}$$

The variance of the distribution is defined as follows,

$$\sigma^2(t) = \frac{\mu_2}{\mu_0} - \frac{\mu_1^2}{\mu_0^2}, \tag{8.15}$$

the coefficient of dispersion, c_d, is change with respect to time. So, we formulate c_d in terms of the rate of change of the variance of the distribution, σ^2, as follows

$$c_d(t) = \frac{1}{2}\frac{d\sigma^2}{dt}, \tag{8.16}$$

8.4 Numerical Scheme

Finite difference method [214] is the most suitable technique for nonlinear problems related to regular geometries so, to find the solution of the non - dimensional governing equations 8.10 subject to the initial and boundary conditions 8.11 - 8.12 we used this method. The computational grid are defined in the following form where the discretization of concentration, $c(r, z, t)$, is written as $c(r_i, z_j, t_n)$ or $c^n_{i,j}$.

$$\begin{aligned} &r_i = i\Delta r, (i = 0, 1, 2, 3, 4, ...N), \qquad r_N = 1 \\ &z_j = j\Delta z, (j = 0, 1, 2, 3, 4, ...M), \\ &t_n = (n-1)\Delta t, (n = 1, 2, ...), \end{aligned} \tag{8.17}$$

where i, j and n are the space and time indexes, $\Delta r, \Delta z$, and Δt are the increment in radial, axial and time respectively. We used central difference approximation, for all the spatial derivatives, as follows:

$$\frac{\partial c}{\partial z} = \frac{c^n_{i,j+1} - c^n_{i,j-1}}{2\Delta z}, \tag{8.18}$$

$$\frac{\partial^2 c}{\partial z^2} = \frac{c^n_{i,j+1} - 2c^n_{i,j} + c^n_{i,j-1}}{(\Delta z)^2}, \tag{8.19}$$

and forward difference approximation for all the time derivatives, as

$$\frac{\partial c}{\partial t} = \frac{c^{n+1}_{i,j} - c^n_{i,j}}{2\Delta t}, \tag{8.20}$$

moreover, at $r = 0$ equation 8.10 converts as follows [3]

$$\lim_{r\to 0} \frac{1}{r}\frac{\partial c}{\partial r} = \lim_{r\to 0} \frac{\partial^2 c}{\partial r^2}, \tag{8.21}$$

---

[3] When $r \to 0$, we found that the denominator is also approaching to zero and make the term indeterminate, which is inappropriate for the physical state of the respiratory system. Therefore, to remove this kind of inconsistency we used L'hospital rule of limit here.

we got its discretized form of equation 8.10 as follows

$$c_{i,j}^{n+1} = \left(1 - \frac{2r_1}{Pe^2} - 4r_2 - \epsilon\lambda\Delta t\right) c_{i,j}^{n} + \left(\frac{r_1}{Pe^2} - \frac{\Delta z r_1}{2\epsilon}\right) c_{i,j+1}^{n}$$
$$+ \left(\frac{r_1}{Pe^2} + \frac{\Delta z r_1}{2\epsilon}\right) c_{i,j-1}^{n} + 2r_2 \left(c_{i+1,j}^{k} - c_{i-1,j}^{n}\right), \tag{8.22}$$

and at $0 < r \leq 1$ we got

$$c_{i,j}^{n+1} = \left(1 - \frac{2r_1}{Pe^2} - 2r_2 - \epsilon\lambda\Delta t\right) c_{i,j}^{n} + \left(\frac{r_1}{Pe^2} - \frac{(1-r^2)\,\Delta z r_1}{2\epsilon}\right) c_{i,j+1}^{n}$$
$$+ \left(\frac{r_1}{Pe^2} + \frac{(1-r^2)\,\Delta z r_1}{2\epsilon}\right) c_{i,j-1}^{n} + r_2 \left(c_{i+1,j}^{n} + c_{i-1,j}^{n}\right) + \frac{\Delta r r_2}{2} \left(c_{i+1,j}^{n} - c_{i-1,j}^{n}\right), \tag{8.23}$$

where

$$r_1 = \frac{\Delta t}{\Delta z^2}, \;\; r_2 = \frac{\Delta t}{\Delta r^2}.$$

The initial and boundary conditions are found as

$$c_{i,1}^{n} = c_{i,M+1}^{n} = 0, \;\; c_{2,j}^{n} = c_{0,j}^{n}. \tag{8.24}$$

We got concentration distribution at the $(n+1)^{th}$ time level in terms of the concentration at n^{th} time level in equation 8.22 - 8.23 respectively.

8.5 Results and Discussion

The initial slug length (z_s) is varied from 0.008 to 0.02. So, in this study we fixed z_s at 0.02, in all the cases. To examine the conjugated effect of the reversible phase exchange and irreversible absorption of species through fibrosis affected tube walls, we used thickness of alveolar wall (l) $\leq$ 3 radius of alveoli (a)/2 (ranged 0.5 - 4.5 micrometer), ϵ = 0.5 and Pe = 10^3 in all the cases. Problem is solved for six different combinations of α, DA and Γ as listed in Table 8.1, where case (i) narrates inert gas case, cases (ii), (iv) and (vi) correlate increment in phase exchange rate, DA; and cases (iii) and (v) correlate increment in absorption rate, Γ. First, we tested the grid dependency for different grid sizes in both the spatial directions, r, and z; and found that the result remains consistent and grid independent, when the grid size is 40x1000 and beyond. So we chose $\Delta r = 0.025$, $\Delta z = 0.001$ along the radial and axial directions and time step $\Delta t = 0.0001$ and did entire calculation for grid size 40x1000 uniformly. In this manner the result appeared to converge with the accuracy of the order 10^{-4} by using the following stability criteria at each time level so that less error occurred in the numerical computation

$$max\left(\frac{\Delta t}{\Delta z^2}\right) \leq 0.5. \tag{8.25}$$

For accuracy and numerical code validation, we compared our results with the published results [128], for five cases (case (i) - (v)) as shown in Figure 8.2 (see, Table 8.2). The following interpretations can be drawn:

1. The dispersion coefficient tends to steady value very rapidly, after $t = 0.2$ in Lau and Ng [128] but in our results, it reaches to its steady state after $t = 0.45$ in case (i) by the inclusion of wall thickness (l), variable diffusion with semi-permeability.

2. Cases (ii) and (iii) consequent to the very slow phase exchange rate, the dispersion coefficient in these cases does not achieve the steady-state values in a short time due to the slow absorption effect.

3. Results of Lau and Ng [128], for case (iv) consequent to fast phase exchange rate, where the dispersion coefficient goes up to a local peak at $t = 1$ and then it decreases to move towards a steady value whereas in our result diffusion through thick wall delayed the local peak time and curve goes to steady state after $t = 1.5$. This means that the dispersion coefficient can move towards a steady-state limit in a longer time limit if the wall thickness is considered with the increment in Damkohler number ($1 < DA \leq 20$).

4. By evaluating cases (iii) and (v) from Lau and Ng [128], it is found that the dispersion coefficient in case (v) is slightly higher but finally smaller than that in case (iii) but in our result the dispersion coefficient in case (v) is very smaller than the case (iii).

Hence, we observed by this comparison that our results performed slightly different behavior due to the inclusion of equation (8.3) consequently, we found that thickness of alveolar wall affect the coefficient of diffusivity, which is physically true by the Fick's law.

8.5.1 Mean breakthrough curves based on the area-mean concentration for different axial points

For six particular cases of short distance development of the mean breakthrough curves are obtained through the area-mean concentration and shown in Figure 8.3(a)-8.3(d) for four dimensionless axial positions, ranging from short distance, $z = 0.05 - 0.3$.

In Figure 8.3(a), during the early phase (z = 0.05) from the injection point (z_s = 0.02), the transport is largely kinematic, and the solute spread is dominated by convection, the curve is strongly asymmetric, exhibiting a peak upon its initial sharp rise, followed by a gradual decline first according to the kinematic limit at time, t = 0.05, and then branching out from this limit because of radial diffusion, as shown in cases (i)-(iii) and (v). The concentration then decreases and the curve has an infinitely long tail either due to increase in absorption rate (Γ from 0.1 to 1) or due to diffusion (compare cases (iii) & (v)). As soon as the near-wall solute diffuses inward into the faster moving inner part, as shown in case (iv) and case (vi), the breakthrough curve deviates from the kinematic limit (i.e. convection limit), giving rise to a point of inflection or a shoulder in the curve. Here, the emergence of the shoulder is stronger than the other cases; either due to the accumulation of species or low diffusion due to high 1$\leq DA \leq$ 20 (compare cases (ii), (iv) & (vi)). Now, if we focus on convergence, case (i) converges to zero faster i.e. t = 0.15 than other cases, however, cases (iv) and (vi) become constant after t = 0.17.

At a farther distance from the injection point (z = 0.1), in Figure 8.3(b), the shoulder part of the curve becomes more developed and sharp as compared to the previous graph. Trends are the same for Figure 8.3(c) (z = 0.15), convection peak decreases in case (i) and the diffusional peak becomes the main feature of the mean breakthrough curve with the last residue of a convection regime appearing as a shoulder on the left of the curve in cases (ii)-(vi). The second peak becomes wide and high due to relatively fast retentive or absorptive effects (in cases (ii), (iii) & (v)). Due to the thickness of the wall, very few chemical species from the immobile phase will be dispersed back to the mobile phase and hence we get high concentration values in cases (iv) & (vi).

At a sufficiently long distance from the injection point (z = 0.3), the sharp initial rise decreases gradually, while the rounded second peak is fully developed to become the center broadened peak due to high retention and absorption (cases (ii), (iii) & (v)). Value of concentration in mobile phase becomes very high (cases (iv) & (vi)) comparable to other cases (may be due to low diffusion, high Damkohler number or accumulation of species cause of thickness (l) of the wall), see Figure 8.3(d). This is the onset of the Taylor and Aris regime; as the axial distribution becomes increasingly symmetrical about its peak approaching a Gaussian distribution. In a compact view, we found by the increment in Damkohler number (0.1$\leq DA \leq$20), the second peak becomes wider and higher or diffusion becomes low. Further, by the increment in axial position (z = 0.05 to 3) with respect to time, concentration becomes high gradually due to low diffusion and accumulation of species caused by the thickness (l) of the wall.

8.5.2 Mean breakthrough curves based on the area-average concentration at different times

The area-mean concentration is plotted in Figure 8.4(a)-8.4(d) to exhibit the dispersion effect of the chemical species for four dimensionless moments of time after dropping star at t = 0.05, t = 0.15, t = 0.3, and t = 0.5 respectively.

During the early phase development or at short time (t = 0.05) from the injection point, the transport is balanced by two peaks, first due to convection and second due to radial diffusion in all cases (i)-(vi), in Figure 8.4(a), area under the distribution curve is markedly increased from cases (ii) to (vi) might be due to increment in DA = 0.1-20 (emergence of accumulation of species or low diffusion). While in this figure we noticed by increasing absorption rate (Γ = 0.1 to 1) area average concentration is decreased (compare cases (iii) & (v)). In Figure 8.4(b), larger spread of the distribution in cases (i)-(vi) arise from the interaction of convection with radial diffusion, and diffusional peak decreased from the previous state. The increase of area under the distribution curves and decline of diffusional peak is a result of releasing species which has been stored as an immobile phase on the wall, back to the flow; clearly seen in cases (iv) and (vi). Figure 8.4(c) shows that, for cases (i)-(iii) & (v), the distribution curves are single-peaked. However, the diffusional peak becomes more developed in cases (iv) & (vi), due to increment in DA (accumulation of species).

In Figure 8.4(d), it can be seen in cases (i)-(iii) & (v), that the curves become symmetrical about the z-axis, supporting the Gaussian form, which is readily developed in this case. While, in cases (iv) & (vi), the diffusional peak continues to broaden to become the dominant feature of the distribution. This is because a long time is required to approach the fully-developed state if $1 < DA \leq 20$. Furthermore, it is obvious that the area under the concentration distribution curve in case (v) is not much different than the case (iii). This follows from the fact that for a very high absorption rate (Γ = 1), the long-time dispersion will be accomplished because all species are taken away from the system.

8.5.3 Effect of a thickness (l) and porosity (ϵ) on diffusion in mobile phase

An interstitial lung disease in which scar tissue is accumulated is termed as fibrosis. As the disease develops the alveolar-capillary units are impacted and exchange of oxygen and carbon dioxide gases is impaired, eventually leading to respiratory failure [81]. In addition, fibrosis causes an increment in the thickness of the alveolar wall, which decreases the rate of diffusion. Hence, when the thickness of the alveolar wall increases two to three times, the rate of gas exchange remarkably decreases.

From Figure 8.5 we found the effect of increment in thickness and decrement in porosity on the diffusion of species. Figure 8.5(a) shows that the diffusion rate through the respiratory wall is decreasing significantly as the thickness of the wall increases. However, the diffusion rate increases significantly as the porosity of the wall increases; Figure 8.5(b). Table 8.3 shows numerical values of diffusivity for different values of wall thickness.

8.6 Conclusion

The short distance and short-time dispersion of a substance in the unsteady flow of reactive solute through a circular tube (e.g. human airways, arteries, air-blood barrier, alveolar duct, pulmonary membrane, etc.), whose wall is thicker than its normal size and lined with a thin liquid layer are examined. At the end, the plot of the dispersion coefficient as a function of the reaction parameters have been examined. The essential conclusions of the present research are stated below:

1. We found that with convection, the solute cloud is completely spread out of a channel in a finite time and get its steady state very rapidly.
2. The second peak of the diffusion regime becomes developed by a high value of the Damkohler number.
3. When we decreased porosity and increased the thickness of the wall from its normal size (thickness $\leq 3a/2$), diffusion is decreased and area average concentration distribution increased due to the accumulation of species.
4. Long time dispersion will be achieved due to the diffusion of all the species for the system, for a very high absorption rate ($\Gamma = 1$).
5. If $DA \leq 1$ and $\Gamma < 1$, it needs less time to advance toward a long-time dispersion.
6. It will take a longer time to approach towards a fully-developed state if $1 < DA \leq 20$.
7. The dispersion coefficient advances toward its steady-state limit in a short time at: (i) absorption rate ($\Gamma < 1$); (ii) Damkohler number ($0 < DA \leq 1$).
8. Diffusion rate through the respiratory wall is diminished as the thickness of the wall increases.
9. Diffusion rate increases with the increment in the porosity of the wall.

10. According to our assumption, by considering the tube wall thickness, the connection speed is not changed, but the diffusion speed is decreased. This will, of course, reduced the spread of the species as well. We conclude from this study that fibrosis will prevent or reduces the exchange of species.

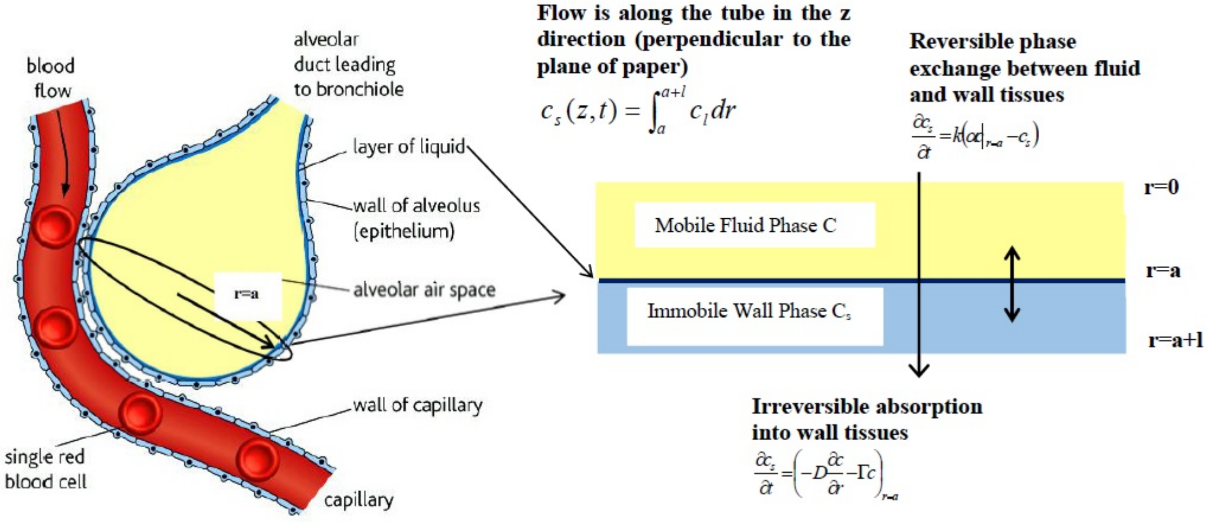

Figure 8.1: Schematic diagram demonstrating a blow-up sectional perspective of the tube wall, where two reactions take place [159].

Table 8.1: Values of the controlling parameters considered for the present study.

Case	DA	α	Γ	Remarks
(i)	0	0	0	Inert gas case
(ii)	0.1	0.5	0.1	Slow phase exchange rate
(iii)	1	0.5	0.1	Moderate phase exchange rate
(iv)	10	0.5	0.1	Fast phase exchange rate
(v)	1	0.5	1	Fast absorption rate
(vi)	20	0.5	0.1	Very fast phase exchange rate

Table 8.2: Comparison between published (Lau and Ng [128]) and present results for dispersion coefficients versus dimensionless time for different cases.

Cases	Author	$t = 0.2$	$t = 0.4$	$t = 0.6$	$t = 0.8$	$t = 1$	$t = 1.2$	$t = 1.4$	$t = 1.6$	$t = 1.8$	$t = 2$	$t = 2.2$	$t = 2.4$
Case 1	Lau et al. [128]	0.00385	0.0029	0.00228	0.00197	0.0018	0.00168	0.00157	0.00146	0.00135	0.00122	0.00111	9.84E-04
-	Present result	0.00529	0.00259	0.00216	0.00215	0.00215	0.00215	0.00215	0.00215	0.00215	0.00215	0.00215	0.00215
Case 2	Lau et al. [128]	0.00355	0.00252	0.00212	0.00201	0.00198	0.00197	0.00197	0.00197	0.00197	0.00197	0.00198	0.00198
-	Present result	0.0041	0.00511	0.00385	0.00372	0.00379	0.00386	0.00393	0.00401	0.00409	0.00417	0.00424	0.00433
Case 3	Lau et al. [128]	0.00895	0.01671	0.02333	0.02921	0.03506	0.03989	0.0433	0.04493	0.04541	0.04538	0.04523	0.04509
-	Present result	0.01	0.0187	0.0269	0.0343	0.0369	0.037	0.0373	0.0378	0.0384	0.0391	0.0397	0.0403
Case 4	Lau et al. [128]	0.01751	0.01754	0.01706	0.01679	0.01662	0.0165	0.01639	0.01626	0.01614	0.016	0.01586	0.01571
-	Present result	0.02301	0.03401	0.03775	0.03745	0.03541	0.03389	0.03311	0.03266	0.03225	0.03182	0.0314	0.03096
Case 5	Lau et al. [128]	0.00329	0.00299	0.00415	0.01596	0.04014	0.05895	0.06474	0.05818	0.04567	0.0322	0.02185	0.01392
-	Present result	0.00365	0.00778	0.01227	0.01684	0.02087	0.02382	0.02616	0.02767	0.02796	0.02618	0.02154	0.01205

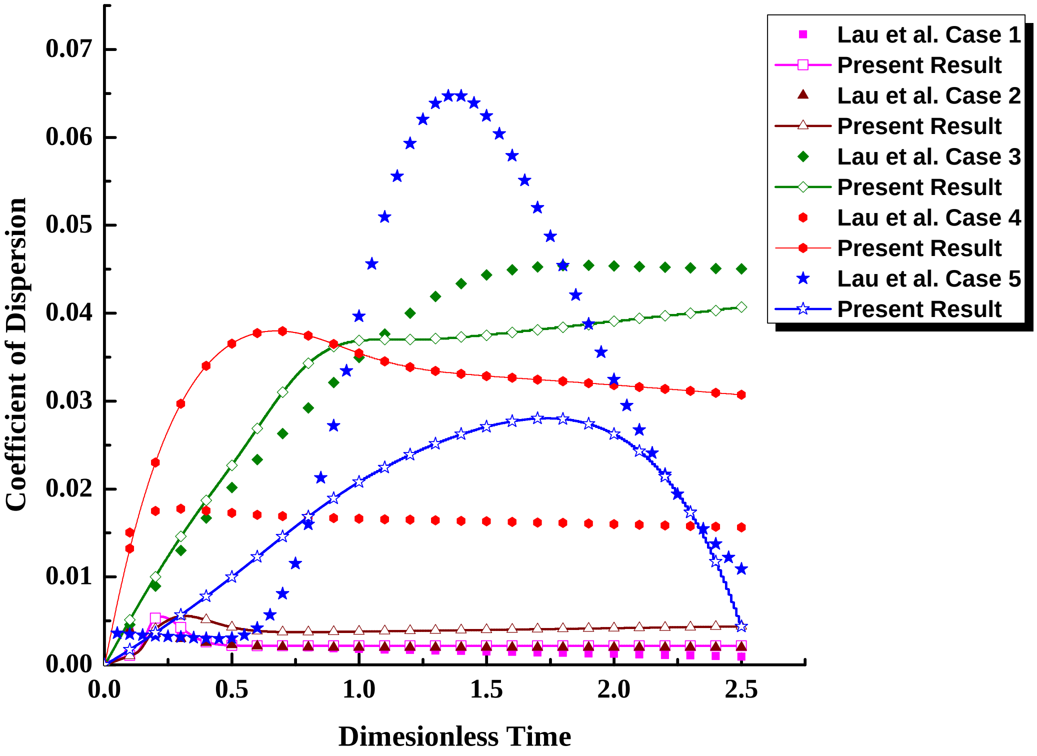

Figure 8.2: Time dependent variation of coefficient of dispersion for different cases as shown in Figure 2.

Table 8.3: Effect of wall thickness and porosity on diffusivity

Thickness (l) in μm	Diffusivity (D)	Porosity (ϵ)	Diffusivity (D)
0.5	5.40E-10	0.5	4E-11
1	2.70E-10	0.55	6.57E-11
1.5	1.80E-10	0.6	1.08E-10
2	1.35E-10	0.65	1.79E-10
2.5	1.08E-10	0.7	3.05E-10
3	9.00E-11	0.75	5.4E-10
3.5	7.71E-11	0.8	1.02E-9
4	6.75E-11	0.85	2.18E-9
4.5	6.00E-11	0.9	5.83E-9

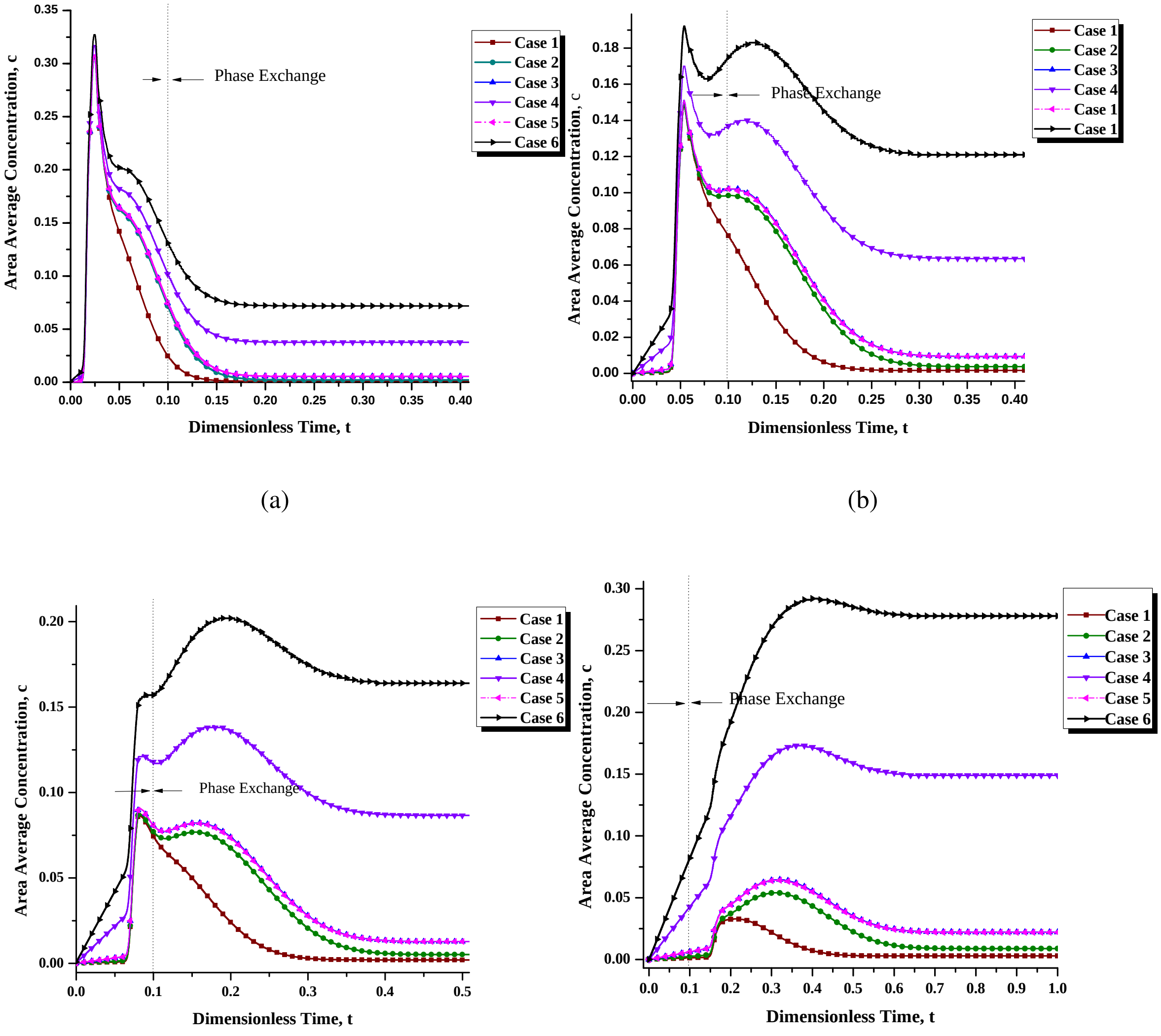

(a)

(b)

(c)

(d)

Figure 8.3: Breakthrough curves based on the area average concentration for short distance development of dispersion in a circular tube, at dimensionless axial positions (a) $z = 0.05$, (b) $z = 0.01$, (c) $z = 0.15$, (d) $z = 0.3$, with l = $4.5 * 10^{-6}$, ϵ=0.5, and $Pe = 1000$.

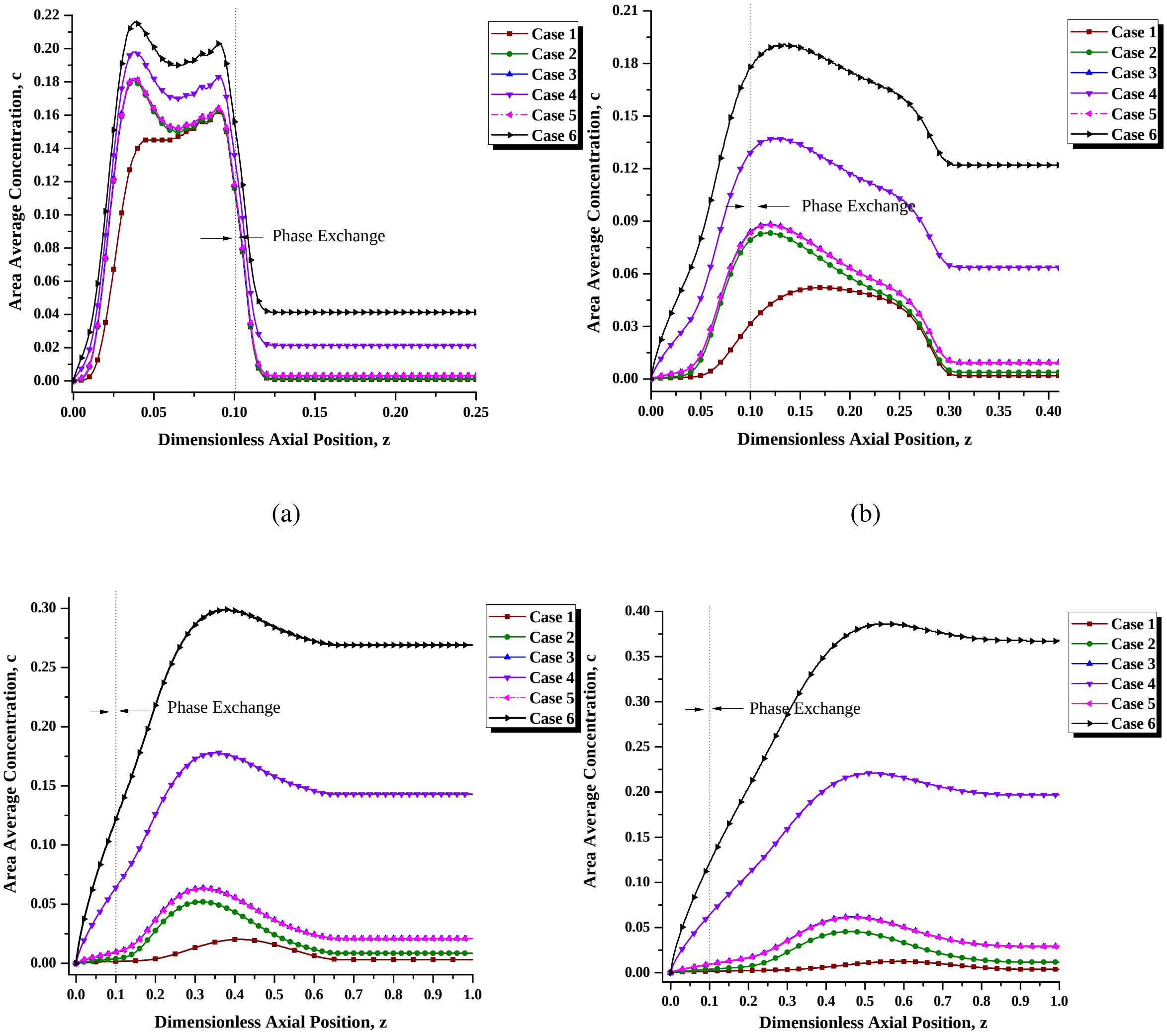

(a) (b)

(c) (d)

Figure 8.4: Breakthrough curves based on the area average concentration for short time development of dispersion in a circular tube, at dimensionless time t = 0.05, t = 0.15, t = 0.3, t = 0.5, with $l = 4.5 * 10^{-6}$, ϵ = 0.5, and Pe = 1000.

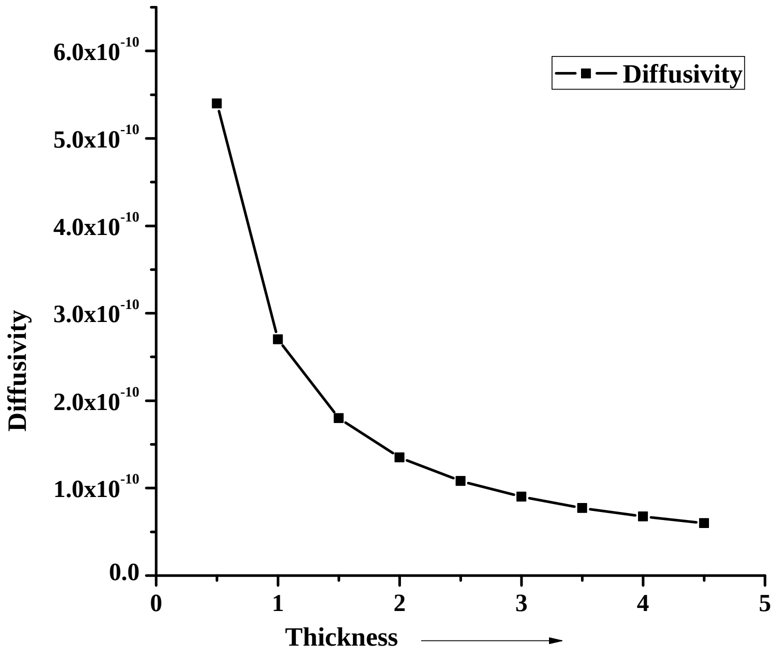

(a)

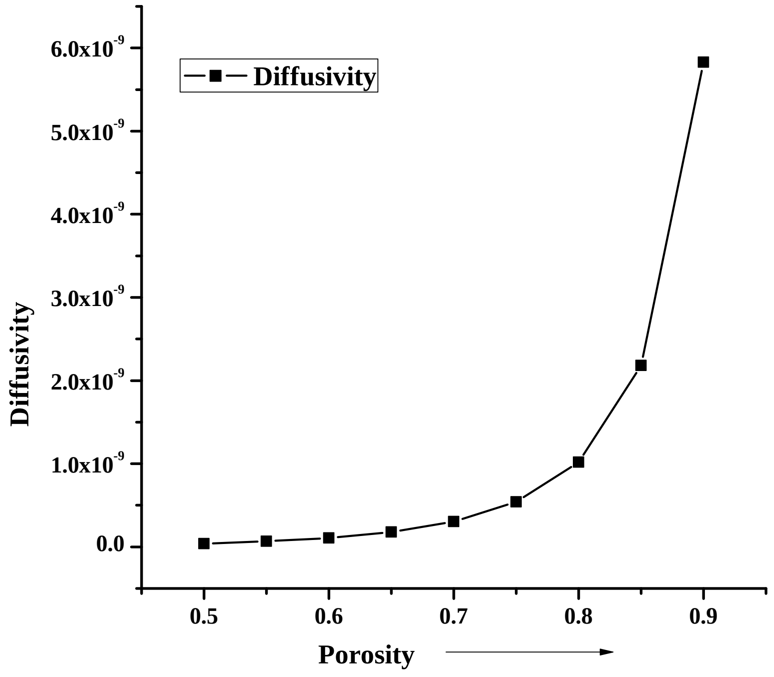

(b)

Figure 8.5: Effect of wall (a) thickness, and (b) porosity on gas diffusion into mobile phase.

Chapter 9: Effect of first order chemical reactions through tissue-blood interface on the partial pressure distribution of inhaled gas

9.1 Introduction

Diffusion is a process which causes gas transportation between alveoli and pulmonary capillary blood through surrounded tissue. Typically, concentration difference or concentration gradient acts as a driving force for movement due to diffusion. However, concentration is not a suitable factor to work as a driving force when considering the migration of gases. This is because much of the gas may be powerless by binding or changing into another chemical form when dissolved in body fluids. In continuation, concentration includes certain molecules that are not absolved to diffuse. So, we need another estimate of the tendency for the diffusion of gases, which can be provided by partial pressure.

In human respiratory system pressure is caused by the movement of molecules against the surface, and in the process of diffusion of gas in blood, or tissue-blood capillary. The pressure exerted by the gases (i.e. oxygen, carbon dioxide, nitrogen, and helium), alone is defined as the partial pressure of that gas, which can be used to estimate the diffusion of a gas. Partial pressure is controlled by the solubility of a gas in lipid, the cross-sectional area of the tube, the distance through which the gas must diffuse and the molecular weight of that gas, in the fluid. Additional factors on which diffusion of the inhaled gas through the membrane depend are thickness and surface area of the membrane, the diffusion coefficient of the gas in the material of the membrane, and the partial pressure difference of the gas between two sides of the membrane [78].

Typically, gas exchange process between blood and tissue is modeled by Krogh cylinder model [118], in which blood is flowing through a cylindrical capillary within a co-axial cylindrical tissue. There are various studies, where Krogh's cylinder model is used in the transportation process.

Whiteley et al. [247] studied spatial as well as temporal variations of inhaled gas partial pressure using Krogh cylinder model and observed that the ordinary differential equation does not provide a good approximation of gas exchange and stated that for gas exchange between blood and tissue the partial differential equations provide a more realistic approximation. Sharma and Jain [204] used Krogh cylinder for exchange of oxygen in peripheral nerve with forward and backward chemical reactions and stated that chemical reactions affect the time profiles of tissue oxygen tension together with the rate of capillary blood flow. Goldman [70] discussed intravascular oxygen transport by using Krogh tissue cylinder model for single capillary and highlighted the physiological importance of intravascular resistance to blood-tissue oxygen transfer. Roy and Aleksander [189] developed a steady-state model to predict the minimum end capillary pressure of oxygen from the erythrocyte to the mitochondrion. McGuire [147] studied oxygen transport from capillaries to exercising skeletal muscles by using a Krogh-type cylinder model. Whereas, most of the modifications in the Krogh model keep the idea of zero radial flux on the outer boundary of the tissue cylinder but this statement is not purely valid due to the irregular arrangement of alternative vessels, which encompasses capillary. Several investigators have extended this model such as Fletcher [60] discussed about the flow of blood in capillary, intra capillary blood kinetics, capillary wall permeability, capillary-tissue geometric relationships, and tissue diffusion properties Popel [172] formulated important features of oxygen transport, intra capillary resistance to transport, myoglobin facilitation of oxygen diffusion, and intracellular heterogeneities due to nonuniform distribution of mitochondria using a mathematical model. By keeping the flow conditions in the capillary, Reneau et al. [183] developed a numerical model for transport of oxygen between capillary and tissue by considering intra capillary diffusion, convective of blood and axial diffusion in the tissue. Blum [19] considered capillary wall resistance for oxygen transport and has solved the steady state problem analytically for zero and first order dissipation of oxygen in the tissue.

Conventionally, the transport of species (either gas or liquid) processed either by convection or by diffusion [97]. However, when both are included with the flow, it is characterized as dispersion [85, 232]. Dispersion happens through the combined effect of convection and molecular diffusion [8] and it is directly proportional to convection and reciprocally proportional to diffusion. Taylor dispersion is eventually a Gaussian function of distance along the pipe axis and derived as an asymptotic series based on the assumption that the diffusion of solute obeys Fick's law [30]. It depends on the diffusivity, aspect ratio, the cross-section of the passage, flow characteristics and characterized through the dispersion coefficient [20]. The dispersion coefficient is a function of the Peclet number, based on the diameter for circular cross-section and varies with the aspect ratio of the cross-section for rectangular channels. Doshi et al. [48] studied the effect of side walls on the dispersion process in open and closed rectangular ducts and found that as the aspect ratio increases, the steady state convection coefficient approaches an asymptotic value, obtained by neglecting side wall effects. Additionally, Parks and Romero [165] generalized the results of previous studied [29, 48] by considering Taylor-Aris dispersion in columns of a nearly rectangular cross-section of large aspect ratio. Lucker et al. [143] studied the impact of blood flow heterogeneity on oxygen partial pressure in the tissue due to moving red blood cells inside microvessels. Sun et al. [227] measured oxygen diffusion for time-dependent diffusion and consumption for small tissue regions containing a single capillary.

The literature sincerely reveals that traditional models (i.e. Krogh cylinder model [118]) did not consider fluid transfer through the interface of a tissue - blood or inter capillary. Additionally, short time dispersion through Krogh cylinder model is not studied yet. So, the aim of this study is to find the effect of the partial pressure distribution when inter capillary oxygen gradients, radial mixing, axial diffusion, and temporal dispersion affect the transportation of gas (oxygen) passing through small diameter blood capillary surrounded by porous tissue, and the capillary material is absorptive and reactive. A mathematical model is used to calculate the coefficient of dispersion by the method of moments for both time and spatial distributions of the partial pressure of inhaled gas inside a respiratory system with the coupled effect of convection and diffusion, where a first-order chemical reaction taking place in the bloodstream.

9.2 Mathematical Formulation

9.2.1 Governing equations

The geometry of the model is shown in Figure 9.1 [78, 159, 195]. The z-axis is positioned along the centerline of the cylinder (alveolar or pulmonary duct) and the circulation of blood flow inside the body section is homogeneous while there is radial symmetry on the axis. We assumed flow is unsteady, laminar through a small diameter long regular straight tube [1]. We applied short time dispersion proposed by (Lau et al. [159] and Saini et al. [195]) in traditional Krogh [118] cylinder model and assumed surrounded tissue is porous and capillary material is absorptive and reactive. Also, due to porosity of tissue, we used flow through interface between tissue and blood, where first order kinetic reactions, reversible and irreversible, are taken under consideration. Due to rhythmic

---

[1] tissue-blood capillary

breathing, exponential decay is assumed as a initial condition. Pure convection in the axial direction, and pure diffusion in the radial direction are taken into consideration. The partial differential equations are used to model inhaled gas transfer in tissue-blood capillary. Gas passes between capillary and tissue by the combined effect of convection and diffusion. Because of radial symmetry, we used cylindrical polar coordinate system. The equation of transport of a species with first order kinetic reactions in terms of the partial pressure inside blood ($p(r, z, t)$) and inside tissue ($p_t(r, z, t)$), in two dimensional form are as follows:
Equation of partial pressure of gas,
in blood,

$$\frac{\partial p}{\partial t} + u_x \frac{\partial p}{\partial z} = D_c \frac{\partial^2 p}{\partial z^2} + \frac{D_c}{r}\frac{\partial}{\partial r}\left(r \frac{\partial p}{\partial r}\right) - \lambda' p, \quad -\infty < z < \infty, \ 0 < r < R_c, \tag{9.1}$$

in tissue,

$$\frac{\partial p_t}{\partial t} + \frac{u_x}{\epsilon}\frac{\partial p_t}{\partial z} = D_t \frac{\partial^2 p_t}{\partial z^2} + \frac{D_t}{r}\frac{\partial}{\partial r}\left(r \frac{\partial p_t}{\partial r}\right), \quad -\infty < z < \infty, \ R_c < r < R_t, \tag{9.2}$$

where $u_x = u_0\left(1 - \frac{r^2}{R_x^2}\right)$. We take, $x = c$ for blood and $x = t$ for tissue.
Then, equation 9.1 and 9.2 becomes

$$\frac{\partial p}{\partial t} + u_0\left(1 - \frac{r^2}{R_c^2}\right)\frac{\partial p}{\partial z} = D_c \frac{\partial^2 p}{\partial z^2} + \frac{D_c}{r}\frac{\partial}{\partial r}\left(r \frac{\partial p}{\partial r}\right) - \lambda' p, \ -\infty < z < \infty, \ 0 < r < R_c, \tag{9.3}$$

$$\frac{\partial p_t}{\partial t} + \frac{u_0\left(1 - \frac{r^2}{R_t^2}\right)}{\epsilon}\frac{\partial p_t}{\partial z} = D_t \frac{\partial^2 p_t}{\partial z^2} + \frac{D_t}{r}\frac{\partial}{\partial r}\left(r \frac{\partial p_t}{\partial r}\right), \ -\infty < z < \infty, \ R_c < r < R_t, \tag{9.4}$$

Equation 9.3 and 9.4, represents the convection - diffusion of species in blood and tissue respectively. The first term in the left hand side of both the equation is for unsteady flow and the second term is for convection. First, second and third terms in the right hand side of equation 9.3 are diffusion, convection, and first order kinetics in blood, while in tissue pure convection is considered.

9.2.2 Initial and boundary conditions

Initial condition, $p(z, r, t_0)$, for $t = t_0$ for $0 \le r \le R_t$ are as follows:

$$\begin{aligned} &p(z, r, t_0) = \exp(-fr), \quad |z| \le z_s, \\ &p(z, r, t_0) = 0, \quad |z| > z_s, \\ &p_t(z, r) = 0 \quad \forall\, z, \end{aligned} \tag{9.5}$$

where z_s is the length of initial slug input and $t_0 \approx 0$.

The following boundary conditions are relevant for the present study:

1. For radial symmetry,

$$\frac{\partial p}{\partial r} = 0, \;\; r = 0, -\infty < z < \infty, \tag{9.6}$$

2. No flux beyond closed boundaries,

$$\frac{\partial p_t}{\partial r} = 0, \;\; r = R_t, -\infty < z < \infty, \tag{9.7}$$

3. Assuming, first order kinetic reactions occur between tissue-blood capillary interface so,

$$\begin{aligned} &- D_c \alpha_c \frac{\partial p}{\partial r} - \alpha_c \Gamma p - K\left(\alpha \alpha_c p - \alpha_t p_t\right) = \alpha_t \frac{\partial p_t}{\partial t} = k\left(\alpha \alpha_c p - \alpha_t p_t\right) - \lambda_t \alpha_t p_t, \\ &r = R_c, -\infty < z < \infty. \end{aligned} \tag{9.8}$$

4. Boundary conditions for tissue,

$$p_t = 0, \;\; R_c < r < R_t, z \to -\infty, \tag{9.9}$$

$$\frac{\partial p_t}{\partial z} = 0, \;\; R_c < r < R_t, z \to +\infty. \tag{9.10}$$

5. Boundary conditions for blood,

$$p = 0, \;\; 0 < r < R_c \;\; z \to -\infty, \tag{9.11}$$

$$\frac{\partial p}{\partial z} = 0, \;\; 0 < r < R_c, z \to +\infty, \tag{9.12}$$

6. Pressure continuous beyond the interface so,

$$p|_{z=R_c^-} = p|_{z=R_c^+}, \tag{9.13}$$

$$\alpha_c D_c \frac{\partial p}{\partial r}|_{z=R_c^-} = \alpha_t D_t \frac{\partial p}{\partial r}|_{z=R_c^+}. \tag{9.14}$$

In the above equations the coefficients λ' and λ_t are the first order reaction rate constants for mobile and immobile phases respectively [166].

According to Henry's law [87], diffusion coefficient incorporates diffusivity, solubility, cross sectional area and tissue thickness. Among these factors, we focused only on tissue porosity. To implement this assumption we used a relation between porosity (ϵ) of tissue and its permeability (K) in equation 9.8, which is defined by Ergun and Orning [57] as follows:

$$K = \frac{\epsilon^3 d^2}{150\left(1-\epsilon\right)^2}, \tag{9.15}$$

where, d is the diameter of tube.

9.3 Methodology

9.3.1 Transformation of the governing equations

To solve the governing equations 9.1 - 9.4 numerically we have to make above equations dimensionless by using following quantities:

$$P^* = \frac{p}{P_0}, P_t^* = \frac{p_t}{R_t P_0}, x^* = \frac{r}{R_c}, X^* = \frac{r}{R_t}, z^* = \frac{z}{R_c^2 u_0/D_c}, Z^* = \frac{z}{R_t^2 u_0/D_t}, t^* = \frac{t}{R_c^2/D_c},$$
$$T^* = \frac{t}{R_t^2/D_t}, DA^* = \frac{kR_c}{D_c}, \alpha^* = \frac{\alpha}{R_c}, \Gamma^* = \frac{R_c\Gamma}{D_c}, Pe = \frac{R_c u_0}{D_c}, \lambda^* = \frac{\lambda' R_c^2}{D_c},$$

where P_0 is the initial pressure by surrounding organs.

After dropping asterisk (*) we got non-dimensional equation for blood as

$$\frac{\partial P}{\partial t} + \left(1-x^2\right)\frac{\partial P}{\partial z} = \frac{1}{Pe^2}\frac{\partial^2 P}{\partial z^2} + \frac{1}{x}\frac{\partial}{\partial x}\left(x\frac{\partial P}{\partial x}\right) - \lambda' P, \tag{9.16}$$

for tissue,

$$\frac{\partial P_t}{\partial t} + \frac{\left(1-X^2\right)}{\epsilon}\frac{\partial P_t}{\partial Z} = \frac{1}{Pe^2}\frac{\partial^2 P_t}{\partial Z^2} + \frac{1}{X}\frac{\partial}{\partial X}\left(X\frac{\partial P_t}{\partial X}\right), \tag{9.17}$$

Transformed initial and boundary conditions from equation 9.5 - 9.14 are defined as

$$\begin{aligned} &P(z,x,t_0) = \exp(-fx), \ \ |z| \le z_s, 0 \le X \le 1, \\ &P(z,x,t_0) = 0, \ \ |z| > z_s, 0 \le X \le 1, \\ &P_t(z,x) = 0, \ \ \forall\, z, \end{aligned} \tag{9.18}$$

$$\frac{\partial P}{\partial x} = 0, \ \ x = 0, -\infty < z < \infty, \tag{9.19}$$

$$\frac{\partial P_t}{\partial X} = 0, \;\; X = 1, -\infty < Z < \infty, \tag{9.20}$$

$$-\frac{D_c \alpha_c}{R_c}\frac{\partial P}{\partial x} - \frac{\alpha_c D_c \Gamma P}{R_c} - K\left(\alpha \alpha_c R_c P - \alpha_t P_t\right) = \frac{\alpha_t D_t}{R_t}\frac{\partial P_t}{\partial t} = k\left(\alpha R_c \alpha_c P - \alpha_t P_t\right) - \frac{\lambda_t D_c \alpha_t P_t P}{R_c^2}, x = 1, -\infty < z < \infty, \tag{9.21}$$

$$\frac{\partial P_t}{\partial z} = 0, \;\; X = 1, z \to \pm\infty, \tag{9.22}$$

$$\frac{\partial P}{\partial z} = 0, \;\; 0 \leq x \leq 1, z = \infty, \tag{9.23}$$

A convection controlled problem requires a sharp gradient. So, we calculated the integral for the sectional average by using Simpson's 1/3 rule for partial pressure distribution $\bar{P}$ at each time level, since $\bar{P}$ is a function of axial coordinate so, the term can be defined as follows

$$\bar{P}(z,t) = 2\int_0^1 prdr, \tag{9.24}$$

additionally, the spatial moments of the partial pressure distribution for the mobile phase are specified as

$$O_n = \int_{-\infty}^{\infty} z^n \bar{P} dz \;\; (n = 0, 1, 2...), \tag{9.25}$$

where the, variance of the distribution is found by following formulation,

$$\sigma^2(t) = \frac{O_2}{O_0} - \frac{O_1^2}{O_0^2}. \tag{9.26}$$

The coefficient of partial pressure dispersion P_d, which varies with time, is specified by half the rate of change of the variance of the distribution, σ^2, so the term is defined as follows

$$P_d(t) = \frac{1}{2}\frac{d\sigma^2}{dt}. \tag{9.27}$$

9.4 Numerical Scheme

Finite difference method [214] is the most suitable technique for nonlinear problems related to regular geometries so, to find the solution of the non - dimensional governing equations 9.16-9.17

subject to the initial and boundary conditions 9.18 - 9.23 we used this method. The computational grid are defined in the following form where the discretization of concentration, $P(r, z, t)$, is written as $P(r_i, z_j, t_n)$ or $P_{i,j}^n$.

$$
\begin{aligned}
&x_i = i\Delta r, (i = 0, 1, 2, 3, 4, ...N)\ r_N = 1,\\
&z_j = j\Delta z, (j = 0, 1, 2, 3, 4, ...M),\\
&t_k = (k-1)\Delta t, (k = 1, 2, ...),
\end{aligned}
$$

where i, j and k are the space and time index; $\Delta r, \Delta z$, and Δt are the increment in axial, radial and time respectively. We used central difference approximations, for all the spatial derivatives, as follows:

$$\frac{\partial P}{\partial z} = \frac{P_{i,j+1}^k - P_{i,j-1}^k}{2\Delta z}, \tag{9.28}$$

$$\frac{\partial^2 P}{\partial z^2} = \frac{P_{i,j+1}^k - 2P_{i,j}^k + P_{i,j-1}^k}{(\Delta z)^2}, \tag{9.29}$$

and forward difference approximation for first order time derivative at point (x_i, z_j, t_k) as follows

$$\frac{\partial P}{\partial t} = \frac{P_{i,j}^{k+1} - P_{i,j}^k}{2\Delta t}. \tag{9.30}$$

moreover, at $r = 0$ equation 9.16 - 9.17 converts as [2]

$$\lim_{r\to 0} \frac{1}{r}\frac{\partial p}{\partial r} = \lim_{r\to 0} \frac{\partial^2 p}{\partial r^2}, \tag{9.31}$$

$$
\begin{aligned}
P_{i,j}^{k+1} = &\left(1 - \frac{2r_1}{Pe^2} - 4r_2 - \lambda'\Delta t\right) P_{i,j}^k + \left(\frac{r_1}{Pe^2} - \frac{\Delta z r_1}{2}\right) P_{i,j+1}^k + \left(\frac{r_1}{Pe^2} + \frac{\Delta z r_1}{2}\right) P_{i,j-1}^k\\
&+ 2r_2\left(P_{i+1,j}^k - P_{i-1,j}^k\right),
\end{aligned} \tag{9.32}
$$

and at $0 < x \leq 1$, as follows:

$$
\begin{aligned}
P_{i,j}^{k+1} = &\left(1 - \frac{2r_1}{Pe^2} - 2r_2 - \lambda'\Delta t\right) P_{i,j}^k + \left(\frac{r_1}{Pe^2} - \frac{(1-x^2)\Delta z r_1}{2}\right) P_{i,j+1}^k\\
&+ \left(\frac{r_1}{Pe^2} + \frac{(1-x^2)\Delta z r_1}{2}\right) P_{i,j-1}^k + r_2\left(P_{i+1,j}^k + P_{i-1,j}^k\right) + \frac{\Delta x r_2}{2}\left(P_{i+1,j}^k - P_{i-1,j}^k\right),
\end{aligned} \tag{9.33}
$$

---

[2] When $r \to 0$, we found that the denominator is also approaching to zero and make the term indeterminate, which is inappropriate for the physical state of the respiratory system. Therefore, to remove this kind of inconsistency we used L'hospital rule of limit here.

equation 9.17 for tissue, at $x = 0$, get its discretized form as follows

$$\begin{aligned} P^{k+1}_{t_{i,j}} = {} & \left(1 - \frac{2r_1}{Pe^2} - 4r_2\right) P^k_{t_{i,j}} + \left(\frac{r_1}{Pe^2} - \frac{\Delta z r_1}{2\epsilon}\right) P^k_{t_{i,j+1}} + \left(\frac{r_1}{Pe^2} + \frac{\Delta z r_1}{2\epsilon}\right) P^k_{t_{i,j-1}} \\ & + 2r_2 \left(P_{t^k_{i+1,j}} - P^k_{t_{i-1,j}}\right), \end{aligned} \tag{9.34}$$

and at $0 < x \leq 1$, as follows

$$\begin{aligned} P^{k+1}_{t_{i,j}} = {} & \left(1 - \frac{2r_1}{Pe^2} - 2r_2\right) P^k_{t_{i,j}} + \left(\frac{r_1}{Pe^2} - \frac{(1-x^2)\,\Delta z r_1}{2\epsilon}\right) P^k_{t_{i,j+1}} + r_2 \left(P^k_{t_{i+1,j}} + P^k_{t_{i-1,j}}\right) \\ & + \left(\frac{r_1}{Pe^2} + \frac{(1-x^2)\,\Delta z r_1}{2\epsilon}\right) P^k_{t_{i,j-1}} + \frac{\Delta x r_2}{2} \left(P^k_{t_{i+1,j}} - P^k_{t_{i-1,j}}\right), \end{aligned} \tag{9.35}$$

where

$$r_1 = \frac{\Delta t}{\Delta z^2}, \quad r_2 = \frac{\Delta t}{\Delta x^2}.$$

The initial and boundary conditions from equation 9.18 - 9.23 in discretized form are as follows:

$$P^k_{i,1} = 0, \;\; P^k_{i,2} = P^k_{i,0}, \;\; P^k_{t_{i,1}} = 0, \;\; P^k_{t_{i,2}} = P^k_{t_{i,0}}, \;\; P^k_{2,j} = P^k_{0,j}, \tag{9.36}$$

Equation 9.32 - 9.35 gives partial pressure distribution at the $(k+1)^{th}$ time level in terms of partial pressure at k^{th} time level.

9.5 Results and Discussion

In this study we fixed some parameters in all the cases (see, Table 9.2). Problem have been solved for eight different combinations of α, DA and Γ as listed below in Table 9.3, where case (i) no gas exchange case, cases (ii) to (vii) correspond to the increase of phase exchange rate, DA, and cases (iii) and (viii) correspond to the increase of absorption rate, Γ. The initial slug length (z_s) is varied from 0.008 to 0.02.

First, we tested the grid dependency for different grid sizes in both the spatial directions, r and z; and found that the results remain consistent and grid independent, when the grid size is 40x1000, for $\Delta r = 0.025$, $\Delta z = 0.001$ along the radial and axial directions by choosing the time step $\Delta t = 0.0001$. The grid mesh is uniform both axially and radially. In this manner, entire calculations are done by taking the grid size 40x1000. The result appeared to converge with the accuracy of the order

10^{-4}. Following stability criteria is used to deal with the accuracy at each time level so that less error occurred in the numerical computation

$$\max\left(\frac{\Delta t}{\Delta x^2}\right) \leq 0.5. \tag{9.37}$$

Before discussing the analysis of the present problem a numerical code validation and predictive accuracy of the model are checked by comparing output data produced by present model removing radial mixing and intra capillary gas transport with respective results generated by model of Saini et al. [193] for partial pressure at breath rate (f) = 1 to 10 and represented in Figure 9.2.

Saini et al. [193] studied unsteady partial pressure of inert gas by generalized diffusion equations without considering radial mixing and intra capillary flow. Figure 9.2 shows variation in partial pressure with axial distance. We found that our numerical result is validated with their result of up to 99.9%. So, we can say, our results are in excellent agreement with those of Saini et al. [193].

9.5.1 Mean breakthrough curves based on the area-average partial pressure for different axial points

For eight particular cases of short distance development of the mean breakthrough curves are obtained through the area-mean partial pressure and shown in Figure 9.3 for four dimensionless axial positions, ranging from a short distance, z = 0.05 to 0.3. The following observations are made.

In Figure 9.2, during the early phases (z = 0.05) from the injection point (z_s=0.002), the transport is largely kinematic, and the solute spread is dominated by convection, the curve is strongly asymmetric, exhibiting a peak upon its initial sharp rise, followed by a gradual decline first according to the kinematic limit at time, t = 0.075, and then branching out from this limit because of radial diffusion from blood to tissue, in all the cases (i)-(viii). As soon as the gas diffuses outward from the faster moving inner part, the breakthrough curve deviates from the kinematic limit, and giving rise to a point of inflection or a shoulder in the curve, as in cases (ii)-(viii). However, the emergence of the shoulder is stronger in cases (vi), (vii) than in cases (iii), (viii). The reason of increment in the partial pressure of the gas in blood might be the higher value of DA, $50 \leq DA \leq 100$, which cause lower diffusion of diffusion (cases (vi)-(vii)). After this at t = 0.10, the partial pressure of gas in blood starts decreasing and curve infinitely long tail after t = 0.20, either due to increment in absorption rate ($0.1 \leq \Gamma \leq 1$) or due to continuous diffusion (case (ii)-(v) & (viii)).

At a farther distance from the injection point (z = 0.1), in Figure 9.3(a), convection peak is reduced and the shoulder part of the curve becomes more developed and sharp as compared to the previous graph. A similar trend emerges in Figure 9.3(b) (z = 0.15), where convection peak decreases in all the cases and the diffusional peak become the main feature of the mean breakthrough curve. Due to highly permeable tissue, a large quantity of gas from the immobile phase will be dispersed back to the mobile phase and hence we got high partial pressure of the gas in blood in cases (vi) & (vii).

At a sufficiently long distance from the injection point (z = 0.3), the sharp initial rise gradually replaced by a gentle rise, while the rounded second peak is fully developed to become the broadened peak in cases (i)-(iv) & (viii). Value of partial pressure of the gas in mobile phase becomes very high (cases (vi) & (vii)) comparable to other cases (may be due to low diffusion, high Damkohler number or backflow of gas caused by a highly permeable wall, (Figure 9.3(c)). This is the onset of the Taylor-Aris regime, as the axial distribution become increasingly symmetrical about its peak approaching a Gaussian distribution (in cases (i), (iii) & (viii)).

9.5.2 Mean breakthrough curves based on the area-average partial pressure at different time

Graphs of area-mean partial pressure are plotted in Figure 9.4 to demonstrate the dispersion effect of the chemical species for four dimensionless moments of time at t = 0.05, t = 0.15, t = 0.3, and t = 0.5 respectively.

During the early phase development or at short time (t = 0.05) from the injection point (z_s = 0.002), the transport is balanced by two peaks, first due to convection and second due to radial diffusion in all the cases (i)-(viii), in Figure 9.4(a), area under the distribution curve is markedly increased form cases (iv)-(vii) due to decrement in diffusion rate (increment in DA 10 to 100). While in this figure we noticed by increasing absorption rate (Γ = 0.1 to 1) area average partial pressure of gas in blood is decreased (compare cases (iii) & (viii)). In Figure 9.4(b), the larger spread of the distribution, in all the cases, arise from the interaction of convection with radial diffusion through permeable tissue, and diffusional peak decline from the previous state. The increase of area under the distribution curves and decline of the diffusional peak is a result of releasing gas which has been stored in immobile phase, back to the flow due to highly permeable tissue shown in cases (vi) and (vii).

Figure 9.4(c) shows that, for cases (i)-(iii) & (viii), the distribution curves are single-peaked. However, diffusion peaks become more developed at this stage. In cases (v)-(vii), due to increment in the partial pressure of the gas in the blood.

In Figure 9.4(d), it is clear that the skewness is very small in cases (i)-(iii) & (viii), supporting that the Gaussian form is readily developed in this case. In case (v) & (vii), the diffusional peak continues to broaden to become the dominant feature of the distribution. This is because a long time is required to approach the fully-developed state if $10 < DA \leq 100$. In addition, it is clear that the area under the partial pressure distribution curve in case (v) is not much different than the case (iii).

This follows from the fact that for a very high absorption rate (Γ = 1), the long-time dispersion will be attained because all the gas is taken away from the system.

9.5.3 Impact of breathing rate (f) on partial partial pressure of immobile phase

Figure 9.5(a) showed the variation in area average partial pressure with respect to axial position (at t = 0.05, porosity (ϵ) = 0.9) and Figure 9.5(b) showed the variation in area average partial pressure with respect to time (on axial position = 0.05, ϵ = 0.9) at breathing rate (f) = 1-9 per minutes. From these figures, we observed that the partial pressure of gas first decreased in immobile phase with respect to axial position and time by increasing value of f up to 5 and after that partial pressure is suddenly increased by increasing value of f. The sudden change in the distribution of partial pressure might be due to highly porous tissues ϵ = 0.9, since the over-inflation of the alveoli (air sacs in the lung) involve impaired exchange of gases, therefore, as the breathing rate increased partial pressure increases.

9.5.4 Impact of porosity (ϵ) on partial pressure of immobile phase

In Figure 9.6(a), single peak appears when $\epsilon = 0.4$ and it becomes double as we increase ϵ up to 0.9. The appearance of second peak is due to increment in diffusion which causes continuous exchange of gases from tissue to blood. Consequently, there is a decrement in area average partial pressure in tissue. Similar results are found with respect to time in Figure 9.6(b). Hence, by increasing porosity of tissue, exchange of gas increases between immobile and mobile phases. Consequently, from Figure 9.6, we observed that by increasing porosity of tissue, partial pressure of immobile phase or tissue with respect to time and axial distance is decreased.

9.5.5 Coefficient of dispersion of partial pressure from mean

Results obtained by present analysis (Table 9.4) are shown in Figure 9.7. The following interpretations are drawn.

1. The dispersion coefficient tends to a steady value after t = 0.25 in cases (i) to (v) and (viii), however for cases (vi) and (vii) it decreases with respect to time.

2. In cases (ii)-(iv) & (viii), the dispersion coefficient achieved steady-state values in a short time due to fast diffusion; $DA \leq 10$.

3. Cases (v)-(vii) consequent to slow diffusion and high absorption rate ($1 < DA \leq 100$ and $\Gamma \geq 1$), where dispersion coefficient moves towards steady-state limit in a long time. In other way we can say that long time dispersion is achieved under this cases (v)-(vii).

9.6 Conclusion

In this work we calculated the partial pressure distribution through a circular cylinder in which blood capillary is surrounded by tissue (i.e alveolar region, human airways and pulmonary membrane etc.) and undergoes linear first order kinetic reaction to exchange gas through the interface (tissue-blood barrier). We assumed porosity or permeability of tissue due to aging, emphysema, asthma or tuberculosis through which reversible and irreversible reactions occur (exchange of gas).

The governing equations are solved numerically by applying the finite difference method, we have examined short distance and short-time dispersion of gas in unsteady flow. The mean breakthrough curves are drawn with respect to axial distribution and time progression for partial pressure dispersion. The essential conclusions of the present work are stated below:

1. The second peak of the diffusion regime become more developed by the higher value of the Damkohler number ($10 < DA \leq 100$) and a higher retention rate ($\Gamma = 1$).
2. We found that with convection, the solute is completely spread out in a finite time and get its steady state very rapidly.
3. By increasing the value of porosity, the partial pressure distribution decreases in tissue because of most of the gas transfer to the mobile phase.
4. If the phase exchange rate is higher ($10 < DA \leq 100$) and porosity (ϵ) = 0.9, it need more extended time to advance toward a long-time dispersion.
5. In the accompanying circumstances, the dispersion coefficient advanced toward its steady-state limit in a short time at absorption rate ($\Gamma \leq 0.1$) and Damkohler number ($1 \leq DA \leq 10$).
6. As the breathing rate increases the partial pressure of the gas inside tissue first decreases and after some time it increases gradually with breathing rate.
7. Under the consideration of wall porosity or highly permeable wall, the convection speed is not changed but the diffusion of gas through tissue increases, which causes an increment in the partial pressure gradient of gas in blood phase.

Therefore, results obtained in this article regarding dispersion through circular is helpful to optimize the reactive condition of tissue-blood capillary inside the pulmonary region of the lung, where surrounded tissue of blood capillary become loose or excessively permeable due to aging, emphysema, asthma, and tuberculosis [155] etc.

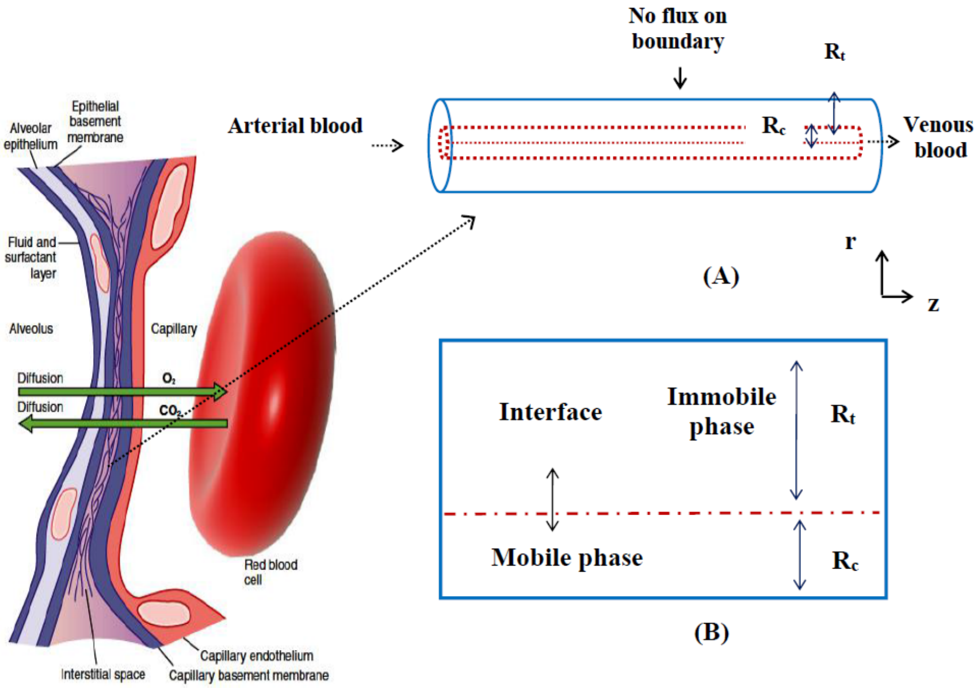

Figure 9.1: Pulmonary region, (A) tissue-blood capillary model with the impact of first order kinetic reactions between mobile (blood) and immobile phase (tissue), (B) cross sectional view of tissue-blood interface [78, 159, 195].

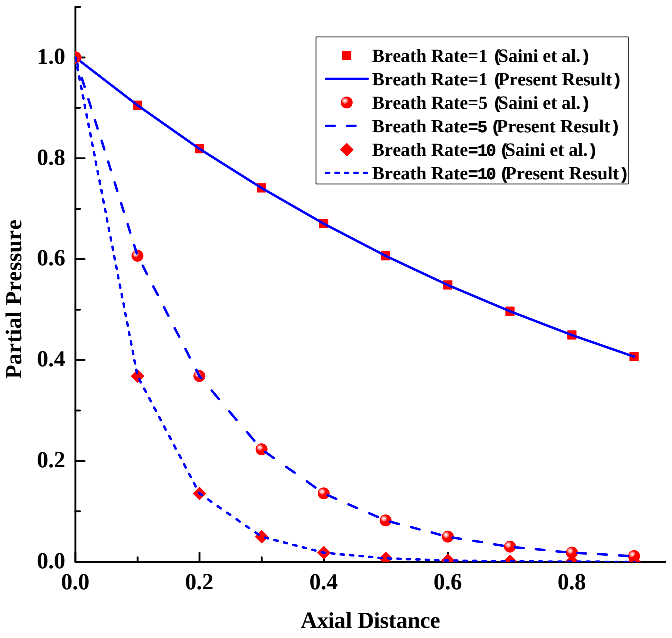

Figure 9.2: Result validation for partial pressure at breath rate $f = 1$ to 10.

Table 9.1: Comparison of present results with published results (Saini et al. [193]) for various values of breathing rate f

	Breath Rate=1		Breath Rate=5		Breath Rate=10	
Distance	Saini et al. (2010) [193]	Present Result	Saini et al. (2010) [193]	Present Result	Saini et al. (2010) [193]	Present Result
0	1	1	1	1	1	1
0.1	0.90484	0.90483	0.60653	0.60652	0.36788	0.36786
0.2	0.81873	0.81872	0.36788	0.36787	0.13534	0.13533
0.3	0.74082	0.74081	0.22313	0.22303	0.04979	0.04979
0.4	0.67032	0.67031	0.13534	0.13533	0.01832	0.01831
0.5	0.60653	0.60652	0.08209	0.08207	0.00674	0.00674
0.6	0.54881	0.5488	0.04979	0.04979	0.00248	0.00248
0.7	0.49659	0.49658	0.0302	0.03016	9.11882E-4	9.11881E-4
0.8	0.44933	0.44932	0.01832	0.01831	3.35462E-4	3.35461E-4
0.9	0.40657	0.40656	0.01111	0.0111	1.2341E-4	1.234E-4

Table 9.2: Numerical parameters with there units

Variable	Name	Value	unit
D	Diffusion coefficient in blood	$1.62 * 10^{(} - 9)$	m^2/s
a	Radius of blood capillary	$2.5 * 10^{(} - 6)$	m
ϵ	Porosity of alveoli	0.7	-
f	Rate change parameter	1	$/min$
α_c	Solubility of oxygen in plasma	$2.49 * 10^{(} - 2)$	mol/m^3
α_t	Solubility of oxygen in tissue	$2.78 * 10^{(} - 2)$	mol/m^3
z_s	Initial slug length	0.02	-
Pe	Peclet Number	10^3	-

Table 9.3: Values of the controlling parameters considered for the present study where cases (ii)-(vii) correspond to the increase of phase exchange rate and cases (iii) and (viii) correspond to the increase of absorption rate

Case	α	DA	Γ	Remarks
(i)	0	0	0	No gas (oxygen) exchange
(ii)	0.5	0.1	0.1	Very Slow phase exchange rate
(iii)	0.5	1	0.1	Weak absorption rate
(iv)	0.5	10	0.1	Slow phase exchange rate
(v)	0.5	20	0.5	Moderate phase exchange rate
(vi)	0.5	50	1	Fast phase exchange rate
(vii)	0.5	100	1	Very fast phase exchange rate
(viii)	0.5	1	1	Fast absorption rate

Table 9.4: Coefficients of dispersion versus dimensionless time for all cases (i)-(viii)

time(t)	Case 1	Case 2	Case 3	Case 4	Case 5	Case 6	Case 7	Case 8
0.1	5.75E-10	6E-10	6E-10	7.65E-10	9.45E-10	1.485E-9	2.335E-9	6.15E-10
0.2	1.2E-10	1.505E-10	1.505E-10	4.015E-10	6.75E-10	1.46E-9	2.65E-9	1.595E-10
0.3	1.705E-12	3.13E-11	3.13E-11	2.93E-10	5.75E-10	1.365E-9	2.52E-9	3.45E-11
0.4	1.335E-15	2.985E-11	2.985E-11	2.93E-10	5.75E-10	1.345E-9	2.425E-9	3.405E-11
0.5	3.605E-17	3.015E-11	3.015E-11	2.945E-10	5.75E-10	1.325E-9	2.33E-9	3.56E-11
0.6	3.6E-17	3.04E-11	3.04E-11	2.96E-10	5.75E-10	1.305E-9	2.24E-9	3.72E-11
0.7	3.6E-17	3.07E-11	3.07E-11	2.97E-10	5.75E-10	1.285E-9	2.15E-9	3.885E-11
0.8	3.6E-17	3.1E-11	3.1E-11	2.985E-10	5.75E-10	1.265E-9	2.07E-9	4.06E-11
0.9	3.6E-17	3.13E-11	3.13E-11	3E-10	5.75E-10	1.25E-9	1.985E-9	4.24E-11
1	3.6E-17	3.16E-11	3.16E-11	3.015E-10	5.75E-10	1.23E-9	1.91E-9	4.43E-11

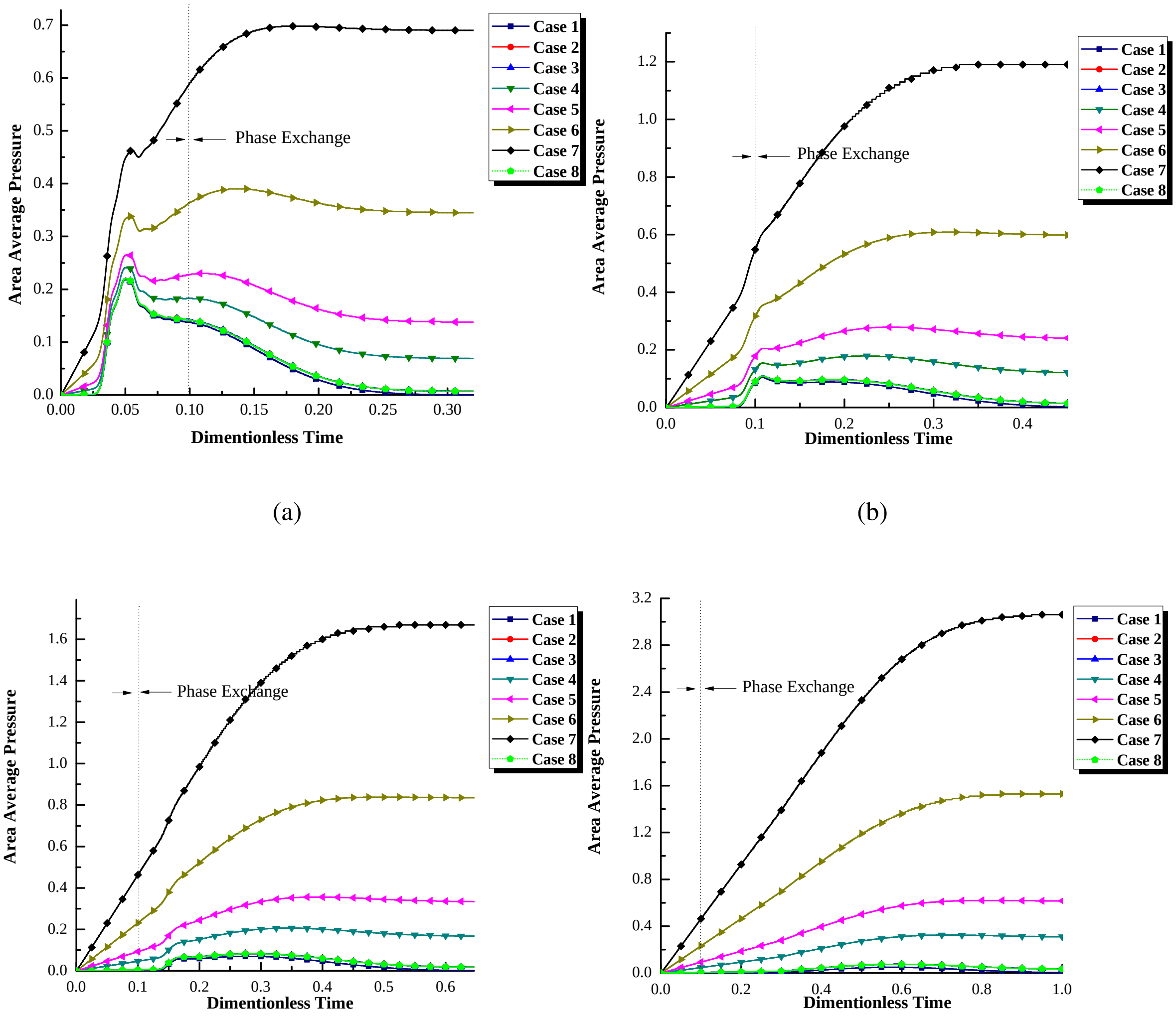

(a)

(b)

(c)

(d)

Figure 9.3: Breakthrough curves based on the area average partial pressure for short distance development of dispersion in a circular tube, at dimensionless axial positions (a) z = 0.05, (b) z = 0.01, (c) z = 0.15, and (d) z = 0.3,with Pe = 1000.

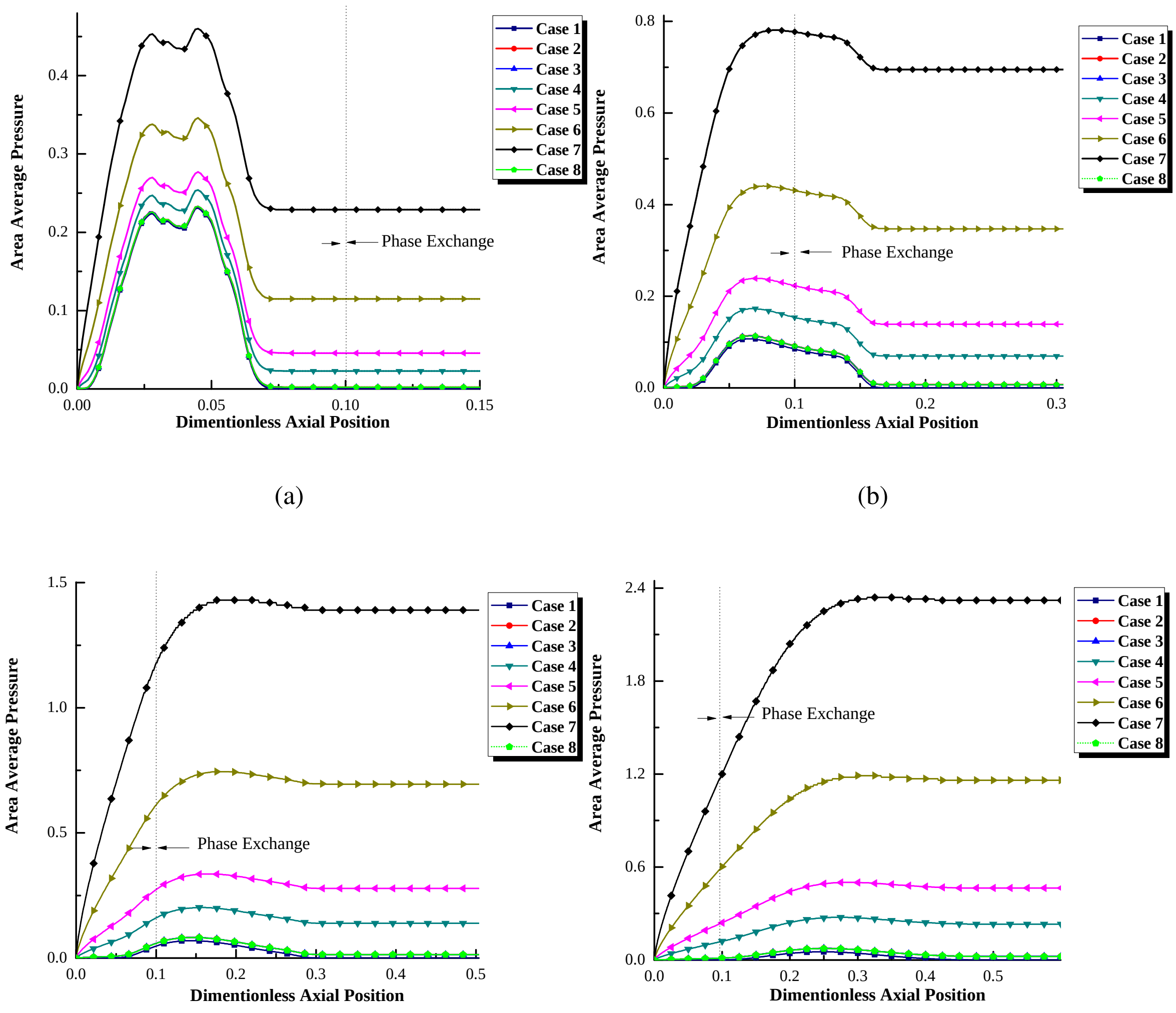

(a)

(b)

(c)

(d)

Figure 9.4: Breakthrough curves based on the area average partial pressure for short time development of dispersion in a circular tube, at dimensionless time (a) $t = 0.05$, (b) $t = 0.15$, (c) $t = 0.3$, and (d) $t = 0.5$, with $Pe = 1000$.

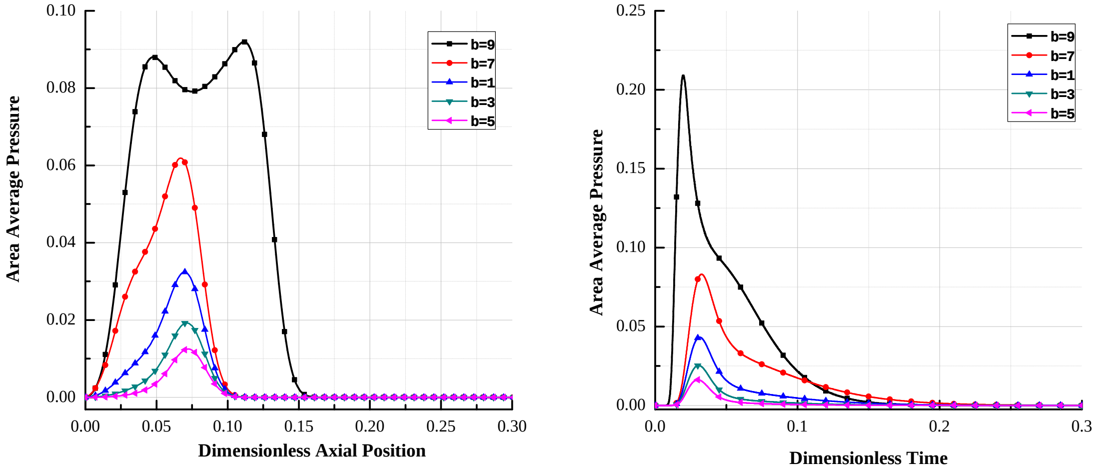

(a) (b)

Figure 9.5: Area-mean partial pressure profile of immobile phase at (a) z = 0.5 and (b) t = 0.05 at ϵ = 0.9, for β = 1 to 9.

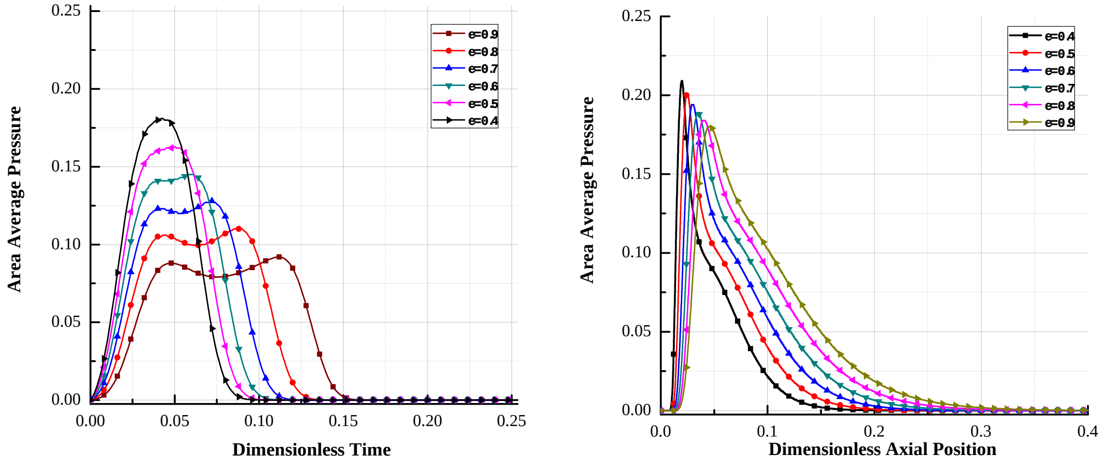

(a) (b)

Figure 9.6: Area-mean partial pressure profile of immobile phase at (a) z = 0.5 and (b) t = 0.05 at f = 1, for porosity ϵ = 0.4-0.9.

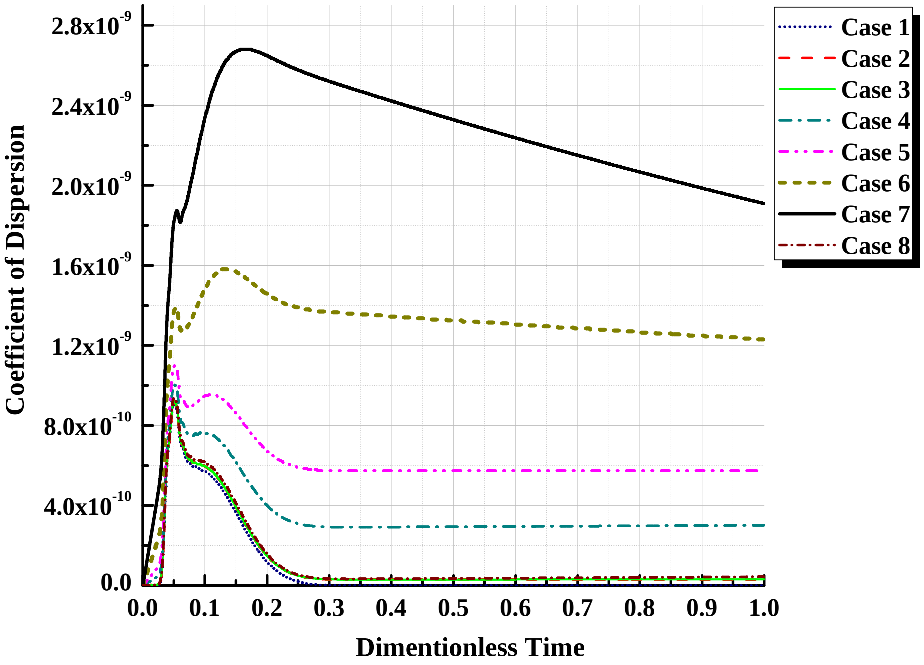

Figure 9.7: Coefficient of dispersion of mobile phase at $z = 0.05$ for all cases (i)-(viii).

Future Work

In the present thesis, the research carried out is a step taken forward in the direction to get the numerical simulation of various nonlinear problems arising due to inhalation of nonspherical nanoparticles utilizing conventional finite difference methods by assuming flow in regular geometry (airway, alveolar duct). Various conditions arise due to deposition of particle which is taken under consideration by incorporating the idea of particle shape factor and variable porosity. Effect of short time dispersion to understand the gas exchange and chemical species transport process are also considered. The present work for respiratory and lung mechanics can be extended further as:

1. Filtration efficiency of the lung with respect to other shapes and types of nonspherical nanoparticles such as (copper, silver, gold, titanium, etc.) in two or three-dimensional flow may be calculated.

2. Problem related to Couette flow can be extended to study the flow through lower airways or whole lung generations which may lead to a more general solution. Additionally, we can take other cases such as the movement of only one wall, when there is no pressure gradient, etc.

3. It is worth extending the study by analyzing the pressure of gas exchange between blood and tissue with other parameters such as variable porosity, solubility, and cross-sectional area. These parameters can be individually described within the model and may lead to a more general solution.

4. For problems related to nanoparticle deposition we have considered flow in the axial direction, but it can be extended by considering flow in radial direction too.

5. We can use two phases of gas transportation and carry out stability analysis between gas-blood barrier.

6. We can perform particle deposition and filtration efficiency analysis at a different height, weight, temperature, and gravity.

Appendix-A

Finite difference method

During the era of 1950 - 1970 finite difference method (FDM) was the most popular numerical technique applied to get solution of real life and practical problems where the domain is simple and structured. In this method simple arithmetic and finite discretization techniques were applied to solve complex differential equations mathematically; afterward, those mathematical equations are solved by developing computational code on C, C++, MATLAB, FORTRAN, etc. However, various numerical methods appeared to solve nonlinear complex partial differential equations but due to the simple applicability of finite difference method, it is still the most relevant method to get solution of these equations. FDM is used for solving different kind of boundary value and practical engineering problems that occur in many fields such as, heat transfer [120, 121, 154], stress or strain mechanics, fluid dynamics in river and air, biological system (immersed boundary cells), chemical processing, electromagnetics, and many other problems [72, 73]. It has been applied to a number of physical problems, linear or nonlinear, steady or unsteady, different boundary shapes and conditions, and many more. The most important aspect in FDM is to utilize a Taylor series expansion to discretize the differential equations of initial values and/or boundary values problems. The essential steps of this method are first chosen as an appropriate FDM scheme and replace every derivative of the equation directly by an algebraic expression. In this way, complex nonlinear ordinary or partial differential equation converts into a system of linear (non - linear) equations, which is solved by using computational programming. To solve the problem computationally one can the grid size should be very fine so that the error in the solution can be minimized to an acceptable level.

Process of applying FDM in the physical problem

The central theme in the finite difference simulation is the conversion of a physical problem involving the continuous variation of a field variable $f(x, y, z, t)$, into an approximate numerical formulation containing discrete value of f at spatial points (x_i, y_j, t_k) and the time levels t_p [214]. The spatial points are called nodes of the finite difference grid. The governing differential equations of the physical problem are approximated at the nodes, to generate algebraic equations for the nodal values of f. Finite difference method can be explained briefly in the following steps:

- Divide the whole domain into n regular nodes of equal length h (Figure 9.8)
- Replace the derivatives of different order in differential equation by using appropriate finite

difference approximation at each internal node by using following Taylor series of approximation as defined below,

$$f(x+h) = f(x) + hf'(x) + \frac{h^2}{2} f''(x) + ... \tag{9.38}$$

Forward difference equation,

$$f' = \frac{f_{i+1} - f_i}{h} + O(h), \tag{9.39}$$

$$f'' = \frac{f_{i+2} - f_{i+1} + f_i}{h^2} + O(h). \tag{9.40}$$

Backward difference,

$$f' = \frac{f_i - f_{i-1}}{h} + O(h), \tag{9.41}$$

$$f'' = \frac{f_i - f_{i-1} + f_{i-2}}{h^2} + O(h). \tag{9.42}$$

Central difference,

$$f' = \frac{f_{i+1} - f_{i-1}}{2h} + O(h^2), \tag{9.43}$$

$$f'' = \frac{f_{i+1} - f_i + f_{i-1}}{h^2} + O(h^2), \tag{9.44}$$

- Apply the boundary conditions
- Solve the discretized (set of algebraic) equations by a suitable matrix inversion or iterative technique.

Finite difference methods using enthalpy formulation of phase change problems include explicit method, semi implicit method, and fully implicit method. The explicit method is conditionally stable, while others are unconditionally stable.

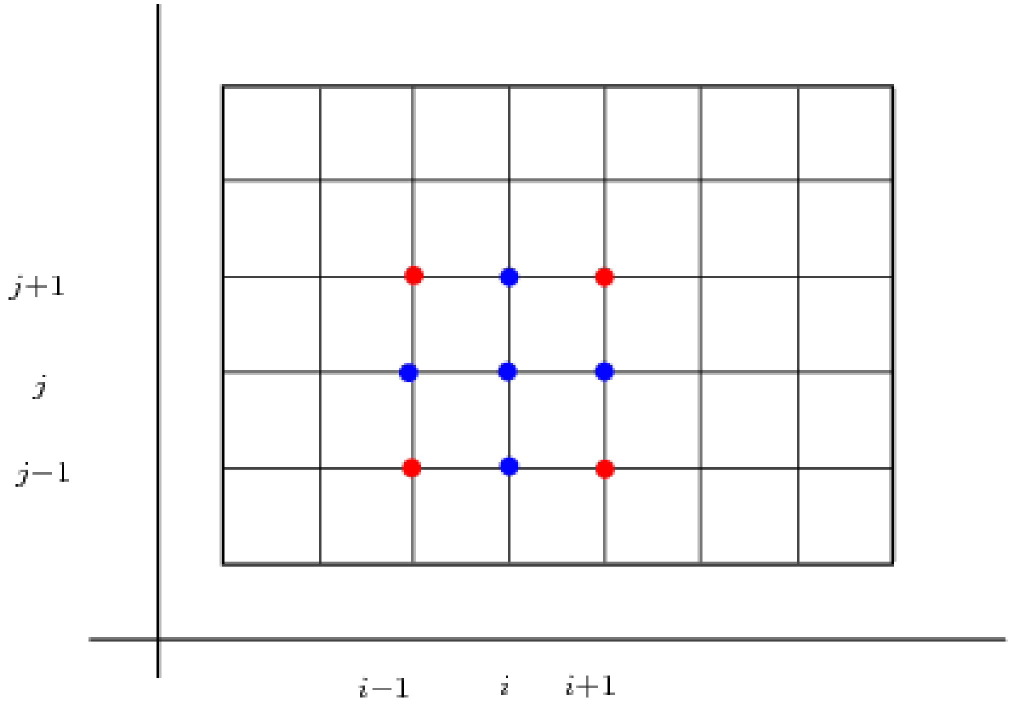

Figure 9.8: Computational uniform grid generation in finite difference method.

Bibliography

[1] Abrahamyan, M. G. (2018). Some aspects of the physics of gas flow in the respiratory system. *International Journal of Clinical and Experimental Medical Sciences*, 4(1):1–4.

[2] Agrawal, M., Adlakha, N., and Pardasani, K. R. (2010). Three dimensional finite element model to study heat flow in dermal regions of elliptical and tapered shape human limbs. *Applied Mathematics and Computation*, 217:4129–4140.

[3] Al-Mayah, A., Moseley, J., and Brock, K. K. (2008). Contact surface and material nonlinearity modeling of human lungs. *Physics in Medicine and Biology*, 53(1):305–317.

[4] Albaiceta, G., Blanch, L., and Lucangelo, U. (2008). Static pressure-volume curves of the respiratory system: were they just a passing fad? *Current Opinion in Critical Care*, 14(1):80–86.

[5] Alimohamadi, H. and Imani, M. (2014). Finite element simulation of two-dimensional pulsatile blood flow through a stenosed artery in the presence of external magnetic field. *International Journal for Computational Methods in Engineering Science and Mechanics*, 15(4):390–400.

[6] Almeida, M., Andrade, J. J., Buldyrev, S., Cavalcante, F., and Stanley, H. a. S. B. (1999). Fluid flow through ramified structures. *Physical Review E, Statistical Physics, Plasmas, Fluids, and Related Interdisciplinary Topics*, 60(5):5486–94.

[7] Andreassen, S., Steimle, K. L., Mogensen, M. L., de la Serna, J. B., Rees, S., and Karbing, D. S. (2010). The effect of tissue elastic properties and surfactant on alveolar stability. *Journal of Applied Physiology: Respiratory, Environmental and Exercise Physiology*, 109(5):1369–1377.

[8] Aris, R. (1958). On the dispersion of linear kinematic waves. *Proceedings of the Royal Society of London. Series A, Mathematical and Physical*, 245(1241):268–277.

[9] Asgharian, B., Menache, M. G., and Miller, F. J. (2004). Modeling age-related particle deposition in humans. *Journal of Aerosol Medicine*, 17(3):213–224.

[10] Axe, J. and Abbrecht, P. (1985). Analysis of the pressure-volume relationship of excised lungs. *Annals of Biomedical Engineering*, 13(2):101–117.

[11] Balashazy, I., Hofmann, W., Farkas, A., and Madas, B. G. (2008). Three-dimensional model for aerosol transport and deposition in expanding and contracting alveoli. *Inhalation Toxicology*, 20(6):611–621.

[12] Barton, N. (1983). On the method of moments for solute dispersion. *Journal of Fluid Mechanics*, 126:205–218.

[13] Behnkea, M. S., Kreylinga, W. G., Schulzb, H., Takenakaa, S., Butler, J. P., Henryd, F. S., and Tsuda, A. (2012). Nanoparticle delivery in infant lungs. *Proceedings of the National Academy of Sciences of the United States of America*, 109(13):5092–5097.

[14] Behrakis, P., Baydur, A., Jaeger, M., and Milic-Emili, J. (1983). Lung mechanics in sitting and horizontal body positions. *Chest*, 83(4):643–649.

[15] Belkaa, M., Lizala, F., Jedelskya, J., and Elcnera, Jakub Philip K. Hopkeb, M. J. (2018). Deposition of glass fibers in a physically realistic replica of the human respiratory tract. *Journal of Aerosol Science*, 117:149–163.

[16] Berg, E. J. and Robinson, R. J. (2011). Stereoscopic particle image velocimetry analysis of healthy and emphysemic alveolar sac models. *Journal of Biomechanical Engineering*, 133(6):061004– 061012.

[17] Birbrair, A., Zhang, T., Files, D., Mannava, S., Smith, T., Wang, Z., Messi, M., Mintz, A., and Delbono, O. (2014). Type-1 pericytes accumulate after tissue injury and produce collagen in an organ-dependent manner. *Stem Cell Research and Therapy*, 5(6):1–18.

[18] Bleuer, B. and Weibel, E. (1988). Morphometry of the human pulmonary acinus. *The Anatomical Record*, 220(4):401–414.

[19] Blum, J. (1960). Concentration profiles in and around capillaries. *The American Journal of Physiology*, 198(5):991–998.

[20] Brenner, H. and Edwards, D. (1993). *Macrotran sport processes*. Stoneham, MA.

[21] Bronzino, J. (2000). *Respiratory system in the biomedical engineering handbook*. Taylor & Francis Inc, Bosa Roca, United States.

[22] Carlson, B. E., Anderson, J. C., Raymond, G. M., Dash, R. K., and Bassingthwaighte, J. B. (2008). Modeling oxygen and carbon dioxide transport and exchange using a closed loop circulatory system. *Advances in Experimental Medicine and Biology*, 614:353–360.

[23] Cengel, Y. and Cimbala, J. (2013). *Fluid mechanics fundamentals and applications solutions manual*. McGraw-Hill.

[24] Chakravarty, S. and Datta, A. (1992). Pulsatile blood flow in a porous stenotic artery. *Mathematical and Computer Modelling*, 16(2):35–54.

[25] Chandran, K. B., Swanson, W. M., Ghista, D. N., and Vayo, H. W. (1974). Oscillatory flow in thin-walled curved elastic tubes. *Annals of Biomedical Engineering*, 2:392–412.

[26] Chang, H., Weber, M., and King, M. (1988). Mucus transport by high pusle rate non symmetrical oscillatory air flow. *Journal of Applied Physiology: Respiratory, Environmental and Exercise Physiology*, 65(3):1203–1209.

[27] Chatterjee, J., Haik, Y., and Chen, C. J. (2003). Size dependent magnetic properties of iron oxide nanoparticles. *Journal of Magnetism and Magnetic Materials*, 257:113–118.

[28] Chaturani, P. and Samy, R. P. (1986). Pulsatile flow of casson's fluid through stenosed arteries with applications to blood flow. *Biorheology*, 23:499–511.

[29] Chatwin, P. (1970). The approach to normality of the concentration distribution of solute in a solvent flowing along a straight tube. *Journal of Fluid Mechanics*, 43(2):321–352.

[30] Chatwin, P. and Sullivan, P. (1982). The effect of aspect ratio on rectangular longitudinal diffusivity channels. *Journal of Fluid Mechanics*, 120(1):347–358.

[31] Chena, X., Wenqi, Z., Tomb, J., Kleinstreuer, C., Fengd, Y., and He, X. (2016). Experimental-computational study of fibrous particle transport anddeposition in a bifurcating lung model. *Particuology*, 28:102–113.

[32] Chitra, M. and Karthikeyan, D. (2018). Mathematical modeling on unsteady mhd oscillatory blood flow in an inclined tapered stenosed artery with permeable wall: effects of slip velocity. *International Journal of Mathematics and its Applications*, 6(1):83–89.

[33] Chitwood, D. E., Devinny, J. S., and Reynolds, F. E. (1999). Evaluation of a two-stage biofilter for treatment of potw waste air. *Environmental Progress*, 18(3):212–22.

[34] Chuang, H., Hsiao, T., Wang, S., Tsay, S., and Lin, N. (2016). Characterization of particulate matter profiling and alveolar deposition from biomass burning in northern thailand. *Aerosol and Air Quality Research*, 16:2897–2906.

[35] Crowder, T., Rosati, J., Schroeter, J., Hickey, A., and TB, M. (2002). Fundamental effects of particle morphology on lung delivery: predictions of stokes' law and the particular relevance to dry powder inhaler formulation and development. *Pharmaceutical Research*, 19(3):239–245.

[36] Cunningham, E. (1910). On the velocity of steady fall of spherical particles through fluid medium. *Proceedings of the Royal Society*, 83:357.

[37] Darcy, H. (1856). *Les fontaines publiques de la volle de dijon*. Dalmont, V, Lyon Public Library.

[38] David, S., Butler, J., and Lewis, R. (2007). *Hole's human anatomy physiology*. Dubuque, IA: McGraw-Hill, 15 edition.

[39] Davidson, M. R. and Schroter, R. (1983). Theoretical model for absorption of gases by the bronchial wall. *Journal of Fluid Mechanics*, 129:313–335.

[40] Davies, G. and Reid, L. (1970). Growth of the alveoli and pulmonary arteries in childhood. *Thorax*, 25(6):669–681.

[41] Day, M. A. (1990). The no-slip condition of fluid dynamics. *Erkenntnis*, 33(3):285–296.

[42] DeGroot, C. and Straatman, A. (2018). A porous media model of alveolar duct flow in the human lung. *Journal of Porous Media*, 21:405–422.

[43] DeGroot, C. and Straatman, A. G. (2016). A conjugate fluid-porous approach for simulating airflow in realistic geometric representations of the human respiratory system. *Journal of Biomechanical Engineering*, 138(3):034501– 034507.

[44] Dey, S. K. (1999). A novel explicit finite difference scheme for partial differential equations. *Mathematical Modelling and Analysis*, 4(1):70–78.

[45] Dey, S. K. (2003). Computational modeling of the breast cancer treatment by immunotherapy, radiation and estrogen inhibition. *Scientiae Mathematicae Japonicae*, 58.

[46] Dey, S. K. and Dey, S. C. (2015). Mathematical modeling of breast cancer treatment. In Sarkar, S., Basu, U., and De, S., editors, *Applied Mathematics*, volume 146, pages 149–160. Springer.

[47] Donaldson, K., Aitken, R., Tran, L., Stone, V., Duffin, R., Forrest, G., and Alexander, A. (2006). Carbon nanotubes: a review of their properties in relation to pulmonary toxicology and workplace safety. *Toxicological Sciences*, 92(1):5–22.

[48] Doshi, M. R., Daiya, P. M., and Gill, W. N. (1978). Three-dimensional laminar dispersion in open and closed rectangular conduits. *Chemical Engineering Science*, 33(7):795–804.

[49] Dunnill, M. S. (1962). Postnatal growth of the lung. *Thorax*, 17:329–333.

[50] Dutta, A., Vasilescu, D., Hogg, J., Phillion, A., and Brinkerhoff, J. (2017). Simulation of airflow in an idealized emphysematous human acinus. *Journal of Biomechanical Engineering*, 140(7):071001–071010.

[51] Dyachenko, A. I. and Lyubimov, G. A. (1988). Propagation of sound in pulmonary parenchyma. *Plenum Publishing Corporation, New York, Washington*, 23:641–652.

[52] Dyachenko, A. I. and Manyuhina, O. V. (2006). Modeling of weak blast wave propagation in the lung. *Journal of Biomechanics*, 39(11):2113–2122.

[53] Ellahi, R., Rahman, S., Nadeem, S., and Vafai, K. (2015). The blood flow of prandtl fluid through a tapered stenosed arteries in permeable walls with magnetic field. *Communications in Theoretical Physics*, 63(3):353–358.

[54] Elnajjar, E., Haik, Y., Hamdan, M., and Khashan, S. (2013). Heat transfer characteristics of multi-walled carbon nanotubes suspension in a developing channel flow. *Heat Mass Transfer*, 49(9):1681–1687.

[55] Emery, J. L. and Mithal, A. (1961). The number of alveoli in the terminal respiratory unit of man during late intrauterine life and childhood. *Archives of Disease in Childhood*, 35(184):544–547.

[56] Eom, J., Xu, X., De, S., and Shi, C. (2010). Predictive modeling of lung motion over the entire respiratory cycle using measured pressure-volume data, 4dct images, and finite-element analysis. *Medical Physics*, 37(8):4389–4400.

[57] Ergun, S. and Orning, A. A. (1949). Fluid flow through randomly packed columns and fluidized beds. *Industrial & Engineering Chemistry*, 41(6):1179–1184.

[58] Fang, T. and Lee, C. F. (2006). Exact solutions of incompressible couette flow with porous walls for slightly rarefied gases. *Heat and Mass Transfer*, 42(3):255–262.

[59] Feng, Q., Liu, Y., Huang, J., Chen, K., Huang, J., and Xiao, K. (2018). Uptake, distribution, clearance, and toxicity of iron oxide nanoparticles with different sizes and coatings. *Scientific Reports*, 8(1):1–13.

[60] Fletcher, J. (1978). Mathematical modelling of the microcirculation. *Mathematical Biosciences*, 38(3-4):159–202.

[61] Freitag, L., Kim, C., Long, W., Venegas, J., and A, W. (1989). Mobilization of mucus by airway oscillations. *Acta Anaesthesiologica Scandinavica. Supplementum*, 90:93–101.

[62] Fuchs, N. (1994). *The mechanics of aerosols*. American Association for the Advancement of Science.

[63] Fulford, G. and Blake, J. (1986). Muco-ciliary transport in the lung. *Journal of Theoretical Biology*, 121(4):381–402.

[64] Fung, Y. (1974). A theory of elasticity of the lung. *Journal of Applied Mechanics*, 41(1):8–14.

[65] Fung, Y., Perrone, N., and Anliker, M. (1972). Biomechanics: its foundation and objects. Englewood Cliffs, N.J. : Prentice-Hall.

[66] Gefen, A., Elad, D., and Shiner, R. (1999). Analysis of stress distribution in the alveolar septa of normal and simulated emphysematic lungs. *Journal of Biomechanics*, 32(9):891–897.

[67] Geiser, M., Rutishauser, B. R., Kapp, N., Schürch, S., Kreyling, W., Schulz, H., Manuela, S., Hof, V. I., Heyder, J., and Gehr, P. (2005). Ultrafine particles cross cellular membranes by nonphagocytic mechanisms in lungs and in cultured cells. *Environmental Health Perspectives*, 113(11):1555–1560.

[68] Gersten, K. and Gross, J. (1974). Flow and heat transfer along a plane wall with periodic suction. *Zeitschrift Fur Angewandte Mathematik Und Physik*, 25(3):399–408.

[69] Gokhale, Y., Kumar, J., Hintz, W., Warnecke, G., and Tomas, J. (2008). *Population balance modelling for agglomeration and disintegration of nanoparticles*, chapter Micro-macro-interaction: in structured media and particle systems, pages 299–309. Springer.

[70] Goldman, D. (2008). Theoretical models of microvascular oxygen transport to tissue. *Microcirculation*, 15(8):795–811.

[71] Guo, Z., Kim, S., and Sung, H. (1997). Pulsating flow and heat transfer in a pipe partially filled with a porous medium. *International Journal of Heat and Mass Transfer*, 40(17):4209–4218.

[72] Gupta, A. K. and Katiyar, V. (2006). A new anisotropic continuum model for traffic flow. *Physica A: Statistical Mechanics and its Applications*, 368(2):551–559.

[73] Gupta, A. K. and Sharma, S. (2010). Nonlinear analysis of traffic jams in an anisotropic continuum model. *Chinese Physics B*, 19(11):110503.

[74] Gupta, P. S., Gupta, A. S., and Taylor, G. I. (1972). Effect of homogeneous and heterogeneous reactions on the dispersion of a solute in the laminar flow between two plates. *Proceedings of the Royal Society of London. A. Mathematical and Physical Sciences*, 330(1580):59–63.

[75] Haber, S., Yitzhak, D., and Tsuda, A. (1985). Gravitational deposition in a rhythmically expanding and contracting alveolus. *Journal of Applied Physiology: Respiratory, Environmental and Exercise Physiology*, 95(2):657–671.

[76] Haghigh, A. R. and Asl, M. S. (2015). Mathematical modeling of micropolar fluid flow through an overlapping arterial stenosis. *International Journal of Biomathematics*, 8(4):1550056–1550071.

[77] Haik, Y., Aldajah, S., and Elnajjar, E. (2013). Filter and process of use to produce carbon nano-tubes from automotive exhausts. *Patents and Intellectual Property*.

[78] Hall, J. E. and C, G. A. (2010). *Guyton and hall textbook of medical physiology*. Philadelphia, PA, Saunders Elsevier.

[79] Hallak, B., Specht, E., Herz, F., Gropler, R., and Warnecke, G. (2017). Influence of particle size distribution on the limestone decomposition in single shaft kilns. *Energy Procedia*, 120:604–611.

[80] Hansen, J. E., Ampaya, E. P., Bryant, G. H., and Navin, J. J. (1975). Branching pattern of airways and air spaces of a single human terminal bronchiole. *Journalof Applied Physiology*, 38(6):983–989.

[81] Hao, W., Marsh, C., and Friedman, A. (2015). A mathematical model of idiopathic pulmonary fibrosis. *Plos One*, pages 1–19.

[82] Hassan, M. S. and Lau, R. W. M. (2009). Effect of particle shape on dry particle inhalation: study of flowability, aerosolization, and deposition properties. *American Association of Pharmaceutical Scientists*, 10(4):1252–1262.

[83] Hatze, H. (1974). The meaning of the term: 'biomechanics'. *Journal of Biomechanics*, 7(2):189–190.

[84] Heller, J. (1960). An unmixing demonstration. *American Journal of Physics*, 28(4):348–353.

[85] Hennessy, T. (1974). The interaction of diffusion and perfusion in homogeneous tissue. *Bulletin of Mathematical Biology*, 36:505–526.

[86] Henry, F. S. and Tsuda, A. (2016). Onset of alveolar recirculation in the developing lungs and its consequence on nanoparticle deposition in the pulmonary acinus frank. *Journal of Applied Physiology: Respiratory, Environmental and Exercise Physiology*, 120(1):38–54.

[87] Henry, W. (1803). Experiments on the quantity of gases absorbed by water, at different temperatures, and under different pressures. *Philosophical Transactions of the Royal Society of London*, 93:29–274.

[88] Hess, D. (2008). Aerosol delivery devices in the treatment of asthma. *Respiratory Care*, 53(6):699–723.

[89] Heyder, J. (2004). Deposition of inhaled particles in the human respiratory tract and consequences for regional targeting in respiratory drug delivery. *Proceedings of the American Thoracic Society*, 1(4):315–320.

[90] Hinds, W. C. (1999). *Aerosol technology: properties, behavior, and measurement of airborne particles*. John Wiley & Sons, 2 edition.

[91] Hislop, A. and Reid, L. (1974). Development of the acinus in the human lung. *Thorax*, 29(1):90–94.

[92] Hodge, D. S. and Devinny, J. S. (1995). Modeling removal of air contaminants by biofiltration. *Journal of Environmental Engineering*, 121(1):21–32.

[93] Hoet, P. H., Hohlfeld, I. B., and Salata, O. V. (2004). Nanoparticles-known and unknown health risks. *Journal of Nanobiotechnology*, 2(12):1–15.

[94] Hofmann, W. (1982). Mathematical model for the postnatal growth of the human lung. *Respiration Physiology*, 49(1):115–129.

[95] Hogberg, S. M., Akerstedt, H. O., Lundström, T. S., and Freund, J. B. (2010). Respiratory deposition of fibers in the non-inertial regime-development and application of a semi-analytical model. *Aerosol Science and Technology*, 44(10):847–860.

[96] Hussain, M., Kumar, J., and Tsotsas, E. (2015). Modeling aggregation kinetics of fluidized bed spray agglomeration for porous particles. *Powder Technology*, 270:584–591.

[97] Hussain, S., Fernandez, M. R., Braun, G., Doyle, F., and Ruoslahti, E. (2014). Quantity and accessibility for specific targeting of receptors in tumours. *Scientific Reports*, 4:1–7.

[98] Ilegbusi, O., Seyfi, B., and Salvin, R. (2014). Patient-specific model of lung deformation using spatially dependent constitutive parameters. *Mathematical and Computer Modelling of Dynamical Systems*, 20(6):546–556.

[99] Ismail, Z., Abdullah, I., Mustapha, N., and Amin, N. (2008). A power-law model of blood flow through a tapered overlapping stenosed artery. *Applied Mathematics and Computation*, 195(2):669–680.

[100] Jahed, M., Lai-Fook, S., Bhagat, P., and Kraman, S. (1989). Propagation of stress waves in inflated sheep lungs. *Journal of Applied Physiology: Respiratory, Environmental and Exercise Physiology*, 66(6):2675–2680.

[101] Jiang, Q., Zhang, Z., and Wang, Y. (2000). Thermal stability of low dimensional crystals. *Materials Science and Engineering: A*, 286(1):139 – 143.

[102] Jiang, Y. and Grotberg, J. (1993). Bolus contaminant dispersion in oscillatory tube flow with conductive walls. *Journal of Biomechanical Engineering*, 115(4A):424–431.

[103] Jones, R. L., Lester, R. T., and Brown, N. E. (1995). Effects of high pulse rate chest wall compression on respiratory system mechanics in normal and cystic fibrosis patients. *Canadian Respiratory Journal*, 2(1):40–46.

[104] Kapur, J. N. (1985). *Mathematical models in biology and medicine*. Affiliated East-West Press.

[105] Kenneth, S. (2006). *Anatomy and physiology: the unity of form and function*. McGraw-Hill Education.

[106] Khaled, A. and Vafai, K. (2003). The role of porous media inmodeling flowand heat transfer in biological tissues. *International Journal of Heat and Mass Transfer*, 46(26):4989–5003.

[107] Khanafer, K., Cook, K., and Marafie, A. (2012). The role of porous media in modeling fluid flow within hollow fiber membranes of the total artificial lung. *Journal of Porous Media*, 15(2):113–122.

[108] Kim, J., Heise, R. L., Reynolds, A. M., and Pidaparti, R. M. (2017). Aging effects on airflow dynamics and lung function in human bronchioles. *Aging Effects on Airflow Dynamics and Lung Function in Human Bronchioles*, 12(8):1–20.

[109] King, M., Agarwal, M., and Shukla, J. (1993). A planar model for mucociliary transport: effect of mucus viscoelasticity. *Biorheology*, 30(1):49–61.

[110] Kittelson, D. (1998). Engines and nanoparticles: a review. *Journal of Aerosol Science*, 29(5-6):575–588.

[111] Kittelson, D. B., Watts, W. F., and Johnson, J. P. (2004). Nanoparticle emissions on minnesota highways. *Atmospheric Environment*, 38(1):9–19.

[112] Kittelson, D. B., Watts, W. F., and Johnson, J. P. (2006). On-road and laboratory evaluation of combustion aerosols-part1: summary of diesel engine results. *Journal of Aerosol Science*, 37(8):913–930.

[113] Kleinstreuer, C. and Feng, Y. (2013). Computational analysis of non-spherical particle transport and deposition in shear flow with application to lung aerosol dynamics-a review. *Journal of Biomechanical Engineering*, 135(2):021008–021027.

[114] Kleinstreuer, C., Zhang, Z., and Donohue, J. (2008). Targeted drug-aerosol delivery in the human respiratory system. *Annual Review of Biomedical Engineering*, 10:195–220.

[115] Koeppen, B. M. and Stanton, B. A. (2009). *Berne and levy physiology*. Mosby, 6 edition.

[116] Kohn, H. (1893). Zur histologie der indurierenden fibrinosen pneumonie. *Munchener Medicinische Wochenschrift*, 40:42–45.

[117] Koullapis, P., Kassinos, S., Bivolarova, M., and Melikov, A. (2016). Particle deposition in a realistic geometry of the human conducting airways: effects of inlet velocity profile, inhalation flowrate and electrostatic charge. *Journal of Biomechanics*, 49(11):2201–2212.

[118] Krogh, A. (1919). The supply of oxygen to the tissue and the regulation of the capillary circulation. *The Journal of Physiology*, 52(6):457–474.

[119] Kulkarni, P., Baron, P. A., and Willeke, K., editors (2011). *Aerosol measurement: principles, techniques, and applications*. John Wiley and Sons.

[120] Kumar, A., Kumar, S., Katiyar, V. K., and Telles, S. (2017a). Dual phase lag bio-heat transfer during cryosurgery of lung cancer: comparison of three heat transfer models. *Journal of Thermal Biology*, 69:228237.

[121] Kumar, A., Kumar, S., Katiyar, V. K., and Telles, S. (2017b). Phase change heat transfer during cryosurgery of lung cancer using hyperbolic heat conduction model. *Computers in Biology and Medicine*, 84(1):20–29.

[122] Kumar, B. and Naidu, K. (1996). A pulsatile suspension flow simulation in a stenosed vessel. *Mathematical and Computer Modelling*, 23(5):75–86.

[123] Kumar, J. and Warnecke, G. (2010). A note on moment preservation of finite volume schemes for solving growth and aggregation population balance equations. *SIAM Journal on Scientific Computing*, 32(2):703–713.

[124] Kumari, K. and Goyal, M. (2017). Viscous dissipation and mass transfer effects on mhd oscillatory flow in a vertical channel with porous medium. *Advances in Dynamical Systems and Applications*, 12(2):205–216.

[125] Kurbatova, P., Bessonov, N., Volpert, V., Tiddens, H., Cornu, C., Nony, P., and Caudri, D. (2015). Model of mucociliary clearance in cystic fibrosis lungs. *Journal of Theoretical Biology*, 372:81–88.

[126] Kuwahara, F., Sano, Y., Liu, J., and Nakayama, A. (2009). A porous media approach for bifurcating flow and mass transfer in a human lung. *Journal of Heat Transfer*, 131(10):101013–101015.

[127] Lai, S. K., Wang, Y. Y., Wirtz, D., and Hanes, J. (2009). Micro and macrorheology of mucus. *Advanced Drug Delivery Reviews*, 61(2):86–100.

[128] Lau, M. and Ng, C. O. (2007). On the early development of dispersion in flow through a tube with wall reactions. *International Journal of Mechanical, Aerospace, Industrial, Mechatronic and Manufacturing Engineering*, 1(9):485–490.

[129] Laurent, S., Forge, D., Port, M., Roch, A., Robic, C., Elst, L. V., and Muller, R. N. (2008). Magnetic iron oxide nanoparticles: synthesis, stabilization, vectorization, physicochemical characterizations, and biological applications. *Chemical Reviews*, 108(6):2064–2110.

[130] Lee, T., Liu, X., Li, G., and Low, H. (2007). Numerical study on sinusoidal fluctuated pulsatile laminar flow through various constrictions. *Communications in Computational Physics*, 2(1):99–122.

[131] Lewis, M. A. and Owen, M. R. (2001). The mechanics of lung tissue under high-frequency ventilation. *SIAM Journal on Applied Mathematics*, 61(5):1731–1761.

[132] Li, D., Xu, Q., Liu, Y., Libao, Y., and Jun, J. (2014). Numerical simulation of particles deposition in a human upper airway. *Advances in Mechanical Engineering*, pages 1–13.

[133] Liepsch, D. (1993). Fundamental flow studies in models of human arteries. *Frontiers of Medical and Biological Engineering : The International Journal of the Japan Society of Medical Electronics and Biological Engineering*, 5:51–5.

[134] Liepsch, D. (2002). An introduction to biofluid mechanics? basic models and applications. *Journal of Biomechanics*, 35(4):415–435.

[135] Liepsch, D. (2006). Biofluid mechanics-an interdisciplinary research area of the future. *Technology and Health Care : Official Journal of the European Society for Engineering and Medicine*, 14:209–14.

[136] Liepsch, D., Pallotti, G., Coli, L., Donati, G., Losinno, F., Freyrie, A., and Stefoni, S. (2003). Fluidodynamic evaluation of arteriovenous fistulae for hemodialysis. *The Journal of Vascular Access*, 4(3):92–105.

[137] Lillehoj, E. and Kim, K. (2002). Airway mucus: its components and function. *Archives of Pharmacal Research*, 25(6):770–780.

[138] Liu, B. and Tang, D. (2010). Computer simulations of atherosclerotic plaque growth in coronary arteries. *Molecular and Cellular Biomechanics*, 7(4):193–202.

[139] Liu, Y., Chandra, K., and Rosenberg, D. (1975). Angular acceleration of viscoelastic (kelvin) material in a rigid spherical shell-a rotational head injury model. *Journal of Biomechanics*, 8(5):285–292.

[140] Long, C., Suh, H., and Koutrakis, P. (2000). Characterization of indoor particle sources using continuous mass and size monitors. *Journal of the Air & Waste Management Association*, 50(7):1236–1250.

[141] Longmire, M., Choyke, P. L., and Kobayashi, H. (2008). Clearance properties of nano-sized particles and molecules as imaging agents: considerations and caveats. *Nanomedicine*, 3(5):703–717.

[142] Lu, T. W. and Chang, C. F. (2012). Biomechanics of human movement and its clinical application. *Kaohsiung Journal of Medical Sciences*, 28(2):S13–S25.

[143] Lucker, A., Weber, B., and Patrick, J. (2015). A dynamic model of oxygen transport from capillaries to tissue with moving red blood cells. *American Journal of Physiology Heart and Circulatory Physiology*, 308(3):H206–H216.

[144] Manhas, N. and Pardasani, K. R. (2014). Modelling mechanism of calcium oscillations in pancreatic acinar cells. *Journal of Medical Imaging and Health Informatics*, 4:1–7.

[145] Mazumdar, J. (1999). *An introduction to mathematical physiology and biology (cambridge studies in mathematical biology)*, chapter Biofluid Mechanics. Cambridge University Press.

[146] Mazumder, B. and Paul, S. (2012). Dispersion of reactive species with reversible and irreversible wall reactions. *Heat and Mass Transfer*, 48(6):933–944.

[147] McGuire, B. J. and Secomb, T. W. (2001). A theoretical model for oxygen transport in skeletal muscle under conditions of high oxygen demand. *Journal of Applied Physiology: Respiratory, Environmental and Exercise Physiology*, 91(5):2255–2265.

[148] Mehmood, O. U., Mustapha, N., and Shafie, S. (2012). Unsteady two-dimensional blood flow in porous artery, with multi-irregular stenoses. *Transport in Porous Media*, 92(2):259–275.

[149] Menache, M. G. and Graham, R. C. (1997). Conducting airway geometry as a function of age. *Annals of Occupational Hygiene*, 41(1):531–536.

[150] Miguel, A. F. (2012). *Lungs as a natural porous media: architecture, airflow characteristics and transport of suspended particles*, volume 13, pages 115–137. Springer, Berlin, Heidelberg.

[151] Milhorn, H. T. J., Benton, R., Ross, R., and Guyton, A. C. (1965). A mathematical model of the human respiratory control system. *Biophysical Journal*, 5:27–46.

[152] Miller, F., Mercer, R. R., and Crapo, J. D. (1993). Lower respiratory tract structure of laboratory animals and humans: dosimetry implications. *Aerosol Scicnce and Technology*, 18(3):257–271.

[153] Mina, E. M., Ghorbaniasl, G., and Lacor, C. (2018). Study of nanoparticles deposition in a human upper airway model using a dynamic turbulent schmidt number. *Ain Shams Engineering Journal*, 9(4):2389–2398.

[154] Mishra, T. N. and Rai, K. N. (2015). Implicit finite difference approximation for time fractional heat conduction under boundary condition of second kind. *International Journal of Applied Mathematical Research*, 4(1):135–149.

[155] Mujwar, S. and Pardasani, K. R. (2015). Prediction of riboswitch as a potential drug target and design of its optimal inhibitors for mycobacterium tuberculosis. *International Journal Computational Biology and Drug Design*, 8(4):326–347.

[156] Murphy, M. and Pokhrel, D. (2009). Optimization of an adaptive neural network to predict breathing. *Medical Physics*, 36(1):40–47.

[157] Nagaiah, C., Rudiger, S., Warnecke, G., and Falcke, M. (2012). Adaptive space and time numerical simulation of reaction-diffusion models for intracellular calcium dynamics. *Applied Mathematics and Computation*, 218(20):10194–10210.

[158] Nanda, K. K., Sahu, S. N., and Behera, S. N. (2002). Liquid-drop model for the size-dependent melting of low-dimensional systems. *Physical Review A*, 66(1):013208–013216.

[159] Ng, C. O. and Rudraiah, N. (2008). Convective diffusion in steady flow through a tube with a retentive and absorptive wall. *Physics of Fluids*, 20(7):073604–073625.

[160] Nithiarasu, P. and Ravindran, K. (1998). A new semi-implicit time stepping procedure for buoyancy driven flow in a fluid saturated porous medium. *Computer Methods in Applied Mechanics and Engineering*, 165(1-4):147–154.

[161] Oakes, J., Day, S., Weinstein, S., and Robinson, R. (2010). Flow field analysis in expanding healthy and emphysematous alveolar models using particle image velocimetry. *Journal of Biomechanical Engineering*, 132(2):021008–021009.

[162] Ochs, M., Nyengaard, J. R., Jung, A., Knudsen, L., Voigt, M., Wahlers, T., Richter, J., and Gundersen, H. (2004). The number of alveoli in the human lung. *American Journal of Respiratory and Critical Care Medicine*, 169(1):120–124.

[163] Omlor, A. J., Nguyen, J., Bals, R., and Dinh, Q. T. (2015). Nanotechnology in respiratory medicine. *Respiratory Research*, 16(1):1–9.

[164] Ozkaya, N., Nordin, M., Goldsheyder, D., and Leger, D. (2012). *Fundamentals of biomechanics:equilibrium, motion, and deformation*. Springer-Verlag New York, 3 edition.

[165] Parks, M. L. and Romero, L. A. (2007). Taylor-aris dispersion in high aspect ratio columns of nearly rectangular cross section. *Mathematical and Computer Modelling*, 46(5-6):699–717.

[166] Paul, S. and Mazumder, B. S. (2009). Transport of reactive solutes in unsteady annular flow subject to wall reactions. *European Journal of Mechanics - B/Fluids*, 28(3):411–419.

[167] Peterman, B. and Longtin, A. (1984). Multicompartment model of lung dynamics. *Computers and Biomedical Research, an International Journal*, 17(6):580–589.

[168] Philips, C. and Kaye, S. R. (1998). Approximate solutions for developing shear dispersion with exchange between phases. *Journal of Fluid Mechanics*, 374:195–219.

[169] Poland, C. A., Duffin, R., Kinloch, I., Maynard, A., Wallace, W. A. H., Seaton, A., Stone, V., Brown, S., MacNee, W., and Donaldson, K. (2008). Carbon nanotubes introduced into the abdominal cavity of mice show asbestos-like pathogenicity in a pilot study. *Nature Nanotechnology*, 3(7):423–428.

[170] Pollak, H. O. (2012). *Mathematical modeling handbook*. Teachers College Columbia University.

[171] Ponalagusamy, R. (2017). A two-layered suspension (particle-fluid) model for non-newtonian fluid flow in a catheterized arterial stenosis with slip condition at the wall of stenosed artery. *Korea-Australia Rheology Journal*, 29(2):87–100.

[172] Popel, A. (1989). Theory of oxygen transport to tissue. *Critical Reviews in Biomedical Engineering*, 17(3):257–321.

[173] Pozin, N. (2017). *Multiscale lung ventilation modeling in health and disease*. PhD thesis, Université Pierre Et Marie Curie-Paris.

[174] Preziosi, L. and Farina, A. (2002). On darcy's law for growing porous media. *International Journal of Non-Linear Mechanics*, 37(3):485–491.

[175] Pruthi, N. and Multani, N. (2012). Influence of age on lung function tests. *Journal of Exercise Science and Physiotherapy*, 8(1):1–6.

[176] Purnama, A. (1988). Boundary retention effect on contaminant dispersion in parallel shear flows. *Journal of Fluid Mechanics*, 195:393–412.

[177] Qi, W. H., Wang, M. P., and Liu, Q. H. (2005). Shape factor of nonspherical nanoparticles. *Journal of Materials Science*, 40(9-10):2737–2739.

[178] Qiao, H., Liu, W., Gu, H., Wang, D., and Wang, Y. (2015). The transport and deposition of nanoparticles in respiratory system by inhalation. *Journal of Nanomaterials*, pages 1–8.

[179] Quirk, J., Sukstanskii, A., Woods, J., Lutey, B., Conradi, M., Gierada, D., Yusen, RD Castro, M., and Yablonskiy, D. (1985). Experimental evidence of age-related adaptive changes in human acinar airways. *Journal of Applied Physiology: Respiratory, Environmental and Exercise Physiology*, 120(2):159–165.

[180] Raghu, G., Collard, H., Egan, J., Martinez, F., Behr, J., Brown, K., Colby, T., Cordier, J., Flaherty, K., Lasky, J., Lynch, D., Ryu, J., Swigris, J., Wells, A., Ancochea, J., Bouros, D., Carvalho, C., Costabel, U., Ebina, M., Hansell, D., Johkoh, T., Kim, D., King, T. J., Kondoh, Y., Myers, J., Müller, N., Nicholson, A., Richeldi, L., Selman, M., Dudden, R., Griss, B., Protzko, S., and Schünemann, H. (2011). An official ats/ers/jrs/alat statement: idiopathic pulmonary fibrosis: evidence-based guidelines for diagnosis and management. *American Journal of Respiratory and Critical Care Medicine*, 183:788–824.

[181] Rana, J. and Murthy, P. V. S. N. (2017). Unsteady solute dispersion in small blood vessels using a two-phase casson model. Proceedings of the Royal Society a: Mathematical, Physical and Engineering Sciences.

[182] Reddy, J. V. R., Srikanth, D., and Mandal, P. K. (2017). Computational hemodynamic analysis of flow through flexible permeable stenotic tapered artery. *International Journal of Applied and Computational Mathematics*, 3(1):1261–1287.

[183] Reneau, D., Bruley, D., and Knisely, M. (1967). A mathematical simulation of oxygen release, diffusion and consumption in the capillaries and tissue of the human brain. *Chemical Engineering in Medicine and Biology*, 135:135–241.

[184] Rissler, J., Nicklasson, H., Gudmundsson, A., Wollmer, P., Swietlicki, E., and Londahl, J. (2017). A set-up for respiratory tract deposition efficiency measurements (15-5000 nm) and first results for a group of children and adults. *Aerosol and Air Quality Research*, 17(6):1244–1255.

[185] Roman, M., Rossiter, H., and Casaburi, R. (2016). Exercise, ageing and the lung. *European Respiratory Journal*, 48(5):1471–1486.

[186] Rosati, R. J., Burton, R., McGregor, G., McCauley, R., Tang, W., and Spencer, R. (2013). Development of a three-dimensional model of the human respiratory system for dosimetric use. *Theoretical Biology and Medical Modelling*, 10(28):1–13.

[187] Ross, M. H. and Pawlina, W. (2015). *Histology a text and atlas with correlated cell and molecular biology*. Lippincott Williams and Wilkins, 7 edition.

[188] Rouleau, W. T. and Osterle, J. F. (1995). The application of finite difference methods to boundary-layer type flows. *Journal of the Aeronautical Sciences*, 22(4):249–254.

[189] Roy, T. and Popel, A. (1996). Theoretical predictions of end-capillary po2 in muscles of athletic and nonathletic animals at vo2max. *The American Journal of Physiology*, 271(2):H721–H737.

[190] Rozanek, M. and Roubik, K. (2007). Mathematical model of the respiratory system comparison of the total lung impedance in the adult and neonatal lung. *International Journal of Biomedical Sciences*, 2(4):249–252.

[191] Saffman, P. (1962). On the stability of laminar flow of a dusty gas. *Journal of Fluid Mechanics*, 13(1):120–128.

[192] Saha, J., Kumar, J., and Heinrich, S. (2016). A volume-consistent discrete formulation of particle breakage equation. *Computers & Chemical Engineering*, 97:147–160.

[193] Saini, A., Katiyar, V., and Pratibha (2010). Numerical simulation of the transport of inert gases in lung tissue. *International Journal of Applied Mathematics and Mechanics*, 6:46–57.

[194] Saini, A., Katiyar, V. K., and Parida, M. (2016). Two dimensional model of pulsatile flow of a dusty fluid through a tube with axisymmetric constriction. *World Journal of Modelling and Simulation*, 12(1):70–78.

[195] Saini, A., Katiyar, V. K., and Pratibha (2014). Effects of first order chemical reactions on the dispersion coefficient associated with laminar flow through the lungs. *International Journal of Biomathematics*, 7(2):1–12.

[196] Saini, A., Katiyar, V. K., and Pratibha (2015). Numerical simulation of gas flow through a biofilter in lung tissues. *World Journal of Modelling and Simulation*, 11(1):33–42.

[197] Saini, A., Katiyar, V. K., and Pratibha (2017). Two-dimensional model of nanoparticle deposition in the alveolar ducts of the human lung. *Applications and Applied Mathematics: An International Journal*, 12(1):305–318.

[198] Salathe, E., Wang, T., and Gross, J. (1980). Mathematical analysis of oxygen transport to tissue. *Mathematical Biosciences*, 51(1-2):89–115.

[199] Schlichting, H. and Gersten, K. (2017). *Numerical methods in boundary-layer theory*. Springer, Berlin, Heidelberg.

[200] Seraa, T., Uesugi, K., Yagi, N., and Yokota, H. (2013). Numerical simulation of airflow and microparticle deposition in a synchrotron micro-ct-based pulmonary acinus model. *Computer Methods in Biomechanics and Biomedical Engineering*, 18(13):1427–1435.

[201] Seth, G. S., Ansari, M. S., and Nandkeolyar, R. (2011). Unsteady hydromagnetic couette flow within a porous channel. *Tamkang Journal of Science and Engineering*, 14(1):7–14.

[202] Shang, Y., Inthavong, K., and Tu, J. Y. (2015). Detailed micro-particle deposition patterns in the human nasal cavity influenced by the breathing zone. *Computers and Fluids*, 114:141–150.

[203] Sharma, G. and Goodwin, J. (2006). Effect of aging on respiratory system physiology and immunology. *Clinical Interventions in Aging*, 1(3):253–260.

[204] Sharma, G. C. and Jain, M. (2004). A computational solution of mathematical model for oxygen transport in peripheral nerve. *Computers in Biology and Medicine*, 34(7):633–645.

[205] Sharma, N. and Gupta, A. K. (2017). Impact of time delay on the dynamics of seir epidemic model using cellular automata. *Physica A: Statistical Mechanics and its Applications*, 471(1):114–125.

[206] Sharma, P. (1992). Free convection effects on the flow past a porous medium bounded by a vertical infinite surface with constant suction and constant heat flux. ii. *Journal of Physics D Applied Physics*, 25(2):162–166.

[207] Sharma, P. R., Ali, S., and Katiyar, V. K. (2011). Mathematical modeling of heat transfer in blood flow through stenosed artery. *Journal of Applied Sciences Research*, 7(1):68–78.

[208] Siddiqui, A., Siddiqa, S., and Naqvi, A. (2018). Effect of constant wall permeability and porous media on the creeping flow through round vessel. *Journal of Applied & Computational Mathematics*, 7(2):1–6.

[209] Simakin, A. V., Voronov, V. V., Shafeev, G. A., Brayner, R., and Verduraz, F. B. (2001). Nanodisks of au and ag produced by laser ablation in liquid environment. *Chemical Physics Letters*, 348(3):182 – 186.

[210] Singh, J., Gupta, P. K., and Rai, K. N. (2011). Solution of fractional bioheat equations by finite difference method and hpm. *Mathematical and Computer Modelling*, 54:2316–2325.

[211] Singh, K. and Verma, G. N. (1995). Three-dimensional oscillatory flow through a porous medium with periodic permeability. *Zeitschrift fur Angewandte Mathematik und Mechanik*, 75(8):599–604.

[212] Sinha, P. and Prasad, D. (1995). Lubrication of rollers by power law fluids considering consistency variation with pressure and temperature. *Acta Mechanica*, 111(3-4):223–239.

[213] Sleeth, D., Balthaser, S., Collingwood, S., and Larson, R. (2016). Estimation of the human extrathoracic deposition fraction of inhaled particles using a polyurethane foam collection substrate in an iom sampler. *International Journal of Environmental Research and Public Health*, 13(3):1–14.

[214] Smith, G. (1986). *Numerical solution of partial differential equations*. Oxford University Press, U.S.A., 3 edition.

[215] Sorek, S. and Sideman, S. (1986). A porous medium approach for modelling heart mechanics. *Mathematical Biosciences*, 81(1):1–14.

[216] Srivastava, V. and Rai, K. N. (2010). A multi-term fractional diffusion equation for oxygen delivery through a capillary to tissues. *Mathematical and Computer Modelling*, 51(5-6):616–624.

[217] Steimlea, K., Mogensena, M., Karbinga, D., Sernab, J. B. d. l., and Andreassena, S. (2011). A model of ventilation of the healthy human lung. *Computer Methods and Programs in Biomedicine*, 101:144–155.

[218] Stober, W. (1972). Dynamic shape factors of nonspherical aerosol particles. *Assessment of Airborne Particles, Charles C Thomas Publisher, Springfield*, 46(1):329–333.

[219] Sturm, R. (2011). Theoretical and experimental approaches to the deposition and clearance of ultrafine carcinogens in the human respiratory tract. *Thoracic Cancer*, 2(2):61–68.

[220] Sturm, R. (2014). Theoretical deposition of nanotubes in the respiratory tract of children and adults. *Annals of Translational Medicine*, 2(1):1–11.

[221] Sturm, R. (2015). A computer model for the simulation of nanoparticle deposition in the alveolar structures of the human lungs. *Annals of Translational Medicine*, 3(19):281.

[222] Sturm, R. (2016). Bioaerosols in the lungs of subjects with different ages-part 1: deposition modeling. *Annals of Translational Medicine*, 4(11):1–12.

[223] Sturm, R. (2017). Bioaerosols in the lungs of subjects with different ages-part 2: clearance modeling. *Annals of Translational Medicine*, 5(5):1–8.

[224] Sturm, R. (2018). Theoretical deposition of variably sized platelets in the respiratory tract of healthy adults. *AME Medical Journal*, 3(5):1–10.

[225] Sturm, R. and Hofmann, W. (2009). A theoretical approach to the deposition and clearance of fibers with variable size in the human respiratory tract. *Journal of Hazardous Materials*, 170(1):210–218.

[226] Su, W. and Cheng, Y. S. (2006). Deposition of fiber in a human airway replica. *Journal of Aerosol Science*, 37(11):1429–1441.

[227] Sun, L., Park, J., and Barrera, A. L. (2017). A compartmental model for capillary supply. *Letters in Biomathematics*, 4(1):133–147.

[228] Sussman, R., Cohen, B., and Lippmann, M. (1991). Asbestos fiber deposition in a human tracheobronchial cast. i. experimental. *Inhalation Toxicology*, 3(2):145–160.

[229] Svartengren, M., Falk, R., and Philipson, K. (2005). Long-term clearance from small airways decreases with age. *European Respiratory Journal*, 26(4):609–615.

[230] Tal, A. (2006). Simplified models for gas exchange in the human lungs. *Journal of Theoretical Biology*, 238(2):474–495.

[231] Tawhai, M. and Lin, C. (2010). Image-based modeling of lung structure and function. *Journal of Magnetic Resonance Imaging*, 32(6):1421–1431.

[232] Taylor, G. (1953). Dispersion of soluble matter in solvent flowing slowly through a tube. *Proceedings of the Royal Society of London. Series A, Mathematical and Physical*, 219(1137):186–203.

[233] Tian, L., Shang, Y., Chen, R., Bai, R., Chen, C., Inthavong, K., and Tu, J. (2017). A combined experimental and numerical study on upper airway dosimetry of inhaled nanoparticles from an electrical discharge machine shop. *Particle and Fibre Toxicology*, 14(1):1–18.

[234] Tiwari, J. N., Tiwari, R. N., and Kim, K. S. (2012). Zero-dimensional, onedimensional, two-dimensional and three-dimensional nanostructured materials for advanced electrochemical energy devices. *Progress in Materials Science*, 57(4):724–803.

[235] Tomkiewicz, R., Biviji, A., and King, M. (1994). Effects of oscillating rheological properties mucous gel simulants. *Biorheology*, 31(5):511–520.

[236] Tsuda, A., Henry, F., and Butler, J. P. (1985). Chaotic mixing of alveolated duct flow in rhythmically expanding pulmonary acinus. *Journal of Applied Physiology*, 79(3):1055–1063.

[237] Vafai, K. and Tien, C. (1982). Boundary and inertia effects on convective mass transfer in porous media. *International Journal of Heat Mass Transfer*, 25(8):1183–1190.

[238] Vankan, W., Huyghe, J., Janssen, J., Huson, A., Hacking, W., and Schrenner, W. (1997). Finite element analysis of blood flow through biological tissue. *International Journal of Engineering Science*, 35(4):375–385.

[239] Varnera, V. D. and Nelson, C. M. (2017). Computational models of airway branching morphogenesis. *Seminars in Cell & Developmental Biology*, 67:170–176.

[240] Varshney, G., Katiyar, V. K., and Kumar, S. (2010). Effect of magnetic field on the blood flow in artery having multiple stenosis: a numerical study. *International Journal of Engineering, Science and Technology*, 2(2):67–82.

[241] Vedel, S., Hovad, E., and Henrik, B. (2014). Time-dependent taylor-aris dispersion of an initial point concentration. *Journal of Fluid Mechanics*, 752:107–122.

[242] Verma, V. K. and Gupta, A. K. (2018). Mhd flow in a porous channel with constant suction/injection at the walls. *International Journal of Pure and Applied Mathematics*, 118(1):111–123.

[243] Wang, Z., Hopke, P. K., Baron, P. A., Ahmadi, G., Cheng, Y. S., Deye, G., and Su, W.-C. (2005). Fiber classification of the influence of average air humidity. *Aerosol Science and Technology*, 39(11):1056–1063.

[244] Weber, L. M. (2011). Pulmonary particle deposition in relation to age, body weight, and species. Master's thesis, Mechanical Engineering.

[245] Weibel, E. (1963a). *Morphometry of the human lung*, chapter Introduction, pages 1–4.

[246] Weibel, E. (1963b). *Morphometry of the human lung*, chapter Organization of the Human Lung, pages 4–9.

[247] Whiteley, J. P., Gavaghan, D. J., and Hahn, C. E. W. (2001). Modelling inert gas exchange in tissue and mixed- venous-blood return to the lungs. *Journal of Theoretical Biology*, 209(4):431–443.

[248] Womersley, J. R. (1955). Method for the calculation of velocity, rate of flow and viscous drag in arteries when the pressure gradient is known. *The Journal of Physiology*, 127(3):553–563.

[249] Wong, K., Mazumdar, J., Pincombe, B., Worthley, S., Sanders, P., and Abbott, D. (2006). Theoretical modeling of micro-scale biological phenomena in human coronary arteries. *Medical & Biological Engineering & Computing*, 44(11):971–82.

[250] Wong, K. K. L., Tu, J., Mazumdar, J., and Abbott, D. (2010). Modelling of blood flow resistance for an atherosclerotic artery with multiple stenoses and poststenotic dilatations. *The ANZIAM Journal*, 51:66–82.

[251] Xu, G. B. and Yu, C. P. (1986). Effects of age on deposition of inhaled aerosols in the human lung. *Aerosol Science and Technology*, 5(3):349–357.

[252] Xu, H., Sun, M., and Zhao, X. (2017). Turing mechanism underlying a branching model for lung morphogenesis. *Plos One*, 12(4):1–20.

[253] Yan, W. W., Liu, Y., Xu, Y. S., and Yang, X. L. (2008). Numerical simulation of air flow through a biofilter with heterogeneous porous media. *Bioresource Technology*, 99:2156–2161.

[254] Yan, W. W., Su, Z. D., and Zhang, H. J. (2012). Effect of non-isothermal condition on heterogeneous flow through biofilter media by lattice boltzmann simulation. *Journal of Chemical Technology & Biotechnology*, 88(3):456–461.

[255] Zendehbudi, G. R. and Moayeri, M. S. (1999). Comparison of physiological and simple pulsatile flows through stenosed arteries. *Journal of Biomechanics*, 32(5):959–965.